MECHANISM OF THE INTRASEASONAL OSCILLATION IN THE SOUTH ASIAN SUMMER MONSOON REGION

A DISSERTATION SUBMITTED TO THE GRADUATE DIVISION OF THE UNIVERSITY OF HAWAI'I IN PARTIAL FULFILLMENT OF THE REQUIREMENTS FOR THE DEGREE OF

DOCTOR OF PHILOSOPHY

IN

METEOROLOGY

DECEMBER 2002

By
Hae-Kyung Lee Drbohlav

Dissertation Committee:

Bin Wang, Chairperson
James B. Nation
Pao-Shin Chu
Tim Li
Fei-Fei Jin

ABSTRACT

The mechanism of the intraseasonal oscillation in the South Asian summer monsoon region (ISO) is examined with a zonally averaged, atmospheric model (2D model), a three dimensional, atmospheric intermediate model (3D model).
In both models an ocean mixed layer model is added to examine the influence of air-sea interactions on the characteristics of the ISO.

Without the ocean mixed layer, an interaction between the baroclinic and barotropic modes of atmosphere can produce the ISO in both 2D and 3D models. The propagation of precipitation is caused by the phase relationship between convection and the barotropic divergence in the atmosphere. Most importantly, in the northern hemisphere, the vertical advection of July-mean easterly wind shear in regions of convection induces barotropic divergence (convergence) to the north (south) of convection. The resulting moisture convergence in the boundary layer induces the northward propagation of precipitation.

The initiation of convection is also produced by the barotropic divergence in the atmosphere. Especially, the strong July-mean vertical motion at 10S causes convergence in the boundary layer between 10S and the equator. The baroclinic mode, on the other hand, acts to enhance existing convection.

The differences between the ISO simulated by the 2D model and 3D models are caused by the zonal variation of winds, and atmospheric waves in the 3D model. The zonal divergence of barotropic winds enhances the westward propagation of convection

along 18N, and the barotropic mode of zonal advection drives the continuous northward movement of convection across the equator. The continuous northward propagation across the equator is also enhanced by the atmospheric waves, since the Rossby wave response to the heating source in both hemispheres creates a divergence in the baroclinic mode near the equator.

The inclusion of air-sea interactions in the 2D and 3D models improves the continuity in the northward propagation of convection. The meridional variation of SST enhances the boundary layer moisture convergence in front of the convection, thereby facilitating the northward propagation of convection. In addition, the SST gradient induced by the dipole type of Rossby-wave-like convection in the Indian ocean may increase the development of convection near the equator.

TABLE OF CONTENTS

LIST OF FIGURES

LIST OF ABBREVIATIONS AND SYMBOLS

overbar: represents the basic-state (July-mean climatology in this study).

prime: represents perturbation (anomalies in the intraseasonal oscillation).

subscript 1: represents variables at upper troposphere (300hPa in this study).

subscript 2: represents variables at lower troposphere (700hPa in this study).

subscript m: represents variables at mid-troposphere (500hPa in this study)

subscript e (or subscript B): represents variables at the top of atmospheric boundary layer (900hPa in this study).

u [m s^{-1}]: Zonal winds.

v [m s^{-1}]: Meridional winds.

ω [Pa s^{-1}]: Vertical pressure velocity.

ϕ [m^2 s^{-2}]: Geopotential.

T [^{0}C]: Atmospheric temperature.

SST (or sst) [^{0}C]: Sea surface temperature.

ST [^{0}C]: Surface temperature.

DSWRF [W m^{-2}]: Downward short wave radiation flux

HFL [W m^{-2}]: Heat fluxes (sensible heat flux + latent heat flux).

LHFL [W m^{-2}]: Latent heat flux.

Q'_m [J kg^{-1} s^{-1}]: Irreversible condensational heating.

q [unitless]: Specific humidity.

P_s [Pa]: Pressure at the model surface (100000 Pa).

P_e [Pa]: Pressure at the top of the boundary layer (90000 Pa).

ΔP [Pa]: Half-depth of the free atmosphere (40000Pa).

R: Specific gas constant (287 J deg^{-1} kg^{-1}).

L_c: Latent heat (2.5×10^6 J kg^{-1}).

ρ_o: Density of water (1.0×10^3 kg m^{-3}).

ρ_o: Air density in the atmospheric boundary layer (1.2×10^3 kg m^{-3}).

C_w [J $^0C^{-1}$]: Heat capacity of water.

C_E : Moisture exchange coefficient (1.5×10^{-3}).

A: Surface albedo (0.06).

S_o [W m^{-2}]: Downward solar radiation flux reaching sea surface under clear sky (320 W m^{-2}) Moisture exchange coefficient (1.5×10^{-3}).

S: Static stability parameter (7.5×10^{-7} at the surface, 9.2×10^{-7} at the lower troposphere, and 3.0×10^{-6} at the upper troposphere).

ϵ [s^{-1}]: Rayleigh friction coefficient (2.0×10^{-6} s^{-1}).

μ [s^{-1}]: Newtonian cooling coefficient (2.0×10^{-6} s^{-1}).

μ_o [s^{-1}]: Damping rate of anomalies in sea surface temperature (24 day^{-1}, 4.8×10^{-7} s^{-1}).

E_x [s^{-1}]: Dissipation coefficient in the boundary layer in the zonal direction (3.6×10^{-5} s^{-1}).

E_y [s^{-1}]: Dissipation coefficient in the boundary layer in the meridional direction (7.2×10^{-5} s^{-1}).

K [m^2 s^{-1}]: Horizontal momentum or thermal diffusion coefficient (5.0×10^5 m^2 s^{-1}).

λ[s]: Proportionality between perturbation cloudiness and surface wind convergence (2×10^5 s).

$\bar{h}$ [m]: Mean depth of the mixed layer (land 20m, ocean 55m in this study).

CHAPTER 1
INTRODUCTION

1.1 Background

The 40-50 day oscillation was first discovered by Madden and Julian (1971), who were using spectrum analysis to describe tropospheric, synoptic-scale feature in the tropics. In those days, spectra analysis was widely used to obtain information on waves in the stratosphere. The detection of waves in the stratosphere motivated researchers to use same spectrum analysis to investigate waves in the troposphere.

Madden and Julian computed spectra and cross spectra of surface pressure, zonal winds, and temperatures from the Canton rawinsondes, and found out that these variables had relative maxima at the periods between 41 and 53 days. They also noticed the large coherence between surface pressure, zonal winds, and temperatures at various levels over this period. In addition, this 40-50 day period of the spectra peaks and maxima in coherence were also observed between stations, and the coherence between the stations revealed the existence of a Kelvin-like wave to the east of the eastward-moving convection anomalies, and anticyclonic Rossby-like waves in the region west of convection anomalies.

After Madden and Julian first characterized the intraseasonal oscillation (ISO) as an eastward propagating equatorially trapped, wave number-one, baroclinic oscillation in the tropical wind field, several studies have noticed that the ISO propagates not only eastward but also poleward and westward (e.g., Wang and Rui, 1990). This concurrence

of eastward, northward, and westward propagation is a major feature of the ISO during boreal summer and mostly confined to the Indian Ocean and the Western Pacific.

Especially, the initiation of ISO convection in the equatorial Indian Ocean and the northward propagation of this disturbance have been a focus of studies since monsoon variability may be affected by the northward propagation of convection (Yasunari, 1979; Krishnamurti and Subrahmanyam, 1982; Hartmann and Michelsen 1989; Gautier and Di Julio 1990). For example, during the presence of convection in the northern hemisphere low level- easterlies, and -westerlies are found to the east, and to the west of the convection center, respectively. When these winds are superposed on mean westerlies in the northern Indian Ocean, the strength of the surface winds will increase (decrease) to the west (east)of convection. Thus, depending on where the convection center is located relative to the mean winds flow, the strength of the southwesterlies toward the Asian continent will create the favorable condition for the monsoon onset.

According to observational studies, the oscillation in the Indian Ocean and western North Pacific exhibits a northward movement of deep convection (e.g.,Yasunsri, 1979, 1980, 1981; Krishnamurti et al., 1985; Chen and Murakami, 1988; Gadgil and Srinivasan, 1990; Ouergli and De Felice, 1996). In the Indian Ocean convection originates near the equator and moves northward with a speed of 0.75 degree latitude per day (Krishnamurti and Subrahmanyam, 1982). In off-equatorial region the ISO propagates westward from western Pacific (date line) to the Indian Ocean along 10-20 N with a phase speed of 5 m/s (e.g., Nitta, 1987; Murakami, 1980; Wang and Rui, 1990; Lau and Lau, 1990).

Following observational studies, a number of theories have been proposed to explain the structure and propagation of summer ISO in the Indian Ocean and Western Pacific. According to Knutson et al. (1986), the initiation of equatorial outgoing long wave radiation (OLR) anomalies in the Indian monsoon region is associated with the eastward propagating equatorial OLR anomalies. Hu and Randall (1994, 1995), however, suggested that the initiation of convection near the equator in the Indian Ocean is a result of a stationary oscillating heat source that is forced by the nonlinear interaction among radiation, convection and surface moisture flux. Wang and Xie (1997) used an intermediate model to show that the initiation of the equatorial disturbance over the Indian Ocean may be caused by the westward propagation of moist Rossby waves, which are emanated from an equatorial eastward moving coupled Kelvin-Rossby wave packet.

In attempt to explain the northward propagation Webster (1983) introduced the role of the land surface heat fluxes, while Goswami and Shukla (1984), and Anderson and Stevens (1987) emphasized the interaction between convection and radiative relaxation in controlling the moist static stability.

The problem associated with these previous theories is that SST is assumed to be fixed, thus convection does not influence SST on intraseasonal timescales (e.g., Emanuel, 1987; Neelin et al., 1987; Wang and Xie, 1997, 1998). In recent years, the relationship between convection and SST has been documented (e.g.,Flatau et al., 1997; Waliser et al., 1999), as well as that of surface heat fluxes and disturbance (e.g., Jones and Weare, 1996; Lin and Jonson, 1996; Lau and Sui, 1997; Jones et al., 1998).

Therefore, the consideration of an interactive sea surface temperature (SST) in order to simulate the influence of convection on surface heat fluxes and SST is a new direction in recent researches. With the same token, the inclusion of an interactive SST in simulating the northward propagation of convection seems crucial for a better understanding of its propagation- mechanisms.

The goal of the dissertation is to improve the current understanding of boreal summer intraseasonal oscillation (BSISO) in the Indian Ocean. Firstly, observational data are analyzed to identify air-sea interaction of BSISO in the Indian Ocean. Secondly, the mechanism of air-sea interaction in the Indian Ocean is examined using two- and three- dimensional intermediate models. Experiments range from the case of the most simplified simulation using the zonally averaged model without ocean mixed layer to the most complicated case of three dimensional simulation with ocean mixed layer. By increasing the dimension and adding ocean mixed layer, the importance of local air-sea interactions versus the large scale dynamics on BSISO in the Indian Ocean is assessed.

CHAPTER 2
BOREAL SUMMER INTRASEASONAL OSCILLATION IN THE NCEP REANALYSIS DATA

2.1 Introduction

In this chapter observational data are used to identify the signal of the interaction between SST and convection in northward propagating ISO. In addition, the consistency between SST variability and convection with atmospheric variables such as winds, downward solar radiation fluxes (DSWRF) and surface heat fluxes (HFL, the sum of sensible heat flux and latent heat fluxes) is checked. This analysis renders a reference of air-sea interaction on which the model is built and verified.

2.2 Data and methods

The band-filtered (20-70 day) pentad means are computed from the daily averaged NCEP/NCAR reanalysis data of OLR, ST (1000 hPa), HFL, DSWRF, and surface winds (10m) for each summer (May, 30-Aug, 29) from 1982 to 1995. It should be noticed that NCEP/NCAR reanalysis data are constructed from both model results and observational data, and should be examined with caution. Nevertheless, a complete temporal and spatial coverage is an advantage of this data set over in-situ data sets.

In order to construct the structure of ISO, the band-filtered pentad -means of ST, winds, HFL, OLR, and DSWRF are zonally averaged (60-100E), and lagged cross correlations are calculated for these zonally averaged (60-100E) data. Finally, lagged cross correlations of 14 year of data are averaged.

The lagged cross correlation function $R_{xy}(k)$ between the state variables, x and y is defined by

$$R_{xy}(k) = \begin{cases} \dfrac{\left[\dfrac{1}{n}\sum_{t=1}^{n-k}(x_t-\bar{x})(y_{t+k}-\bar{y})\right]}{\left[\sigma_x\sigma_y\right]^{1/2}}, & k=0,1,\ldots,K; \\ \dfrac{\left[\dfrac{1}{n}\sum_{t=1-k}^{n}(x_t-\bar{x})(y_{t+k}-\bar{y})\right]}{\left[\sigma_x\sigma_y\right]^{1/2}}, & k=-1,-2,\ldots,-K. \end{cases}$$

where $\bar{x}$ and $\bar{y}$ denote the mean of times series x and y; σ_x and σ_y denote the variance of x and y. The letter n indicates the number of observations in each time series, and K represents the maximum lag of cross-correlations to be computed. Since the band filtered pentad -mean of each variable is used, the unit of both n and K is pentad.

The lagged cross-correlation function renders the relative role of x and y in their interaction. In other words, $R_{xy}(k)$ at positive (negative) time lags implies that y (k) is followed by x(k).

2.3 Zonally averaged pentad lagged cross correlations over the Indian Ocean

In this section, pentad lagged cross correlations are zonally averaged over the Indian Ocean (60-100E). In figure 2.1 (a), negative OLR (-OLR) at each latitude is correlated with -OLR at equator (reference latitude). Thus, the cross correlation at equator at zero lag in the panel (a) is 1. Figure 2.1. (a) shows that after the break out of

convection at the equator (EQ, zero pentad lag), convection propagates northward and southward.

Cross correlations between -OLR at equator and surface temperature (ST) at each latitude are shown in figure.2.1b. At the equator ST increases 2 pentads before convection. Once convection is organized at 0 pentad lag, ST decreases and the reduction of ST lasts for 3 pentads. The similarity in meridional structure between positive cross correlations (in positive pentad lag) in panel (a) and positive cross correlation (in negative pentad lag) in panel (b), with 2 pentads phase difference, suggested that the increase of ST is essential for the development of convection.

More than 3 pentads before the establishment of convection at the equator, a negative anomaly of HFL at the equator develops and propagates northward subsequently(Fig. 2.1c). As a result, the region between 5 N and 20 N experiences a decrease of HFL when convection develops at the equator at zero lag. It should be noticed that at the equator the decrease of HFL leads the increase of ST by 2 pentads, while in sub-equatorial region (around 15 N) the decrease of HFL concurs with the increase of ST. This difference in responding timescale seems due to the small heat content of landmass which extends from about 10 N to 20 N. When convective activity begins at the equator heat fluxes increase and the increase of heat fluxes is followed by the decrease of ST by one pentad (Fig. 2.1b). In southern hemisphere (5 S and 10S) the HFL diminishes around 1~2 pentad lag.

The meridional structure of downward shortwave radiation flux (DSWRF) is shown figure 2.1d. The similarity between figure 2.1d and figure 2.1a implies that a

decrease (increase) of DSWRF is associated with the existence (absence) of convection. The increase of DSWRF (Fig. 2.1d) in the northern hemisphere from -3 to 0 pentad lag favors the increase of ST (Fig. 2.1b) in the northern hemisphere in this period.

The relationship between surface zonal winds and -OLR is shown in figure 2.1e. At the equator easterlies are found at least three pentad before the enhance of convection. From -1 pentad to 2 pentad, when convection prevails at the equator, the winds are westerly. It is noticed that in the northern and equatorial Indian Ocean easterlies (westerlies) concur with the decrease (increase) of HFL. Since mean zonal winds in the northern Indian Ocean are westerlies, the cancellation between mean zonal winds and 20-70 day band filtered winds results in the decrease of HFL under easterlies. In the southern equatorial Indian Ocean, on the other hand, the latitude of easterlies (westerlies) coincides with the area of increasing (decreasing) HFL. This pattern is also the result of the interaction between mean zonal winds in the southern equatorial Indian Ocean (easterlies) and the intraseasonal winds in these latitudes.

The panel (f) in figure 2.1 presents the lagged cross correlation between -OLR at the equator and surface meridional winds at each latitude. The positive correlation and the negative correlation imply southerlies and northerlies, respectively. Around -1.5 pentad winds converges at the equator. Another convergence region is found at 1 pentad lag at 12 S. The location of convergence is typically ahead of convection or with convection.

In general, the increase of westerlies, the increase of HFL, and the decrease of ST concur in the northern equatorial Indian Ocean. Thus, the increase of surface

temperature might contribute to the northward propagation of convection. In the southern equatorial Indian Ocean, however, the decrease of surface temperature precedes the increase of surface heat fluxes by 2 pentads. As a consequence, the decrease of surface heat fluxes may not directly influence the southward propagating convection. As mentioned earlier, the short time lag among variables in the northern parts of the Indian Ocean can be caused by the small heat content of the Indian continent. In summary, it is shown that variations of convection and surface temperature are apparent and consistent with the variability of winds and heat fluxes.

2.4 Spatial variations of lagged-cross correlation

A complete cycle of northward propagating ISO in the Indian Ocean is described based on the the spatial variations of lagged cross correlation for 850 hPa winds, surface heat fluxes, the downward shortwave radiation flux, and outgoing long wave radiation (OLR). OLR is averaged over the equatorial Indian Ocean (2.5 S~2.5 N, 65~95 E), and -OLR is used as a reference of the lagged cross correlation. Note that minus OLR rather than OLR is used to imply convection. In figure 2.2(a) the spatial variation of the cross correlation between 850 hPa wind and the area averaged -OLR at -3 pentad lag are shown. In other words, it exhibits the change of 850 hPa wind field three pentad (15 days) before the development of the convective activity in the area covering from 2.5 S to 2.5 N, and from 65 E to 95 E. The intraseasonal winds in the northern Indian Ocean at -3 pentad are westerlies (Fig. 2.2a). The zonal component of the seasonal mean winds in the northern Indian Ocean are also westerlies (figure not shown). The interaction between

the mean westerlies and intraseasonal westerlies in this region results in the enhancement of the local wind speed. This enhancement of the local wind speed increases surface heat fluxes (Fig. 2.2b), which reduce surface temperature (Fig. 2.2d). In addition, the decrease of downward shortwave radiation flux (Fig. 2.2c) also causes a drop in surface temperature in the northern Indian Ocean and the tip of the Indian continent.

Meanwhile, the locally reversed Hadley circulation renders a subsidence in the southern equatorial Indian Ocean. The divergent winds at the equator (Fig. 2.2a) are easterlies, which interacts with seasonal mean westerlies. As a result, the surface heat fluxes at the equator is suppressed (Fig. 2.2b). The decrease of surface heat fluxes (Fig.2. 2b) and the increase of downward solar radiation flux (Fig. 2.2c) are responsible for the increase of surface temperature at the equator at -3 pentad (Fig. 2.2d). This increase of ST at the equator (Fig. 2.2d) facilitate the development of convection at zero lag by increasing the convective instability (e.g., the increase of moist convergence, the increase of low-level atmospheric temperature). Responding to the equatorial heating (Fig.2.2d), low-level equatorial winds are westerlies with cyclonic circulation at 5S (Fig. 2.2e). The cyclonic circulation in the southern hemisphere enhances the local Hadley circulation and inhibits convection in the northern Indian Ocean and continent. In addition, low-level easterlies in the northern Indian Ocean limit the surface fluxes. Due to the weak surface heat fluxes (Fig. 2.2f) and the strong downward shortwave radiation fluxes (Fig. 2.2g) the surface temperature in the northern Indian Ocean and the continent rises (Fig. 2.2h). To the contrary, the surface temperature along the equator diminishes.

2.5 Conclusion

The meridional structure of atmospheric variables in the Indian Ocean reveals that

- Convection at the equator moves both northward and southward.
- Increase of surface temperature leads the initiation of convection by 2 pentads.
- Increase of OLR leads the increase of surface temperature by 1 pentad.
- Interaction between seasonal winds and ISO winds governs the variability of latent heat fluxes, and influences the air-sea interaction.

CHAPTER 3

BOREAL SUMMER INTRASEASONAL OSCILLATION IN ZONALLY AVERAGED INTERMEDIATE MODEL

3.1 Introduction

The fundamental theories that have been developed to explain the eastward propagation of ISO can be classified in three groups (Flatau et al.,1997). The first groups is called wave-CISK (Conditional Instability of the Second Kind). In the wave-CISK theory convergence occurs in the region between easterlies and westerlies in an eastward propagating Kelvin wave. This low-level moisture convergence produces a new convective center which drives slow eastward motion of the whole system by releasing latent heat. This theory also suggests that westward propagating convection is a manifestation of Rossby waves. One problem of the wave-CISK theory is that results of numerical models are sensitive to convective parameterizations. In other word, wave-CISK modes develop only when Kuo-like parameterization is used in the model.

In contrast with the wave-CISK theory, Emanuel(1987) and Neelin et al. (1987) proposed a wind-induced surface heat exchange (WISHE) theory. According to this theory, convection forces low-level easterly winds to the east and low-level westerly winds to the west of convection region. As a result, in the presence of the mean equatorial easterly winds, the surface zonal winds will increase to the east and decrease to the west of convection. Since the surface heat fluxes are largely governed by wind speed, enhanced surface heat fluxes to the east of convection increases the low-level moist static energy, which leads unstable eastward propagation modes. The defect of WISHE is that

mean winds were taken to be easterlies. In reality, mean winds in Indian Ocean and Western Pacific are westerlies (Wang, 1988). In addition, Jones and Wear (1996) found that positive (upward) anomalies of latent heat fluxes are located to the west of convection, which is contrary to the prediction of WISHE.

The air-sea convective intraseasonal interaction (ASCII) is the latest theory which emphasized the different role of surface heat fluxes in the maintenance of ISO. In ASCII theory SST drops to the west of convection, due to the strong evaporation and oceanic vertical mixing, whereas SST increases to the east of convection in the region of weak easterlies. Thus, in the region to the east of convection, the increase of surface entropy favors the development of new convective center. By incorporating the effect of convection on SST, Flatau et al. (1997) were able to explain the eastward propagating ISO.

Although ASCII is a prominent theory in describing the eastward propagating ISO, it has not been applied to the northward propagating ISO. In this chapter, a zonally averaged intermediate model without interactive SST (without ASCII) is used to examine the physical mechanism of northward propagating ISO. In the first part of this chapter, the mechanism of ISO without the interactive SST is examined. In the second part, interactive SST (ASCII) is incorporated in the model so that its influence on the period, and the intensity of the oscillation is analyzed.

3.2 Model

3.2.1 Zonally averaged intermediate model

The two dimensional model (2D model) is zonally averaged version of an intermediate intraseasonal model (WX model, hereafter) used by Wang and Xie (1997). The 2D model represents an area average from 60E to100E, corresponding roughly to the south Asian summer monsoon region . The prescribed monthly mean state variables are also averaged over this longitude. Thus, the model results are dependent on the mechanism within the Indian Ocean without the explicit influence from the western Pacific.

The model consists of a 2-level free atmosphere, and one boundary layer. The meridional and time resolutions are 2^0 and 10 minutes, respectively. Momentum and continuity equations are applied at the upper (300hPa) and lower level (700hPa) of free atmosphere, and the thermodynamic and hydrodynamic equations are written in the middle level (level between upper- and lower-levels). These linearized primitive equations in a p coordinate, equatorial β-plan are:

$$\frac{\partial u'}{\partial t} = -\overline{v}\frac{\partial u'}{\partial y} - v'\frac{\partial \overline{u}}{\partial y} - \overline{\omega}\frac{\partial u'}{\partial p} - \omega'\frac{\partial \overline{u}}{\partial p} + \beta y v' - \varepsilon u' + K\frac{\partial^2 u'}{\partial y^2} \qquad (3.1a)$$

$$\frac{\partial v'}{\partial t} = -\overline{v}\frac{\partial v'}{\partial y} - v'\frac{\partial \overline{v}}{\partial y} - \overline{\omega}\frac{\partial v'}{\partial p} - \omega'\frac{\partial \overline{v}}{\partial p} - \beta y u' - \frac{\partial \phi'}{\partial y} - \varepsilon v' + K\frac{\partial^2 v'}{\partial y^2} \qquad (3.1b)$$

$$\frac{\partial T'}{\partial t} = -\overline{v}\frac{\partial T'}{\partial y} - v'\frac{\partial \overline{T}}{\partial y} + \frac{P}{R}\overline{S}\omega' + \frac{P}{R}S'\overline{\omega} + \frac{Q'}{C_p} - \mu T'$$

$$+ \mu\gamma(sst' - sst'_{Domain\ averaged}) + K\nabla^2 T' \qquad (3.1c)$$

$$\frac{\partial v'}{\partial y} + \frac{\partial \omega'}{\partial p} = 0 \qquad (3.1d)$$

$$\frac{\partial \phi'}{\partial p} = -\frac{RT'}{P} \qquad (3.1e)$$

where an overbar and prime represents the basic-state and perturbation, respectively; u, v, ω, ϕ, and T denote zonal and meridional winds, vertical pressure velocity, geopotential, and temperature, respectively; ϵ, μ and R are the Rayleigh friction coefficient, Newtonian cooling coefficient, and specific gas constant; K is the horizontal momentum or thermal diffusion coefficient and S is the dry static stability parameter.

Condensational heating, which is a major driving source of atmospheric circulation, is parameterized based on the moisture and heat budget following Kuo (1974). At the middle level, P_m, it is expressed as (Wang 1988)

$$Q'_m = \frac{\delta b L_c}{\Delta p}\left[-\omega'_m(\overline{q}_2 - \overline{q}_1) - \omega'_e(\overline{q}_e - \overline{q}_2)\right] \qquad (3.2)$$

where Q'_m represents the irreversible condensational heating; b measures the ratio of the amount of water vapor that condenses to the total moisture in the atmosphere; L_c is the latent heat; Δp is the half-depth of the free atmosphere; ω'_m and and ω'_e represent vertical pressure velocities at P_m and the top of the boundary layer P_e; and $\overline{q}_e$, $\overline{q}_2$, and $\overline{q}_1$ are the specific humidity of the basic state at the boundary layer, the lower and upper troposphere, respectively. The basic-state specific humidity is assumed to decay exponentially with height (Wang, 1998). Thus, the vertical distribution of moisture content is determined by the basic state surface specific humidity, $\overline{q}_s$.

The governing equations in the barotropic boundary layer can be described as (Wang, and Li, 1993):

$$\beta y v'_B - E_x u'_B = 0 \qquad (3.3a)$$

$$-\beta y u'_B - \frac{\partial \phi'_e}{\partial y} + \frac{R(P_s - P_e)}{2 P_e}\frac{\partial sst'}{\partial y} - E_y v'_B = 0 \qquad (3.3b)$$

$$\omega'_e = (P_s - P_e)(\frac{\partial v'_B}{\partial y}) \qquad (3.3c)$$

where P_s is pressure at the model surface; ϕ'_e denotes perturbation geopotential at P_e; u'_B and v'_B are perturbation zonal and meridional winds in the boundary layer; sst' represents perturbation sea surface temperature (SST); and E_x and E_y are Rayleigh friction coefficients in the zonal and meridional directions.

From Eq. (3.3), the Ekman pumping velocity can be written as

$$\omega'_e = D_3 \frac{\partial^2 \phi'_e}{\partial y^2} + D_4 \frac{\partial \phi'_e}{\partial y} - \frac{R(P_s - P_e)}{2 P_e}[D_3 \frac{\partial^2 sst'}{\partial y^2} + D_4 \frac{\partial sst'}{\partial y}] \qquad (3.4)$$

Where the coefficients are

$$D_3 = -\frac{(P_s - P_e)E_x}{E_x E_y + \beta^2 y^2}$$

$$D_4 = \frac{2(P_s - P_e)E_x \beta^2 y}{(E_x E_y + \beta^2 y^2)^2}$$

Due to mass conservation in a vertical column, the Ekman pumping velocity in the barotropic boundary layer is related to free atmosphere convergence as following:

$$\omega'_e = -\Delta P \sum_{k=1}^{2} \frac{\partial v'_k}{\partial y} \qquad (3.5).$$

Combining (3. 4) and (3. 5) leads to an elliptical equation for ϕ'_e:

$$D_3 \frac{\partial^2 \phi'_e}{\partial y^2} + D_4 \frac{\partial \phi'_e}{\partial y} = -\Delta P \sum_{k=1}^{2} (\frac{\partial v'_K}{\partial y}) + \frac{R(P_s - P_e)}{2 P_e}[D_3 \frac{\partial^2 sst'}{\partial y^2} + D_4 \frac{\partial sst'}{\partial y}] \qquad (3.6)$$

Here, the assumption, $\phi'_e = \phi'_2$ is made in order to close a set of equations. The domain of the 2D model is confined to an equatorial B plane between 40 S and 40 N. At the meridional boundaries the fluxes of mass, momentum, and heat normal to the boundaries vanishes.

In order to incorporate the interactive SST into the 2D models, SST anomaly (sst′) is approximated as followings (Wang and Xie, 1998):

If the mean surface temperature ($\overline{sst}$) is greater than or equal to 22 ^{0} C

$$\frac{\partial sst'}{\partial t} = D_{rad}\left(\frac{\partial v'_2}{\partial y}\right) - D_{eva}\left(\mathrm{sgn}^* \sqrt{(u'_2 * 0.4)^2}\,(\overline{sst} - 20) + \sqrt{(\overline{u}_2 * 0.4)^2}\, sst'\right) - \mu_o sst' \qquad (3.7a)$$

Otherwise,

$$\frac{\partial sst'}{\partial t} = D_{rad}\left(\frac{\partial v'_2}{\partial y}\right) - D_{eva}\ 1.8\ \left(\mathrm{sgn}^* \sqrt{(u'_2 * 0.4)^2}\right) \qquad (3.7b)$$

where over bar and prime denotes basic-state and perturbation quantities, respectively; *sst* denotes sea surface temperature; u_2 and v_2 are low-level zonal wind and meridional wind, respectively; *sgn*>0, when $\overline{u} * u' \geq 0$, otherwise sgn<0; ρ_a is air density in the atmospheric boundary layer. In the study by Hendon and Salby (1994), one event of ISO tens to have little correlation with the next one. It suggested that SST between oscillations should be set back to the mean state before the next ISO event occurs. Since the period of the ISO induced by the atmospheric dynamics were 24 days in this studies, the damping rate of sst′ (μ_o) is set to be (24 days)$^{-1}$.

D_{rad}, and D_{eva} are, respectively, the mixed layer heating coefficients associated with radiation, and evaporation processes. These coefficients are defined by

$$D_{rad} = \frac{0.622(1-A)S_o\lambda}{\rho_o C_w \bar{h}} \qquad (3.8a)$$

$$D_{eva} = \frac{\rho_a C_E L_c K_q}{\rho_o C_w \bar{h}} \qquad (3.8b)$$

$$\mu_o = \frac{\gamma}{\rho_o C_w \bar{h}} \qquad (3.8c)$$

where A, and S_0, are surface albedo, the downward solar radiation flux reaching sea surface under clear sky, respectively; ρ_o and C_w are the density and heat capacity of water, respectively; $\bar{h}$ represents the mean depths of the mixed layer (land 20m, ocean 55m); C_E, and L_c are moisture exchange coefficient, and latent heat; λ measures the proportionality between perturbation cloudiness and surface wind convergence; K_q=8.9 × 10^{-4} K^{-1} (Wang and Li, 1993), and γ=1.8$Wm^{-2}K^{-1}$ (Seager et al. 1988).

The 2D model used in this chapter are different from the original model in four aspects. First, the 2D model is a zonal mean version of the 3D model. In other words, atmospheric variable are averaged along zonal (x) direction. As a result, zonal geopotential gradient, zonal diffusion, zonal advection, and zonal divergence are neglected. The zonally averaged (from 60E to 100E) July mean of surface temperature, winds, and specific humidity are used as basic states.

Second, the long wave radiation cooling in eq. (3.1c) is modified. In the original model, the middle-tropospheric temperature perturbation from the basic equilibrium state is relaxed back at the rate of Newtonian cooling rate, whereas in the 2D model the

equilibrium temperature is assumed to have the same temperature as SST with reduced amplitude. As a result, not only the temperature perturbation in the middle troposphere but also the deviation of SST from its domain average affects the longwave radiation cooling in the 2D model (Wang and Li, 1993).

Third, the effect of surface temperature gradient is added to the boundary layer in the 2D model. In the WX model the momentum balance in the boundary layer holds among the geopotential gradient force, Coriolis force, and a Rayleigh friction. When air flows over the ocean this air parcel can be heated by the ocean surface sensible and latent fluxes. Wang and Li (1993) assumed that the gradient surface air temperature is equal to the SST gradient. Following the assumption of Wang and Li, the influence of surface temperature on the atmospheric boundary layer is approximated as equation (3.6).

Finally, the physics of the ocean mixed layer is implemented in the WX model. In the WX model monthly mean observational SST data is fed into the model as an initial condition. In the 2D model, the perturbation of SST from its monthly mean state is calculated. As indicated in the equation (3.7) determinant factors of SST anomaly are atmospheric cloudiness, wind-induced ocean surface evaporation, and Newtonian cooling. These three factors are chosen from the ocean mixed layer model by Wang and Xie (1998), and utilized in the 2D model as a first approximation. Flatau et al. (1997) also used a similar simple mixed layer model in which the ocean mixed layer physics is combined to the general atmospheric model.

3.2.2 Basic states

Two dimensional model represents an area -average from 60E to 100E. Thus, basic state that is used in this model is also zonally averaged from 60E to 100E. The zonal average mean flow is calculated using a July-mean circulation which is derived from the European Center for Medium-Range Weather Forecasts (ECMWF) grid analysis data for the period 1979-92. The 200- and 850 hPa winds are used as the mean winds at the upper (300hPa)- and lower (700hPa) levels of the model. This discrepancy in levels between basic state and anomalies is believed to be trivial in the model simulation. The mean temperature at the middle level is determined from geopotential thickness between 200 and 850 hPa by assuming hydrostatic balance. The vertical P velocity at the middle level is consistent with the mass continuity determined by the given winds field. The basic state free atmospheric moisture content, specific humidity, is calculated based on surface air temperature and dew point temperature. The complete description can be found in paper by Wang and Xie (1997).

In figure 3.1 the basic state of the 2D model is shown. The maximum of low-level easterlies and westerlies are found at 14S and 12N, respectively (Fig. 3.1a). In the upper troposphere, westerlies are dominant south to the 12S, while easterlies are dominant elsewhere (Fig. 3.1a). The vertical wind shear becomes zero at 8S, and westerly wind shear (easterly wind shear) is found in the area south (north) to 8S (Fig. 3.1c).

The July-mean meridional winds in the low atmosphere are southerlies in the whole domain (Fig. 3.1b). In the upper atmosphere, southerlies are persistent except the

region south to 28S (Fig. 3.1b). The vertical shear in the meridional winds is northerly shear, which means that the northerly wind increases with increasing height (Fig. 3.1 c).

The midtropospheric vertical motion (Fig. 3.1 d) indicates that a local maximum of sinking motion is found near the equator, and the maximum rising motion is found near 10S and 10N. The July-mean specific humidity (Fig. 3.1e) increase from southern boundary toward the northern hemisphere. A relatively sharp decrease of specific humidity is found north of 20N, since the existence of land decreases the specific humidity. The spatial variation of low-level July-mean winds and midtropospheric vertical motion is shown in figure 3.1f. Note that within the domain in this study (60E-100E), the zonal variation of basic states is much smaller than the meridional variation. Thus, zonally average basic state adequately represents//. the spatial variation in this domain.

3.3 Simulation of intraseasonal oscillation without the ocean mixed layer

3.3.1 Variation of u ′, v ′, and precipitation

Figure 3.2 shows (a) precipitation rate (mm/day), (b) low-level zonal wind, and (c) low-level meridional wind (m/sec) simulated from the 2D model without ocean mixed layer. Shading indicates precipitation greater than 2 mm/day. There are two locations of strong precipitation (Fig. 32a). One covers from 10N to 25N, and the other is located between 10S and the equator. The southern part of precipitation is not as organized as its counterpart in the northern hemisphere. The period of the oscillation is about 15-20 days.

The low-level winds in figure 3.2 (b) and (c) show that convection (precipitation) is followed by westerlies and southerlies.

It should be noted that the moisture convergence in the lower level of the atmosphere is the main source of precipitation, and consequently, the heat source of the atmospheric circulation. In addition, the convergence in the 2D model is dependent on the latitudinal variation of the meridional wind. As a result, it is necessary to examine the relationship between meridional wind and precipitation.

In figure 3.3 the precipitation rate and meridional winds at 300hPa from day 49 (a) to day 69 (h) are presented. At day 49, convection is located at latitude between 10N and 15N. When this convection moves northward from day 49 to day 61, its intensity decreases from more than 8mm/day (day 49) to less than 1mm/day (day 61).

Meanwhile, new convection is initiated in the area between 10S and the equator at day 53. The new convection propagates to the equator from day 53 to day 61. When convection approaches the equator at day 63, it divides into four different areas. Two of them are located to the north of the equator, and the other two are located in the southern hemisphere. The convection in the northern hemisphere intensifies, while convection in the southern hemisphere dissipates around day 65. From day 65, convection in the northern hemisphere keeps moving northward, and reaches 20N at day 69.

The life cycle of the precipitation rate illustrates the northward propagation of convection, which is initiated in the latitude between 10S and the equator. It also indicates that the northward propagation is not clear when convection passes the equator. Then what is the mechanism of the northward propagation and initiation of convection found in

a life cycle of precipitation rate? In order to understand the life cycle of precipitation rate, it is necessary to examine the factors that govern the precipitation rate.

In the 2D model, the specific humidity is absent in the upper atmosphere. Hence, the precipitation rate (Pr) is governed by the moisture convergence in the boundary layer and in the low-level of free atmosphere. That is

$$\mathrm{Pr} \approx -(\tfrac{\partial v_e'}{\partial y})\overline{q}_e - (\tfrac{\partial v_2'}{\partial y})\overline{q}_2 \qquad (3.9)$$

where subscription e and 2 indicate the boundary layer and low-level atmosphere (700hPa), respectively. Thus, $\overline{q}_e$ and $\overline{q}_2$ are specific humidity of July-mean climatology in boundary layer and lower atmosphere. Since the divergence in the boundary layer is balanced by the convergence in upper atmosphere or in lower atmosphere, the equation is 3.9 can be written as

$$\begin{aligned}\mathrm{Pr} &\approx -(\tfrac{\partial v_e'}{\partial y})\overline{q}_e - (\tfrac{\partial v_2'}{\partial y})\overline{q}_2 \\ &\approx -(-\tfrac{\partial v_1'}{\partial y} - \tfrac{\partial v_2'}{\partial y})\overline{q}_e - (\tfrac{\partial v_2'}{\partial y})\overline{q}_2 \\ &\approx \tfrac{\partial v_1'}{\partial y}\overline{q}_e + \tfrac{\partial v_2'}{\partial y}\overline{q}_e - \tfrac{\partial v_2'}{\partial y}\overline{q}_2 \qquad (3.10).\end{aligned}$$

The subscript 1 indicates the upper-level atmosphere (300hPa). In equation (3.10), the divergence in the upper atmosphere ($\frac{\partial v_1'}{\partial y} > 0$) increases the precipitation by inducing the convergence of moisture in the boundary layer $(i.e.\ \frac{\partial v_e'}{\partial y}\overline{q}_e \approx -\frac{\partial v_1'}{\partial y}\overline{q}_e < 0)$. The divergence in the lower atmosphere ($\frac{\partial v_2'}{\partial y} > 0$) also induces the moisture convergence in

the boundary layer $(i.e.\ \frac{\partial v_e'}{\partial y}\overline{q}_e \approx -\frac{\partial v_2'}{\partial y}\overline{q}_e < 0)$. On the other hand, the divergence in low atmosphere induces the moisture divergence in the low atmosphere $(\frac{\partial v_2'}{\partial y}\overline{q}_2 > 0)$. Thus, the total effect of low-level divergence $(\frac{\partial v_2'}{\partial y} > 0)$ results in a moderate increase of precipitation $(\frac{\partial v_2'}{\partial y}(\overline{q}_e - \overline{q}_2) > 0)$. As a result, the divergence in 700hPa or 300hPa increases the precipitation.

That is

$$\Pr \approx (\frac{\partial v_1'}{\partial y})\overline{q}_e + (\frac{\partial v_2'}{\partial y})(\overline{q}_e - \overline{q}_2) \qquad (3.11).$$

In order to diagnose meridional divergence in upper and lower atmosphere, the variation of meridional winds (v') in both layers is examined. The controlling factors of meridional wind are examined using the momentum equation in section 3.3.2.

3.3.2 Momentum equation of meridional wind anomalies

The local tendency of low-level (700hPa) meridional winds (panel a), the sum of Coriolis force and gropotential force (panel b) and sum of the other components in tendency equation (panel c) are shown for 15N (Fig. 3.4), 0N (Fig. 3.5), and 10S (Fig. 3.6). The vertical dotted line indicates the day at which the maximum precipitation rate is found at 15N. It is evident that regardless of the latitudinal location, the sum of Coriolis force and geopotential gradient force produces (Figs. 3.4b, 3.5b, and 3.6b) can produce the local tendency of meridional winds at 700hPa (Figs. 3.4a, 3.5a, and 3.6a).

The dominance of Coriolis force and geopotential gradient force (panel b) in controlling the local variation of upper-level (300hPa) meridional winds (panel a) is shown for 15N (Fig. 3.7), 0N (Fig. 3.8), and 10S (Fig. 3.9), as well. In conclusion, Coriolis force and geopotential gradient force are the most dominant terms that explain hthe local tendency of meridional winds at 15N, 0N and 10S in both upper- and lower-level of atmosphere.

3.3.3 Effect of meridional divergence on precipitation rate

In the previous section, it is verified that the momentum equation of meridional winds can be approximated by the sum of Coriolis force and geopotential gradient force. That is

$$\frac{\partial v'}{\partial t} \approx -\frac{\partial \phi'}{\partial y} - Byu' \qquad (3.12).$$

Note that the precipitation rate is proportional to meridional divergence in upper level or in low level of free atmosphere as shown in equation 3.11. In order to relate the variation of meridional winds with precipitation rate, the local derivative of equation 3.11 is taken. That is

$$\begin{aligned} \frac{\partial}{\partial t}\Pr &\approx \frac{\partial}{\partial t}\left(\frac{\partial v_1'}{\partial y}\right)\overline{q}_e + \frac{\partial}{\partial t}\left(\frac{\partial v_2'}{\partial y}\right)(\overline{q}_e - \overline{q}_2) \\ &= \frac{\partial}{\partial y}\left(\frac{\partial v_1'}{\partial t}\right)\overline{q}_e + \frac{\partial}{\partial y}\left(\frac{\partial v_2'}{\partial t}\right)(\overline{q}_e - \overline{q}_2) \qquad (3.13). \end{aligned}$$

After substituting the approximation of meridional momentum equation (Eq. 3.12) into equation of local tendency of precipitation rate (Eq. 3.13), we get

$$\frac{\partial}{\partial t}\Pr \approx \frac{\partial}{\partial y}(-\frac{\partial \phi_1'}{\partial y} - Byu_1')\overline{q}_e + \frac{\partial}{\partial y}(-\frac{\partial \phi_2'}{\partial y} - Byu_2')(\overline{q}_e - \overline{q}_2)$$
$$= \{\frac{\partial}{\partial y}(-\frac{\partial \phi_1'}{\partial y}) + \frac{\partial}{\partial y}(-Byu_1')\}\overline{q}_e$$
$$+ \{\frac{\partial}{\partial y}(-\frac{\partial \phi_2'}{\partial y}) + \frac{\partial}{\partial y}(-Byu_2')\}(\overline{q}_e - \overline{q}_2) \qquad (3.14).$$

The physical meaning of each terms in tendency equation of precipitation (Eq. 3.14) can be explained as the following. For convenience let's assume that the local tendency of meridional winds are governed by the geopotential gradient force, only. That is

$$\frac{\partial}{\partial t} v'_{G.G.F} = -\frac{\partial \phi'}{\partial y} \qquad (3.15).$$

The subscription G.G.F is used to indicate the wind induced by geopotential gradient force. Then term, $\frac{\partial}{\partial y}(-\frac{\partial \phi'}{\partial y})$ can be rewritten as

$$\frac{\partial}{\partial y}(-\frac{\partial \phi'}{\partial y}) = \frac{\partial}{\partial y}(\frac{\partial}{\partial t} v'_{G.G.F})$$
$$= \frac{\partial}{\partial t}(\frac{\partial v'_{G.G.F}}{\partial y}) \qquad (3.16).$$

It indicates that the minus laplacian of geopotential $(-\frac{\partial^2 \phi'}{\partial y^2})$ is equivalent to the increase

in divergence of meridional winds induced by the geopotential gradient force. The increase of divergence due to the geopotential gradient force is usually found near the center of convection in upper level of the atmosphere. When latent heat is released associated with convection, the rising air parcel from the mid-atmosphere increases the pressure in the upper level of atmosphere. The increase of pressure at the center of convection in upper level induces the meridional divergence near convection.

With the similar logic, the gradient of Coriolis force [$\frac{\partial}{\partial y}(-Byu_1')$] in equation (3.14) can be understood as an increase of the upper-level divergence induced by Coriolis force. For example, when local maximum of westerlies developes in the northern hemisphere, the local maximum of westerlies (u' > 0) generates the local maximum of northerly acceleration though the Coriolis force (-βyu'< 0). Because of these northerly acceleration at the center of convection, divergence (convergence) of meridional winds increases to the north (to the south) of the maximum of westerlies.

In figure 3.10 (a) the tendency of the moisture convergence (i.e. $\approx \frac{\partial}{\partial t}\mathrm{Pr}$, equation 3.14) in 700hPa and boundary layer becomes

$[-\frac{\partial}{\partial y}\frac{\partial \phi_1'}{\partial y}\overline{q}_e - \frac{\partial}{\partial y}Byu_1'\overline{q}_e - \frac{\partial}{\partial y}\frac{\partial \phi_2'}{\partial y}(\overline{q}_e - \overline{q}_2) - \frac{\partial}{\partial y}Byu_1'(\overline{q}_e - \overline{q}_2)]$ for day 49 is presented (-o-o-). These terms are used in equation 3.14 to diagnose the tendency of precipitation rate. Also shown in panel (a) is precipitation rate obtained from the 2D model (-•-•-).

On day 49, when maximum precipitation is found at 14N, the positive tendency of moisture convergence is found to be centered around 15N. This increase of moisture convergence will enhance the precipitation there. This, in turn, will induce the northward propagation of convection. The other region of increasing moisture convergence is found in the latitude between 10S and equator. Thus, this region is favorable for the initiation of new convection.

In graph 3.10b the tendency of boundary layer moisture convergence induced by divergence at 300hPa ($\frac{\partial}{\partial y}(-\frac{\partial \phi_1'}{\partial y} - Byu_1')\overline{q}_e$) is shown. The term

[$\frac{\partial}{\partial y}(-\frac{\partial \phi_2'}{\partial y} - Byu_2')(\overline{q}_e - \overline{q}_2)$] in graph 3.10c indicates the total effect of divergence at 700hPa on the tendency of moisture convergence. It is evident that the magnitude of term involving the upper-level divergence [$\frac{\partial}{\partial y}(-\frac{\partial \phi_1'}{\partial y} - Byu_1')\overline{q}_e$, Fig. 3.10b] is much larger than that involving the low-level divergence [$\frac{\partial}{\partial y}(-\frac{\partial \phi_2'}{\partial y} - Byu_2')(\overline{q}_e - \overline{q}_2)$, Fig. 3.10c]. It implies that the upper-level divergence is more influential than lower-level divergence on the tendency of precipitation rate. The reason is that while the divergence at 700hPa induces the moisture convergence in the boundary layer [$\frac{\partial}{\partial y}(-\frac{\partial \phi_2'}{\partial y} - Byu_2')\,\overline{q}_e > 0$, equation 3.14], it automatically produces the moisture divergence at 700hPa [$-\frac{\partial}{\partial y}(-\frac{\partial \phi_2'}{\partial y} - Byu_2')\,\overline{q}_2 < 0$, equation 3.14], the total effect of low-level divergence is just a slight increase of moisture convergence [$\frac{\partial}{\partial y}(-\frac{\partial \phi_2'}{\partial y} - Byu_2')(\overline{q}_e - \overline{q}_2) > 0$, equation 3.14].

On day 57, convection (implied by the local maximum of precipitation rate) is present in the latitude between 10S and equator, while the existing convection in the northern hemisphere moves northward (Fig. 3.11a). In the southern hemisphere, the maximum increase of moisture convergence is found in the latitude between 5S and equator (Fig. 3.11a). This maximum increase of moisture convergence near the equator

will lead convection to this location. It is also evident that the tendency of moisture convergence (Fig. 3.11a) coincides with that of moisture convergence induced by the divergence at 300hPa (Fig. 3.11b).

On day 60, the maximum precipitation is found in the latitude between 5S and equator (Fig. 3.12a). Again, the positive tendency of moisture convergence is found to the north of convection (Fig. 3.12a). Due to this moisture convergence to the north of convection, convection moves to further north on day 64.

On day 64, precipitation is found in three locations. Among three locations, the precipitation at 8N shows a maximum value (Fig. 3.13a). The tendency of moisture convergence to the north of convection in the northern hemisphere (10N) is larger than that in the southern hemisphere (4S, Fig. 3.13a). This meridional structure in the tendency of moisture convergence (Fig. 3.13a) is mostly induced by the upper-level divergence as shown in Figure 3.13b.

Since the July-mean specific humidity increases with latitude untill 14N, convection tends to be intensified as it propagates northward. On day 65, convection at 8N is fully intensified, whereas convection at the equator and southern hemisphere is suppressed (Fig. 3.14a). Behind (to the south of) convection, the moisture tends to diverge, while the convergence of moisture increases ahead (to the north) of convection (Fig. 3.14a). The change in moisture convergence induced by the upper-level divergence (Fig. 3.14b) is the most dominant factor in governing the tendency of moisture convergence in figure 3.14a.

Throughout a life cycle of convection, it is found that the increase of moisture convergence, located to the north of the existing convection, drives the existing convection to move northward. It is also suggested that the increase of moisture convergence initiates the new convection in the southern hemisphere. The spatial and temporal variation in *the tendency of moisture convergence is explicitly governed by the upper-level divergence.* In other words, the divergence at 300hPa enhances moisture convergence in the boundary layer, and this increase of moisture convergence is a cause of the initiation and the propagation of convection. Consequently, equation 3.14 can be further simplified as

$$\frac{\partial}{\partial t} pr \approx \frac{\partial}{\partial y}\left(-\frac{\partial \phi_1'}{\partial y}\right)\overline{q}_e + \frac{\partial}{\partial y}(-Byu_1')\overline{q}_e \qquad (3.17).$$

The equation 3.17 suggests that the tendency of precipitation can be explained by analyzing the variation of meridional divergence in upper level (300hPa).

3.3.4 Impact of meridional divergence at 300hPa on precipitation

In figure 3.15 the tendency of upper-level divergence (panel a), the tendency of upper-level divergence induced by geopotential gradient force (panel b), the tendency of upper-level divergence induced Coriolis force (panel c), and the precipitation rate (-•-) are shown. By comparing figures 3.15b and 3.15c, one can identify the relative importance between geopotential gradient force and Coriolis force in governing the tendency of precipitation rate, shown in equation 3.17.

When the maximum precipitation rate, indicating convection, is located at 14N (Fig. 3.15a) the upper-level divergence increases at the center of convection (14N) and to

the north of convection (16N). While the geopotential gradient force increases the upper-level divergence (Fig. 3.15b) at the center of convection, the increase of upper-level divergence induced by Coriolis force (Fig. 3.15c) is located to the north of the convective center.

Since the latent heat release associated with precipitation forces air-parcel to rise, the upper-level pressure at the center of convection increases. Consequently, the horizontal divergence and convergence in the upper level are generated at the center (14N) and adjacent to the center (16N) of convection, respectively (Fig. 3.15b).

While the upper-level divergence at the center of convection is enhanced by the geopotential gradient force, the upper-level divergence to the north of convection (16N) and the divergence between 12S and 6S (Fig. 3.15c) is intensified by Coriolis force (Fig. 3.15c). Especially, the increase of upper-level divergence in the southern hemisphere on day 49 facilitates the initiation of new convection in the latitude between 10S and 5S on day 57 (Fig. 3.16a).

When the new convection develops in the southern hemisphere on day 57, the maximum tendency of upper-level divergence is found near the equator (Fig. 3.16a). It implies that convection will move close to the equator in the future. This increase of upper-level divergence near the equator (Fig. 3.16a) is probably caused by the Coriolis force since the divergence component induced by Coriolis force (Fig. 3.16c) has the maximum value near the equator as well.

Convection located at 8S on day 57 moves to 2S on day 60 (Fig. 3.17a). The divergence at 300hPa increases at the center of convection and to the north of convection

(Fig. 3.17a). It should be noticed that when convection was located away from the equator, the Coriolis force was a primary force to produce the upper-level divergence to the north of convection. However, on day 60, when convection is located close to the equator, the geopotential gradient force seems to be more dominant in producing the upper-level divergence than the Coriolis force. It is due to the decrease of Coriolis parameter (βy) as it approaches the equator.

According to the geopotential gradient force (Fig. 3.17b), the upper-level convergence is found to the south of the center of convection. For example, in the region south (4S) to the convective center, the mid-tropospheric temperature drops following the dissipation of the previous convection (Figure not shown). As a result, the upper-level geopotential decreases, and the upper-level convergence develops at 4S.

On the other hand, the upper-level atmosphere (300hPa) to the north of the convective center, such as the equator, shows a slight positive in divergence (Fig. 3.17b). In this region atmosphere is free of convection. Thus, the downward motion in this region increases the local mid-tropospheric temperature though the adiabatic warming. Due to the warming of mid-troposphere, the upper-level pressure increases, which may be responsible for the slight divergence in the upper-level atmosphere in the northern hemisphere.

On day 64, the local maximum of precipitation is located at 8N (Fig. 3.18a), whereas the other two are located at the equator and 6S. These three convection areas located in southern-, northern- hemisphere, and the equator compete against one another for moisture convergence. Since the upper-level divergence (Fig. 3.18a) is governed by

the upper-level geopotential gradient force (Fig. 3.18b), the stronger convection produces the stronger upper-level divergence, which provides positive feedback to convection by enhancing the moisture convergence in the boundary layer. Since the climatological July mean specific humidity increases with latitude, it is more likely that convection in the northern hemisphere will be intensified though the positive feedback between convection and upper-level divergence. This in return, will suppress the other convection areas located at the equator and in the southern hemisphere.

The precipitation rate at 8N increases from 4.5 mm/day on day 64 to close to 8mm/day on day 65 (Fig. 3.19a). While convection in the northern hemisphere intensifies, convection in the southern hemisphere and equator disappears. The upper-level geopotential gradient force induces the maximum increse of upper-level divergence at the center of convection (Fig. 3.19b), while the upper-level Coriolis force induces the maximum increase of upper-level divergence (convergence) to the north (south) of convection (Fig. 3.19c). In addition, the Coriolis force enhances the upper-level divergence between 12S and 6S (Fig. 3.19c).

The Coriolis force in the upper level (300hPa) is a dominant force that enhances the upper-level divergence to the north of convection, and induces the northward propagation of convection, except near the equator. This tendency of upper-level divergence is an effective predictor, since it is explicitly related to the tendency of precipitation rate. From above conclusion, we can further simplify the precipitation-tendency-equation (Eq. 3.17) as

$$\frac{\partial}{\partial t} pr \approx \frac{\partial}{\partial y}(-Byu_1')\overline{q}_e \qquad (3.18).$$

The equation 3.18 links the upper-level divergence induced by the Coriolis force to the tendency of precipitation rate. Main variables of equation 3.18 are zonal winds in the upper atmosphere, and the precipitation rate. Thus, by studying the relationship between these two variables one can explain how the upper-level zonal winds impact convection, as well as the feedback of convection on the upper-level zonal winds. In next two sections, the feedback between convection and upper-level zonal winds and vice versa are elaborated.

3.3.5 Influence of zonal winds at 300hPa on convection

In this section, the focus is on the meridional variation of upper-level zonal winds, which increases the tendency of the precipitation. In equation 3.18, it is explicitly shown that the meridional divergence of zonal winds at 300hPa is responsible for the increase of precipitation. It should be noticed that since the Coriolis parameter (βy) gets close to zero near the equator, the influence of upper-level zonal winds ($-\beta u_1' \overline{q}_e$) rather than the influence of meridional divergence of upper level zonal winds ($-\beta y \frac{\partial u_1'}{\partial y} \overline{q}_e$) governs precipitation near the equator [i.e. $\frac{\partial}{\partial y}(-\beta y u_1')\overline{q}_e \approx -\beta u_1' \overline{q}_e$ *in* 3.18]

However, the influence of upper-level zonal winds on the propagation of convection across the equator is not substantial in the 2D model, the focus is on the initiation of convection in the southern hemisphere on day 49, the propagation of convection from the southern hemisphere to the equator on day 57, and the northward

propagation of convection starting from 8N to 20 N. Thus, the meridional variation of upper-level zonal winds is examined for day 49, day 57, and day 65.

In figure 3.20a, zonal winds at 300hPa (-o-), and precipitation rate (-•-) on day 49 is presented. The maximum westerly is found at the center of maximum precipitation at 14N, and the maximum easterly is found at 12S. The maximum westerly at 14N generates the Coriolis force ($-\beta y u'$) which accelerates northerlies, while at 12S, maximum of easterly accelerates northerlies though the Coriolis force ($-\beta y u'$) (Fig. 3.20b).

That is

$$14N: \quad u_1' > 0 \ (\max.westelires), \quad By > 0 \ (North.\ hemisph.)$$
$$\frac{\partial v_1'}{\partial t} \approx -Byu_1' < 0 \quad (14N) \qquad (3.9a),$$
$$12S: \quad u_1' < 0 \ (\max.eastelires), \quad By < 0 \ (South.\ hemisph.)$$
$$\frac{\partial v_1'}{\partial t} \approx -Byu_1' < 0 \quad (12S) \qquad (3.9b).$$

As a result of the increase of northerlies at14N, the divergence (16N) and the convergence (12N) are produced to the north and to the south of the convective center, respectively (Fig. 3.20c). The acceleration of northerlies at 12S (Fig. 3.20b) also generates the divergence at 10S (Fig. 3.20c).

On day 57, when the new convection is initiated in the southern hemisphere, the upper-level zonal winds from 14S to12N are easterlies, and the local maximum of easterly is found near the equator (Fig. 3.21a). Since the Coriolis parameter (βy) changes its sign across the equator, the Coriolis force induced by easterlies in the northern (southern hemisphere) hemisphere accelerates the southerlies (northerlies) (Fig. 3.21b).

Acceleration of southerlies to the north of the equator, and the acceleration of northerlies to the souther of the equator result in a maximum divergence of meridional winds at the equator (Fig. 3.21c). This maximum upper-level divergence at the equator facilitates convection in the southern hemisphere to move toward the equator.

When convection arrives at 8N, upper-level westerlies are dominant at the center of convection (Fig. 3.22a). The Coriolis force on the upper-level westerlies accelerates the northerly component at 10N (Fig. 3.22b). If the Coriolis parameter is constant (f-plane), the maximum increase of northerly component should be found in the latitude of maximum westerlies. In this model the Coriolis parameter varies, and the maximum acceleration of northerly component is found to the north of maximum westerlies. In any case, the Corioils force (Fig. 3.22b) enhances the upper-level divergence to the north of the convective center (Fig. 3.22c). This upper-level divergence induces the moisture convergence in the boundary, and forces the existing convection to move northward.

In summary, upper-level zonal winds may affect convection in two ways. First, the local maximum of upper-level easterlies in the southern hemisphere can initiate convection by producing the upper-level divergence to the north of maximum easterlies. Second, the maximum of upper-level westerlies at the center of convection in the northern hemisphere can move convection northward by generating the upper-level divergence to the north of existing convection. It is the Coriolis force on the local maximum of easterlies (westerlies) in the southern hemisphere (northern hemisphere) that generates the upper-level divergence in the region north of convection. So far, the impact

of upper-level zonal winds on the propagation and the initiation of convection is analyzed.

Then, why is the maximum of upper-level westerlies found at the center of convection in the northern hemisphere? In addition, why is the local maximum of upper-level easterlies is found between 10S and the equator, when convection is located in the northern hemisphere? By answering these questions, one can understand the feedback of convection on the upper-level zonal winds. In next section, the variation of upper- level zonal winds is examined by analyzing the momentum equation in zonal direction.

3.3.6 Momentum equation of zonal wind anomalies

In this section, the momentum equation of zonal wind anomalies in the upper-level atmosphere (300hPa) is examined. The reason of focusing on upper level is that the upper-level divergence, induced by the Coriolis force on zonal winds, is the most dominant force to predict the precipitation rate as shown in (3.18). That is

$$\frac{\partial}{\partial t} pr \approx \frac{\partial}{\partial y}(-By\, u_1')\, \overline{q}_e \qquad (3.18).$$

In figure3.23 components of zonal momentum equation at 300hPa at 15N are shown. The vertical dotted line along day 32, day 50, day 67, and day 85 indicates the day when the maximum precipitation rate is found at 15N. The local tendency of zonal winds shows that the westerly component increases upon the arrival of convection (Fig. 3.23a). It is consistent with the previous results. That is, the upper-level westerlies are found at the center of convection. The increase of westerlies at the center of convection

shown in the local tendency (Fig. 3.23a) is caused by the vertical advection of July-mean zonal winds ($-\omega'\frac{\partial\bar{u}}{\partial p} > 0$, Fig. 3.23d). It is due to the rising motion at the center of convection that conveys the westerly momentum of July-mean zonal winds to the upper level. The decrease of westerlies in local tendency of zonal wind anomalies on day 51, and day 68 (Fig. 3.23a) is due to the Coriolis force that deflects the upper- level northerlies behind convection ($By v' < 0$, Fig. 3.23f).

In order to emphasize that the vertical advection of July-mean zonal winds governs the tendency of upper-level zonal wind anomalies at 15N, components of zonal momentum equation at 300hPa (Fig. 3.24a) are divided into two groups (Figs. 3.24b and 3.24c). The fist group consists of the vertical advection of July-mean zonal winds (Fig. 3.24b). The other terms in the momentum equation are combined to form the second group (Fig. 3.24c). It is evident that the vertical advection of July-mean zonal winds ($-\omega'\frac{\partial\bar{u}}{\partial p}$, Fig. 3.24b) alone can sufficiently produce the local tendency of upper-level zonal winds at 15N ($\frac{\partial u'}{\partial t}$, Fig. 3.24a).

At the equator, the easterly component in local tendency increases on day 50 and day 67 (Fig. 3.25a). Theses are days when convection is located at 15N, and the suppression prevails at the equator and in the southern hemisphere. The increase of easterly component in local variation is caused by the meridional advection of zonal wind anomalies by July-mean meridional winds ($-\bar{v}\frac{\partial u'}{\partial y}$, Fig. 3.25), and the meridional

advection of July-mean zonal winds by the meridional wind anomalies ($-v'\frac{\partial \bar{u}}{\partial y}$, Fig. 3.25c).

In July the upper-level meridional winds are northerlies ($\bar{v}<0$, Fig. 3.1b). On day 50 and day 67 convection is located at 15N, and upper- level northerlies ($v'<0$) are found to the south of the convective center. Accordingly, upper -level winds are northerlies at the equator as well as in the southern hemisphere.

Since the sign of Coriolis parameter changes across the equator, Coriolis force on the upper- level northerlies accelerates easterlies (i.e. $\frac{\partial u'}{\partial t} \approx \beta y v' < 0$) in the north of the equator and westerlies (i.e. $\frac{\partial u'}{\partial t} \approx \beta y v' > 0$) in the south of the equator. As a result, on day 50 and day 67 the upper-level easterlies increase with latitude from the equator to the convective center at 15N ($\frac{\partial u'}{\partial y}<0$, Fig. 3.26b). Therefore, at the equator, the meridional advection of zonal wind anomalies by the July-mean meridional winds becomes negative ($-\bar{v}\frac{\partial u'}{\partial p}<0$) when convection is located at 15N. This negative advection of zonal wind anomalies is one factor that causes the upper-level easterly anomalies at the equator on day 50 and day 67.

The other term that causes the easterly component in the tendency equation on day 50 and day 67 (Fig. 3.25a) is a meridional advection of July-mean zonal winds by meridional wind anomalies ($-v'\frac{\partial \bar{u}}{\partial y}$, Fig. 3.25c). In the upper atmosphere (300hPa), the July-mean zonal winds are easterly ($\bar{u}<0$) in the northern hemisphere, and westerly

($\bar{u} > 0$) in the southern hemisphere (Fig. 3.27a). Thus, the upper-level July-mean easterly increases with increasing latitude ($\frac{\partial \bar{u}}{\partial y} < 0$, Fig. 3.27a).

On day 50, and day 67 convection is located at 15N, so that the low level- and upper level- meridional anomaly winds are southerlies and northerlies, respectively (Fig. 3.27b). Thus, during the absence of convection at the equator, the upper-level northerlies ($v' < 0$) induces the negative advection of July-mean zonal winds ($-v' \frac{\partial \bar{u}}{\partial y} < 0$). This negative advection of July-mean zonal winds is responsible for the increase of easterly at the equator on day 50, and day 67. It is again confirmed in figure 3.28 that the increase of upper-level easterly in the absence of convection at the equator (Fig. 3.28a) is caused by the sum of the meridional advection of July-mean zonal wind, and the meridional advection of zonal wind anomalies (Fig. 3.28b). The other terms (Fig. 3.28c) are trivial in the development of upper-level easterly at the equator on day 50 and day 67.

At 10S, the increase of easterly component in the upper- level zonal winds ($\frac{\partial u'}{\partial t} < 0$, Fig. 3.29a) on day 52 and day 69 are induced by the negative meridional advection of July-mean zonal winds ($-v' \frac{\partial \bar{u}}{\partial y} < 0$, Fig. 3.29b) and the negative vertical advection of zonal wind anomalies ($-\bar{\omega} \frac{\partial u'}{\partial p} < 0$, Fig. 3.29e).

At 300hPa, the maximum of July-mean westerly is found to the south of 25S, while the maximum of July-mean easterly is found between 10N and 15N (Fig. 3.1a). Thus, the meridional gradient of the July-mean zonal winds at 300hPa is negative

($\frac{\partial \bar{u}}{\partial y} < 0$). Since convection is located at 15N, the upper-level meridional winds at 10S are northerlies ($v' < 0$). As a result, the meridional advection of July-mean zonal winds in the upper atmosphere is negative ($-v' \frac{\partial \bar{u}}{\partial y} < 0$, Fig. 3.29c), and this negative advection increases the upper-level easterlies at 10S.

It should be remembered that on day 50 and day 67 the low-level zonal winds at 10S are easterlies (Figs. 3.2b, and 3.26b). The existence of convection at 15N drives the low-level southerlies at 10S, and the Coriolis force on this low-level southerlies results in the low-level easterlies at 10S. The dominance of low-level easterlies at 10S causes the westerly vertical shear ($\frac{\partial u'}{\partial p} < 0$). The combination of the westerly vertical advection ($\frac{\partial u'}{\partial p} < 0$) and the July-mean upward motion at 10S ($\bar{\omega} < 0$, Fig. 3.1d) leads to the negative vertical advection of zonal wind anomalies ($-\bar{\omega} \frac{\partial u'}{\partial p} < 0$, Fig. 3.29e) on day 50 and day 67. This negative vertical advection is the other reason that upper-level easterlies increase at 10S on day 50 and day 67.

In figure 3.30 the group made of the meridional advection of July-mean zonal winds ($-v' \frac{\partial \bar{u}}{\partial y}$) and the vertical advection of zonal wind anomalies ($-\bar{\omega} \frac{\partial u'}{\partial p}$) (Fig. 3.30b) is compared with the local derivative of upper-level zonal wind anomalies ($\frac{\partial u'}{\partial t}$, Fig. 3.30a). It is evident that the negative meridional advection of July-mean zonal winds and the negative vertical advection of zonal wind anomalies ($-v' \frac{\partial \bar{u}}{\partial y} - \bar{\omega} \frac{\partial u'}{\partial p} < 0$, Fig.

3.30b) leads the increase of upper-level easterlies in the local derivative ($\frac{\partial u'}{\partial t}<0$, Fig. 3.30 a).

In summary, in the area north of 10N, the vertical advection of July-mean zonal winds ($-\omega'\frac{\partial \overline{u}}{\partial p}$) accelerates the upper-level westerlies at the center of convection. At the equator the meridional advection of zonal winds ($-\overline{v}\frac{\partial u'}{\partial y}-v'\frac{\partial \overline{u}}{\partial y}$) enhances the upper-level easterlies. At 10S, the meridional advection of July-mean zonal winds and the vertical advection of zonal wind anomalies ($-v'\frac{\partial \overline{u}}{\partial y}-\overline{\omega}\frac{\partial u'}{\partial p}$) are responsible for the increase of upper-level easterlies.

When convection is located in the northern hemisphere, these upper-level westerlies at the center of convection promote the northward propagation, whereas upper-level easterlies at the equator and in the southern hemisphere facilitate the new development of convection. Especially, the increase of upper-level easterlies induced by the vertical advection by July-mean rising motion (i.e. $\frac{\partial u'}{\partial t}\approx-\overline{\omega}\frac{\partial u'}{\partial p}<0$) is a unique feature at 10S.

3.3.7 Impact of July-mean flows on intraseasonal oscillation

From the previous section, it is suggested that the vertical advection of zonal wind anomalies ($-\overline{\omega}\frac{\partial u'}{\partial p}$), and the vertical advection of July-mean zonal winds ($-\omega'\frac{\partial \overline{u}}{\partial p}$) are essential for the initiation and the propagation of convection, respectively. In this

section, it is attempted to confirm this suggestion using six experiments. In each experiment, the vertical advection of zonal wind anomalies ($-\overline{\omega}\frac{\partial u'}{\partial p}$), and the vertical advection of July-mean zonal winds ($-\omega'\frac{\partial \overline{u}}{\partial p}$) are artificially enhanced or reduced.

In three experiments, the vertical advection of zonal wind anomalies ($-\overline{\omega}\frac{\partial u'}{\partial p}$) is set to be 0% (Exp.1), 30% (Exp.2), and 70% (Exp.3) of the original value. That is

$$Exp.1 \quad -\overline{\omega}\frac{\partial u'}{\partial p} * 0.0 \quad (3.20a)$$
$$Exp.2 \quad -\overline{\omega}\frac{\partial u'}{\partial p} * 0.3 \quad (3.20b)$$
$$Exp.3 \quad -\overline{\omega}\frac{\partial u'}{\partial p} * 0.7 \quad (3.20c).$$

By comparing results among expt1, expt2, and expt3, one may identify the effect of the vertical advection of zonal wind anomalies on the intraseasonal oscillation. When $-\overline{\omega}\frac{\partial u'}{\partial p}$ is set to be zero, the initial disturbance produced on day 1 is dissipated by day 10 (Fig. 3.31a). When the magnitude $-\overline{\omega}\frac{\partial u'}{\partial p}$ is increased from 30% (Fig. 3.31b) to 70% (Fig. 3.31c) the frequency of convection increases, as well as the intensity of convection. It indicates that $-\overline{\omega}\frac{\partial u'}{\partial p}$ plays an important role for the repetition of the life cycle (periodicity) of convection.

In experiments 4, 5, and 6 the weight of the vertical advection of July-mean zonal winds ($-\omega'\frac{\partial \overline{u}}{\partial p}$) is changed from 70% to 140% of its original value. As the weight of vertical advection increases from 70% (Fig. 3.32a) to 140% (Fig. 3.32c) of the original value (Fig. 3.32b), the frequence and the propagating velocity increases. It suggests that

the vertical advection of July-mean zonal winds can affect both the periodicity and the northward propagation of convection in the northern hemisphere.

3.3.8 Barotropic mode and baroclinic mode in the atmosphere

In this section, the barotropic mode and the baroclinc mode in the atmosphere are examined. In this examination, the barotropic mode is defined as the sum of any variable in the upper atmosphere (300hPa) and the lower atmosphere (700hPa), while the baroclinic mode is defined as the difference in variables between the upper atmosphere and lower atmosphere. That is

$$BarotropicMode\ of\ X: \quad \frac{X\ (in\ 300\,hPa)\ +X\ (in\ 700hPa)}{2} \qquad (3.21a)$$

$$BaroclinicMode\ of\ X: \quad \frac{X\ (in\ 300\,hPa)\ -X\ (in\ 700hPa)}{2} \qquad (3.21b).$$

Here, X represents any arbitrary variable. The reason of this classification is that the barotropic mode and baroclinic mode are connected with the moisture convergence in the atmospheric boundary layer and in the low level of the atmosphere, respectively.

According to the continuity equation, the barotropic mode of divergence controls the moisture convergence in the boundary layer. Thus, when the barotropic divergence at 300hPa increases, so does the moisture convergence in the boundary layer. On the other hand, the increase of divergence at 700hPa enhances the barotropic mode of divergence ($\frac{Div_{300\,hPa}+Div_{700\,hPa}}{2}$), but reduces the baroclinic mode of divergence

$(\frac{Div_{300hPa} - Div_{700hPa}}{2})$, at the same time. As a result, the convergence in the boundary layer is enhanced, but the convergence at 700hPa is suppressed.

In previous section, the tendency of the precipitation rate is expressed as

$$\begin{aligned}\frac{\partial}{\partial t}\Pr &\approx \frac{\partial}{\partial y}(-\frac{\partial\phi_1'}{\partial y} - Byu_1')\overline{q}_e + \frac{\partial}{\partial y}(-\frac{\partial\phi_2'}{\partial y} - Byu_2')(\overline{q}_e - \overline{q}_2) \\ &= \{\frac{\partial}{\partial y}(-\frac{\partial\phi_1'}{\partial y}) + \frac{\partial}{\partial y}(-Byu_1')\}\overline{q}_e \\ &\quad + \{\frac{\partial}{\partial y}(-\frac{\partial\phi_2'}{\partial y}) + \frac{\partial}{\partial y}(-Byu_2')\}(\overline{q}_e - \overline{q}_2) \qquad (3.14).\end{aligned}$$

Since

$$u_1' = \frac{u_1'+u_2'}{2} + \frac{u_1'-u_2'}{2} \qquad (3.22a),$$

$$u_2' = \frac{u_1'+u_2'}{2} - \frac{u_1'-u_2'}{2} \qquad (3.22b),$$

$$\phi_1' = \frac{\phi_1'+\phi_2'}{2} + \frac{\phi_1'-\phi_2'}{2} \qquad (3.22c),$$

$$\phi_2' = \frac{\phi_1'+\phi_2'}{2} - \frac{\phi_1'-\phi_2'}{2} \qquad (3.22d)$$

the equation (3.14) can be rewritten as

$$\begin{aligned}\frac{\partial}{\partial t}pr &\approx -\frac{\partial}{\partial y}(\frac{\partial}{\partial y}\frac{\phi_1'+\phi_2'}{2} + \beta y\frac{u_1'+u_2'}{2})(2\overline{q}_e - \overline{q}_2) \\ &\quad -\frac{\partial}{\partial y}(\frac{\partial}{\partial y}\frac{\phi_1'-\phi_2'}{2} + \beta y\frac{u_1'-u_2'}{2})(\overline{q}_2) \qquad (3.23)\end{aligned}$$

The first term, $-\frac{\partial}{\partial y}(\frac{\partial}{\partial y}\frac{\phi_1'+\phi_2'}{2} + \beta y\frac{u_1'+u_2'}{2})(2\overline{q}_e - \overline{q}_2)$, indicates the moisture convergence induced by the barotropic mode of the atmosphere (barotropic mode of moisture convergence, hereafter), and the second term, $-\frac{\partial}{\partial y}(\frac{\partial}{\partial y}\frac{\phi_1'-\phi_2'}{2} + \beta y\frac{u_1'-u_2'}{2})(\overline{q}_2)$, represents the moisture convergences due to the baroclinic mode of the atmosphere (baroclinic mode of moisture convergence, hereafter).

In figure 3.33, the baroclinic mode of moisture convergence $-\frac{\partial}{\partial y}(\frac{\partial}{\partial y}\frac{\phi_1'-\phi_2'}{2}+\beta y\frac{u_1'-u_2'}{2})(\overline{q}_2)$, and precipitation rate are shown for day 65, day 67, and day 69. At each day the maximum of baroclinic moisture convergence is found at the center of convection. The symmetry of the moisture convergence with respect to the convective center implies that the baroclinic mode may not be influential on the propagation of convection.

For examples, when the latent heat is released at the center of convection, the rising air-parcel is concentrated in the upper level of the atmosphere. Thus, the horizontal divergence and convergence develop in the upper- and the lower- atmosphere, respectively. The upper-level divergence and the low-level convergence drive more moisture into the convective center, so that convection becomes intensified. In this case, convection is intensified by the baroclinic mode , since the sign of geopotential gradient force in the upper atmosphere is opposite to that in the lower atmosphere. As a result, the baroclinic mode tends to intensify the *existing convection.*

Shown in figure 3.34 is the barotropic mode of moisture convergence $-\frac{\partial}{\partial y}(\frac{\partial}{\partial y}\frac{\phi_1'+\phi_2'}{2}+\beta y\frac{u_1'+u_2'}{2})(2\overline{q}_e-\overline{q}_2)$ at day 65, day 67, and day 69. In the case of barotropic mode, moisture convergence (divergence) is found in the area north (south) of convection. This asymmetry in the barotropic mode of the moisture convergence with respect to the convective center leads convection northward. Why does the barotropic mode have the asymmetric structure of moisture convergence with respect to the convective center? It turns out that in the barotropic mode, the moisture convergence due

to the Coriolis force [$-\frac{\partial}{\partial y}(\beta y \frac{u_1'+u_2'}{2})(2\overline{q}_e - \overline{q}_2)$, Fig. 3.35] is more dominant than that induced by the geopotential gradient force [$-\frac{\partial}{\partial y}(\frac{\partial}{\partial y}\frac{\phi_1'+\phi_2'}{2})(2\overline{q}_e - \overline{q}_2)$, Fig. 3.36]. Thus, when the barotropic zonal winds are westerlies ($\frac{u_1'+u_2'}{2} > 0$) at the center of convection,the Coriolis force on these westerlies produces the barotropic mode of divergence [$-\frac{\partial}{\partial y}(\beta y \frac{u_1'+u_2'}{2})(2\overline{q}_e - \overline{q}_2)$] to the north of convective center. Eventually, this barotropic mode of divergence generates the moisture convergence at the boundary layer and forces convection to move northward.

In fact, when convection is located in the northern hemisphere the barotropic mode of zonal wind is westerly ($\frac{u_1'+u_2'}{2} > 0$) at the center of convection. It is due to the fact that even in the barotropic mode, the tendency of zonal wind ($\frac{\partial u'}{\partial t}$, Fig. 3.37a) is strongly governed by the vertical advection of July-mean zonal wind ($-\omega'\frac{\partial \overline{u}}{\partial p}$, Fig. 3.37b). At the center of convection in the northern hemisphere, the rising motion advects the July-mean westerlies throughout layers. Since westerly anomalies increase in both the upper and lower level of the atmosphere due to the vertical advection of July-mean westerlies, the barotropic mode of wind becomes westerly.

It should be remembered that the increase of upper-level westerlies at the center of convection induces the upper-level divergence to the north of convection in the northern hemisphere. It is also mentioned that the vertical advection of the July-mean zonal winds is critical for the intensification of upper-level westerlies at the convective center.

Similarly, the barotropic mode of the vertical advection of July-mean zonal winds induces the barotropic mode of divergence to the north of convection by increasing the westerlies at the center of convection in both layers. As a result, the divergence in both layers to the north of convection generates the moisture convergence in the atmospheric boundary layer.

While westerlies in the barotropic mode is found at the center of convection in the northern hemisphere, the barotropic mode of zonal wind at the equator and at 10S becomes easterly, similar to zonal wind at 300hPa. The increase of easterly in the barotropic mode at the equator ($\frac{\partial u_1'}{\partial t} + \frac{\partial u_2'}{\partial t} < 0$, Fig. 3.38a) is caused by the negative meridional advection ($-v_1' \frac{\partial \bar{u}_1}{\partial y} - v_2' \frac{\partial \bar{u}_2}{\partial y} - \bar{v}_1 \frac{\partial u_1'}{\partial y} - \bar{v}_2 \frac{\partial u_2'}{\partial y} < 0$, Fig. 3.38b), while at 10S, the negative meridional advection of July mean zonal winds, and the negative vertical advection of zonal wind anomalies ($-v_1' \frac{\partial \bar{u}_1}{\partial y} - v_2' \frac{\partial \bar{u}_2}{\partial y} - \bar{\omega}_1 \frac{\partial u_1'}{\partial p} - \bar{\omega}_2 \frac{\partial u_2'}{\partial p} < 0$, Fig. 3.39b) accelerate the easterly in the barotropic mode ($\frac{\partial u_1'}{\partial t} + \frac{\partial u_2'}{\partial t} < 0$, Fig. 3.39a). At both latitudes, the tendency of zonal winds in the barotropic mode is similar to the tendency of upper-level zonal winds, discussed in the previous section.

3.4 Simulation of intraseasonal oscillation with the ocean mixed layer

3.4.1 Variation of precipitation rate, latent heat flux, and sea surface temperature

In this section the simulation from the 2D model with the interactive SST is presented. The effect of the ocean mixed layer on the intraseasonal oscillation is discussed. The influence of the evaporation, and the influence of sea surface temperature gradient are assessed, separately.

Shown in figure 3.40 are (a) precipitation rate, (b) latent heat flux, and (c) surface temperature from the 2D model with ocean mixed layer (interactive SST). Compared to the case without ocean mixed layer, three differences are found. First, the magnitude of precipitation is increased significantly. Second, the period between convection has increased to 30days in the northern hemisphere. Third, the propagation of convection becomes continuous starting from 5N.

In figure 3.40b, the latent heat flux (LHFL) increases associated with convection. Between convection, latent heat flux is negative, indicating that heat flux is going into the ocean. The 30day oscillation of the surface temperature is shown in figure 3.40c. As convection develops in the northern hemisphere the interaction between ISO winds and July-mean winds enhances the evaporation, which reduces the surface temperature.

3.4.2 Influence of mixed layer on intraseasonal oscillation

In the previous section three changes in precipitation rate are discussed. In this section the physical mechanism of those changes is explained. It is already discussed that

the interactive SST changes the period and the intensity of the oscillation. The period of precipitation increases from 17 days to 28 days after the interactive SST is incorporated.

In the case of the 2D model without the interactive SST, the moisture convergence induced by winds is the main source of convection. Thus, the divergence (convergence) in the barotropic mode to the north of convection enhances (suppresses) the moisture convergence in the boundary layer in the region north of convection, and facilitates the northward propagation of convection.

When the air-sea interaction is incorporated the duration of convection depends on not only the moisture convergence but also the increase of moisture supply by the latent heat flux. To the south (north) of convection, the low- level winds are westerlies (easterlies) in the northern hemisphere. Since the July mean zonal winds in low atmosphere are westerlies, the interaction between basic state winds and wind anomalies result in the increase (decrease) of evaporation south (north) of the convective center. Consequently, the increase of moisture supply behind convection, as well as the decrease of moisture supply ahead of convection hampers the northward movement of convection.

In order to examine the effect of evaporation on the precipitation, the precipitation rate is simulated for different weights of evaporation (Fig. 3.41). In experiments, 0% (Fig. 3.41a), 50% (Fig. 3.41b), and 100% (Fig. 3.41c) of evaporation is allowed in the simulation of the precipitation rate, respectively. It should also be noticed that in above three experiments, the influence of sst' gradient in the boundary layer is excluded, since the purpose of these experiments is to determine the effect of evaporation on the increase of available moisture.

It is evident that when the weight of evaporation increases, the period of the oscillation increases, while the propagation speed of convection decreases. As mentioned before, the increase of evaporation associated with the strong winds in convection draws the moisture from the ocean surface to the atmosphere, and this supply of moisture increases the duration of convection. As a result, the northward movement of convection is delayed, and the period of convection increases.

Now, the effect of sst′ gradient on the convergence in the boundary layer is examined in figure 3.42. Throughout these experiments, 100% of evaporation is used, while the sst′ gradient in the Ekman velocity equation (Eq. 3.4) changes from 0% (Fig. 3. 42a) to 200% (Fig. 3 42c) of the original value (Fig. 3.42b).

That is

$$\omega_e' = D_3 \frac{\partial^2 \phi_e'}{\partial y^2} + D_4 \frac{\partial \phi_e'}{\partial y} - \frac{R(P_s - P_e)}{2P_e}[D_3 \frac{\partial^2 sst'}{\partial y^2} + D_4 \frac{\partial sst'}{\partial y}]*0.0 \quad in\ Fig.3.42a$$

$$\omega_e' = D_3 \frac{\partial^2 \phi_e'}{\partial y^2} + D_4 \frac{\partial \phi_e'}{\partial y} - \frac{R(P_s - P_e)}{2P_e}[D_3 \frac{\partial^2 sst'}{\partial y^2} + D_4 \frac{\partial sst'}{\partial y}]*1.0 \quad in\ Fig.3.42b$$

$$\omega_e' = D_3 \frac{\partial^2 \phi_e'}{\partial y^2} + D_4 \frac{\partial \phi_e'}{\partial y} - \frac{R(P_s - P_e)}{2P_e}[D_3 \frac{\partial^2 sst'}{\partial y^2} + D_4 \frac{\partial sst'}{\partial y}]*2.0 \quad in\ Fig.3.42c.$$

As the influence of sst′ gradient increases from 0% to 200%, the frequency of oscillation increases, and the duration of convection decreases. The negative sst′ behind convection, and the positive sst′ ahead of convection produces the sst′ gradient force that enhances the convergence ahead of convection. As a result, the new convection can be easily developed ahead of the existing convection. In addition, when convection is located at 15N, the positive sst′ near the equator enhances the convergence in the boundary layer and facilitates the initiation of convection near the equator.

3.5 Conclusion

In this section the physical mechanism of the initiation and the northward propagation of convection in zonally averaged model (2D model) is summarized.

Why is the new convection in the southern hemisphere initiated in the latitude between 10S and the equator?

The reason is that in the southern hemisphere the maximum of July-mean upward motion ($\overline{\omega} < 0$) is found at 10S . When convection is located at 15N, the July-mean upward motion at 10S induces the negative vertical advection of zonal wind anomalies ($-\overline{\omega}\frac{\partial u'}{\partial p} < 0$). As a result, the increase of upper-level easterlies is found at 10S. The Coriolis force on these upper-level easterlies strengthens the upper-level northerlies ($-Byu' < 0$) at 10S (Fig. 3.43a). Consequently, the increase of northerlies at 10S derives the upper-level divergence to the north of 10S, and this upper-level divergence induces the moisture convergence in the boundary layer that initiates convection (Fig. 3.43a).

Why does convection in the northern hemisphere propagates northward?

Convection in the northern hemisphere propagates northward due to the positive vertical advection of July-mean zonal winds ($-\omega'\frac{\partial \overline{u}}{\partial p} > 0$) at the center of convection. Due to this positive vertical advection upper-level westerlies increase at the center of convection (Fig. 3.43b). The Coriolis force on the upper-level westerlies ($-Byu' < 0$) in the northern hemisphere induces the increase of northerlies at the center of convection (Fig. 3.43b). Consequently, the upper-level meridional winds are diverging (converging) to the north (south) of the convective center. The upper-level divergence to the area north of convection facilitates

northward propagation of existing convection by inducing the moisture convergence in the boundary layer.

Why don't we see the consistent northward propagation of convection in the southern hemisphere?

When convection is initiated in the latitude between 10S and 5S, its northward propagation to the northern hemisphere is not continuous. In the northern hemisphere, the northward propagation of convection is caused by the vertical advection of the July-mean zonal winds ($-\omega' \frac{\partial \bar{u}}{\partial p}$). In order for this term to be influential strong rising motion at the center of convection, and large vertical shear are needed. Since the July-mean specific humidity in the southern hemisphere is not as high as that in the northern hemisphere, the intensity of convection is not strong enough to produce the strong rising motion at the center of convection. In addition, the vertical shear of the July-mean zonal winds in the latitude between 10S and the equator is much smaller than that in the northern hemisphere (Fig. 3.1 c). Lastly, the tendency of upper-level divergence induced by the Coriolis force ($-\frac{\partial}{\partial y}\beta y u'$) is reduced to be ($-\beta u'$), since the magnitude of Coriolis parameter (βy) is reduced significantly near the equator.

$$(i.e. -\frac{\partial}{\partial y}\beta y u' = -\beta u' - \beta y \frac{\partial u'}{\partial y} = -\beta u')$$

• The baroclinic mode of atmosphere tends to intensify the existing convection, whereas the barotropic mode of atmosphere induces propagation and initiation of convection.

• The barotropic mode of the vertical advection of July-mean zonal winds induces the barotropic mode of divergence to the north of convection by increasing the westerlies at the center of convection in both layer. As a result, the

divergence in both layers to the north of convection generates the moisture convergence in the atmospheric boundary layer, and affects convection to move northward.

• The effect of the increase (decrease) in evaporation to the south (north) of convection in the northern hemisphere delays the northward propagation of the convection.

• The sst′ gradient force induced by cold sst′ (warm sst′) in the region behind (a head of) convection enhances the boundary layer convergence north of convection, and promotes the northward propagation of the convection.

• The effect of evaporation and the sst′ gradient on convection is opposite with each other. In the 2D model, the total effect of this air-sea interaction is the increase of period and the intensity of oscillation, as well as the slight decrease in the propagation speed. In addition, the northward movement of convection from 5N to 20N is more continuous with air-sea interaction than that without the air-sea interaction.

CHAPTER 4

BOREAL SUMMER INTRASEASONAL OSCILLATION IN THE THREE DIMENSIONAL INTERMEDIATE MODEL

4.1 Introduction

In this chapter boreal summer intraseasonal oscillation is examined with three dimensional intermediate model. The main difference between two dimensional model (2D model), and three dimensional model (3D model) is that the 3D model includes large-scale atmospheric wave dynamics. The importance of large-scale atmospheric dynamics on the intraseasonal oscillation is debatable. Hu and Randall (1994, 1995) used a highly simplified radiative-convective model to show that low-frequency oscillations can be produced in radiative-convective systems with active surface evaporation. The success of their simulation, in which dynamics and its interaction with convection is deliberately omitted, suggests that the oscillation can occur without support from large-scale dynamics. Wang and Xie (1996), however, contend that the initiation of the equatorial disturbance over the Indian Ocean may be caused by the westward propagation of moist Rossby waves in an intermediate model. Consequently, they argued that an atmospheric wave dynamics are an important component of the intraseasonal oscillation.

Another basic difference between the 2D and 3D models is that zonal variation is included in the 3D model. In other words, in the 2D model, the meridional variation of meridional winds governs the initiation and the propagation of convection. In the 3D model, however, the variation of zonal winds are as important as that of meridional

winds, since the divergence and advection rely on the variation of both zonal and meridional wind fields.

It is suggested that the basic state through the vertical and horizontal advection can enhance or reduce the intraseasonal winds. In the 3D model, the zonal variation of the basic state is included, so that the structure of mean state is more complicated. Furthermore, in the 2D model the zonal geopotential gradient is excluded in zonal momentum equation. Thus, the vertical advection of July-mean zonal winds governs most of the variation of zonal wind anomalies. In the 3D model the presence of the zonal geopotential gradient force may change the relative importance among terms in the zonal wind momentum equation, and change the impact of July-mean state on the oscillation.

The air-sea interaction in the 2D model results in the increase of oscillation period and the intensity, as well as the improvement of the propagation from 5N to 20N. In the 3D model more extensive analysis on the effect of SST is conducted. For example, by applying different weight for each term in the Ekman pumping velocity, the effect of SST anomalies in the atmospheric boundary layer is examined.

In order to understand the differences between the mechanisms of the 2D and 3D models, results from the 3D model will be described by the spatial and temporal variation among precipitation, zonal winds, and meridional winds. When the atmospheric winds are described each component of the momentum equation will be illustrated. By examining components of zonal and meridional momentum equations, the components that contribute to the zonal-, and meridional- propagation of convection can be identified.

Once the physical mechanism of the meridional propagation of convection is identified, it is compared with that from the 2D model.

4.2 Model

4.2.1 Three dimensional intermediate model

The basic difference between the 2D and 3D models is that in the 3D model zonal variation of atmospheric and mixed layer variables are included. Accordingly, the zonal advection, zonal divergence and zonal geopotential gradient force are produced in the 3D model. The basic features of the 3D model are the same as the 2D model. The model consists of 2-level free atmosphere, and one boundary layer. Momentum and continuity equations are written at the upper and lower level of free atmosphere, and the thermodynamic and hydrodynamic equations are written in the middle level (level between upper- and lower-levels). Those linearized primitive equations in a P coordinate, equatorial β-plan are (Wang and Xie, 1997) :

$$\frac{\partial u'}{\partial t} = -\overline{u}\frac{\partial u'}{\partial x} - u'\frac{\partial \overline{u}}{\partial x} - \overline{v}\frac{\partial u'}{\partial y} - v'\frac{\partial \overline{u}}{\partial y} - \overline{\omega}\frac{\partial u'}{\partial p} - \omega'\frac{\partial \overline{u}}{\partial p}$$
$$+ Byv' - \frac{\partial \phi'}{\partial x} - \varepsilon u' + K\nabla^2 u', \qquad (4.1.a)$$

$$\frac{\partial v'}{\partial t} = -\overline{u}\frac{\partial v'}{\partial x} - u'\frac{\partial \overline{v}}{\partial x} - \overline{v}\frac{\partial v'}{\partial y} - v'\frac{\partial \overline{v}}{\partial y} - \overline{\omega}\frac{\partial v'}{\partial p} - \omega'\frac{\partial \overline{v}}{\partial p}$$
$$- Byu' - \frac{\partial \phi'}{\partial y} - \varepsilon v' + K\nabla^2 v', \qquad (4.1.b)$$

$$\frac{\partial T'}{\partial t} = -\overline{u}\frac{\partial T'}{\partial x} - u'\frac{\partial \overline{T}}{\partial x} - \overline{v}\frac{\partial T'}{\partial y} - v'\frac{\partial \overline{T}}{\partial y} + \frac{P}{R}\overline{S}\omega' + \frac{P}{R}S'\overline{\omega}$$
$$+ \frac{Q'}{C_p} - \mu T' + K\nabla^2 T', \qquad (4.1.c)$$

$$\frac{\partial u'}{\partial x} + \frac{\partial v'}{\partial y} + \frac{\partial \omega'}{\partial p} = 0, \qquad (4.1.d)$$

$$\frac{\partial \phi'}{\partial p} = -\frac{RT'}{p}, \qquad (4.1.e)$$

where overbars and primes represent basic-state and perturbation quantity; u, v, ω, ϕ, and T denote zonal and meridional winds, vertical pressure velocity, geopotential, and temperature; ϵ, μ and R are the Rayleigh friction coefficient, Newtonian cooling coefficient, and specific gas constant; K is the horizontal momentum or thermal diffusion coefficient; and S is the dry static stability parameter. The condensational heating at the middle atmosphere P_m is expressed as

$$Q'_m = \frac{\delta b L_{cl}}{\Delta p}[-\omega'_m(\overline{q}_2 - \overline{q}_1) - \omega'_e(\overline{q}_e - \overline{q}_2)] \qquad (4.2)$$

where Q'_m represents the irreversible condensational heating; b measures the ratio of the amount of water vapor that condenses out to that moistening the atmosphere; L_c is the latent heat; ΔP is the half-depth of the free atmosphere; ω'_m and ω'_e represent vertical pressure velocities at the middle atmosphere P_m and the top of the boundary layer P_e, respectively; and $\overline{q}_e$, $\overline{q}_2$, and $\overline{q}_1$ are specific humidity of the basic state in the boundary layer, the lower and upper troposphere, respectively.

The governing equations in the barotropic boundary layer can be described as (Wang and Li, 1993):

$$By v'_B - \frac{\partial \phi'_e}{\partial x} + \frac{R(p_s - p_e)}{2p_e}\frac{\partial sst'}{\partial x} - E_x u'_B = 0 \qquad (4.3a)$$

$$-By u'_B - \frac{\partial \phi'_e}{\partial y} + \frac{R(p_s - p_e)}{2p_e}\frac{\partial sst'}{\partial y} - E_y v'_B = 0 \qquad (4.3b)$$

$$\omega'_e = (p_s - p_e)\left(\frac{\partial u'_B}{\partial x} + \frac{\partial v'_B}{\partial y}\right) \qquad (4.3c).$$

where P_s is pressure at the model surface; ϕ'_e denotes perturbation geopotential at P_e; u'_B and v'_B are vertically averaged perturbation zonal and meridional winds in the boundary

layer; sst' represents perturbation sea surface temperature(SST); and E_x and E_y are Rayleigh friction coefficients in the zonal and meridional directions.

From (4.3), the Ekman pumping velocity can be written as

$$\omega_e' = D_1 \frac{\partial^2 \phi_e'}{\partial x^2} + D_2 \frac{\partial \phi_e'}{\partial x} + D_3 \frac{\partial^2 \phi_e'}{\partial y^2} + D_4 \frac{\partial \phi_e'}{\partial y}$$
$$- \frac{R(P_s - P_e)}{2P_e}[D_1 \frac{\partial^2 sst'}{\partial x^2} + D_2 \frac{\partial sst'}{\partial x} + D_3 \frac{\partial^2 sst'}{\partial y^2} + D_4 \frac{\partial sst'}{\partial y}] \quad (4.4)$$

where the coefficients are

$$D_1 = -\frac{(P_s - P_e)E_y}{E_x E_y + B^2 y^2}$$
$$D_2 = \frac{(P_s - P_e)B}{E_x E_y + B^2 y^2} - \frac{2(P_s - P_e)B^3 y^2}{(E_x E_y + B^2 y^2)^2}$$
$$D_3 = -\frac{(P_s - P_e)E_x}{E_x E_y + B^2 y^2}$$
$$D_4 = \frac{2(P_s - P_e)E_x B^2 y}{(E_x E_y + B^2 y^2)^2}.$$

Due to mass conservation in a vertical column, the Ekman pumping velocity in the barotropic boundary layer is related to free atmosphere convergence as following:

$$\omega_e' = -\Delta p \sum_{k=1}^{2} (\frac{\partial u_k'}{\partial x} + \frac{\partial v_k'}{\partial y}) \qquad (4.5).$$

Combining (4. 4) and (4. 5) leads to an elliptical equation for ϕ'_e :

$$D_1 \frac{\partial^2 \phi_e'}{\partial x^2} + D_2 \frac{\partial \phi_e'}{\partial x} + D_3 \frac{\partial^2 \phi_e'}{\partial y^2} + D_4 \frac{\partial \phi_e'}{\partial y}$$
$$= -\Delta P \sum_{k=1}^{2} (\frac{\partial u_k'}{\partial x} + \frac{\partial v_k'}{\partial y}) + \frac{R(p_s - p_e)}{2p_e}[D_1 \frac{\partial^2 sst'}{\partial x^2} + D_2 \frac{\partial sst'}{\partial x}]$$
$$+ \frac{R(p_s - p_e)}{2p_e}[D_3 \frac{\partial^2 sst'}{\partial y^2} + D_4 \frac{\partial sst'}{\partial y}] \qquad (4.6).$$

Here, the assumption, $\phi'_e = \phi'_2$ is made in order to close a set of equations.

In order to incorporate the air-sea interaction into the 3D models, sst′ is approximated as followings (Wang and Xie, 1998):

For the mean surface temperature ($\overline{sst}$) greater than or equal to 22^0 C

$$\frac{\partial sst'}{\partial t} = D_{rad}\left(\frac{\partial u_2'}{\partial x} + \frac{\partial v_2'}{\partial y}\right) - D_{eva}\left(\mathrm{sgn} * \sqrt{(u_2' * 0.4)^2} * (\overline{sst} - 20) + \sqrt{(\overline{u}_2 * 0.4)^2} * sst'\right) - \mu_o sst' \qquad (4.7a)$$

Otherwise ($\overline{sst} < 22^0 C$),

$$\frac{\partial sst'}{\partial t} = D_{rad}\left(\frac{\partial u_2'}{\partial x} + \frac{\partial v_2'}{\partial y}\right) - D_{eva} * 1.8 * \left(\mathrm{sgn} * \sqrt{(u_2' * 0.4)^2}\right) \qquad (4.7b).$$

where u_2 and v_2 are low- level zonal wind and meridional wind, respectively; sgn>0, when $\overline{u} * u' \geq 0$, otherwise sgn<0; ρ_a is air density in the atmospheric boundary layer; and D_{rad}, and D_{eva} are, respectively, the mixed layer heating coefficients associated with radiation and evaporation processes. These coefficients are defined by

$$D_{rad} = 0.622(1-A)S_o\lambda / \rho_o C_w \overline{h} \qquad (4.8a)$$
$$D_{eva} = \rho_o C_E L_C K_q / \rho_o C_w \overline{h} \qquad (4.8b)$$
$$\mu_o = \gamma / \rho_o C_w \overline{h} \qquad (4.8c)$$

where A and S_0 are surface albedo and the downward solar radiation flux reaching sea surface under clear sky; ρ_o and C_w are the density and heat capacity of water; $\overline{h}$ represents the mean depth of the mixed layer; C_E and L_c are moisture exchange coefficient and latent heat; λ measures the proportionality between perturbation cloudiness and surface wind convergence; K_q=8.9 × 10^{-4} K^{-1} (Wang and Li, 1993), and γ=1.8$Wm^{-2}K^{-1}$ (Seager et al.

1988). The dimension of the model is 5^0 in longitude and 2^0 in latitude. The zonal boundary condition is periodic around the globe. At the meridional boundaries the fluxes of mass, momentum, and heat normal to the boundary vanish.

4.2.2 Basic state

The basic state of the 3D model is derived from the same source as the 2D model. That is, the climatological July-mean circulation of the European Center for Medium-Range Weather Forecasts (ECMWF) data is used for the period 1979-92. The specific humidity is calculated based on surface air temperature and dew point temperature from ECMWF data for July. In figure 4.1 the July-mean specific humidity (Fig. 4.1a), July-mean winds at 850hPa (Fig. 4.1b), and 200hPa (Fig. 4.1bc) are shown. The vertical shear of zonal- and meridional winds in the Indian region (60E-120E) from the equator to 20N is the easterly shear (easterly increases with height), and the northerly shear (northerly increases with height), respectively (figure not shown).

4.3 Intraseasonal oscillation in 3 D model without the ocean mixed layer

4.3.1 The life cycle of low-level winds, and precipitation in the intraseasonal oscillation

Sequential maps of the low-tropospheric winds and precipitation rate associated with the intraseasonal oscillation are shown in figure 4.2. The initial perturbation is same as that in the study by Wang and Xie (1997). That is the initial wind perturbation is purely zonal and has a cosine shape in both the zonal and meridional direction (Fig. 4.2a). The

geopotential and temperature fields are determined by semigeostrophic and hydrostatic balances.

After the initial perturbation is located at 40E, winds and precipitation cell propagate eastward so that on day 4, the maximum precipitation is found at 60E. At the same time, the disturbance of winds and precipitation at 60E is divided into three cells. The first one, which is originated from the initial perturbation, is located at the equator, while the second and the third ones are located at 15N and 10S, respectively (Fig. 4.2b).

The precipitation cell located at the equator moves eastward, and reaches180E on day 13 (Fig. 4.2c). Meanwhile, the off-equatorial westward propagation cells are found near 120E. Both the dipole structure of precipitation cells at 60E, and the equatorial disturbance weaken on day19 (Fig. 4.2d), and disappear on day 20 (Fig. 4.2e). On day 22 the only disturbance found is the westward propagating off equatorial disturbance covering from 75E to 120E (Fig. 4.2f).

The disturbance keeps moving westward, and on day 25 the center of maximum precipitation is located at 16N and 75E (Fig. 4.2g). The disturbance has intensified when it reaches between 60E and 75E on day 25 (Fig. 4.2g). After the northern part of precipitation has intensified by day 28, the new disturbance developes in the southern hemisphere between 10S and the equator (Fig. 4.2h). On day31 disturbance in the southern hemisphere starts moving toward the equator, and disturbance at the equator along 105E is intensified (Fig. 4.2i). While this disturbance propagates eastward along the equator from day 31 to day 40, a series of off-equatorial disturbances is emanated from the equatorial disturbance on day 40 (Fig. 4.2j).

The general feature found in the life cycle of convection of the intraseasonal time scale is same as that described in the study of Wang and Xie (1997). That is, the Kelvin wave-like disturbance at the equator propagates eastward, and emanates Rossby-wave-like off equatorial disturbances near 120E. These off-equatorial disturbances propagate westward, and reach the Indian Ocean, near 60E. While the off-equatorial convection dissipates in the Indian Ocean, the new convection is initiated at the equator and propagates eastward.

4.3.2 Longitudinal variation of precipitation and low-level winds

In this section, the longitudinal variation of precipitation, low-level zonal and meridional winds at different latitudes are discussed. The cross section along the specific latitude facilitates the identification of the origin of disturbance in a certain latitude. For example, at 70E and15N there are two types of disturbances (Fig. 4.3a). The first type of disturbance originates from the western Pacific, around 110E on day 17, day 42, and day 70. This type of disturbance moves westward and intensifies near 60E on day 27 and day 50. The second type of disturbance is found near 70E, 15N on day 8, day 37, and day 62 (Fig. 4.3a). Different from the first type, the zonal movement of these disturbances is insignificant.

At the equator the maximum precipitation rate at 70E is found on day 6, day 30, and day 57 (Fig. 4.3b). These disturbances originate from 70E, and propagate eastward till they reach the dateline. At the equator, stationary disturbances at 70E are also found

on day 15, day 37, and day 65. Along10S eastward propagating disturbances start from 60E on day 5, day 34, and day 60 (Fig. 4.3c).

The life cycle of convection illustrated in figure 4.3 is consistent with the life cycle shown in figure 4.2. For example, the eastward moving convection along the equator shown in Fig. 4.3b represents the first half of the life cycle. The westward moving convection in Fig. 4.3c indicates the last half of the cycle, in which the off-equatorial disturbance is emanated from eastward propagation convection near 110E, and propagates westward along 18N.

4.3.3 Meridional variation of precipitation and low-level winds

In order to compare results from the 3D model with those from the 2D model, precipitation rate, low-level zonal winds, and low- level meridional winds are zonally averaged over the domain from 60E to 100E (Fig. 4.4). The basic difference between the 2D and 3D models is found in the meridional structure of the precipitation rate (Fig. 4.4a). Not only northward moving disturbances are detected with a period of 25 days, but also meridionally stationary disturbances are found at 20N.

These stationary disturbances near 20E are a result of the westward propagating convection along 15N shown in figure 4.3a. When convection is emanated from the equatorial convection and moves westward, crossing the longitude of 100E, it is already located in the northern hemisphere. Therefore, when the results from the three dimensional model are zonally averaged over the longitude from 60E to 100E, convection in this zonally averaged intraseasonal oscillation seems to be meridionally stationary near 20N.

The maximum amplitude in zonal winds is found at 15N (Fig. 4.4b). The positive zonal wind anomalies are found south of the maximum precipitation. At the same time, winds in the southern hemisphere (5S-10S) are easterlies. In both hemispheres, low-level meridional winds change from northerlies to southerlies upon an arrival of convection.

4.3.4 The physical mechanism of propagation

The propagation of convection in the 3D model consists of three directions, such as eastward, westward, and northward propagation. Along the equator, the eastward propagation of convection is dominant. This eastward propagating disturbance is well known as a Kelvin wave type disturbance. The Kelvein wave is a gravity wave, and propagates eastward along the equator due to its boundary condition. Since the characteristic of the Kelvin wave is already well known, the focus of this section is given to the physical mechanism of northward and westward propagation of convection.

In the model, precipitation rate (Pr) is determined by the moisture convergence in the atmospheric boundary layer, and in the lower level (700hPa) of free atmosphere.

That is

$$\mathrm{Pr} = -(P_s - P_e)(\tfrac{\partial u_e'}{\partial x} + \tfrac{\partial v_e'}{\partial y})\overline{q}_e - \Delta P(\tfrac{\partial u_2'}{\partial x} + \tfrac{\partial v_2'}{\partial y})\overline{q}_2 \qquad (4.9)$$

where subscription e and 2 indicate the boundary layer and low-level atmosphere(700hPa), respectively; $\overline{q}_e$ and $\overline{q}_2$ are specific humidity of July-mean climatology in boundary layer and low atmosphere; and ΔP is the half-depth of the free atmosphere.

The divergence in the boundary layer is balanced by the convergence in upper atmosphere or in lower atmosphere, that is

$$\Delta P\{(\tfrac{\partial u_1'}{\partial x}+\tfrac{\partial v_1'}{\partial y})+(\tfrac{\partial u_2'}{\partial x}+\tfrac{\partial v_2'}{\partial y})\}=-(P_s-P_e)(\tfrac{\partial u_e'}{\partial x}+\tfrac{\partial v_e'}{\partial y}) \qquad (4.10).$$

Here, the subscription 1 indicates the upper level of atmosphere (300hPa). Substituting (4.10) to (4.9) gives

$$\Pr=\Delta P\{(\tfrac{\partial u_1'}{\partial x}+\tfrac{\partial v_1'}{\partial y})+(\tfrac{\partial u_2'}{\partial x}+\tfrac{\partial v_2'}{\partial y})\}\overline{q}_e-\Delta P(\tfrac{\partial u_2'}{\partial x}+\tfrac{\partial v_2'}{\partial y})\overline{q}_2 \qquad (4.11).$$

The second term on the rhs of (4.11) can be rewritten as

$$-\tfrac{\Delta P}{2}\{(\tfrac{\partial u_1'}{\partial x}+\tfrac{\partial u_2'}{\partial x})-(\tfrac{\partial u_1'}{\partial x}-\tfrac{\partial u_2'}{\partial x})+(\tfrac{\partial v_1'}{\partial y}+\tfrac{\partial v_2'}{\partial y})-(\tfrac{\partial v_1'}{\partial y}-\tfrac{\partial v_2'}{\partial y})\}\overline{q}_2$$
$$=-\Delta P(\tfrac{\partial u_2'}{\partial x}+\tfrac{\partial v_2'}{\partial y})\overline{q}_2 \qquad (4.12).$$

By substituting (4.12) into (4.11), we get

$$\begin{aligned}\Pr &= 2\Delta P\{\tfrac{\partial}{\partial x}(\tfrac{u_1'+u_2'}{2})+\tfrac{\partial}{\partial y}(\tfrac{v_1'+v_2'}{2})\}\overline{q}_e\\ &-\Delta P\{\tfrac{\partial}{\partial x}(\tfrac{u_1'+u_2'}{2})-\tfrac{\partial}{\partial x}(\tfrac{u_1'-u_2'}{2})+\tfrac{\partial}{\partial y}(\tfrac{v_1'+v_2'}{2})-\tfrac{\partial}{\partial y}(\tfrac{v_1'-v_2'}{2})\}\overline{q}_2\\ &=\Delta P\{\tfrac{\partial}{\partial x}(\tfrac{u_1'+u_2'}{2})+\tfrac{\partial}{\partial y}(\tfrac{v_1'+v_2'}{2})\}(2\overline{q}_e-\overline{q}_2)\\ &+\Delta P\{\tfrac{\partial}{\partial x}(\tfrac{u_1'-u_2'}{2})+\tfrac{\partial}{\partial y}(\tfrac{v_1'-v_2'}{2})\}\overline{q}_2 \qquad (4.13).\end{aligned}$$

When the barotropic mode (A^+) and baroclinic mode (A^-) of arbitrary variable(A) are defined as

$$\textit{Barotropic mode of } A: A^+=\tfrac{A_1+A_2}{2} \qquad (4.14a)$$
$$\textit{Baroclinic mode of } A: A^-=\tfrac{A_1-A_2}{2} \qquad (4.14b),$$

the equation (4. 13) becomes

$$\mathrm{Pr} = \Delta P\{\tfrac{\partial u'^{+}}{\partial x} + \tfrac{\partial v'^{+}}{\partial y}\}(2\overline{q}_e - \overline{q}_2) + \Delta P\{\tfrac{\partial u'^{-}}{\partial x} + \tfrac{\partial v'^{-}}{\partial y}\}\overline{q}_2 \qquad (4.15).$$

The first term and second term in (4.15) indicate moisture convergence associated with the barotropic mode and the baroclinic mode of the atmosphere. The barotropic mode of divergence is connected with the convergence in the boundary layer as shown in (4.10). For example, when the divergence prevails in both the upper level and lower level of the atmosphere, a strong convergence develops in the boundary layer in order to balance the divergence in the atmosphere. This strong moisture convergence in the atmospheric boundary layer may initiate convection.

Once convection develops, the release of the latent heat inside convection lifts the air parcel, so that the pressure in the upper atmosphere increases. The increase of pressure in upper atmosphere results in the upper-level divergence, and this upper-level divergence facilitates the increase in the low-level convergence. In this case, the upper-level divergence and the low-level convergence increase the upward motion, and intensify convection. This is how the baroclinic mode of divergence enhances the existing convection.

In chapter 2, the barotropic and baroclinic modes of atmosphere in the 2D model were examined. It was found that the barotropic mode of atmospheric divergence initiates convection, and the baroclinic mode plays a part in intensifying the existing convection. In following sections, the role of barotropic and baroclinic modes on the propagation and the intensity of convection is analyzed.

4.3.4 (a) Physical mechanism of westward propagation

In the 3D model, convection propagates along not only the meridional direction but also the zonal direction. Note that in nature the eastward propagation of convection along the equator occurs throughout the entire year, while, the northward and westward propagation of convection is a distinct features of the boreal summer intraseasonal oscillation. The physical mechanism of the northward and westward propagation of convection is a main focus of this study, since the eastward propagation is primarily determined by Kelvin wave-like propagation.

In order to understand the westward moving component of convection, equation (4.15) is modified as the following. That is,

$$\frac{\partial \mathrm{Pr}}{\partial t} \approx \frac{\partial}{\partial t}\{\frac{\partial u'^{+}}{\partial x} + \frac{\partial v'^{+}}{\partial y}\}(2\overline{q}_e - \overline{q}_2) + \frac{\partial}{\partial t}\{\frac{\partial u'^{-}}{\partial x} + \frac{\partial v'^{-}}{\partial y}\}\overline{q}_2 \qquad (4.16a).$$

In (4.16a), the local variation of precipitation rate ($\frac{\partial \mathrm{Pr}}{\partial t}$) depends on the local variation of the barotropic and baroclinic modes of the atmosphere.

In figure 4.5 the variation of moisture convergence due to the changes in the barotropic mode of divergence (barotropic moisture convergence , hereafter) along 18N is shown. The local maximum of precipitation rate (-•-), is found near 110E on day 45 (Fig. 4.5a). From day 45 to day 54 (Fig. 4.5d), the precipitation propagates westward from 110E to 62E.

From day 45 to day 54, the barotropic moisture convergence (-∘-) to the west of the maximum precipitation rate (-•-) increases, while that in the region to the east of convection decreases. It is suggested that this asymmetrical longitudinal structure of the

barotropic moisture convergence, with respect to the area of precipitation, is responsible for the westward movement of the precipitation along 18N.

The barotropic moisture convergence is further analyzed by dividing into the zonal direction and the meridional direction of moisture convergence. That is

$$\frac{\partial \mathrm{Pr}}{\partial t} \approx \frac{\partial}{\partial t}\{\frac{\partial u'^{+}}{\partial x}\}(2\overline{q}_e - \overline{q}_2) + \frac{\partial}{\partial t}\{\frac{\partial v'^{+}}{\partial y}\}(2\overline{q}_e - \overline{q}_2) \qquad (4.16b).$$

The first term indicates the barotopic mode of zonal moisture convergence, and the second term indicates the barotropic mode of meridional moisture convergence.

In figure 4.6, the barotopic mode of zonal moisture convergence (-∘-) along 18N is shown with the precipitation rate(-•-). The increase (decrease) of barotropic moisture convergence leads (follows) the westward moving convection from day 45 (Fig. 4.6a) to day 54 (Fig. 4.6d). In the case of the meridional moisture convergence in barotopic mode (Fig. 4.7), the decrease (increase)of moisture convergence (-∘-) is located to the west (east) of convection (-•-). Therefore, according to the above analysis, *the barotropic mode of zonal moisture convergence seems to be the cause of the westward propagation of convection along 18N.*

The role of the baroclinic mode on the westward propagation of convection can be seen in figure 4.8. The maximum increase of moisture convergence in baroclinic mode (-∘-) coincides with the center of the precipitation (-•-). Thus, the zonally symmetrical structure of the moisture convergence, with respect to the convective center, does not facilitate the propagation of convection in any zonal direction. Instead, *the*

baroclinic mode of moisture convergence increases the intensity of the existing convection.

So far, it has been proposed that the asymmetrical zonal structure of the barotropic zonal moisture convergence induces the westward movement of convection. In other words,

$$\frac{\partial \mathrm{Pr}}{\partial t} \approx \frac{\partial}{\partial t}\{\frac{\partial u'^{+}}{\partial x}\}(2\overline{q}_e - \overline{q}_2)$$
$$= \frac{\partial}{\partial x}\{\frac{\partial u'^{+}}{\partial t}\}(2\overline{q}_e - \overline{q}_2) \qquad (4.16c).$$

Then, what generates such a structure? What changes the barotropic mode of zonal winds, so that the zonal convergence is developed to the west of convection? The change in barotropic mode of the zonal winds ($\frac{\partial u'^{+}}{\partial t}$) is dependent on the barotopic mode of each term in the zonal momentum equation. Thus, (4.1a) can be used to determine which term in the zonal momentum equation produces the barotropic zonal divergence, thereby leading to moisture convergence in the boundary layer.

In figure 4.9, the barotropic mode of zonal divergence (-∘-) produced by each term in the momentum equation is shown. It is the barotropic mode of vertical advection of July-mean zonal winds ($-\omega_1' \frac{\partial \overline{u}}{\partial p} - \omega_2' \frac{\partial \overline{u}}{\partial p}$) that induces the barotropic zonal divergence (convergence) to the west (east) of convection (Fig. 4.9e). In July the easterly vertical shear ($\frac{\partial \overline{u}}{\partial p} > 0$) is dominant in the mean state along 18N. Thus, the strong rising motion ($\omega_1' < 0$, and $\omega_2' < 0$) at the center of convection transfers the low-level July-mean

westerly momentum throughout convection. As a result, the westerly anomalies in both layers increase at the center of convection. Since the maximum increase of westerlies is found at the center of convection, divergence (convergence) of zonal winds develops to the west (east) side of the convective center. This barotropic zonal divergence (convergence) to the west (east) of convection enhances (reduces) the moisture convergence in the atmospheric boundary layer, so that convection can propagate westward. That is

$$18N: \frac{\partial \bar{u}}{\partial p} > 0, \ \omega_1' < 0, \quad and \ \ \omega_2' < 0 \quad (convection \ \ center)$$
$$\therefore \frac{\partial u'^{+}}{\partial t} \approx -\omega_1' \frac{\partial \bar{u}}{\partial p} - \omega_2' \frac{\partial \bar{u}}{\partial p} \ > 0 \qquad (4.17).$$

It should be noted that the vertical advection inside convection exhibits the same sign in both layers, while the sign of geopotential gradient force and the Coriolis force in lower atmosphere is opposite to that in the upper atmosphere. Due to its barotropic nature, the vertical advection term (Fig. 4.9e) becomes the most dominant term in the barotropic mode of zonal momentum equation.

4.3.4 (b) Physical mechanism of northward propagation

There are two basic differences between the 2D and 3D models in the northward propagation of convection. First, when northward moving convection in the 2D model reaches the latitude at 16N, it generates the new convection in the southern hemisphere near 10S. In the 3D model, however, the initiation of the new convection near 10S is due to the westward moving Rossby-wave-like convection, whose southern part is intensified as convection approaches the Indian Ocean.

When the Rossby-wave-like convection emanates from the equaotrial Kelvin wave-like convection and propagates westward from 180E to the Indian Ocean, convection in the southern hemisphere is too weak to be noticed. However, when convection in the northern hemisphere reaches the Indian Ocean and intensifies, the southern convection becomes strong, as well. As convection in both hemisphere stalls at 60E (Fig. 4.10a), convection in the southern hemisphere is divided to form a new convective cell at the equator from day 30 (Fig. 4.10b) to day 32 (Fig. 4.10d).

The new equatorial convection, then, propagates northeastward from the equator on day 32 (Fig. 4 10d) to 7N on day 35 (Fig. 4.10g). After convection reaches the location of 10N, 90E the direction of the propagation changes from northeast to northwest (Fig. 4.10h). The northeastward propagation of convection from day 32 (Fig. 4.10d) to day 35 (Fig. 4.10g) renders the other difference between the 2D and 3D models. In the 2D model, the northward propagation of convection is found in the latitude north of 10N, and convection at the equator and the southern hemisphere is not organized (Fig. 3.2). In the 3D model convection in the southern hemisphere and the equator is organized as well as that in the northern hemisphere (Fig. 4.4) and the northward propagation of convection from equator to 10N is recognizable. Thus, in this section it is attempted to answer following three equations:

1. What is the difference in the mechanism of northward propagation between the 2D and 3D models ?

2. What is the difference in the initiation of convection between the 2D model and 3D models?

In order to answer the first question, one cycle of the northward propagation of convection from day 25 to day 66 is analyzed. In the 2D model, the northward propagation of convection is dominant between 10N and 25N. In the 3D model the continuous northward propagation is found from 10N to 20N between day 25 and day 66, and day 44 and day 65.

In figure 4.11, the northward propagation of convection and low-level meridional wind anomalies are illustrated. On day 25 (Fig. 4.11a), and day 44 (Fig. 4.11e) the maximum rate of the precipitation rate is located at 18N. While this convection in the northern hemisphere dissipates from day 25 (Fig. 4.11a) to day 35 (Fig. 4.11d) and from day 44 (Fig. 4.11e) to day 61 (Fig. 4.11i), convection in the southern hemisphere moves northward from 8S on day 25 (Fig. 4.11a) and day 44 (Fig. 4.11e) to 20N on day 44 (Fig. 4.11e) and day 66 (Fig. 4.11k).

The physical mechanism of the northward propagation can be explained using (4.16a). That is

$$\frac{\partial \mathrm{Pr}}{\partial t} \approx \frac{\partial}{\partial t}\{\frac{\partial u'^{+}}{\partial x} + \frac{\partial v'^{+}}{\partial y}\}(2\overline{q}_e - \overline{q}_2) + \frac{\partial}{\partial t}\{\frac{\partial u'^{-}}{\partial x} + \frac{\partial v'^{-}}{\partial y}\}\overline{q}_2 \qquad (4.16a).$$

The local tendency of the precipitation rate is determined by the moisture convergence induced by barotropic or baroclinic components of the atmosphere. For instance, when the divergence in the barotropic mode of the atmosphere increases $[\frac{\partial}{\partial t}\{\frac{\partial u'^{+}}{\partial x} + \frac{\partial v'^{+}}{\partial y}\} > 0]$, it induces convergence in the atmospheric boundary layer, and results in the increase of local precipitation rate ($\frac{\partial}{\partial t}\mathrm{Pr} > 0$).

In figure 4.12 moisture convergence induced by the divergence of the barotropic mode of the free atmosphere (-∘-) from day 44 to day 66 is shown. When convection is located at 18N, and 8S on day 44, the maximum increase of moisture convergence is found to the north of convection, such as the latitudes of 22N and 2S (Fig. 4.12a).

On day 50 convection in the southern hemisphere moves northward to 4S, while convection in the northern hemisphere intensifies. On this day, the local maximum increase of moisture convergence is found at 2N and 22N. Again, the maximum increase of the moisture convergence is located to the north of the existing convection. This leading of moisture convergence is responsible for the northward propagation of convection.

On day 59 (Fig. 4.12c), convection resides at 2N. At the same time, the negative (positive) tendency of the moisture convergence is found at the center (to the north) of convection. Consequently, the precipitation at the center of convection decreases, while the precipitation to the north of convection increases. This pattern continues as convection keeps preceding northward till day 66 (Fig. 4.12g).

This moisture convergence induced by the divergence in the barotropic mode of free atmosphere can be divided into zonal and meridional direction. That is

$$\begin{aligned}\frac{\partial P_T}{\partial t} &\approx \frac{\partial}{\partial t}\{\frac{\partial u'^{+}}{\partial x}+\frac{\partial v'^{+}}{\partial y}\}(2\overline{q}_e-\overline{q}_2)\\ &= \frac{\partial}{\partial t}\frac{\partial u'^{+}}{\partial x}(2\overline{q}_e-\overline{q}_2)+\frac{\partial}{\partial t}\frac{\partial v'^{+}}{\partial y}(2\overline{q}_e-\overline{q}_2) \qquad (4.16b).\end{aligned}$$

In the 2D model, only the second term in the equation (4.16b) exists. Thus, there is no divergence in the zonal direction. In the 3D model, however, not only the

meridional direction but also the zonal direction of divergence should be taken into account.

In figure 4.13, the tendency of the moisture convergence induced by the meridional divergence in the barotropic mode of the free atmosphere is presented. The difference between figure 4. 12 and figure 4.13 is that in figure 4.12 the total effect of both zonal and meridional divergence in the barotropic mode is considered, whereas in figure 4.13 the single effect of meridional divergence is studied. The strong similarity between figure 4.12 and figure 4.13 in the tendency of moisture convergence (-°-) and the precipitation rate (-•-) indicates that the divergence in the meridional direction alone can explain the physical mechanism of the northward propagation.

In summary, the phase difference between the barotropic mode of divergence and convection in the 2D model drives the propagation of convection. *The barotropic mode of the atmosphere in the 3D model, as well, contributes to the propagation of convection by increasing (decreasing) the moisture convergence to the north of (at the center of) convection.*

It should be remembered that the baroclinic mode of divergence in the 2D model had a phase lock with the maximum precipitation rate. That is, the baroclinic mode of free atmosphere renders the maximum increase of moisture convergence at the center of convection. This phase lock between the tendency of the moisture convergence and convection is also found in the baroclinic mode of the 3D model.

Shown in figure 4.14 is the tendency of the moisture convergence induced by the baroclinic mode of the atmosphere. As convection propagates from southern hemisphere

to northern hemisphere from day 44 (Fig. 4.14a) to day 61 (Fig. 4.14e), the center of convection coincides with the increase of the moisture convergence. Since the latent heat released of condensation inside convection enhances the baroclinic mode of the free atmosphere by increasing (decreasing) the upper-level (lower-level) geopotential, the strong phase lock between precipitation and the baroclinic mode of the atmosphere is expected. This phase lock between the baroclinic mode of free atmosphere and convection contributes to the intensification of convection, rather than the propagation of convection.

From day 62 (Fig. 4.14f) to day 66 (Fig. 4. 14g), however, the baroclinic mode of free atmosphere reduces the moisture convergence at the center of the maximum precipitation around 20N. The decrease of moisture convergence at the center of convection are caused by the zonal average data process. In fact, the spatial variation of moisture convergence by the baroclinic mode on day 62 and day 66 indicates that the actual center of convection coincides with the increase of the moisture convergence by the baroclinic mode (figure not shown). In the same latitude, the decrease of moisture convergence is found in the different longitude (Figure not shown). As a result, when results are zonally average from 60E to 100E the center of convection and the decrease of moisture convergence are found at the same latitude.

So far, it is suggested that the barotropic mode of divergence (convergence) to the north of (at the center of) convection drives convection to move northward. Then, what creates this phase lag between the barotropic mode of divergence and the convective center? Since the moisture convergence of barotropic mode can be written as

$$\frac{\partial}{\partial t}\mathrm{Pr} \approx \frac{\partial}{\partial t}\frac{\partial v'^{+}}{\partial y}(2\overline{q}_e - \overline{q}_2)$$

$$\approx \frac{\partial}{\partial y}\left(\frac{\partial v'^{+}}{\partial t}\right)(2\overline{q}_e - \overline{q}_2) \qquad (4.18),$$

the question can be answered by examining which term in the momentum equation induces the barotropic divergence to the north of the convective center.

The influence of the geopotential force and the Coriolis force on the divergence of the barotropic mode on day 61 can be estimated from figure 4.15. In Fig. 4.15a, the divergence induced by the local tendency of the meridional winds is illustrated. In Fig. 4.15b, the divergence of barotropic mode is purely induced by the geopotential gradient force and the Coriolis force. The local maximum of divergence is found to the north of the convective center (Fig. 415b). Furthermore, it turns out to be the Coriolis force that creates the barotropic divergence (convergence) to the north of (to the south of) convection in the northern hemisphere (Fig. 4.15c).

What is the physical meaning of the barotropic divergence induced by the Coriolis force ($\frac{\partial}{\partial y}\{-\beta y u'^{+}\}$)? How does the barotropic mode of Coriolis force ($-\beta y u'^{+}$) induce the divergence to the north of the convective center?

In figure 4.16a, the latitudinal variation of barotropic zonal wind anomalies (-o-) and precipitation rate (-•-) on day 61 are shown. In the northern hemisphere, the strongest barotropic westerlies are found at 10N, where the local maximum of the precipitation rate is located. These barotropic westerlies ($u'^{+} > 0$) at the center of convection and the positive Coriolis parameter of the northern hemisphere ($\beta y > 0$) induce the acceleration of the barotropic northerlies ($-\beta y u'^{+} < 0$, Fig. 4.16b) at the center of convection.

That is

$$\frac{\partial v'^{+}}{\partial t} \approx -\beta y u'^{+} < 0, \quad \because \; u'^{+} > 0, \; and \; \beta y > 0 \quad at \; 10N \qquad (4.19) \; .$$

This increase of barotropic northerlies at the center of convection produces the divergence to the north of the convective center (Fig. 4.16b).

Up to this point, it is explained that the barotropic westerlies associated with convection is responsible for the barotropic divergence to the north of convection. Then, why does the barotropic westerlies develop associated with convection? To answer this equation the momentum equation of barotropic zonal winds is examined in figure 4.17. The most significant component in accelerating the westerlies at the center of convection (Fig. 4.17a) is the vertical advection of July-mean zonal winds (Fig. 4.17d).

In the northern hemisphere, especially near 10N, the easterly vertical shear is dominant in the July-mean wind field. In other words, July-mean zonal winds are westerlies (easterlies) in the lower (upper) atmosphere. When convection develops, the upward motion at the center of convection ($\omega' < 0$) brings the westerly momentum of July-mean zonal winds throughout convection. As a result, the atmosphere at the center of convection experiences the increase of westerlies throughout the atmosphere.

$$\frac{\partial u'^{+}}{\partial t} \approx (-\omega' \frac{\partial \bar{u}}{\partial p})^{+} > 0, \quad \because \; \omega' < 0, \; and \; \frac{\partial \bar{u}}{\partial p} > 0 \quad at \; 10N \qquad (4.20) \qquad .$$

It is suggested that the physical mechanism of the northward propagation from 10N to higher latitudes in the 3D model is the same as that of the 2D model. A particular feature of the 3D model, however, is the northward propagating convection crossing the

equator on day 59 (Fig. 4.18). Since the Coriolis parameter is trivial ($\beta y \approx 0$) near the equator, the effect of the Coriolis force ($-\beta y u'^{+}$) on the northward propagation near the equator is minimal. In fact, the barotropic divergence, produced by the Coriolis force (Fig. 4.18d) at 8S is stronger than that at 8N. When convection is located at the equator, zonal advection terms ($-\overline{u}\frac{\partial v'}{\partial x}, -u'\frac{\partial \overline{v}}{\partial x}$) increase (suppress) the barotropic divergence to the north (south) of the equator (Fig. 4.18c). The same feature is also found at day 29 (Fig. 4.19). That is zonal advection terms ($-\overline{u}\frac{\partial v'}{\partial x}, -u'\frac{\partial \overline{v}}{\partial x}$) increase (suppress) the barotropic divergence to the north (south) of the equator and facilitate the northward propagation of the convection across the equator (Fig. 4.19c)

4.3.4 (c) Physical mechanism of northeastward propagation

Figure 4.19 suggestes that the northward propagation of convection near the equator is strongly influenced by the zonal advection ($-\overline{u}\frac{\partial v'}{\partial x}, -u'\frac{\partial \overline{v}}{\partial x}$). In figure 4.20, the barotropic mode of meridional divergence tendency [$\frac{\partial}{\partial y}(\frac{\partial v'^{+}}{\partial t})$, Fig. 4.20a] and the affect of zonal advection on the barotropic mode of meridional divergence tendency [$\frac{\partial}{\partial y}(-\overline{u}^{+}\frac{\partial v'^{+}}{\partial x} - u'^{+}\frac{\partial \overline{v}^{+}}{\partial x})$, Fig. 4.20b] are presented. In both Fig. 4.20a,b the increase of divergence is found to the northeastern part of the equatorial convection. It indicates that the zonal advection induces not only northward, but also eastward propagation when convection is located near the equator. Among the two types of the zonal advection, it is

the zonal advection by the July-mean zonal winds [$\frac{\partial}{\partial y}(-\overline{u}\frac{\partial v'}{\partial x})^{+}$, Fig. 4.20c] that produces the positive divergence tendency to the northeastern part of equatorial convection [$(\frac{\partial}{\partial y}\frac{\partial v'}{\partial t})^{+} > 0$, Fig. 4.20a]. How is the divergence in the northeastern direction produced? It can be explained by examining the divergence at 700hPa and 300hPa, induced by the zonal advection as shown in Fig. 4.20c.

In figure 4.21 the 850hPa July-mean zonal winds (Fig. 4.21a), low-level anomaly winds (Fig. 4.21b), and the low-level divergence due to the zonal advection [($\frac{\partial}{\partial y}(-\overline{u}\frac{\partial v'}{\partial x})$, Fig. 4.21c] are illustrated. The July-mean wind field show a predominance of westerlies in the northern hemisphere with the maximum at 10N, 60E (Fig. 4.21a). The low-level wind anomalies associated with convection (Fig. 4.21b) resemble the Rossby wave response to a convective heating source (Gill,1980). That is, cyclonic (anticyclonic) circulation of low-level winds develops to the west of the heating source in the northern (southern) hemisphere.

At the region west of the heating source (from 50E to 65E in Fig. 4.21b) in the northern hemisphere, the northerly component of winds increases with increasing longitude ($\frac{\partial v'}{\partial x} > 0$, Fig. 4.21b contour). On the other hand, at the region east of the equatorial heating source (from 65E to 90E), the northerly component of winds decreases with increasing longitude ($\frac{\partial v'}{\partial x} < 0$, Fig. 4.21b contour).

Since the July-mean zonal winds are westerlies in the northern hemisphere ($\overline{u} > 0$, Fig. 4.21a), the advection of meridional winds by July-mean zonal winds ($-\overline{u}\frac{\partial v'}{\partial x}$, Fig. 4.21c vector) is negative (positive) in the area west (east) of the convective center in the northern hemisphere. Consequently, the positive (negative) advection results in the increase (decrease) of meridional wind component (Fig. 4.21c, vector).

$$\frac{\partial v'}{\partial t} \approx -\overline{u}\frac{\partial v'}{\partial x} < 0, \quad \because \overline{u} > 0, \quad \frac{\partial v'}{\partial x} > 0 \ \textit{west of convection}, 10N \qquad (4.21\,a)$$
$$\frac{\partial v'}{\partial t} \approx -\overline{u}\frac{\partial v'}{\partial x} > 0, \quad \because \overline{u} > 0, \quad \frac{\partial v'}{\partial x} < 0 \ \textit{east of convection}, 10N \qquad (4.21\,b).$$

The acceleration of southerlies (northerlies) to the west (east) of the convection along 10N (Fig. 4.21c vector) produces the convergence (divergence) to the west (east) of convection at latitudes between 6S and 10N [$\frac{\partial}{\partial y}(-\overline{u}\frac{\partial v'}{\partial x})$, Fig. 4.21c, contour]. That is

$$\textit{Since } \frac{\partial v'}{\partial t} \approx -\overline{u}\frac{\partial v'}{\partial x} < 0, \ \textit{west of convection along } 10N,$$
$$\frac{\partial}{\partial y}(-\overline{u}\frac{\partial v'}{\partial x}) < 0 \ \textit{west of convection between } 6S \textit{ and } 10N \ (4.22a).$$

$$\textit{Since } \frac{\partial v'}{\partial t} \approx -\overline{u}\frac{\partial v'}{\partial x} > 0, \ \textit{east of convection along } 10N,$$
$$\frac{\partial}{\partial y}(-\overline{u}\frac{\partial v'}{\partial x}) > 0 \ \textit{east of convection between } 6S \textit{ and } 10N \ (4.22b).$$

The dominance of convergence (divergence) in the area west (east) of convection is also found at 300hPa (Fig. 4.22c). Since the direction of both July-mean winds (Fig. 4. 22a), and anomaly winds (Fig. 4.22b) are opposite to those at 700hPa, the divergence induced by zonal advection [$\frac{\partial}{\partial y}(-\overline{u}\frac{\partial v'}{\partial x})$] results in the same pattern between 300hPa

(Fig. 4.22c) and 700hPa (Fig. 4.21c). In conclusion, it is suggested that the zonal advection, produced by the Rossby wave type wind anomalies and July-mean winds, induces the divergence in a northeastern direction in both the upper- and lower-level of the atmosphere, and this divergence facilitates the northeastern propagation of convection from the equator to 10N.

4.3.5 The physical mechanism of the initiation of convection

The initiation of convection near 10S can be produced by both the 2D model (Fig. 3.2a) and the 3D model (Fig. 4.4a). In both models, convection in the southern hemisphere is located between 10S and the equator. The only difference between the 2D model and 3D models is that in the 3D model convection in the southern hemisphere propagates northward continuously, while in the 2D model there is a discontinuity of northward propagation across the equator.

In the case of the 2D model, the initiation of convection between 10S and the equator is facilitated by the meridional advection of the July-mean zonal winds ($-v'\frac{\partial \bar{u}}{\partial y}$) and the vertical advection of zonal winds by July-mean vertical motion ($-\bar{\omega}\frac{\partial u'}{\partial p}$). For example, in the 2D model, the meridional advection ($-v'\frac{\partial \bar{u}}{\partial y}$) and the vertical advection($-\bar{\omega}\frac{\partial u'}{\partial p}$) induce the maximum forcing of the barotropic easterlies at 10S . That is

$$\frac{\partial u'^{+}}{\partial t} \approx -(v'\frac{\partial \bar{u}^{+}}{\partial y})^{+} - (\bar{\omega}\frac{\partial u'}{\partial p})^{+} < 0 \quad at\ 10S,\ 2D \qquad (4.23).$$

Furthermore, barotropic easterlies at 10S increase the southerly component through the Coriolis force ($\frac{\partial v'^{+}}{\partial t} \approx -\beta y u'^{+} < 0$), and this increases of southerlies at 10S enhances the barotropic divergence ($\frac{\partial}{\partial y}\frac{\partial v'^{+}}{\partial t} > 0$) to the north of 10S.

In the 3D model convection also initiates in the latitude between 10S and the equator. Does it imply that the mechanism of initiation in the 2D model is still valid in the 3D model? When convection is located at 25N on day 44, the local maximum of barotropic easterlies is found at 12S (Fig. 4.23a). The Coriolis force on these easterlies enhances southerlies at 12S ($\frac{\partial v'^{+}}{\partial t} \approx -\beta y u'^{+} < 0$, Fig. 4.23c), so that the divergence [$\frac{\partial}{\partial y}(-\beta y u'^{+}) > 0$] develops between 12S and the equator (Fig. 4.23b). The initial mechanism of convection in the 3D model, depicted in figure 4.23c, is consistent with that found in the 2D model. Now, the question is whether the local maximum of barotropic easterlies at12S is induced by the same mechanism as in the 2D model.

In figure 4.24, the zonal momentum equation of the barotropic mode on day 44 is divided into each component. The latitudinal variation in the tendency of barotropic zonal winds (Fig. 4.24a) is consistent with the latitudinal variation of barotropic zonal wind anomalies in figure 4.23a.. That is when convection is located at 20N, local maxima of easterly acceleration are found in the latitude of 12S and 2S (Fig. 4.24a). This increase of easterlies between 12S and the equator comes from the negative meridional advection (Figs. 4.24b and 4.24c), and the vertical advection by July-mean vertical motion (Fig. 4.24e). The negative geopotential gradient force between 25S and

12S (Fig. 4.24g) is always balanced by the positive Coriolis force (Fig. 4.24f). Thus, the sum of Coriolis force and geopotential gradient force becomes positive throughout the southern hemisphere (Fig. 4.24h).

The latitude between 25S and 10N in figure 4.24 is selected, and shown in figure 4.25 in order to concentrate, in detail, on the southern hemisphere. The negative meridional advection (Figs. 4. 25b and 4.25c) and the negative vertical advection by July -mean vertical motion (Fig. 4.25e) play a part in the acceleration of barotropic easterlies in the southern hemisphere (Fig. 4. 25a).

It is clearly illustrated in figure 4.26 that the tendency of barotropic zonal winds (Fig. 4.26 a) in the southern hemisphere is governed by the sum (Fig. 4.26b) of meridional advection terms [$-(\overline{v}\frac{\partial u'}{\partial y})^{+} - (v'\frac{\partial \overline{u}}{\partial y})^{+}$] and the vertical advection by July-mean vertical motion [$-(\overline{\omega}\frac{\partial u'}{\partial p})^{+}$]. The other terms in the zonal momentum equation (Fig. 4.26c) produce the tendency that is opposite to the tendency of the zonal winds (Fig. 4.26a).

It seems that the mechanism of the initiation of convection in the southern hemisphere in the 2D model is still valid in the 3D model. At the same time, it is possible that the westward propagating Rossby-wave-like convection in the 3D model, with the maximum precipitation rate at 20N and 2S in the Indian Ocean, may have the influence on the initiation of convection.

4.3.6 The role of atmospheric waves in the 3D model

The basic physical mechanism of the initiation and the propagation of convection in the 3D model is similar to that of the 2D model. However, there is fundamental difference between the 2D model 3D models. That is, the presence of atmospheric waves in the 3D model. For example, in the 2D model, the July-mean upward motion ($\overline{\omega} < 0$) at 10S is critical for the initiation of convection in the southern hemisphere (Fig. 3.42). In the 3D model, the dipole structure of the westward moving Rossby-wave-like convection can predetermine the latitude, from which convection is initiated. In this section, three experiments are conducted to evaluate the effect of atmospheric Rossby wave response to a convective heating source in the Indian Ocean.

In the first experiment, the isolated heating is imposed at the location of 80E, 12N (Fig. 4.27). In this experiment convection in the northern hemisphere resembles the northern part of Rossby-wave-like convection in the 3D model. When the maximum heating source is found at 12N (Fig. 4.27a), the baroclinic mode of the atmosphere responds to the heating by generating the clockwise circulation to the west of the heating source (Fig. 4.27a vector). As a result, in the region west of convection, such as 50E, change of wind direction from easterlies to westerlies is found across 12N (Fig. 4. 27a). The presence of anti-cyclonic circulation in the baroclinic mode to the west of the convective center produces the local maximum of the easterly in the southwestern quadrant of convection (Fig. 4.27b). Thus, the zonal divergence in the baroclinic mode is found to the east of the maximum easterlies (Fig. 4.27b contour).

In Figure 4.27c the baroclinic divergence in the meridional direction (contour) is presented with the baroclinic winds. Since the Rossby wave response is concentrated to the west of the heating source, winds in the southeastern quadrant of convection are northerlies (Fig. 4.27c). Thus, the meridional convergence prevails in the region south of 5N, and east of 70E. In the 2D model, where atmospheric waves are absent, the baroclinic mode of meridional divergence intensifies the existing convection, and suppress any new development of convection elsewhere. In other words, convection in the northern hemisphere induces the baroclinic meridional convergence in the southern hemisphere, which suppresses the new development of convection. In that sense, the baroclinic meridional convergence (Fig. 4.27c) to the southeast of convection resembles the role of baroclinic mode in the 2D model.

On the other hand, the role of the baroclinic mode to the west of convection in the 3D model is different from that in the 2D model due to the influence of the atmospheric waves. For example, the Rossby wave response in the 3D model is easterlies in the area southwest to the convective center (Fig. 4.27c). Since the wave response becomes weaker further from the heating source, the winds change from easterlies to northerlies as the latitude decreases (Fig. 4 27c). Therefore, meridional divergence develops in the region between pure easterlies (5N) and pure northerlies (15S) (Fig. 4.27c). In summary, *the Rossby wave response to convection in the northern hemisphere can play a favorable role for the new development of convection in the region between 10S and 5N by producing a baroclinic divergence zone to the southwest of convection.*

In the second experiment, the isolated heating is imposed at 12S, 75E (Fig. 4. 28a) in order to examine the effect of Rossby wave response to convection in the southern hemisphere. The Rossby wave response to the heating source in the southern hemisphere creates anti-clockwise circulation to the west of the convective center (Fig. 4.28a, vector). Hence, easterly winds are found in the northwest-quadrant of convection. The divergence produced by these baroclinic winds is located in the region northwest of convection (Fig. 4.28a). Both zonal (Fig. 4.28b) and meridional divergence (Fig. 4.28c) are responsible for this total divergence shown in figure 4.28a.

The zonal divergence is found in the northeast quadrant of convection since the maximum easterlies is located in the northwest quadrant of convection (Fig. 4.28b). Since the wave response decreases with increasing distance from the heating source, easterlies near the equator west to the heating source become southerlies at 16N. Hence, the local maximum of meridional divergence is found in the northwest quadrant of convection (Fig. 4.28c), between the latitude of 10N and 10S. It should be observed that the variation of the baroclinic winds and the divergence field associated with convection in the northern hemisphere (Fig. 4.27a) is consistent with that in the southern hemisphere (Fig. 4.28a).

In the third experiment, the isolated heating is placed in both the northern and southern hemispheres (Fig. 4.29a). The Rossby wave response to convection in both hemispheres (Fig. 4.29) includes the characteristics of experiment 1 (Fig. 4.27) and experiment 2(Fig. 4.28).

The Rossby wave response to the west of convection produces anti-cyclonic circulation in baroclinic winds in both hemispheres. As a result, the local maximum of easterlies is found near the equator from 30E to 60E (Fig. 4.29a). This local maximum of easterlies in the western Indian Ocean (30E to 60E) induces the zonal divergence in the eastern Indian Ocean (60E to 100E).

As a part of the anti-cyclonic circulation, winds become southerlies (northerlies) to the west of convection in northern hemisphere (southern hemisphere). This change of meridional winds between hemispheres produces the meridional divergence at the equator (Fig. 4.29c). The sum of zonal divergence (Fig. 4.29b) and the meridional divergence (Fig. 4.29c) results in divergence between the two convective areas from 50E to 70E (Fig. 4.29a). It should be noticed that the divergence near the equator (from 50E to 70E) is located to the west of the two convective centers (80E). Due to this discrepancy in longitude between the divergence near the equator (50E-70E) and the convective centers (80E) in both hemispheres, the divergence near the equator is less influenced by the geopotential gradient force that suppresses the any new development of convection near the equator. Without the presence of Rossby wave, the variation of winds is located in the same longitude as the convective centers and greatly influenced by the geopotential gradient force which is associated with two convective centers. As a result, the initiation of the convection near the equator will be minimal (Figure not shown). It is the atmospheric wave that favors the initiation of convection near the equator by producing the equatorial baroclinic divergence to the west of the convective centers.

4.3.7 Experiments

In this section, a series of experiments are presented to support the physical mechanism of intraseasonal oscillation suggested in the 3D model. Inevitably, atmospheric waves in 3D model are involved in the initiation and propagation of convection. However, the main physical mechanism of initiation and propagation of convection in the 2D model can be found in the 3D model as well. For example, it is suggested that the vertical shear of July-mean zonal winds ($\frac{\partial \overline{u}}{\partial p}$) influences the propagation of convection from 10N to 20N, while the mean vertical motion at 10S ($\overline{\omega}$) is important for the initiation of convection between 10S and the equator.

In this section, six experiments are conducted to examine the above suggestions. The result from the 3D model using the July-mean state is served as a control run against each experiment. The first and the second experiments are designed to estimate the importance of the mean vertical motion at 10S ($\overline{\omega}$) in the initiation of convection in the latitude between 10S and the equator (Fig. 4.30).

In the first experiment, the vertical advection of zonal wind anomalies by July-mean vertical motion ($-\overline{\omega}\frac{\partial u'}{\partial p}$) is set to be zero in the area between 40E and 120E, and 45S and 12N (Fig. 4.30a). In the second experiment, the relative importance of this term is doubled (i.e. $-\overline{\omega}\frac{\partial u'}{\partial p}$ * 2) for the same area (Fig. 4.30c). Thus, in the two experiments $-\overline{\omega}\frac{\partial u'}{\partial p}$ * 0 (exp. 1) and $-\overline{\omega}\frac{\partial u'}{\partial p}$ * 2 (exp.2) are used instead of $-\overline{\omega}\frac{\partial u'}{\partial p}$ (control run) in the Indian Ocean (40-120E, 45S-12N).

In the control run, convection is initiated in the latitude between 5S and the equator (Fig. 4.30b). In the first experiment, the initiation of convection in the southern hemisphere is minimal (Fig. 4. 30a) in spite of the fact that the westward moving convection located at 20N is as strong as that in the control run (Fig. 4. 30b). In the 2D model convection was not initiated in the absence of the vertical advection associated with the July-mean vertical motion ($-\overline{\omega}\frac{\partial u'}{\partial p}$, Fig. 3. 42a). In the 3D model, however, the dipole pattern of the westward propagating convection can produce convection in the southern hemisphere without the term $-\overline{\omega}\frac{\partial u'}{\partial p}$ (Fig. 4.30a).

When the term $-\overline{\omega}\frac{\partial u'}{\partial p}$ is included in the control run the initiation and northward propagation of convection are intensified (Fig. 4.30b). It implies that the vertical advection associated with the July-mean vertical motion ($-\overline{\omega}\frac{\partial u'}{\partial p}$) is essential for the initiation of convection that subsequently propagates northward.

In the second experiment (Fig. 4.30c), in which the vertical advection is doubled (i.e. $-\overline{\omega}\frac{\partial u'}{\partial p}$ * 2), the period of the northward propagation decreases from 25 days in the control run to10 days (Fig. 4.30c). In addition, the pattern of the northward propagation becomes similar to that in the 2D model. For example, in the 3D model (Fig. 4. 30b), convection in the southern hemisphere is initiated by the westward moving convection at 15N. The northward propagating convection, which is located at 15N, does not initiate convection in the southern hemisphere in the 3D model. When the effect of July-mean

vertical motion in $-\overline{\omega}\frac{\partial u'}{\partial p}$ is doubled (Fig. 4. 30c), however, all convection at15N produces new convection in the southern hemisphere (Fig. 4.30c). It indicates that the July-mean vertical motion in $-\overline{\omega}\frac{\partial u'}{\partial p}$ is favorable for the initiation of convection in the southern hemisphere in the 3D model as well as in the 2D model.

Experiments 3 (exp. 3, Fig. 4.31a) and 4 (exp. 4, Fig. 4.31c) are used to evaluate the significance of the vertical advection of the July-mean zonal winds ($-\omega'\frac{\partial \overline{u}}{\partial p}$). In experiment 3 (Fig. 4.31a), $-\omega'\frac{\partial \overline{u}}{\partial p}$ is excluded in the longitude between 40E and 120E. As a result, convection in that area becomes weakened (Fig. 4.31a). Especially, the northward propagation of convection is not discernible.

When $-\omega'\frac{\partial \overline{u}}{\partial p}$ is incorporated in the control run (Fig. 4.31b), the intensity of convection, in general, increases (Fig. 4. 31b). In addition, a discontinuity in the northward propagation of convection is found near 10N. Thus, two types of northward propagation are noticeable in the control run. The first type of northward propagation covers latitudes from 5S to 10N, while the second type starts from 10N (Fig. 4. 31b). The first type represents the northeastward propagation of convection, which is explained in section 4.3.4(c). The vertical advection of July-mean zonal winds ($-\omega'\frac{\partial \overline{u}}{\partial p}$) is more influential on the second type than the first type of northward propagation, since the magnitude of the vertical shear ($\frac{\partial \overline{u}}{\partial p}$) is larger in the latitude between 10N and 20N than between 5S and 10N (Fig. 3.1f)

When the value of $-\omega'\frac{\partial\bar{u}}{\partial p}$ is arbitrarily doubled in the experiment 4 (i.e. $-\omega'\frac{\partial\bar{u}}{\partial p}$ *2, Fig. 4.31c) the continuity of the northward propagation has improved in the latitude between 5N and 20N (Fig. 4. 31c). It indicates that $-\omega'\frac{\partial\bar{u}}{\partial p}$ plays an important role in the propagation of convection in the northern hemisphere. In summary, this series of experiments in the 3D model confirms that the physical mechanism of the initiation and the northward propagation of convection in the 3D model is similar to that in the 2D model. In other words, the vertical advection by *July-mean vertical motion* winds ($-\bar{\omega}\frac{\partial u'}{\partial p}$) and the vertical advection of *July-mean zonal winds* ($-\omega'\frac{\partial\bar{u}}{\partial p}$) are fundamental for the initiation and the propagation of convection, respectively.

4.4 Intraseasonal oscillation in 3D model with the ocean mixed layer

4.4.1 The relationship between atmospheric and oceanic variables

In the previous section, the role of the atmospheric internal dynamics on the intraseasonal oscillation is examined. In this section an ocean mixed layer is incorporated with the atmospheric model to understand the role of air-sea interactions on the initiation and the propagation of convection in the 3D model. In order to study the role of air-sea interactions on the intraseasonal oscillation, it is necessary to understand the relationship between atmospheric and oceanic variables.

In figure 4.32, the spatial variation of precipitation rate (a), the low-level zonal winds (b), latent heat flux (c), and sst′ (d) on day 25 is presented. Day 25 is

approximately the day when the second life cycle of the intraseasonal oscillation begins. When the westward propagating convection in both hemispheres reaches 60E and starts dissipating, the new convection develops at the equator (Fig. 4.32a). Since the low-level zonal winds blow toward convection at 60E (Fig. 4.32a), the zonal winds in the region between 70E and 90E are easterlies (Fig. 4. 32b).

Since the low-level, July-mean zonal winds of the northern equatorial Indian Ocean are westerlies (Fig. 4.1b), the interaction between July-mean winds and low-level wind anomalies reduces the latent heat flux in the area from 70E to 90E and from 0N to 30N (Fig. 4.32c). It should be noticed that the spatial variation of SST anomalies (Fig. 4.32d) is opposite to that of latent heat flux (Fig. 4.32c). In fact, the variation of the SST is indirectly related to the latent heat flux, since the increase of latent heat flux induces the negative sst′ tendency ($i.e. \frac{\partial sst'}{\partial t} < 0$, figure not shown). This contributes to the negative sst′ anomalies on day 25 (Fig. 4. 32d).

As the convection near the equator propagates northeastward from day 26 (Fig. 4.33a) to day 27 (Fig. 4.33c), it encounters the positive sst′ near the eastern side of the Bay of Bengal (Fig. 4.33b), and the intensity of convection increases (Fig. 4.33c). It seems that positive SST anomalies near the eastern part of the Bay of Bengal are responsible for the enhancement of convection that passes through.

The other positive SST anomalies are found in the area between 90E and 140E, 15N and 30N on day 26 (Fig. 4.33b), and day 27 (Fig. 4.33d). The positive SST anomalies in this region are induced by the off-equatorial convection located at 110E, 12N (Fig. 4.33a, and Fig. 4. 33c). The off-equatorial convection decreases the latent heat

flux because the low-level easterlies associated with this convection are opposite in direction to the July-mean westerlires. The spatial variation of the zonal winds, latent heat fluxes, and SST anomalies indicates that the relationship between atmospheric and oceanic variables do exist in the intraseasonal time scale. However, in order to present the temporal- and the spatial relationship among variables more efficiently, a statistical method of lagged cross correlation is illustrated in figure 4.34.

In Figure 4.34, the lagged cross correlation among variables is calculated using the result of 120 days from the 3D model. Since the primary interest is to find out the effect of air-sea interaction on the northward propagation of convection, variables are zonally averaged over 60E to 100E before the lagged correlation is performed. In the calculation, the equatorial precipitation is used as a reference point. Consequently, the variables of each latitude are correlated with the precipitation at the equator. Thus, the lag cross correlation of precipitation at zero lag and the equator is one (Fig. 4.34a). In addition, the northward propagation of the positive lag correlation is found in the latitude between 5N and 20N (Fig. 4.34a)

At the equator, the surface temperature anomalies (ST') increase 7days before the precipitation is initiated at the equator (Fig. 4.34b). The increase of ST' also propagates northward slightly leading the northward propagation of convection and reaches the 18N at 2 day lag.

The lag correlation for the latent heat flux (Fig. 4.34c) and the low-level zonal winds (Fig. 4.34e) indicates that upon the arrival of convection at the equator, the westerlies increase and this increase of westerlies enhances evaporation. As a result,

when the westerlies propagate northward with convection (Fig. 4.34 e), the increase of latent heat flux also propagates with convection (Fig. 4.34c). It should be noted that the July-mean zonal winds are westerlies, thus the latent heat flux increases when zonal wind anomalies are westerlies.

Note that the sign of correlation in Fig. 4.34d is opposite to that in Fig. 4.34a. This implies that the variation of downward short wave radiation flux (DSWRF) is just opposite to that of precipitation (Fig. 4.34a). The only visual difference in lagged cross correlation between observation (Fig. 2.1) and the model results (Fig. 4.34) is found in the low-level meridional winds (Fig. 4.34f). However, both imply the same feature that the meridional convergence is important to the existence of convection.

Calculation of the lagged correlation of zonally averaged results from the 3D model accentuates the feature of the northward propagation of convection, and its relationship with other variables. It also facilitates the comparison between model results and observations, whose zonally averaged lagged correlation is calculated and presented in Chapter 2. Since the model results are three dimensional, the analysis of the lagged cross correlation can be expanded further in three dimensions .

In figure 4.35 the lagged cross correlations for the spatial variation of winds and thermodynamic variables associated with the intraseasonal oscillation are calculated for each grid point. The reference parameter used in the calculation is the precipitation averaged over the area from 60E to 95E, 2.5S to 2.5N. Thus, the lagged cross correlation of low-level winds at -6 day lag indicates the changes in the winds 6 days before convection occurs in the equatorial Indian Ocean (reference area). At -6 day lag,

easterlies are dominant at the equatorial Indian Ocean with two anticyclonic anomalies located on each side of the equator (Fig. 4.35a).

Since the July-mean zonal winds are westerlies at the equatorial and northern hemisphere, the easterly ISO winds from the equatorial region up to 15N reduce the latent heat flux(Fig. 4.35b). The DSWRF in this region (0N-15N) is positively correlated with the precipitation in the reference area (Fig. 4.35c), and the positive lagged correlation of DSWRF implies that sub-equatorial Indian Ocean is clear of convection. Eventually, the decrease of latent heat flux and the increase of DSWRF in the northern Indian Ocean causes the increase of ST' (Fig. 4.35d).

On zero day lag, winds converge along 2N near 80E, and this equatorial westerlies are associated with double cyclones, which are symmetric about the equator (Fig. 4. 35e). Note that the wind field, implied by cross correlation on 0 day lag in figure 4.35e, is just opposite to those on -6 day lag (Fig. 4.35a). Correspondingly, the latent heat flux (Fig. 4.35f), DSWRF (Fig. 4.35g), and the ST'(Fig. 4.35h) on 0 day lag show the opposite features to those on -6 day lag.

4.4.2 Physical mechanism of air-sea interaction

The analysis of lagged cross correlations in Section 4.4.1 verifies that the influence of convection and winds on the thermodynamic variables, such as latent heat flux, DSWRF, and SST in the model is consistent with that found in observations. In this section the physical mechanism of the variation in SST and its feedback on convection is examined.

*4.4.2 (a) Physical mechanism of variation in SST anomalies (*sst′*, hereafter)*

In figure 4.36, the precipitation rate (Fig. 4.36a) that propagates along 18N is shown with sst′ (Fig. 4.36b), zonal sst′ gradient (Fig. 4.36c), and the meridional sst′ gradient (Fig. 4.36d). The precipitation intensifies near the longitude of 65E, 85E, and 110E (Fig. 4.36a). Along those longitudes, the variation of sst′ is also found to increase just before or with the initiation of convection, and then decreases(Fig. 4.36b).

The zonal gradient of sst′ associated with convection is less organized compared to the meridional gradient of sst′ (Fig. 4.36c). In other words, the relationship between precipitation and zonal gradient of sst′ varies at different longitudes (Fig. 4.36c), whereas the precipitation closely coincides with the positive meridional gradient of sst′ (Fig. 4.36d). In addition, the magnitude of the zonal gradient of sst′ (Fig. 4.36c) is smaller than that of the meridional gradient of sst′ (Fig. 4.36d). The same strong relationship between precipitation and the meridional sst′ gradient is found for the northward propagating convection in figure 4.37. That is the propagation path of convection (shaded area) can be found in the latitude where the meridional gradient of sst′ is positive (Fig. 4.37d).

Then why the positive meridional gradient is found associated with the precipitation? The positive meridional gradient in sst′ is primarily forced by the atmospheric response to convection. For example, the convection that is located in the northern or southern hemisphere in the Indian Ocean has cyclonic circulation (Fig. 4.38). Since the July-mean zonal winds are westerlies and easterlies in the northern (Fig. 4.38a) and the southern (Fig. 4.38b) hemisphere, respectively, the latent heat flux decreases (increases) to the area north (south) of the convective center. Consequently, the positive

(negative) sst′ is found to the north (south) of the convective center, and the meridional gradient accompanying this convection becomes positive ($\frac{\partial sst'}{\partial y} > 0$). As a result, the meridional gradient of sst′ becomes positive both in the northern and southern hemisphere with the appearance of convection.

In figure 4.39, low-level winds (a), latent heat flux (b), and SST anomalies (c) are zonally averaged over 60-100E. Also shown are the meridional gradient of sst′ (d), and the laplacian of sst′ (e). In the northern hemisphere, westerlies and easterlies are dominant to the south and to the north of convection, respectively (Fig. 4.39a).

Since July-mean zonal winds are westerlies in the northern hemisphere, the interaction between July-mean zonal winds and anomaly winds enhances (suppresses) the latent heat fluxes to the south (north) of convection (Fig. 4.39b). Consequently, sst′ decrease (increase) to the south (north) of convection (Fig. 4.39c).

The increase of SST anomalies across convection (Fig. 4.39c) produces the positive meridional gradient of sst′ near the center of convection (Fig. 4.39d). In fact, the maximum of the positive meridional gradient of sst′ is found slightly to the north of the convective center. For example, on day 47 the maximum of the precipitation rate is found at 14N, while the maximum meridional gradient of the sst′ is found near 17N (Fig. 4.39d).

In figure 4.39e the laplacian of sst′ ($\frac{\partial^2 sst'}{\partial y^2}$) is shown. On day 30 and day 47, when convection is located near 15N, the positive and negative laplacian of sst′ are found to the south and to the north of convection, respectively (Fig. 4.39e).

While understanding the meridional gradient of sst′ ($\frac{\partial sst'}{\partial y}$, Fig. 4.39d) from the spatial variation of sst′ (Fig. 4.39d) is straightforward, envisioning the structure of the laplacian of sst′ ($\frac{\partial^2 sst'}{\partial y^2}$, Fig. 4 39e) is rather difficult. Thus, for convenience, the sst′-induced, meridional wind is defined as v'_{sst} that is purely driven by the sst′ gradient. In this sense, the laplacian of sst′ is equal to the divergence of v'_{sst}.

That is

$$v'_{sst} \cong \frac{\partial sst'}{\partial y} \qquad (4.24a)$$

$$\frac{\partial^2 sst'}{\partial y^2} = \frac{\partial v'_{sst}}{\partial y} \qquad (4.24b).$$

Using equation 4.24b, we can understand the variation of the laplacian of sst′ as a divergence of winds driven by the meridional gradient of sst′. For example, the maximum of meridional gradient of sst′ ($\frac{\partial sst'}{\partial y} > 0$) can be found near 17N on day 30 and day 47 (Fig. 4.39d). According to the definition in equation 4.24a, sst′-induced, meridional winds become southerlies ($v'_{sst} > 0$) near 17N on day 30 and day 47 (Figure not shown). These local maxima of southerlies ($v'_{sst} > 0$) near 17N can induce the convergence ($\frac{\partial^2 v'_{sst}}{\partial y^2} < 0$) and the divergence ($\frac{\partial^2 v'_{sst}}{\partial y^2} > 0$) of sst′-induced, meridional winds in the area north and south of 17N, respectively. Using the relationship between $\frac{\partial v'_{sst}}{\partial y}$ and $\frac{\partial^2 sst'}{\partial y^2}$ in the equation 4.24b, we can envision the positive (negative) laplacian to the south (north) of 17N (Fig. 4.39e).

4.4.2 (b) Feedback of SST on convection

The positive meridional gradient of sst′ induced by the interaction between July-mean winds and the cyclonic circulation associated with convection also impacts convection itself. To illustrate this feed back, it is necessary to examine the equation that connects the boundary layer vertical motion and the variability of sst′ (same as eq. 4.4, described in Section 4.2).

$$\omega_e' = D_1 \frac{\partial^2 \phi_e'}{\partial x^2} + D_2 \frac{\partial \phi_e'}{\partial x} + D_3 \frac{\partial^2 \phi_e'}{\partial y^2} + D_4 \frac{\partial \phi_e'}{\partial y}$$
$$- \frac{R(P_s - P_e)}{2P_e}[D_1 \frac{\partial^2 sst'}{\partial x^2} + D_2 \frac{\partial sst'}{\partial x} + D_3 \frac{\partial^2 sst'}{\partial y^2} + D_4 \frac{\partial sst'}{\partial y}] \quad (4.25),$$

where the coefficients are

$$D_1 = -\frac{(P_s - P_e)E_y}{E_x E_y + B^2 y^2}$$
$$D_2 = \frac{(P_s - P_e)B}{E_x E_y + B^2 y^2} - \frac{2(P_s - P_e)B^3 y^2}{(E_x E_y + B^2 y^2)^2}$$
$$D_3 = -\frac{(P_s - P_e)E_x}{E_x E_y + B^2 y^2}$$
$$D_4 = \frac{2(P_s - P_e)E_x B^2 y}{(E_x E_y + B^2 y^2)^2}.$$

Since the impact of the zonal variation of sst′on ω_e' is an order of magnitude smaller than the meridional variation of sst′(Figure not shown), our focus is on the impact of meridional gradient ($\frac{\partial sst'}{\partial y}$) and laplacian ($\frac{\partial^2 sst'}{\partial y^2}$) of sst′ on the boundary layer vertical motion. Since the coefficient of D_4 (Fig. 4.40a) in the northern hemisphere and southern hemisphere is positive and negative respectively, the positive sst′ gradient in the meridional direction in the northern hemisphere will enhance the vertical motion in the

boundary layer. On the contrary, the same positive meridional sst′ in the southern hemisphere induces downward motion, thereby suppressing the convective activity. That is

$$\omega_e' \approx -\frac{R(P_s-P_e)}{2P_e} D_4 \frac{\partial sst'}{\partial y} < 0, \quad \because \frac{R(P_s-P_e)}{2P_e} > 0, \; D_4 > 0, \frac{\partial sst'}{\partial y} > 0 \;\; in\ N.H. \quad (4.26a)$$

$$\omega_e' \approx -\frac{R(P_s-P_e)}{2P_e} D_4 \frac{\partial sst'}{\partial y} > 0, \quad \because \frac{R(P_s-P_e)}{2P_e} > 0, \; D_4 < 0, \frac{\partial sst'}{\partial y} > 0 \;\; in\ S.H. \quad (4.26b).$$

So far the role of the meridional gradient of sst′ ($\frac{\partial sst'}{\partial y}$) on the vertical motion of the boundary layer is explained. Still, the role of the other term, $\frac{\partial^2 sst'}{\partial y^2}$, on convection needs to be examined. In figure 4.39e it is already shown that the negative (positive) laplacian of sst′ ($\frac{\partial^2 sst'}{\partial y^2}$) is found to the north (south) of convection. Since D_3 (Fig. 4.40b) is negative throughout the latitude, and $\frac{-R(P_s-P_e)}{2P_e}$ equals 15.944, the negative (positive) laplacian of sst′ drives negative (positive) ω_e' to the north (south) of convection (Fig. 4.41).

That is

$$\omega_e' \approx -\frac{R(P_s-P_e)}{2P_e} D_3 \frac{\partial sst'}{\partial y} < 0, \because \frac{R(P_s-P_e)}{2P_e} > 0, \; D_3 < 0, \frac{\partial sst'}{\partial y} < 0 \;\; North.of\ convection \; (4.27a)$$

$$\omega_e' \approx -\frac{R(P_s-P_e)}{2P_e} D_3 \frac{\partial sst'}{\partial y} > 0, \because \frac{R(P_s-P_e)}{2P_e} > 0, \; D_3 < 0, \frac{\partial sst'}{\partial y} > 0 \;\; South\ of\ convection \; (4.27b).$$

In figure 4.42, the portion of Ekman pumping (ω_e') induced by the laplacian of sst′ (Fig. 4.42a) by the gradient of sst′ (Fig. 4.42b) or by both (Fig. 4.42c) in the meridional direction is illustrated. A comparison between figures 4.42a and 4.42b indicates that the influence of $\frac{\partial sst'}{\partial y}$ (Fig. 4.43a) on ω_e' is an order of magnitude smaller

than the influence of $\frac{\partial^2 sst'}{\partial y^2}$ (Fig. 4.43b). Therefore, the influence of $\frac{\partial^2 sst'}{\partial y^2}$ (Fig. 4.43b) nealy accounts for the total effect of sst′on ω_e' (Fig. 4.42c).

The structure of ω_e' induced by the meridional variation of sst′(Fig. 4.42c) indicates that the upward motion is dominant at the equator and near 20N on days 17, 30, and 47. At the same time, the downward motion develops at 8S and 13N (Fig. 4.42c). The upward (downward) motion to the north (south) of convection in the boundary layer (Fig. 4.42c) provides a favorable condition for convection to move northward. Furthermore, the upward motion near the equator can enhance the northward propagation of convection across the equator.

In figure 4.43, the effect of atmosphere (a), and the effect of sst′ (b) on Ekman pumping (ω_e') are compared. The total effect of atmosphere on ω_e' represents the terms of $D_1 \frac{\partial^2 \phi_e'}{\partial x^2} + D_2 \frac{\partial \phi_e'}{\partial x} + D_3 \frac{\partial \phi_e'}{\partial y} D_4 \frac{\partial^2 \phi_e'}{\partial y^2}$ in equation 4.4, while the total effect of sst′ includes the terms of $D_1 \frac{\partial^2 sst'}{\partial x^2} + D_2 \frac{\partial sst'}{\partial x} + D_3 \frac{\partial sst'}{\partial y} D_4 \frac{\partial^2 sst'}{\partial y^2}$. The total effect of the atmosphere indicates that the upward motion by the Ekman pumping is concentrated at 15N and 7S (Fig. 4.43a), in spite of the weak northward propagation of negative Ekman pumping velocity between these latitudes. This dipole type of upward motion implies the dominance of the Rossby-wave-like convection in the atmosphere.

The effect of sst′, on the other hand, enhances the upward motion at the equator and to the north of 20N (Fig. 4.43b). When the Rossby-wave-like convection is located

in both hemispheres, the reduction of the downward short wave radiation flux, and the increase of the latent heat flux result in the negative SST anomalies at the center and behind of convection (refer to Fig. 4.39c).

The cold sst′ behind convection is likely to induce the high pressure in the boundary layer, so that southerlies may develop across convection. As a result, the meridional convergence of these southerlies can be found in front of convection. From this aspect, the upward motion in the Ekman pumping at the equator and near 22N (Fig. 4.43b) is caused by the Rossby-wave-like convection located at 7S and 15N. Consequently, the effect of sst′ on this Rossby-wave-like convection is to enhance convection near the equator and near 22N.

4.4.3 Experiments

In this section a series of experiments are conducted to confirm the physical mechanism of air-sea interactions, provided in Section 4.4.2. It is suggested that sst′ influences the propagation of convection by enhancing (reducing) the upward motion in the boundary layer to the north (south) of convection. Furthermore, the structure of sst′ induced by the dipole type of convection in both hemispheres facilitates the upward motion near the equator and 20N (Fig. 4.43b). The increase of upward motion near the equator may support the continuous northward propagation of convection across the equator, while the upward motion near 20N may enhance the northward propagation to 20N.

The suggested role of sst' on the propagation of convection is tested in experiments 1, 2, and 3. In these experiments, terms of sst' in Ekman pumping (Eq. 4.4) are set to be zero times (Exp.1), five times (Exp.2), and ten times (Exp.3) of the original value. That is

$$Exp.1 \quad -\frac{R(P_s-P_e)}{2P_e}[D_1\frac{\partial^2 sst'}{\partial x^2}+D_2\frac{\partial sst'}{\partial x}+D_3\frac{\partial^2 sst'}{\partial y^2}+D_4\frac{\partial sst'}{\partial y}] * 0 \quad (4.28a)$$

$$Exp.2 \quad -\frac{R(P_s-P_e)}{2P_e}[D_1\frac{\partial^2 sst'}{\partial x^2}+D_2\frac{\partial sst'}{\partial x}+D_3\frac{\partial^2 sst'}{\partial y^2}+D_4\frac{\partial sst'}{\partial y}] * 5 \quad (4.28b)$$

$$Exp.3 \quad -\frac{R(P_s-P_e)}{2P_e}[D_1\frac{\partial^2 sst'}{\partial x^2}+D_2\frac{\partial sst'}{\partial x}+D_3\frac{\partial^2 sst'}{\partial y^2}+D_4\frac{\partial sst'}{\partial y}] * 10 \quad (4.28c).$$

By comparing results among Exp.1, Exp.2, and Exp.3, it is possible to identify the effect of the sst' on the propagation of convection.

When terms of sst' are set to zero (Exp.1, Fig. 4.44a), the dipole type of convection is dominant. In other words, the maximum of precipitation rate in the northern hemisphere is found in the latitude between 10N and 15N, while that in the southern hemisphere is found in the latitude between 10S and 5S (Fig. 4.44a).

When the terms of sst' is increased from 0% (Fig. 4.44a) to 500% (Fig. 4.44b), the northward propagation of convection appears. When the influence of sst' in the Ekman pumping is exaggerated by ten times of the original value, the northward propagation of convection from the southern hemisphere to 20N becomes evident (Fig. 4.44c). In addition, the location of the maximum precipitation rate moves from the latitude between 10N and 15N in experiment 1 (Fig. 4.44a) to between 15N and 20N in experiment 3 (Fig. 4.44c). The increase of continuity in the northward propagation from the southern hemisphere to 20N supports the suggestion that the influence of air-sea interactions are favorable for the northward propagation of convection.

The other side of the air-sea interactions is involved with the influence of convection on the variation of sst$'$. In Section 4.4.2, it is suggested that the interaction between wind anomalies and the July-mean winds contributes to the variation of sst$'$. In experiments 4, 5, and 6, July-mean winds in the 3D model are replaced by an idealized wind.

For example, in experiment 4, the zonal mean winds in both the upper and lower level are set to be 11 m/s (westerly basic state, Fig. 4.46). In experiment 5, the easterly zonal winds of -11 m/s are used as a mean state in both levels (easterly basic state, Fig. 4.47). In experiment 6 the low-level, July-mean winds in the control run are kept, but the upper-level winds are replaced by the low-level winds (i.e. $\overline{u}_{200hPa} = \overline{u}_{850hPa}$, Fig. 4.48).

Furthermore, in experiments 4, 5, and 6 the meridional mean winds, the mean vertical motion, and the vertical shear of zonal winds are neglected. That is

$$
\begin{aligned}
&Exp.4\ \ \overline{u}_{200hPa} = \overline{u}_{850hPa} = 11m/s, \\
&\qquad \overline{v}_{200hPa} = \overline{v}_{850hPa} = 0,\ \ \overline{\omega}_{200hPa} = \overline{\omega}_{850hPa} = 0,\ \ \tfrac{\partial \overline{u}}{\partial p} = 0 \quad (4.29a) \\
&Exp.5\ \ \overline{u}_{200hPa} = \overline{u}_{850hPa} = -11m/s, \\
&\qquad \overline{v}_{200hPa} = \overline{v}_{850hPa} = 0,\ \ \overline{\omega}_{200hPa} = \overline{\omega}_{850hPa} = 0,\ \ \tfrac{\partial \overline{u}}{\partial p} = 0 \quad (4.29b) \\
&Exp.6\ \ \overline{u}_{200hPa} = \overline{u}_{850hPa} = \overline{u}_{850hPa}\ (July\ mean\ state\ in\ control\ run) \\
&\qquad \overline{v}_{200hPa} = \overline{v}_{850hPa} = 0,\ \ \overline{\omega}_{200hPa} = \overline{\omega}_{850hPa} = 0,\ \ \tfrac{\partial \overline{u}}{\partial p} = 0 \quad (4.29c).
\end{aligned}
$$

By comparing results from experiments 4, 5, and 6, the role of the basic state on the variation of sst$'$can be illustrated.

In experiment 4 the basic state winds are westerlies (Fig. 4.46a), Kelvin-wave-like zonal wind anomalies are imposed as the initial perturbation. The Kelvin-wave-like zonal wind preserves its symmetric shape across the equator, with the maximum

westerlies at the equator from day 20 to day 30 (Fig. 4.46a). Since the basic-state winds are also westerlies, the interaction between mean winds and anomaly winds results in the increase of latent heat flux with the maximum value at the equator (Fig. 4.46b).

Corresponding to the meridionally symmetrical structure of the positive latent heat flux (Fig. 4.46b), the meridional structure of the sst′ is also symmetric across the equator (Fig. 4.46c). The minimum sst′ (Fig. 4.46c) at the equator produces a positive (negative) sst′ gradient in the northern (southern) hemisphere (Fig. 4.46d).

The minimum sst′at the equator (Fig. 4.46c) also creates the symmetric structure of the laplacian of sst′ (Fig. 4.46e). That is the negative laplacian is located in both hemispheres, while the positive laplcian of sst′ is found near the equator (Fig. 4.46e). The negative laplacian causes the upward motion of the Ekman pumping (Eq. 4.4), and produces the symmetric structure in convection (shaded area). It can be interpreted that the cold SST at the equator (Fig. 4.46c) induces winds (i.e. $v'_{sst} \approx \frac{\partial sst'}{\partial y}$), which are diverging (i.e. $\frac{\partial v'_{sst}}{\partial y} \approx \frac{\partial^2 sst'}{\partial y^2} > 0$) near the equator, and converging in both hemispheres (Fig. 4.47e). This convergence in the boundary layer generates upward motion and enhances convection.

In experiment 5 (Fig. 4.47) easterlies are used as a basic state. Again, the meridionally symmetric structure in the low-level winds (Fig. 4.47a) produces the symmetrical structure in latent heat flux, thereby inducing the symmetrical structure of

sst′. Consequently, the structure of $\frac{\partial^2 sst'}{\partial y^2}$ (Fig. 4.47e) becomes symmetric with respect to 5N.

The similarity between experiments 4 and 5 is that in both experiments, the meridional structure of latent heat and sst′ is symmetric with respect to the equator, regardless of the direction of the mean winds. The symmetric structure of latent heat fluxes and sst′ in both experiments is due to the absence of the meridional variation in the basic-state zonal winds (i.e. $\frac{\partial \bar{u}}{\partial y} = 0$).

When the basic-state zonal winds vary in the meridional direction (Fig. 4.45) as in experiment 6, the Kelvin-wave-like initial perturbation of anomaly winds (Fig. 4.48a) produces the anti-symmetric structure of latent heat fluxes (Fig. 4.48b) and sst′ (Fig. 4.48c). For instance, the easterly anomalies at 700hPa from day 35 to day 45 (Fig. 4.48a) is superimposed on the westerly (easterly) basic state winds (Fig. 4.45) in the northern (southern) hemisphere. The total winds in the northern hemisphere decreases, whereas that in the southern hemisphere increases from day 35 to day 45 (Figure not shown).

The latent heat flux, which is induced by the total winds, is suppressed (enhanced) in the northern (southern) hemisphere (Fig. 4.48b), and this anti-symmetric structure of latent heat flux results in the anti-symmetric structure of sst′ with respect to the equator (Fig. 4.48c). The meridional structure of sst′ (Fig. 4.48c), in return, generates the anti-symmetric structure in the laplacian of sst′ (Fig .4.48e), whose negative and positive values induce the upward and downward motion in the Ekman pumping, respectively (Eq. 4.4).

The role of sst′ variation, such as $\frac{\partial sst'}{\partial y}$ and $\frac{\partial^2 sst'}{\partial y^2}$, on the Ekman pumping (Eq.4.4) is further examined in experiment 6. In figure 4.49 the portion of Ekman pumping (ω_e') induced by laplacian of sst′ (Fig. 4.49a), by gradient of sst′ (Fig. 4.49b), and by both (Fig. 4.49c) are presented . A comparison among the three figures indicates that the laplacian of sst′ (Fig. 4 .49a) accounts for the total effect of sst′ (Fig. 4.49c) on the Ekman pumping. On day 26 and day 45, the upward motion in the northern hemisphere, and the downward motion in the southern hemisphere are enhanced by the variation of sst′ (Fig. 4.49c).

It should be remembered that in experiments 4 and 5, convection was meridionally symmetric, since convection is enhanced or suppressed in both hemisphere at the same time (Figs. 4.47e and 4.48e). However, in experiment 6 when the zonal mean winds vary with latitude, the asymmetric structure of convection is formed though the enhancement and the suppression of convection in the northern and the southern hemisphere (Fig. 4.49c).

It is know that when the Kelvin-wave-like perturbation is initiated at the equator, the atmospheric Rossby wave response creates the dipole structure of convection by producing cyclonic circulation in both hemispheres. It is speculated from experiments 4, 5, and 6 that the interaction between July-mean zonal winds, and the Kelvin-wave-like wind anomalies may distort the dipole (symmetric) structure of convection by increasing the asymmetry in the structure.

4.5 Conclusion

In chapter 4 the three dimensional model is used to examine the mechanism of the intraseasonal oscillation. The most important features of the intraseasonal oscillation are:

- Barotropic mode of atmosphere controls the propagation and the initiation of convection, while the baroclinic mode intensifies the existing convection.
- Vertical advection of July-mean westerlies ($-\omega' \frac{\partial \bar{u}}{\partial p}$) controls the propagation of convection in the northern hemisphere, while meridional advection and the vertical advection by July mean rising motion ($-\bar{v} \frac{\partial u'}{\partial y} - v' \frac{\partial \bar{u}}{\partial y} - \bar{\omega} \frac{\partial u'}{\partial p}$) at 10S favors the initiation of the convection between 10S and the equator.

- Due to the zonal variation of winds in the 3D model convection exhibits zonal movement, as well as, meridional movement. The zonal divergence in the barotropic mode induces the westward propagation of convection along 18N, and the zonal advection in the barotropic mode causes the northeastward propagation of convection from the equator to 10N.

- Rossby wave response to the dipole type heating source (convection) in the Indian Ocean creates a divergence in the baroclinic mode near the equator, and this baroclinic divergence may enhance convection near the equator.

- Low sst′ behind, and high sst′ in front of convection produces the positive meridional gradient of sst′ ($\frac{\partial sst'}{\partial t} > 0$) that causes boundary winds to converge north of the convection area. Consequently, the northward propagation of convection becomes more evident when air-sea interactions are included in the simulation.

• Due to the meridional variation in the July-mean zonal winds, the interaction between the Kelvin-wave-like wind anomalies and July-mean zonal winds may distort the dipole (symmetric) structure of convection by increasing the asymmetry in the meridional structure.

CHAPTER 5

SUMMARY AND DISCUSSION

5.1 Summary

The dissertation includes 5 chapters. Excluding chapters 1 (introduction) and 5 (summary and discussion), the main results are presented in chapters 2, 3, and 4. The observational study on the air-sea interaction of intraseasonal oscillation (ISO) is in chapter 2, while the simulation of the intraseasonal oscillation in 2- and 3 dimensional models is presented in chapter 3, and chapter 4, respectively. The simulation of ISO in 2 dimensional (chapter3) and 3 dimensional (chapter 4) is further divided into the case with the air-sea interaction, and without the air-sea interaction.

In chapter 2 the lagged cross correlation between convection and atmospheric variables is analyzed. The northward and southward movement are observed not only in convection, but also in the thermodynamic and dynamic variables. In the Indian Ocean the increase of OLR leads the increase of surface temperature by 1 pentad. Two pentads after the increase of ST', convection at the equator starts.

When convection develops at the equator, the Rossby wave response to the equatorial heating source enhances westerlies at the equator and easterlies at 15N. The increase of ISO easterlies in the northern Indian Ocean decreases surface heat flux. This, in turn, causes and the increase of ST' in the northern hemisphere. Eventually, the increase of ST' in the northern hemisphere favors the new development of convection in this region, thereby causing a see-saw type of oscillation in the Indian Ocean.

In chapter 3, the simulation of intraseasonal oscillation using 2-dimensional (2D) model is studied. Without the inclusion of air-sea interaction in the 2D model, the atmosphere alone can produce an oscillation and the northward propagation of convection.

In the northern hemisphere, the vertical advection of the July-mean zonal winds causes the upper-level divergence to the north of convective center. This upper-level divergence induces the moisture convergence in the boundary layer to the north of the convective center. As a result, convection propagates to the north of the existing convective center. In the southern hemisphere, the latitude between 10S and the equator is favorable for the initiation of new convection because of the maximum of the July-mean rising motion at 10S.

The inclusion of air-sea interactions results in the increase of the period and the intensity of the oscillation. A moderate decrease in the propagation speed of convection is also found when air-sea interactions are incorporated into the 2D model. While the increase (decrease) in evaporation to the south (north) of convection in the northern hemisphere delays the northward propagation of the convection, the sst' gradient induced by cold sst' (warm sst') in the region behind (in front of) convection enhances the boundary layer convergence north of convection, thereby promoting the northward propagation of convection. Although the effect of evaporation and sst' gradient on the propagation of convection are different, the continuity of the northward propagation from 5N to 20N is greatly improved when the air-sea interaction is included in the simulation.

In chapter 4 the simulation of intraseasonal oscillation using 3-dimensional (3D) model is studied. Most importanly, the role of the barotropic and baroclinic mode is examined separately. The barotropic mode of the atmosphere induces the propagation and the initiation of convection, while the baroclinic mode intensifies the existing convection. The barotropic mode of the atmosphere is mostly controlled by the vertical advection since it has the same sign in both the upper and lower level of the atmosphere inside regions of convection. The vertical advection of July-mean zonal winds, and the vertical advection by July-mean upward motion influence the propagation and the initiation of convection, respectively, though their impact on the barotropic mode of the atmosphere.

The variation in zonal direction in the 3D model contributes to the continuous northward propagation across the equator. When convection is located near the equator, the zonal advection by July-mean zonal winds facilitates the northward propagation of convection from the equator to 10N. Atmospheric waves also play a role in the intensification of convection near the equator by producing baroclinic divergence near the equator.

When air-sea interactions are included in the 3D model, the northward propagating convection causes negative (positive) sst' to the south (north) of convection. The positive sst' gradient across the convection area induces boundary layer winds, thereby causing convergence to the north of convection. Thus, the inclusion of air-sea interactions improve the simulation of northward propagating convection.

The meridional variation of the basic-state zonal winds is critical for the development of the asymmetric structure of convection across the equator. When Kelvin -wave-like convection is located at the equator, meridionally symmetric winds interact with July-mean zonal winds, which produces an asymmetric structure of convection by enhancing (suppressing) convection in the northern (southern) hemisphere.

5.2 Discussion

In spite of the success in the simulation of boreal summer intraseasonal oscillation, there are a few model limitations due to the simplification of the model physics.

First, the zonally averaged model cannot produce the northward propagating convection across the equator because both the vertical shear and Coriolis force become trivial near the equator. In fact, convection in the southern hemisphere seems to be trapped in the region between 10S and equator due to the change in sign of the vertical shear near 10S, and the change in sign of the Coriolis force near the equator.

Second, the SST anomalies in this study are much smaller than the observational values. For instance, Webster (1994) documented that during the TOGA COARE intensive observational period, the SST drops over 1°C associated with the westerly wind bursts during the convective phase of the ISO.

The small change in sst' in the model simulation is probably caused by the daily average of sst', high frequency of ISO, and the simplification of the ocean mixed layer dynamics. Since the daily variation of sst' is examined in this study, the shorter time scale

of sst′ variation, caused by the westerly wind burst, is not represented in the study. Another possibility is that in reality, the oscillation period is longer than that in the model simulation. As a result, more time is provided for the ocean surface to heat before the arrival of convection. In the model, the oscillation period is shorter than the observation, and the ocean surface may not have enough time to reach its maximum temperature. Lastly, the small SST anomaly can be caused the parameterization used in the ocean mixed layer. In the ocean mixed layer in the simulation, the entrainment and the ocean dynamics are excluded. Since sst′ may drop not only due to evaporation, but also the oceanic vertical mixing, the parameterization of sst′ based only on the net heat fluxes may represent only a portion of SST variation. In fact, other studies using similar mixed layer physics shows the same order of SST anomalies, such as 0.1-0.15 C (Flatau et al.,1997; Waliser et al., 1999). Although the perturbation of SST seems small, the inclusion of this interactive SST improved their simulation significantly. In the future, the result from this study should be compared with that from the more a complete mixed layer model.

Third, all the experiments in this study are conducted using the trace factor on specific terms. In the future, observational cases of weak or strong northward propagation are needed to be composed, and each case of their basic state winds should be used in the AGCM to verify the conclusion in this study.

Forth, the moisture content in the atmosphere in this study is fixed to the July-mean value. In reality, the moisture content varies associated with the condensation, evaporation, and the advection of the moisture in the atmosphere.

Finally, the linear processes in the atmosphere are examined to explain the periodicity and the propagation of convection in this study. The impact of non linear processes on the periodicity and the propagation of convection is needed to be addressed in the future work.

In spite of the above deficiencies in the model simulation, the implication of the physical mechanism suggested in this study contributes to the recent reache on the intraseasonal oscillation. For example, the role of baroclinic and barotropic mode on the intraseasonal oscillation and its interaction within convection are relatively new concepts. Due to the strong baroclinic mode imbedded in the intraseasonal anomalies, researchers have focused on the baroclinic nature of intraseasonal oscillation. Thus, the mechanism associated with the barotropic mode, in which the basic-state winds can interact with the intraseasonal oscillation is a new finding from this study. In the future, the barotropic and the baroclinic modes should be analyzed in the observational data, so that not only the relative magnitude but also the role of each mode on the propagation and the intensification of the intraseasonal oscillation can be scrutinized.

References

Anderson, J. R., and D. E. Stevens, 1987: The presence of linear wavelike modes in a zonally symmetric model of the tropical atmosphere. *J. Atmos. Sci.*, **44**, 2115-2127.

Anderson, J. R., and D. E. Stevens, 1987: The response of the tropical atmosphere to low frequency thermal forcing. *J. Atmos. Sci.*, **44**, 676-686.

Chen, T-C., and T. Murakami, 1988: The 30-50 day variation of convective activity over the western Pacific Ocean with emphasis on the northwestern region. *Mon. Wea. Rev.*, **116**, 892-906.

Emanuel, K. A., 1987: An air-sea interaction model of intraseasonal circulations in the tropics. *J. Atmos. Sci.*, **43**, 981-991.

Flatau, M. P. J. Flatau, P. Phoebus and P. P. Niller, 1997: The feedback between equatorial convection and local radiative and evaporative processes: The implications for intraseasonal oscillations. *J. Atmos. Sci.*, **54**, 2373-2386.

Gadgil, S. and J. Srinivasan, 1990: Low frequency variation of tropical convergence zones. *Meteor. Atmos. Phys.*, **44**, 119-132.

Garcia, R. R., and M. L. Salby, 1987: Transient response to localized episodic heating in the tropics. Part II. Far-field behavior. *J. Atmos. Sci.*, **44**, 499-530.

Gautier, C., and B. DiJulio, 1990: Cloud effects on air-sea interactions during the 1979 Indian summer monsoon as studies from satellite observations. *Meteor. Atmos. Phys.*, **44**, 251-263.

Gill, A. E., 1980: Some simple solutions for heat-induced tropical circulation. *Quart. J. Roy. Meteor. Soc.*, **106**, 447-462.

Goswami, B. N., and J. Shukla, 1984: Quasi-periodic oscillations in a symmetrical general circulation model. *J. Atmos. Sci.*, **41**, 20-37.

Hartmann, D. L., and M. L. Michelsen, 1989: Intraseasonal periodicities in Indian rainfall. *J. Atmos. Sci.*, **46**, 2838-2862.

Hayashi, and S. Miyahara, 1987: A three-dimensional linear response model of the tropical intraseasonal oscillation. *J. Meteor. Soc. Japan*, **65**, 843-852.

Hu, Q., and D. A. Randall, 1994: Low frequency oscillations in radiative-convective systems. *J. Atmos. Sci.*, **51**, 1089-1099.

_____, and D. A. Randall, 1995: Low frequency oscillations in radiative-convective systems. Part II: An idealized model. *J. Atmos. Sci.*, **52**, 478-490.

Jones, C., and B. C. Weare, 1996: The role of low-level moisture convergence and ocean latent heat fluxes in the Madden-Julian Oscillation: an observation analysis using ISCCP data, and ECMWF analysis. *J. climate*, **9**, 3086-3104.

Jones, D. E. Waliser, and C. Gautier, 1998: The influence of the Madden-Julian oscillation on ocean surface heat fluxes and sea surface temperatures. *J. climate*, **11**, 1057-1072.

Kalnay, E., M. Kanamitsu, R. Kistler, W. Collins, D. Deaven, L. Gandin, M. Iredell, S. Saha, K. C. Mo, C. Ropelewski, J. Wang, A. Leetmaa, R. Reynolds, Roy Jenne, and Dennis Joseph, 1996: The NCEP/NCAR 40-year reanalysis project. *Bull. Amer. Meteor. Soc.*, **77**, 437-471.

Knutson, T. R. and K. M. Weickmann, and J. E. Kutzbach, 1986: Global-scale intraseasonal oscillation of outgoing longwave radiation and 250 mb zonal wind during northern hemisphere summer. *Mon. Wea. Rev.*, **114**, 605-623.

Krishnamurti, T. N. and D. Subrahmanyam, 1982: The 30-50 day mode at 850 mb during MONEX. *J. Atmos. Sci.*, **39**, 2088-2095.

_____, D. K. Jayakumar, J. Sheng, N. Surgi, and A. Kumar, 1985: Divergent circulation on the 30 to 50 day time scale. *J. Atmos. Sci.*, **42**, 364-375.

Kuo, H.-L., 1974: Further studies of the parameterization of the influence of cumulus convection on large-scale flow. *J. Atmos. Sci.*, **31**, 1231-1240.

Lau, K.-M., G. J. Yang and S. H. Shen (1988): seasonal and intraseasonal climatology of summer monsoon rainfall over East Asia. *Mon. Wea. Rev.*, **116**: 18-37.

Lau, K.-M., and N.-C. Lau, 1990: Observed structure and propagation characteristics of tropical summertime synoptic scale disturbances. *Mon. Wea. Rev.*, **118**, 1888-1913.

_____, and C. H. Sui, 1997: Mechanism of short-term sea surface temperature regulation: Observations during TOGA COARE. *J. climate*, **9**, 465-472.

Lin, X., and R. H. Johnson, 1996: Kinematic and thermodynamic characteristics of the flow over the western Pacific warm pool during TOGA COARE. *J. Atmos. Sci.*, **53**, 695-715.

Madden, R., and P. R. Julian, 1971: Detection of a 40-50 day oscillation in the zonal wind in the tropical Pacific. *J. Atmos. Sci.*, **28**, 702-708.

Murakami, T., 1980: Empirical orthogonal function analysis of satellite observed outgoing longwave radiation during summer. *Mon. Wea. Rev.*, **108**, 205-222.

Neelin, J.D., I. M. Held, and H. Cook, 1987: Evaporation-wind feedback and low-frequency variability in the tropical atmosphere. *J. Atmos. Sci.*, **44**, 2341-2348.

Nitta, T., 1987: Convective activities in the tropical western Pacific and their impact on the northern hemisphere summer monsoon. *J. Meteor. Soc. Japan*, **65**, 373-390.

Oort, A. H., 1983: Global Atmospheric Circulation Statistics, 1958-73.NOAA Prof. Paper No.14.

Ouergli, A. and P. De Felice, 1996: North-eastward propagating 25-50 day mode and its link with Indian summer monsoon activity. *Meteor. Atmos. Phys.*, **61**, 127-135

Salby, M.. L., and R. R. Garcia, 1987: Transient response to localized episodic heating in the tropics. Part I: Excitation and short-time near-field behavior. *J. Atmos. Sci.*,**44**, 458-498.

Seager, R., S. E. Zebiak, and M. A. Cane, 1988: A model of tropical Pacific sea surface temperature climatology. J.Geophys. Res., **93** (c2), 1265-1280.

Yamagata, T., and Y. Hayashi, 1984: A simple diagnostic model for the 30-50 day oscillation in the tropics. *J. Meteor. Soc. Japan*, **62**, 709-717.

Yasunari, T.,1979: Cloudiness fluctuations associated with the Northern Hemisphere summer monsoon. *J. Meteor. Soc. Japan*, **57**, 227-242.

Yasunari, T., 1980: A quasi-stationary appearance of 30-40 day period in the cloudiness fluctuations during the summer monsoon over India. *J. Meteor. Soc. Japan*, **58**, 225-229.

Yasunari, T., 1981: Structure of an Indian summer monsoon system with a period around 40 days. *J. Meteor. Soc. Japan*, **58**, 225-229.

Waliser, D. E., K. M. Lau, and K-H. Kim, 1999: The influence of coupled sea surface temperatures on the Madden-Julian oscillation: a model perturbation experiment. *J. Atmos. Sci.*, **56**, 333-358.

Wang, B.,1988: Comments on "Air-sea interaction model of intraseasonal oscillation in the tropics. *J. Atmos. Sci.*, **45**, 3521-3525.

Wang, B., and H., Rui, 1990: Synoptic climatology of transient tropical intraseasonal convection anomalies: 1975-1985. *Meteor. Atmos. Phys.*, **44**, 43-61.

_____ , and T. Li, 1993: A simple tropical atmospheric model of relevance to short-term climate variation. *J. Atmos. Sci.*, **50**, 260-284.

_____ , and ____ , 1994: Convective interaction with boundary-layer dynamics in the development of a tropical intraseasonal system. *J. Atmos. Sci.*, **51**, 1386-1400.

_____ , and X. Xie, 1997: A model for boreal summer intraseasonal oscillation. *J. Atmos. Sci.*, **54**, 72-86.

_____ , and _____ , 1998: Coupled modes of the warm pool climate system Part I: The role of air-sea interaction in Madden-Julian oscillation. *J. climate*, **11**, 2116-2135.

Webster, P. J., 1983: Mechanisms of monsoon low-frequency variability: Surface hydrological effects. *J. Atmos. Sci.*, **40**, 2110-2124.

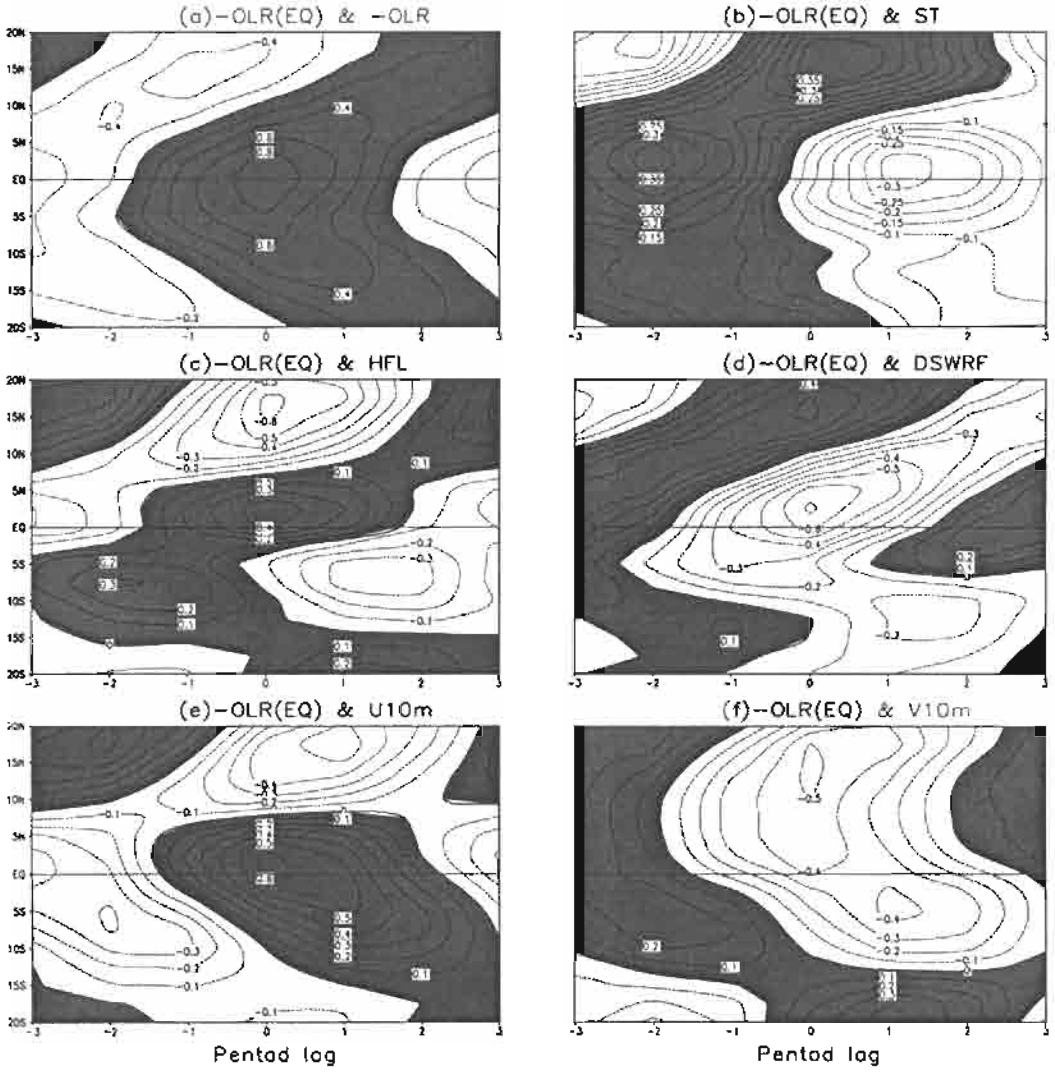

Figure 2.1: Pentad lagged cross correlation between negative outgoing longwave radiation (-OLR) at equatorial Indian Ocean (0N, 60-100E) and (a) OLR, (b) surface temperature (ST), (c) surface heat fluxes, (d) downward shortwave radiation flux (DSWRF), (e) surface zonal wind (U 10m), (f) surface meridional wind (V10m).

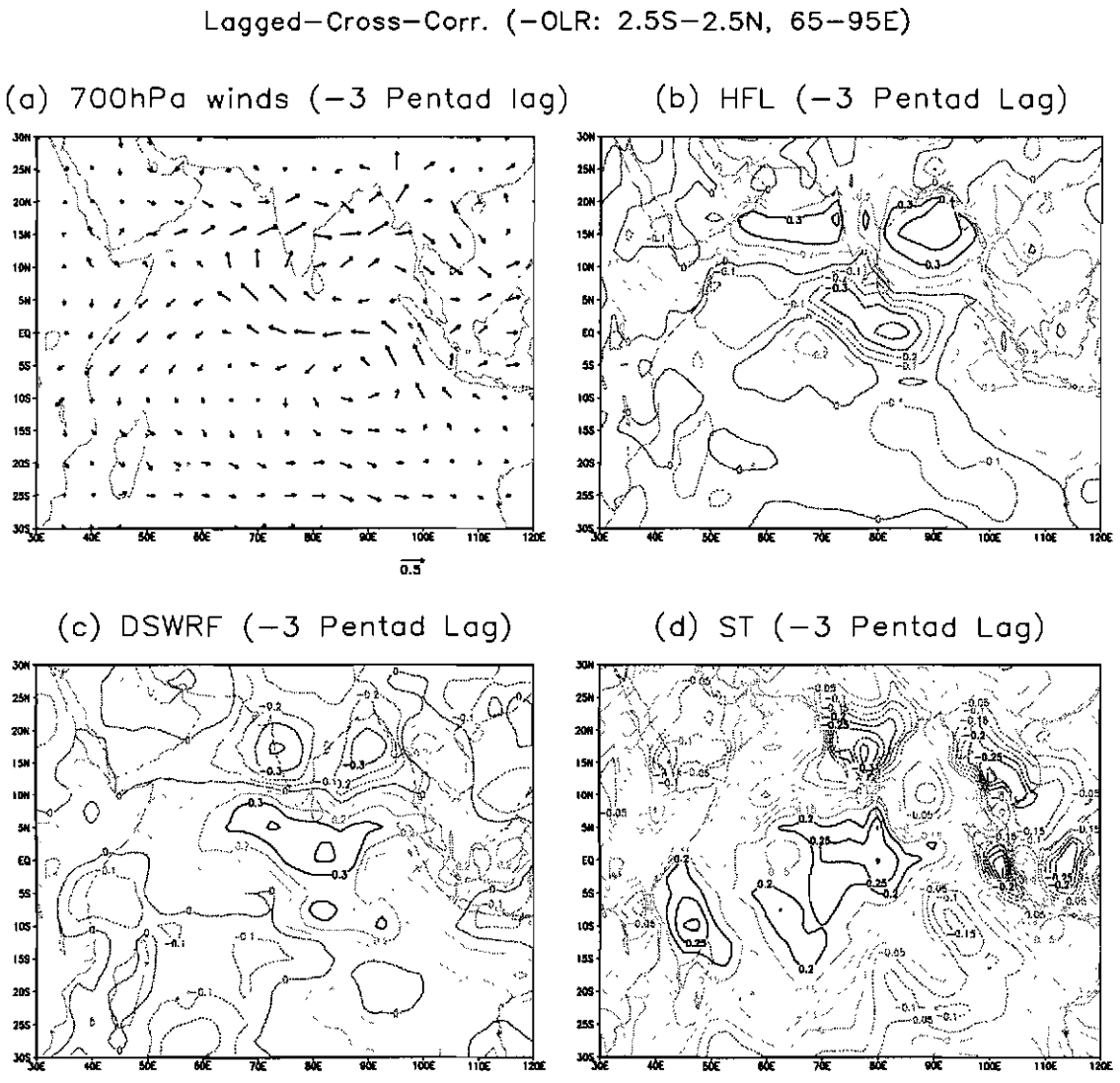

Figure 2.2: Pentad lagged cross correlation between area-averaged negative OLR (-OLR) and (a) 850hPa winds at -3 pentad lag, (b) surface heat fluxes at -3 pentad lag, (c) downward shortwave radiation flux at -3 pentad lag, (d) surface temperature at -3 pentad lag, (e) 850hPa winds at 0 pentad lag, (f) surface heat flux at 0 pentad lag, (g) downward shortwave radiation flux at 0 pentad lag, and (h) surface temperature at 0 pentad lag.

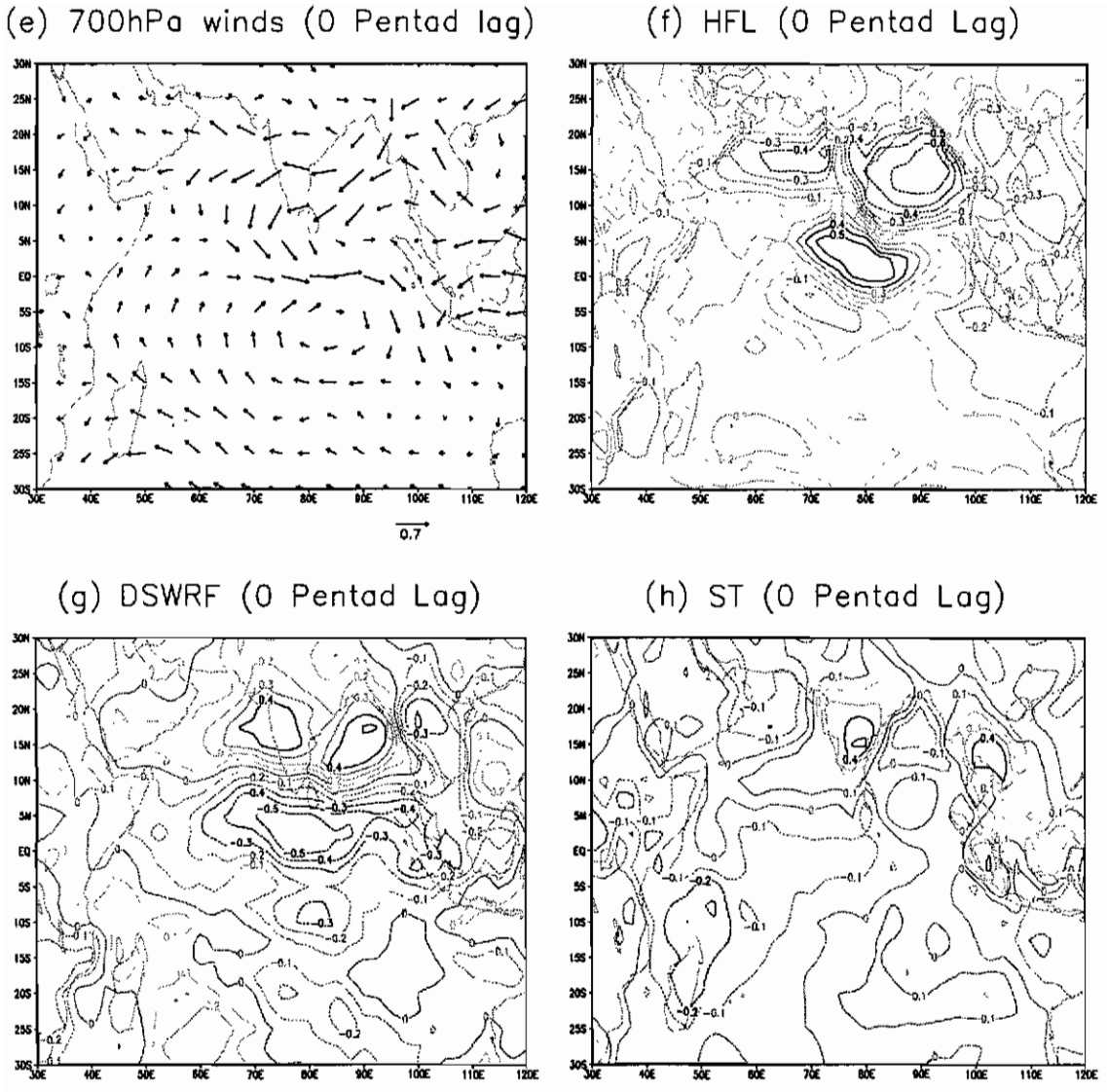

Figure 2.2: (Continued).

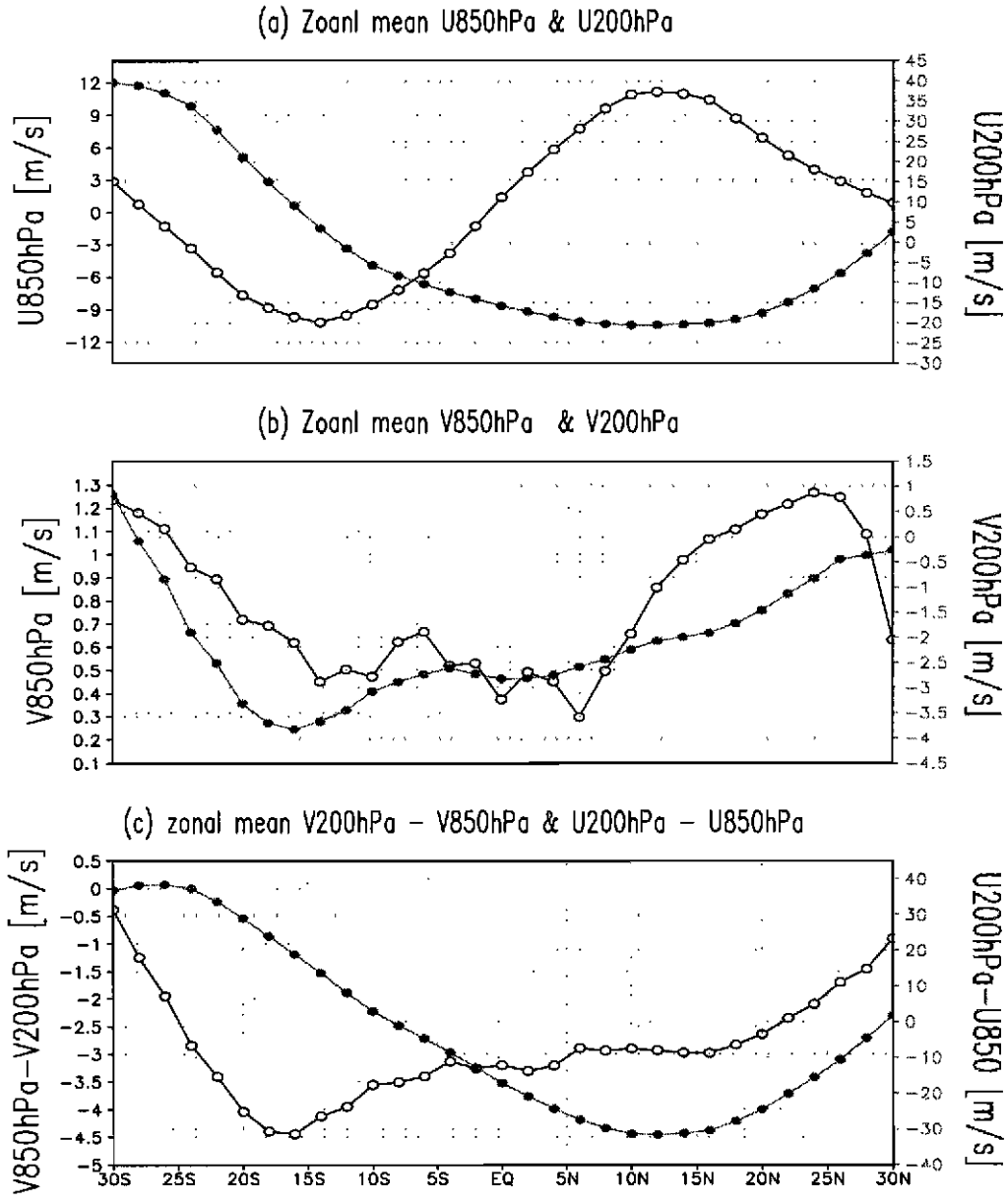

Figure 3.1: Mean state used in zonally averaged two dimensional model (2D model). (a) 850hPa and 200hPa zonal wind, (b) 850hPa and 200hPa meridional wind, (c) vertical shear of zonal and meridional winds between 200hPa and 850hPa, (d) average of vertical motion ($\bar{\omega}$) between 850hPa and 200hPa, (e) specific humidity, and (f) spatial variation of 850hPa winds (vector) and average of vertical motion between 850hPa and 200hPa (contour).

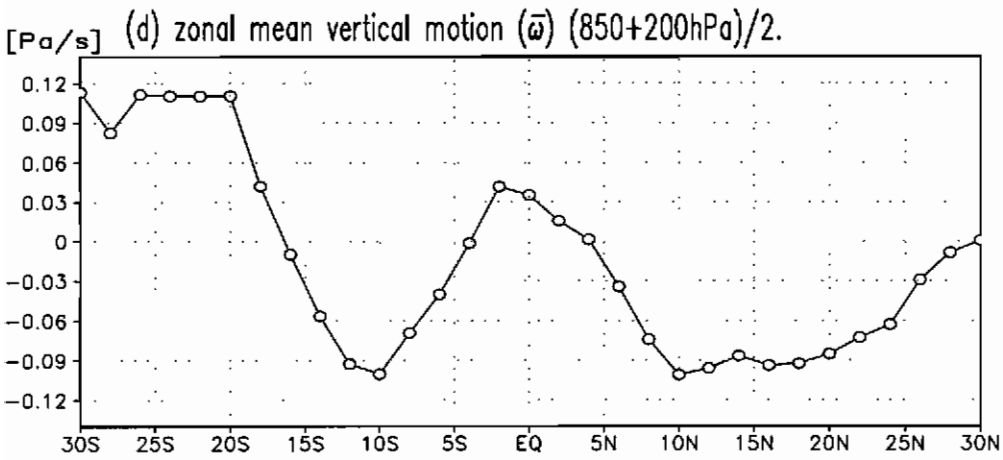

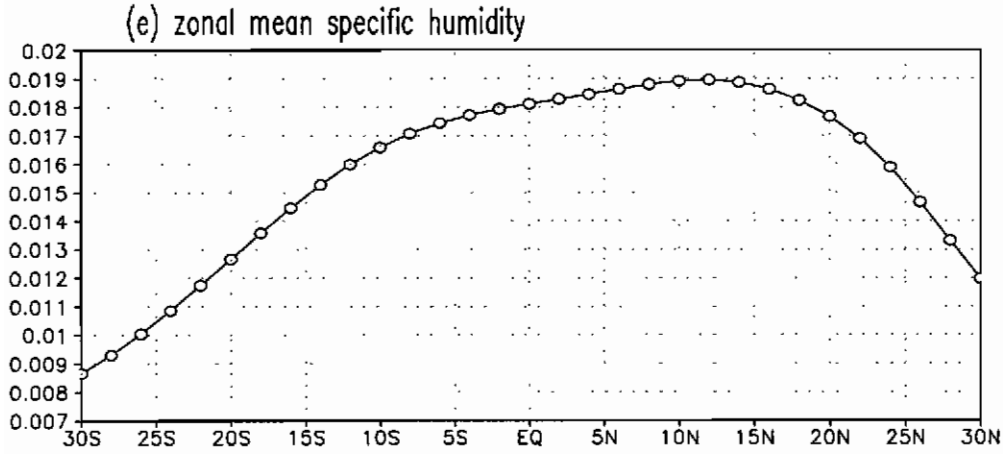

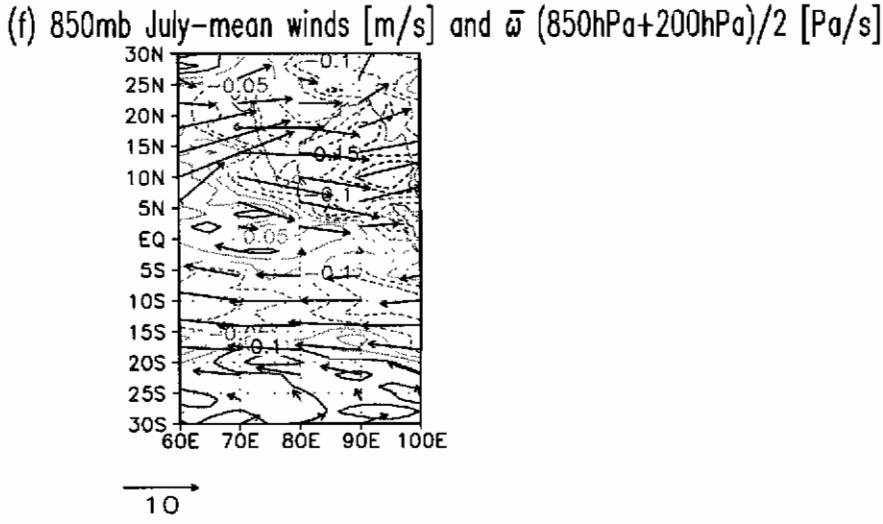

Figure 3.1: (Continued).

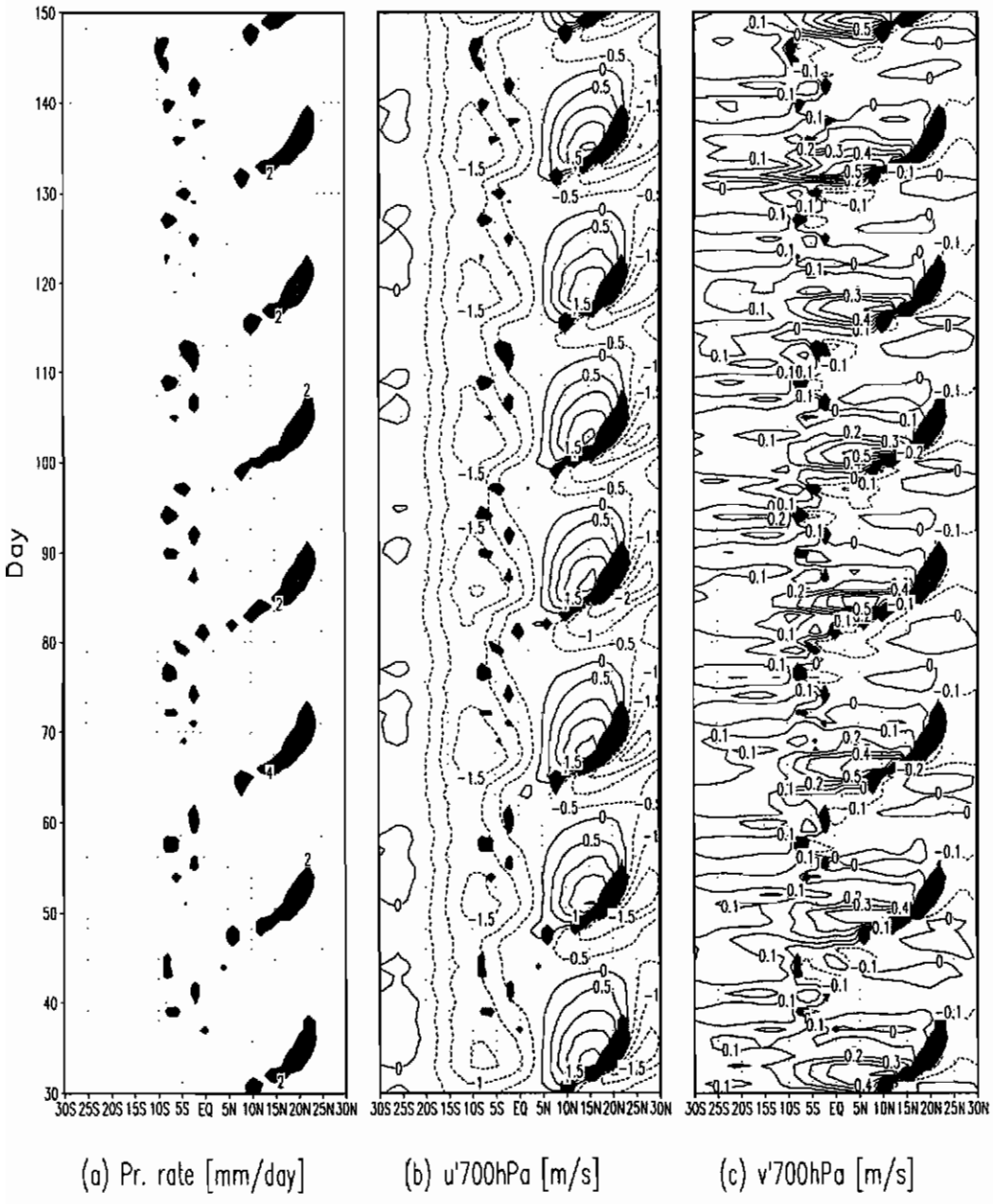

Figure 3.2: Latitude-time section of anomalies from zonally averaged model (2D model) without ocean mixed layer. (a) precipitation rate (mm/day), (b) low level zonal wind (m/s), and (c) low level meridional wind (m/s).

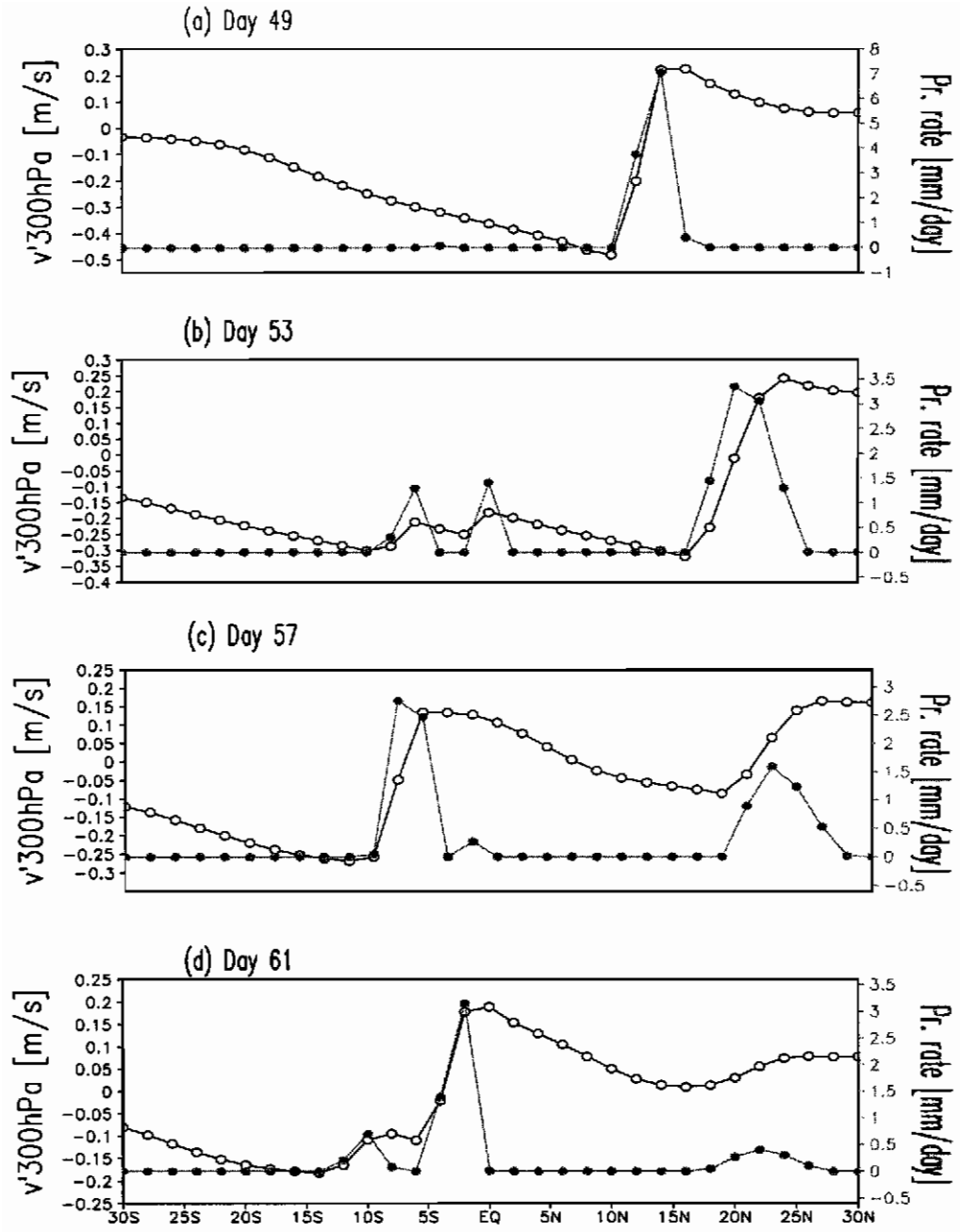

Figure 3.3: Latitudinal variation of meridional winds at 300hPa (v'_{300hPa} , -o-) and precipitation rate (-•-) on (a) day 49, (b) day 53, (c) day 57, (d) day 61, (e) day 63, (f) day 65, (g) day 67, and (h) day 69.

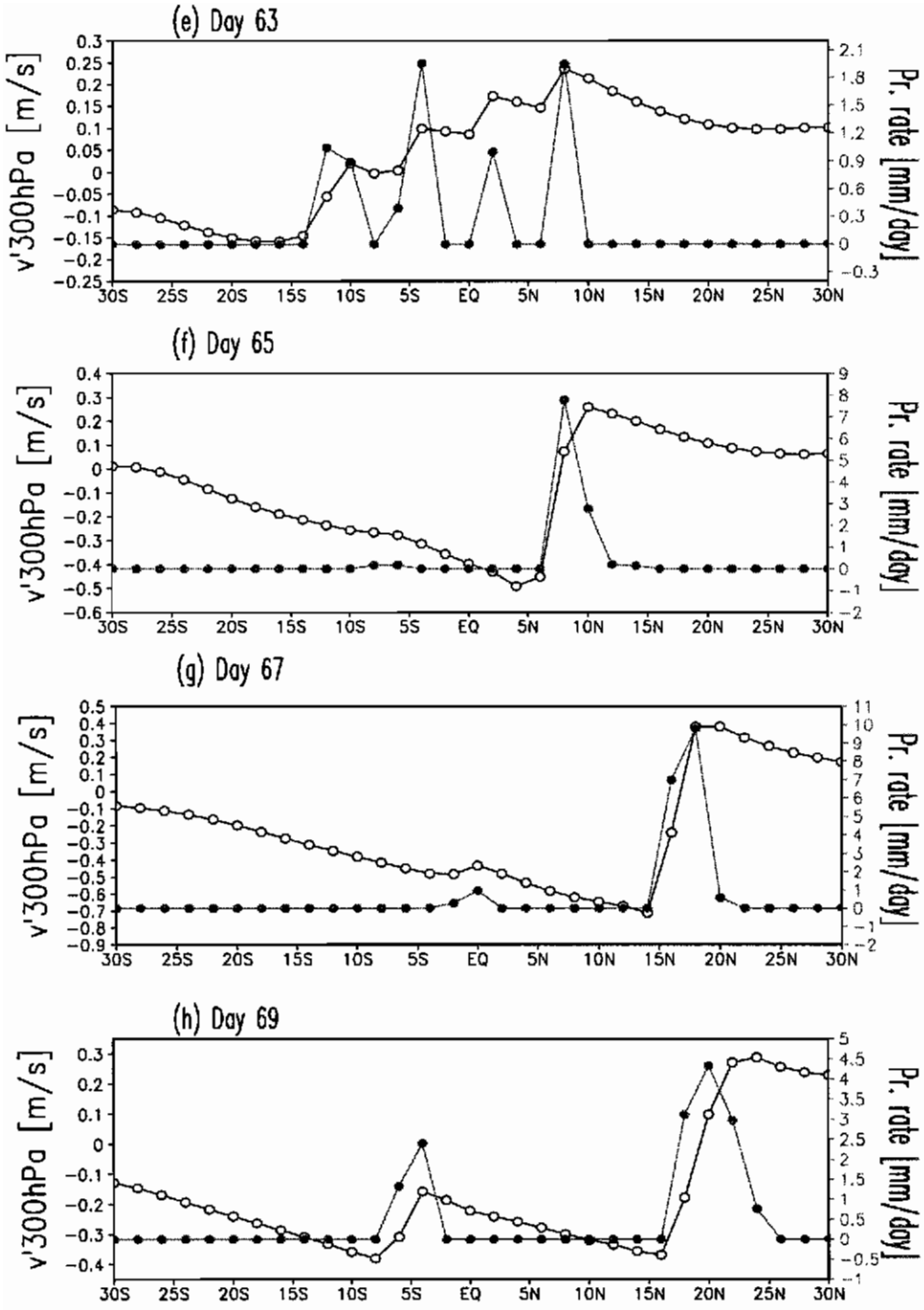

Figure 3.3: (Continued).

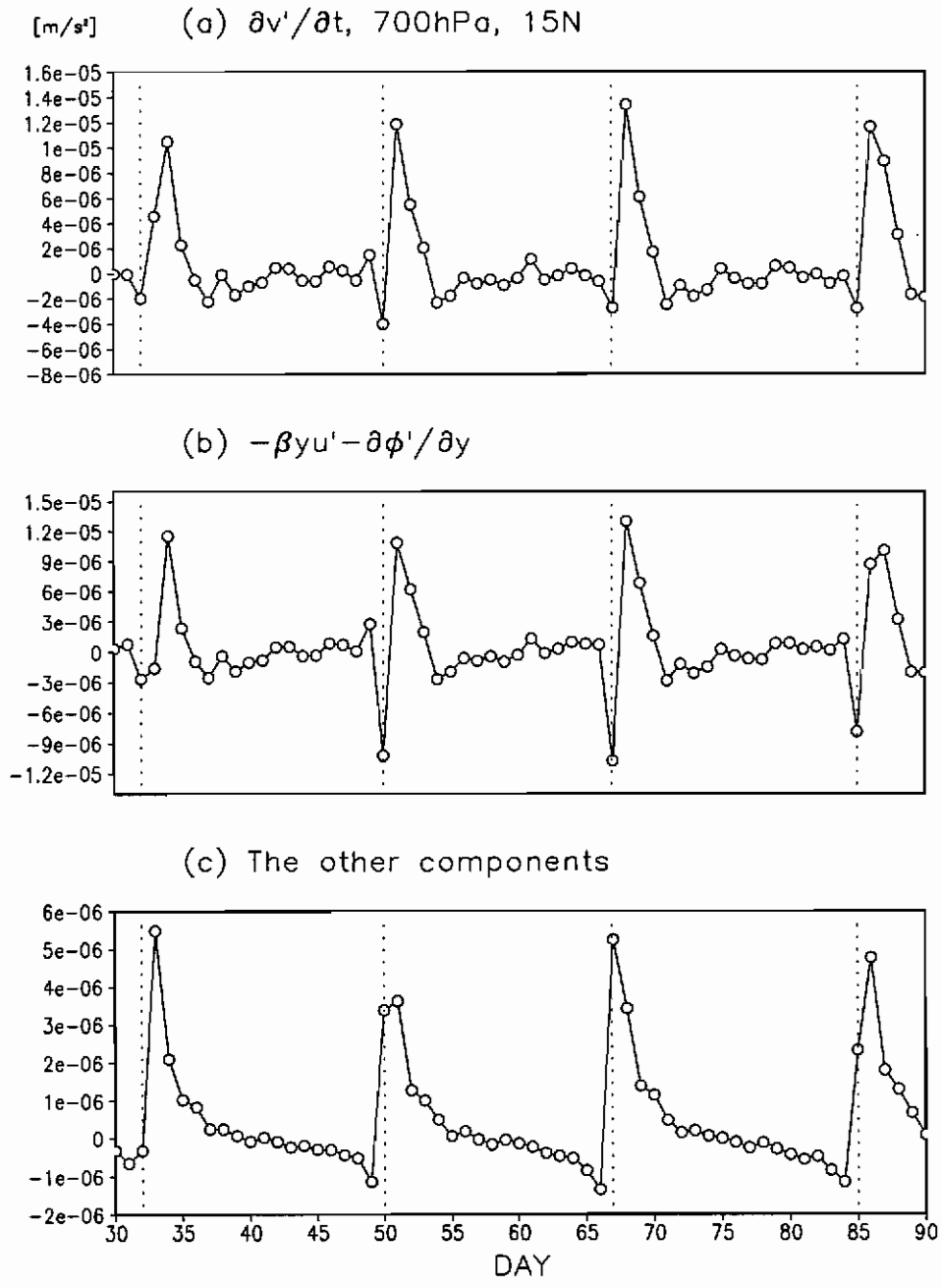

Figure 3.4: Time series (Day) of (a) $\frac{\partial v'}{\partial t}$, (b) sum of $-\beta y u'$ and $-\frac{\partial \phi'}{\partial y}$, and (c) sum of $-\overline{v}\frac{\partial v'}{\partial y}$, $-v'\frac{\partial \overline{v}}{\partial y}$, $-\omega'\frac{\partial \overline{v}}{\partial p}$, and $-\overline{\omega}\frac{\partial v'}{\partial p}$ at 15N, 700hPa.

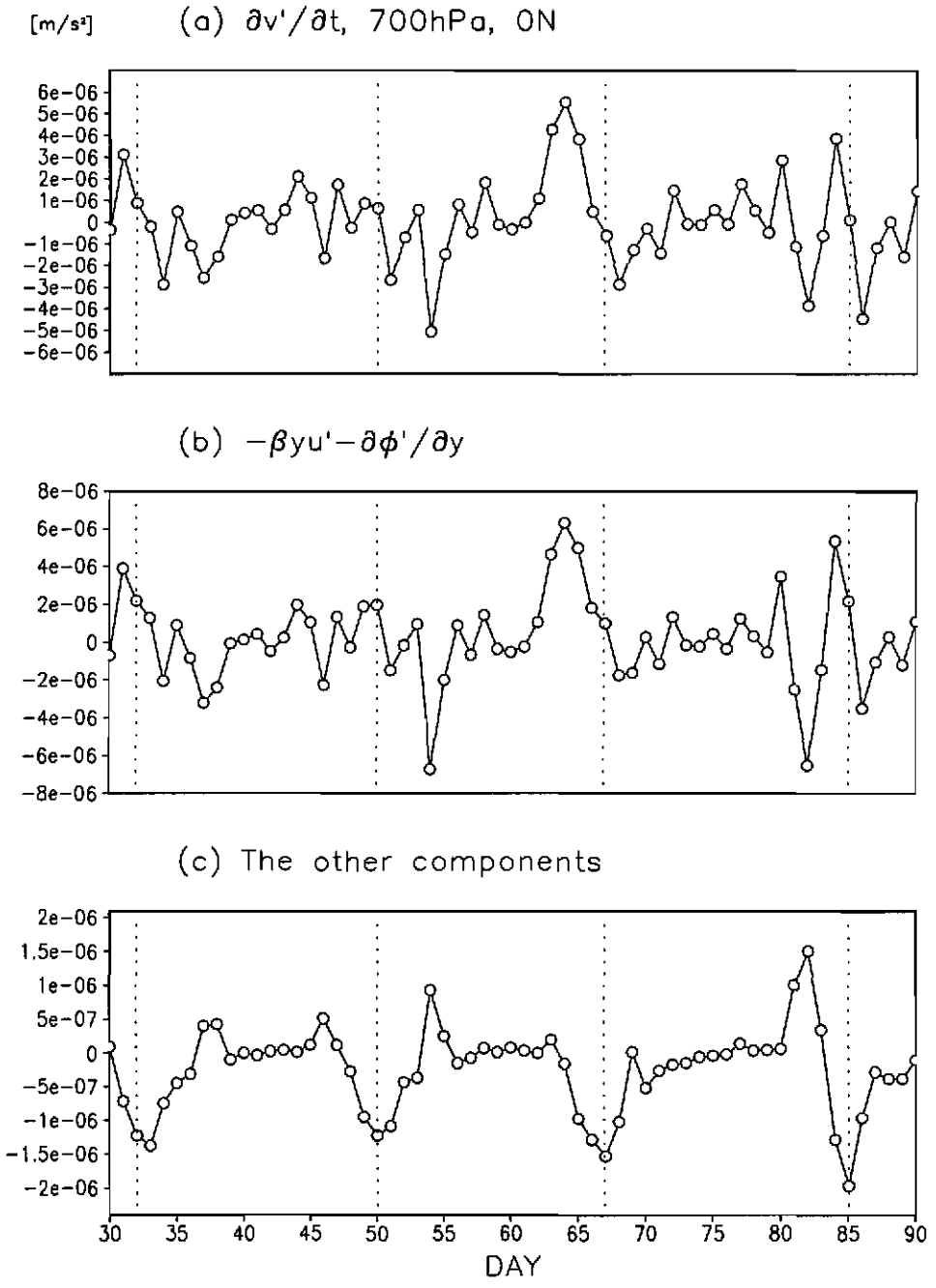

Figure 3.5: Time series (Day) of (a) $\frac{\partial v'}{\partial t}$, (b) sum of $-\beta y u'$ and $-\frac{\partial \phi'}{\partial y}$, and (c) sum of $-\overline{v}\frac{\partial v'}{\partial y}$, $-v'\frac{\partial \overline{v}}{\partial y}$, $-\omega'\frac{\partial \overline{v}}{\partial p}$, and $-\overline{\omega}\frac{\partial v'}{\partial p}$ at 0N, 700hPa.

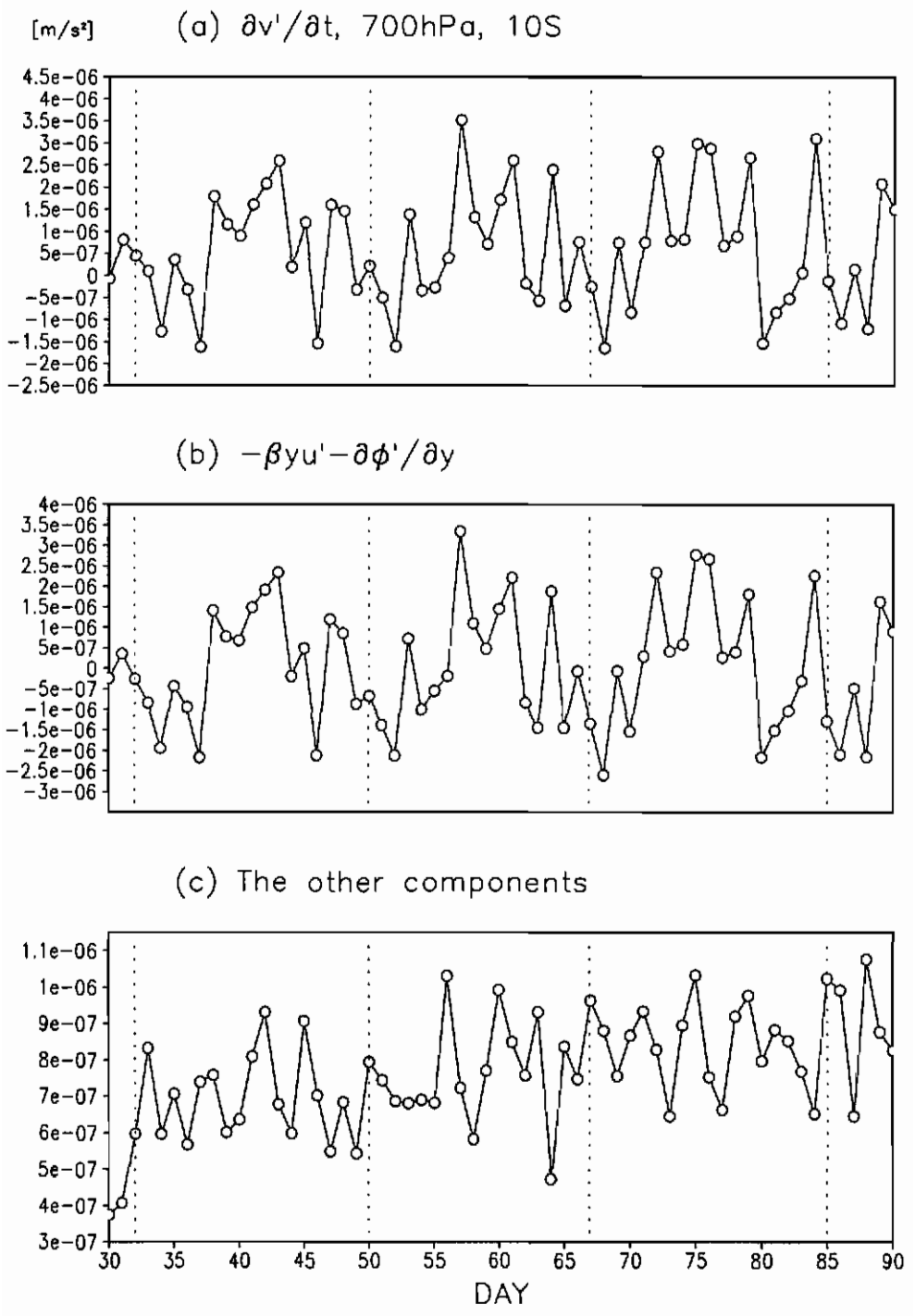

Figure 3.6: Time series (Day) of (a) $\frac{\partial v'}{\partial t}$, (b) sum of $-\beta y u'$ and $-\frac{\partial \phi'}{\partial y}$, and (c) sum of $-\overline{v}\frac{\partial v'}{\partial y}$, $-v'\frac{\partial \overline{v}}{\partial y}$, $-\omega'\frac{\partial \overline{v}}{\partial p}$, and $-\overline{\omega}\frac{\partial v'}{\partial p}$ at 10S, 700hPa.

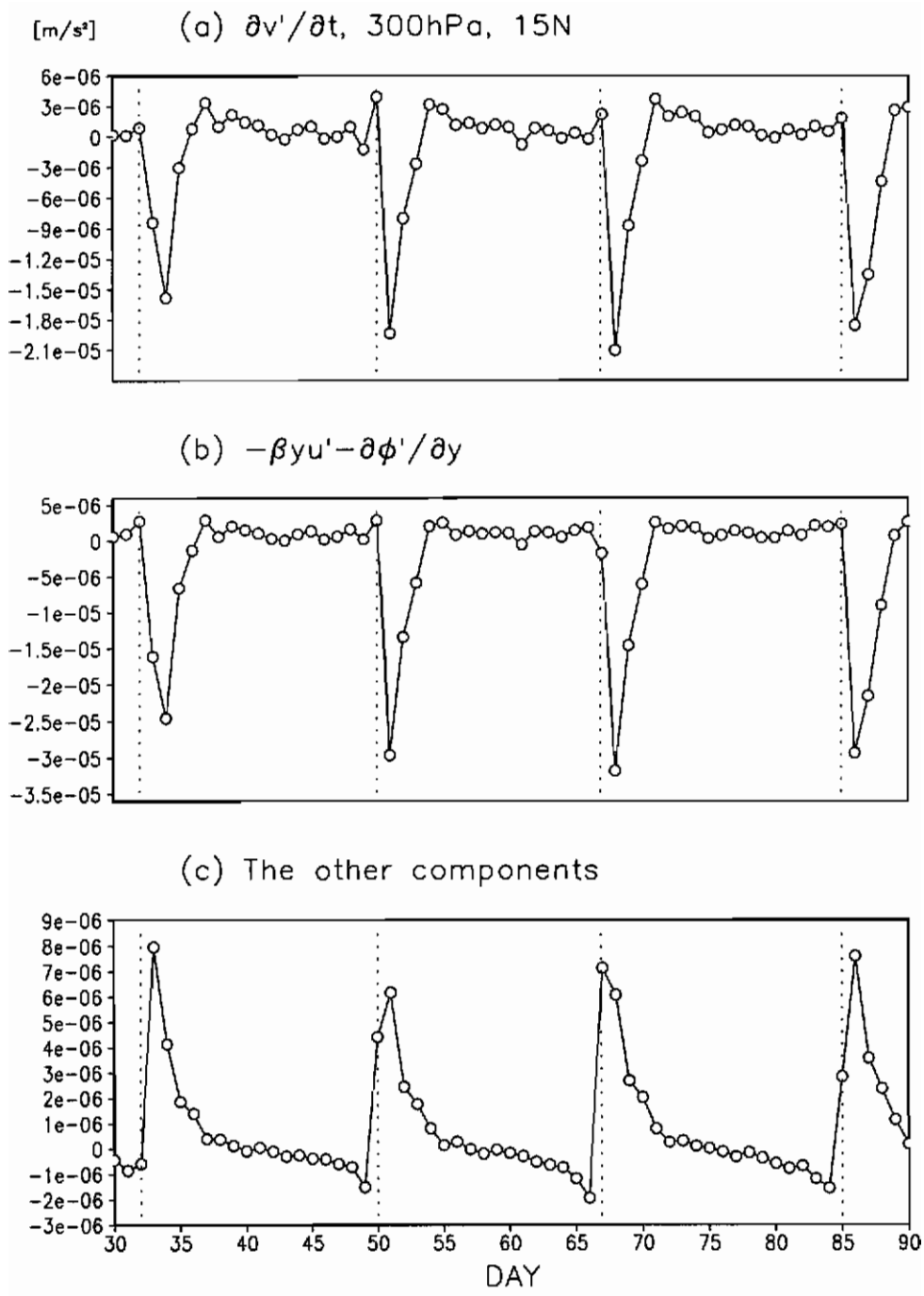

Figure 3.7: Time series (Day) of (a) $\frac{\partial v'}{\partial t}$, (b) sum of $-\beta y u'$ and $-\frac{\partial \phi'}{\partial y}$, and (c) sum of $-\overline{v}\frac{\partial v'}{\partial y}$, $-v'\frac{\partial \overline{v}}{\partial y}$, $-\omega'\frac{\partial \overline{v}}{\partial p}$, and $-\overline{\omega}\frac{\partial v'}{\partial p}$ at 15N, 300hPa.

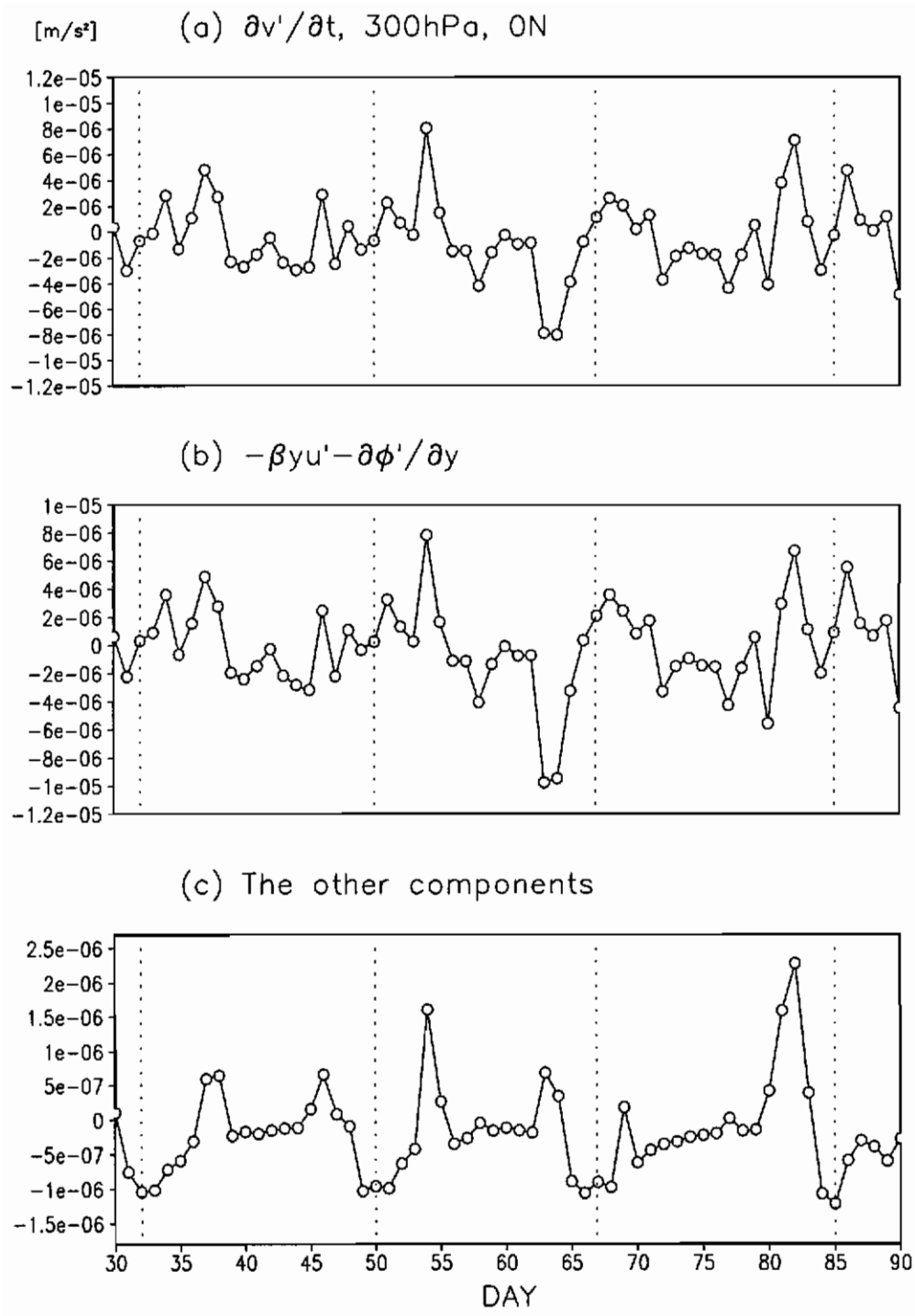

Figure 3.8: Time series (Day) of (a) $\frac{\partial v'}{\partial t}$, (b) sum of $-\beta y u'$ and $-\frac{\partial \phi'}{\partial y}$, and (c) sum of $-\overline{v}\frac{\partial v'}{\partial y}$, $-v'\frac{\partial \overline{v}}{\partial y}$, $-\omega'\frac{\partial \overline{v}}{\partial p}$, and $-\overline{\omega}\frac{\partial v'}{\partial p}$ at 0N, 300hPa.

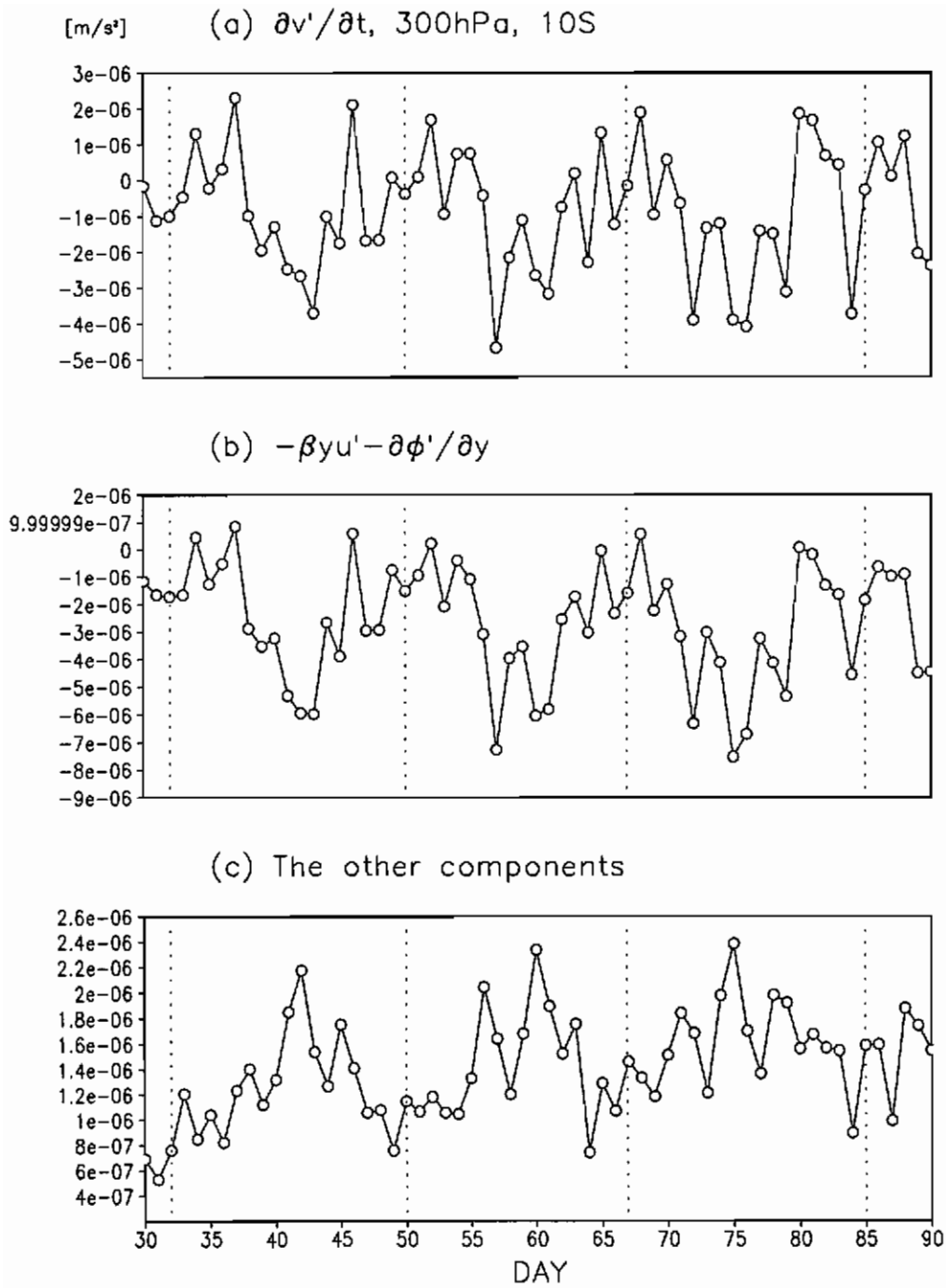

Figure 3.9: Time series (Day) of (a) $\frac{\partial v'}{\partial t}$, (b) sum of $-\beta y u'$ and $-\frac{\partial \phi'}{\partial y}$, and (c) sum of $-\overline{v}\frac{\partial v'}{\partial y}$, $-v'\frac{\partial \overline{v}}{\partial y}$, $-\omega'\frac{\partial \overline{v}}{\partial p}$, and $-\overline{\omega}\frac{\partial v'}{\partial p}$ at 10S, 300hPa.

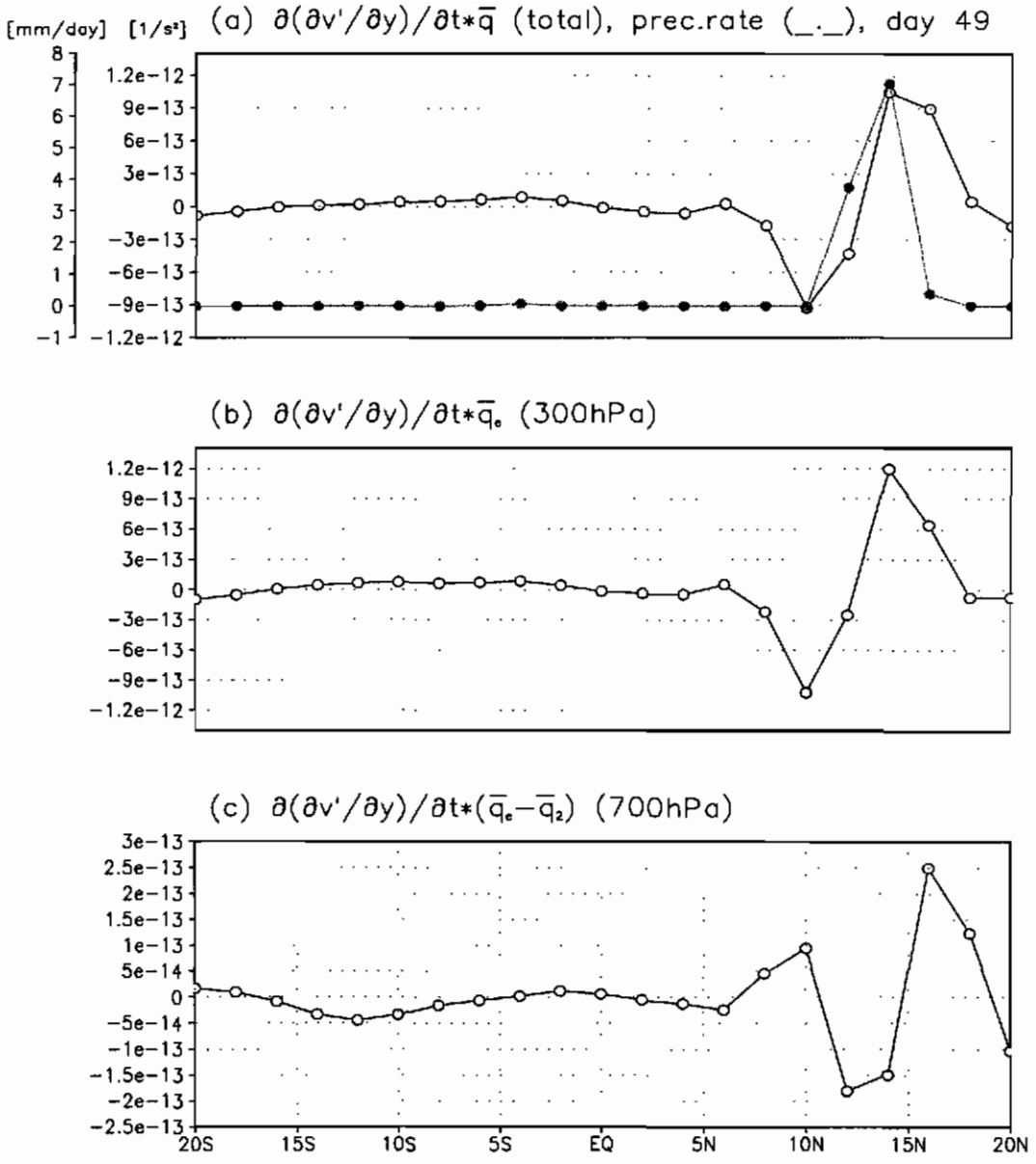

Figure 3.10: (a) Latitudinal variation of precipitation rate (-•-), and sum of $\frac{\partial}{\partial t}\frac{\partial v_1'}{\partial y}\overline{q}_e$ and $\frac{\partial}{\partial t}\frac{\partial v_2'}{\partial y}(\overline{q}_e - \overline{q}_2)$ (-o-), (b) $\frac{\partial}{\partial t}\frac{\partial v_1'}{\partial y}\overline{q}_e$ (-o-), and (c) $\frac{\partial}{\partial t}\frac{\partial v_2'}{\partial y}(\overline{q}_e - \overline{q}_2)$ (-o-) on day 49.

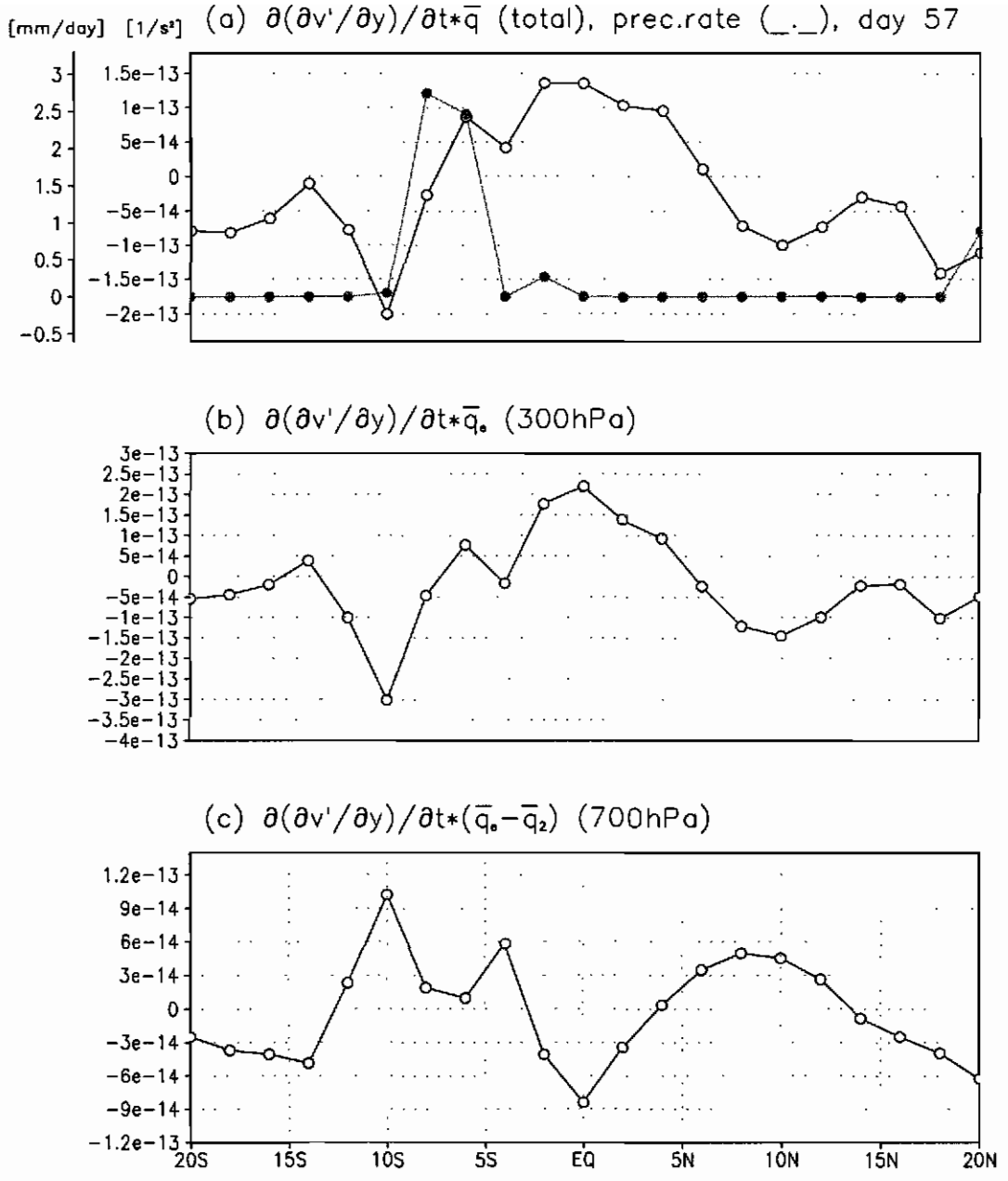

Figure 3.11: (a) Latitudinal variation of precipitation rate (-•-), and sum of $\frac{\partial}{\partial t}\frac{\partial v_1'}{\partial y}\overline{q}_e$ and $\frac{\partial}{\partial t}\frac{\partial v_2'}{\partial y}(\overline{q}_e - \overline{q}_2)$ (-∘-), (b) $\frac{\partial}{\partial t}\frac{\partial v_1'}{\partial y}\overline{q}_e$ (-∘-), and (c) $\frac{\partial}{\partial t}\frac{\partial v_2'}{\partial y}(\overline{q}_e - \overline{q}_2)$ (-∘-) on day 57.

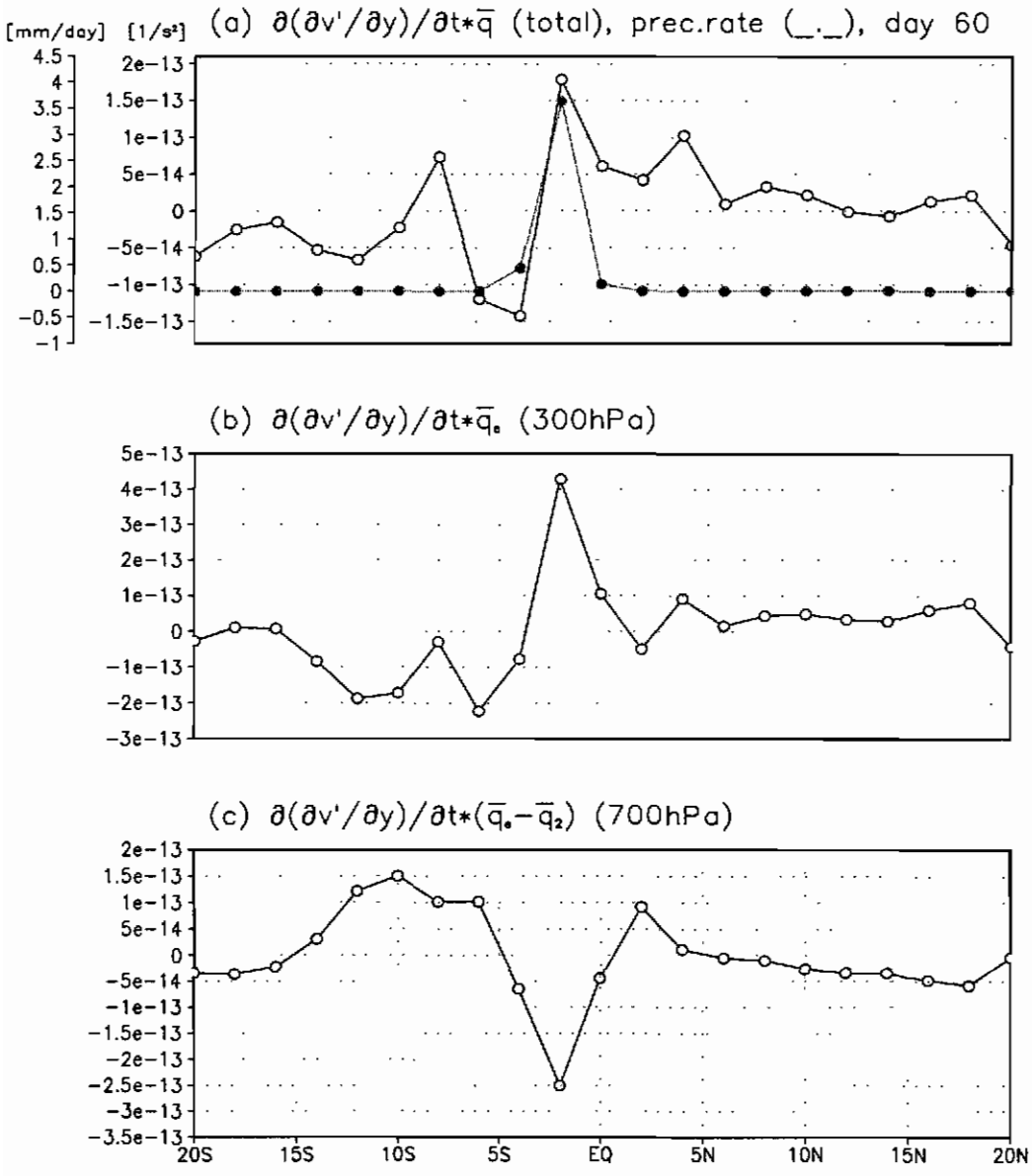

Figure 3.12: (a) Latitudinal variation of precipitation rate (-•-), and sum of $\frac{\partial}{\partial t}\frac{\partial v_1'}{\partial y}\overline{q}_e$ and $\frac{\partial}{\partial t}\frac{\partial v_2'}{\partial y}(\overline{q}_e - \overline{q}_2)$ (-∘-), (b) $\frac{\partial}{\partial t}\frac{\partial v_1'}{\partial y}\overline{q}_e$ (-∘-), and (c) $\frac{\partial}{\partial t}\frac{\partial v_2'}{\partial y}(\overline{q}_e - \overline{q}_2)$ (-∘-) on day 60.

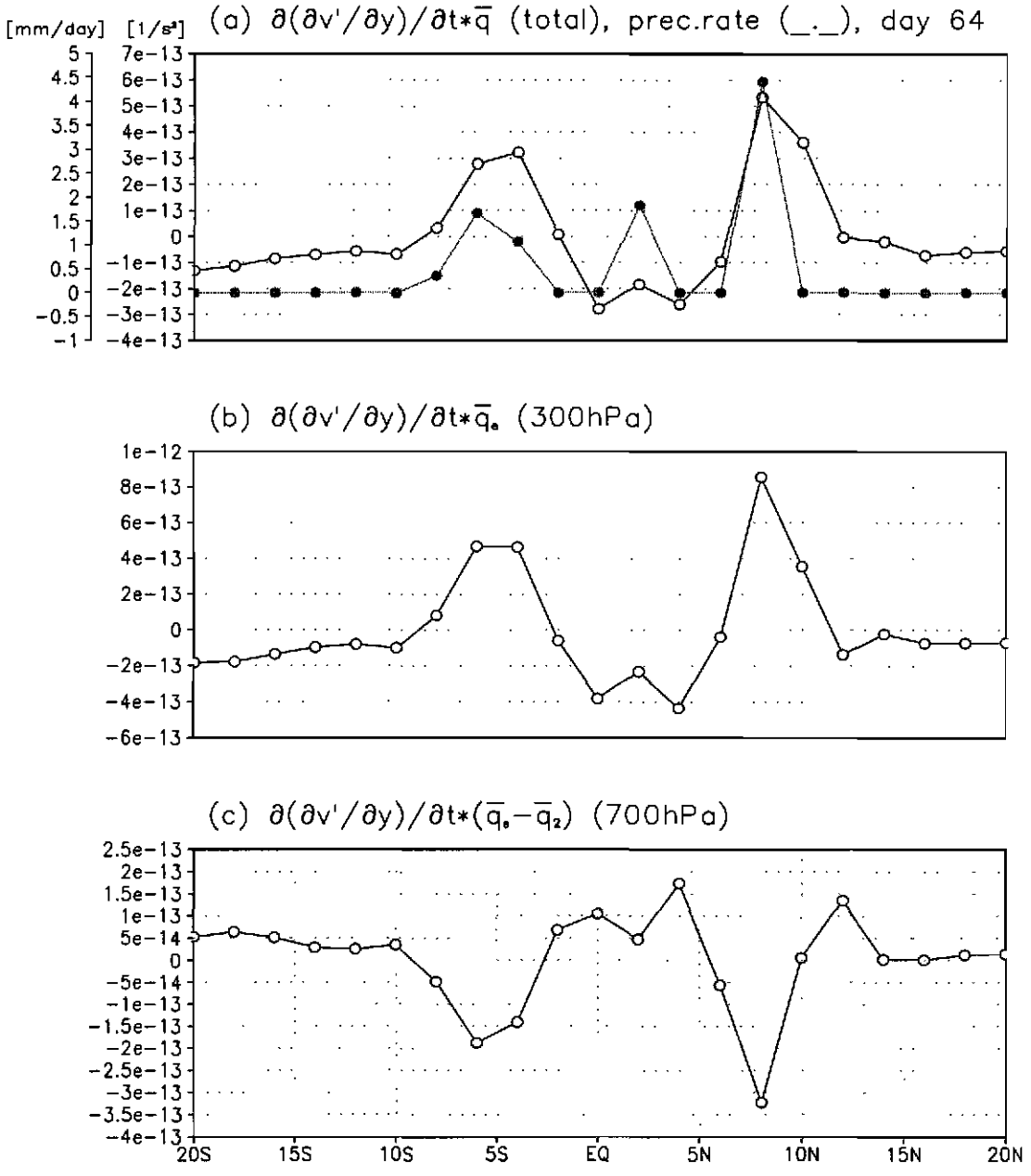

Figure 3.13: (a) Latitudinal variation of precipitation rate (-•-), and sum of $\frac{\partial}{\partial t}\frac{\partial v_1'}{\partial y}\overline{q}_e$ and $\frac{\partial}{\partial t}\frac{\partial v_2'}{\partial y}(\overline{q}_e - \overline{q}_2)$ (-o-), (b) $\frac{\partial}{\partial t}\frac{\partial v_1'}{\partial y}\overline{q}_e$ (-o-), and (c) $\frac{\partial}{\partial t}\frac{\partial v_2'}{\partial y}(\overline{q}_e - \overline{q}_2)$ (-o-) on day 64.

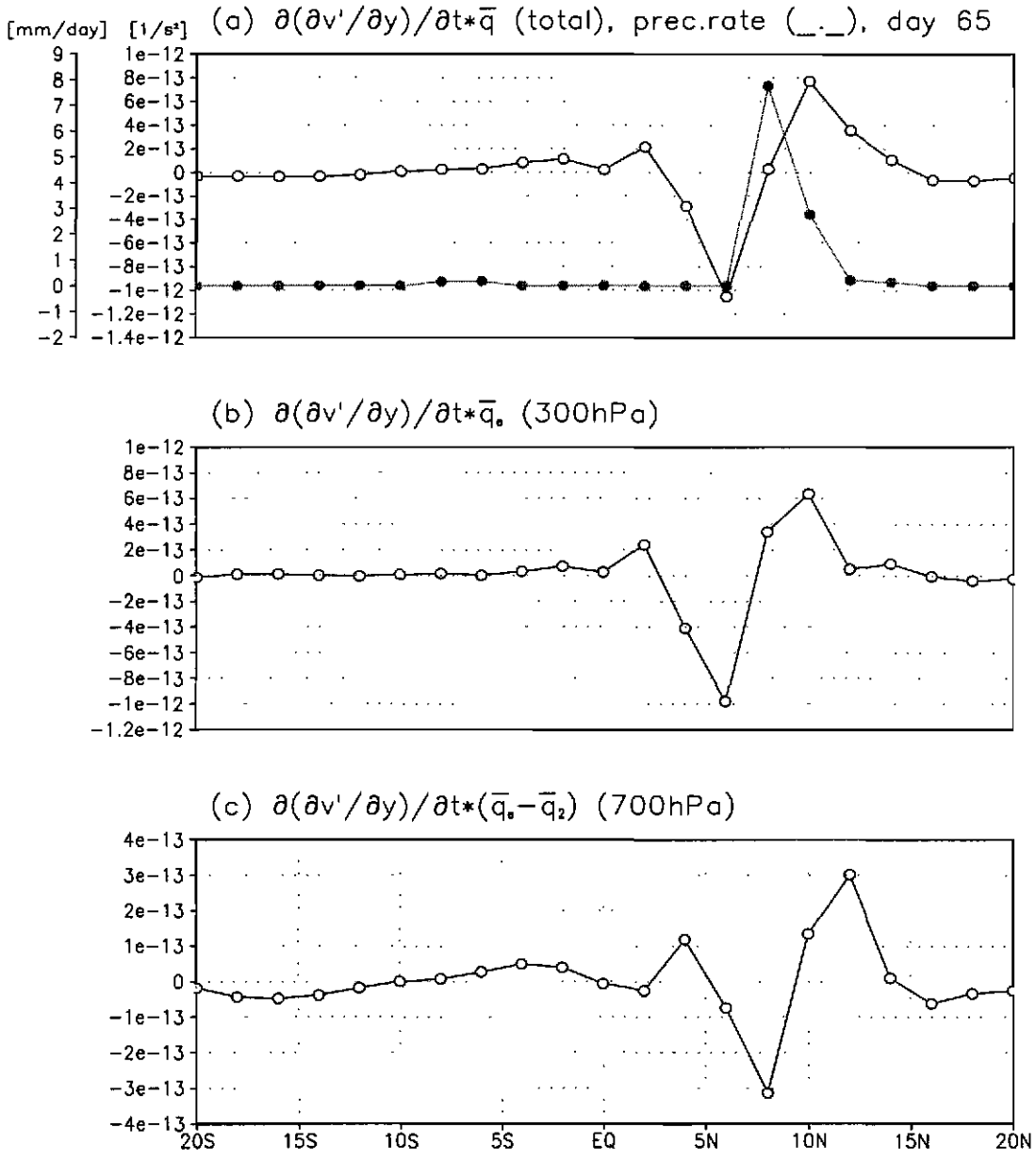

Figure 3.14: (a) Latitudinal variation of precipitation rate (-•-), and sum of $\frac{\partial}{\partial t}\frac{\partial v_1'}{\partial y}\overline{q}_e$ and $\frac{\partial}{\partial t}\frac{\partial v_2'}{\partial y}(\overline{q}_e - \overline{q}_2)$ (-∘-), (b) $\frac{\partial}{\partial t}\frac{\partial v_1'}{\partial y}\overline{q}_e$ (-∘-), and (c) $\frac{\partial}{\partial t}\frac{\partial v_2'}{\partial y}(\overline{q}_e - \overline{q}_2)$ (-∘-) on day 65.

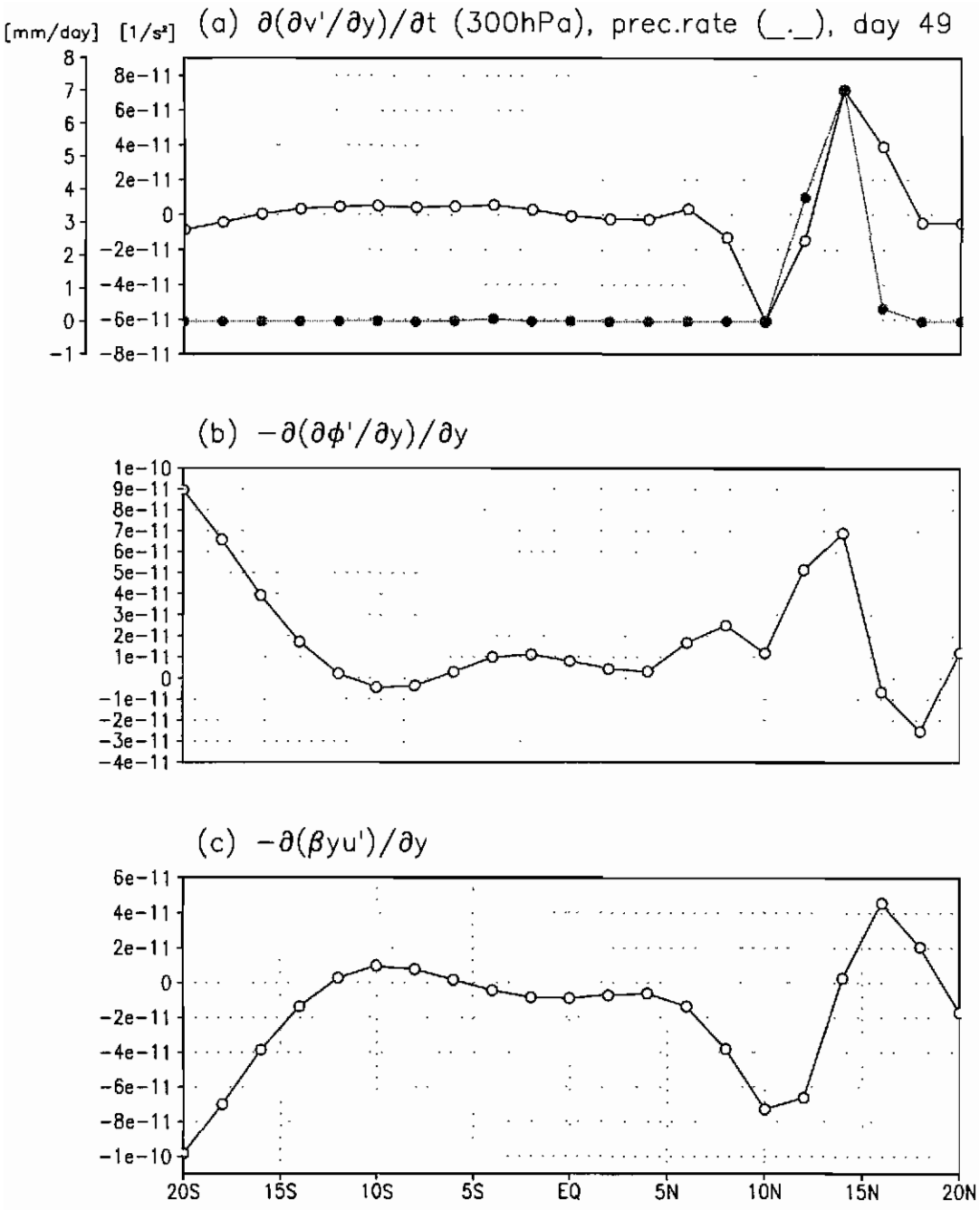

Figure 3.15: (a) Latitudinal variation of precipitation rate(-•-) and $\frac{\partial}{\partial t}\frac{\partial v'}{\partial y}$ (-∘-), (b) $-\frac{\partial}{\partial y}\frac{\partial \phi'}{\partial y}$ (-∘-), and (c) $-\frac{\partial}{\partial y}\beta y u'$ (-∘-) at 300hPa on day 49.

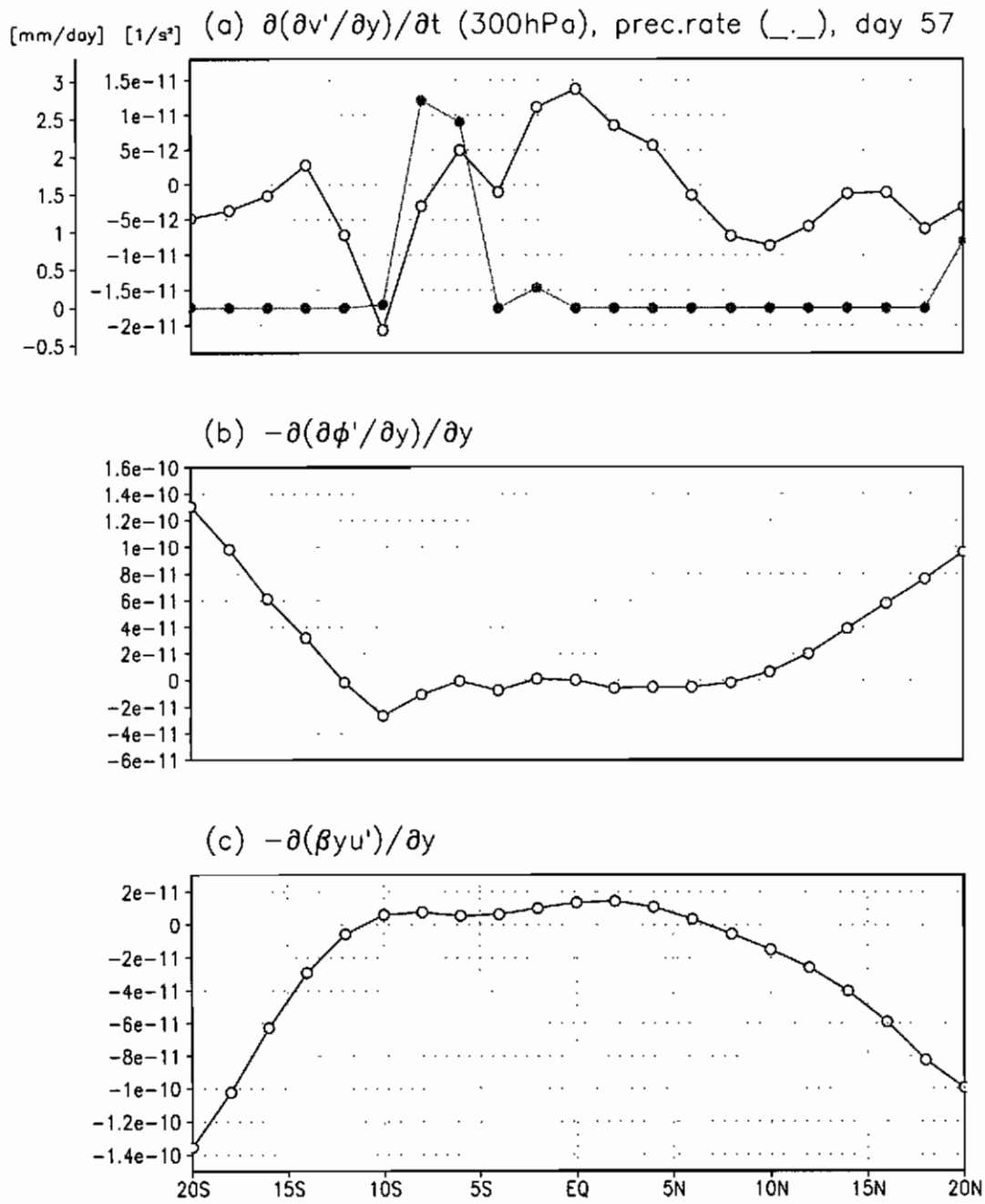

Figure 3.16: (a) Latitudinal variation of precipitation rate(-•-) and $\frac{\partial}{\partial t}\frac{\partial v'}{\partial y}$ (-∘-), (b) $-\frac{\partial}{\partial y}\frac{\partial \phi'}{\partial y}$ (-∘-), and (c) $-\frac{\partial}{\partial y}\beta y u'$ (-∘-) at 300hPa on day 57.

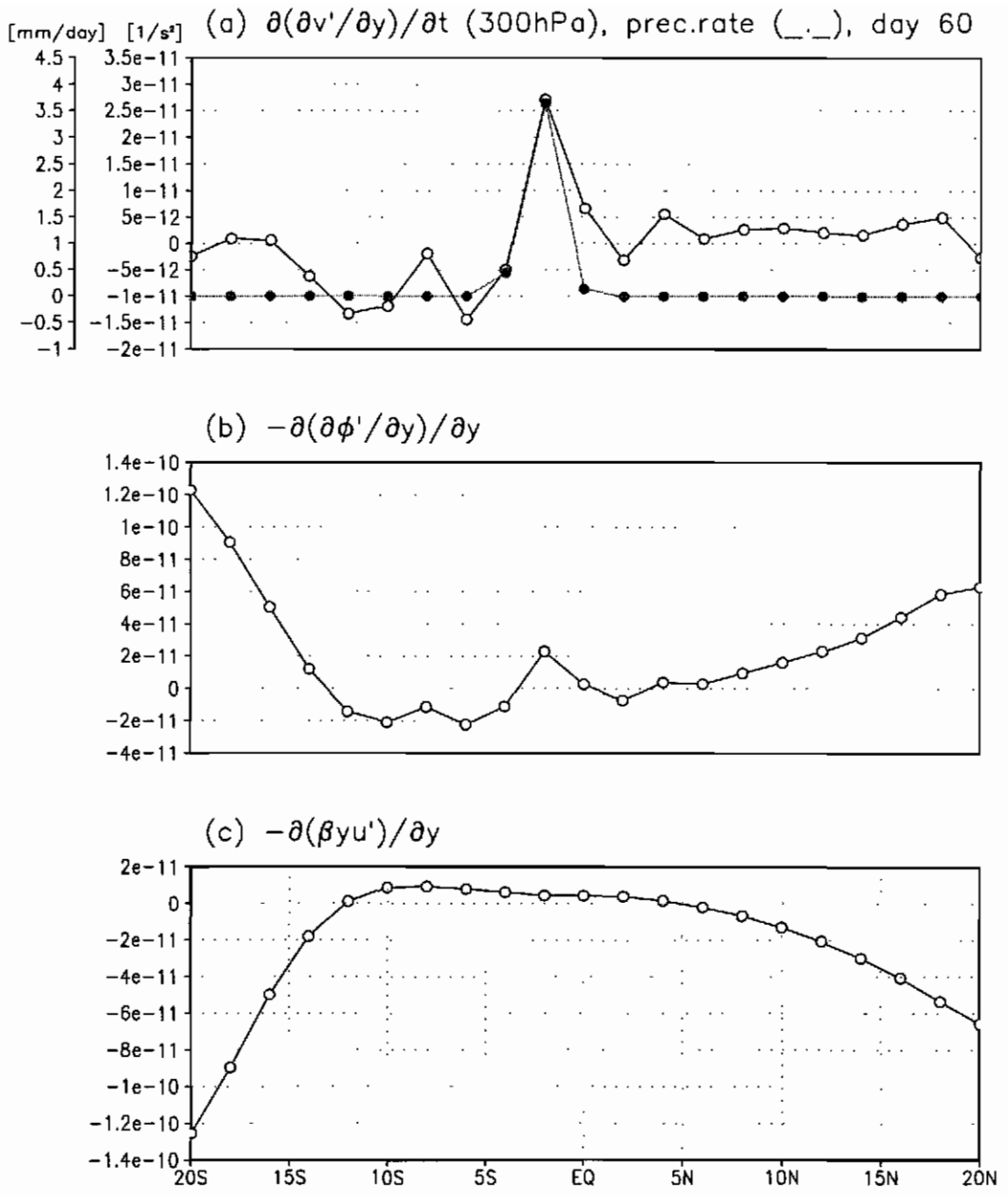

Figure 3.17: (a) Latitudinal variation of precipitation rate(-•-) and $\frac{\partial}{\partial t}\frac{\partial v'}{\partial y}$ (-∘-), (b) $-\frac{\partial}{\partial y}\frac{\partial \phi'}{\partial y}$ (-∘-), and (c) $-\frac{\partial}{\partial y}\beta y u'$ (-∘-) at 300hPa on day 60.

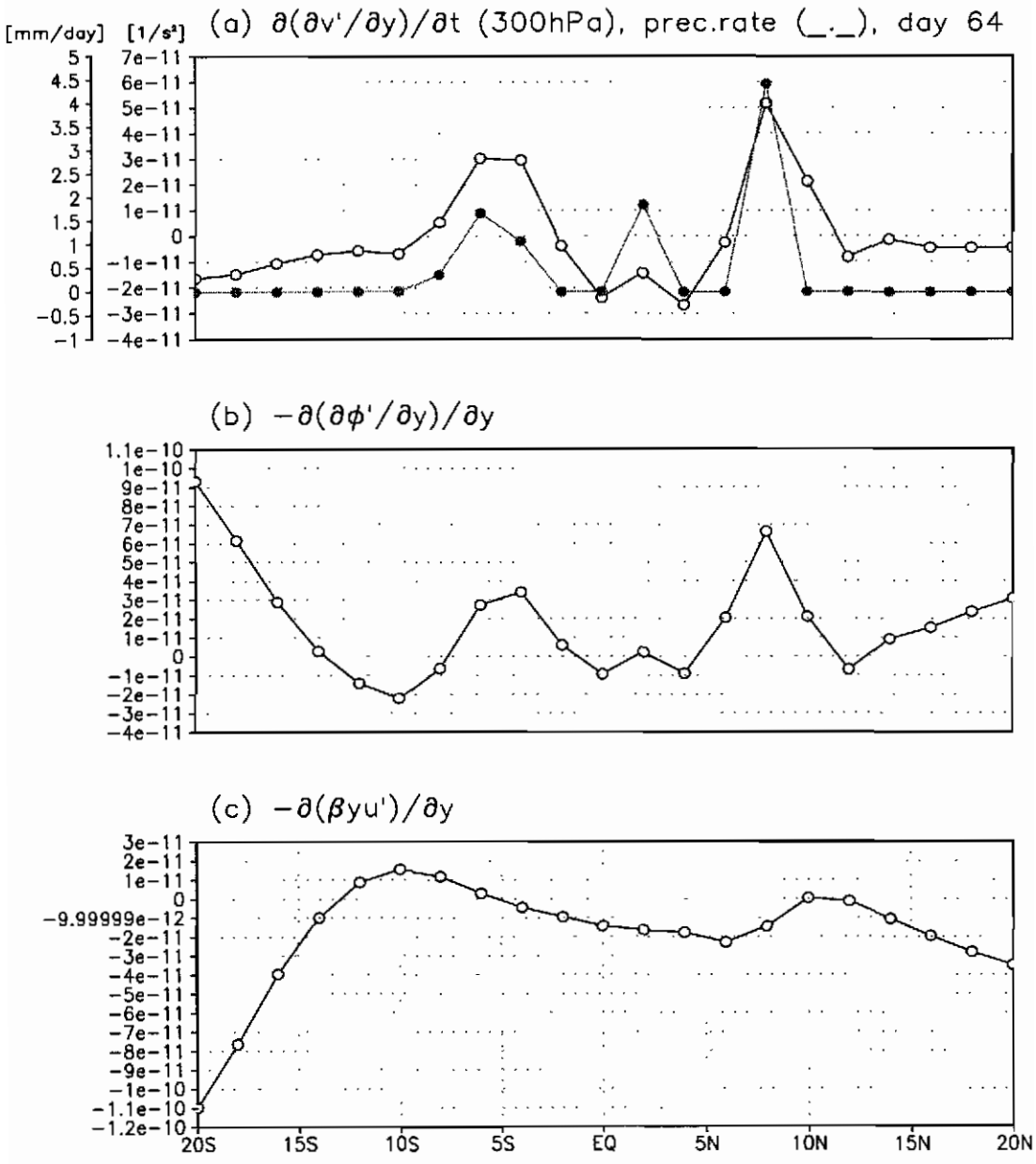

Figure 3.18: (a) Latitudinal variation of precipitation rate(-•-) and $\frac{\partial}{\partial t}\frac{\partial v'}{\partial y}$ (-∘-), (b) $-\frac{\partial}{\partial y}\frac{\partial \phi'}{\partial y}$ (-∘-), and (c) $-\frac{\partial}{\partial y}\beta y u'$ (-∘-) at 300hPa on day 64.

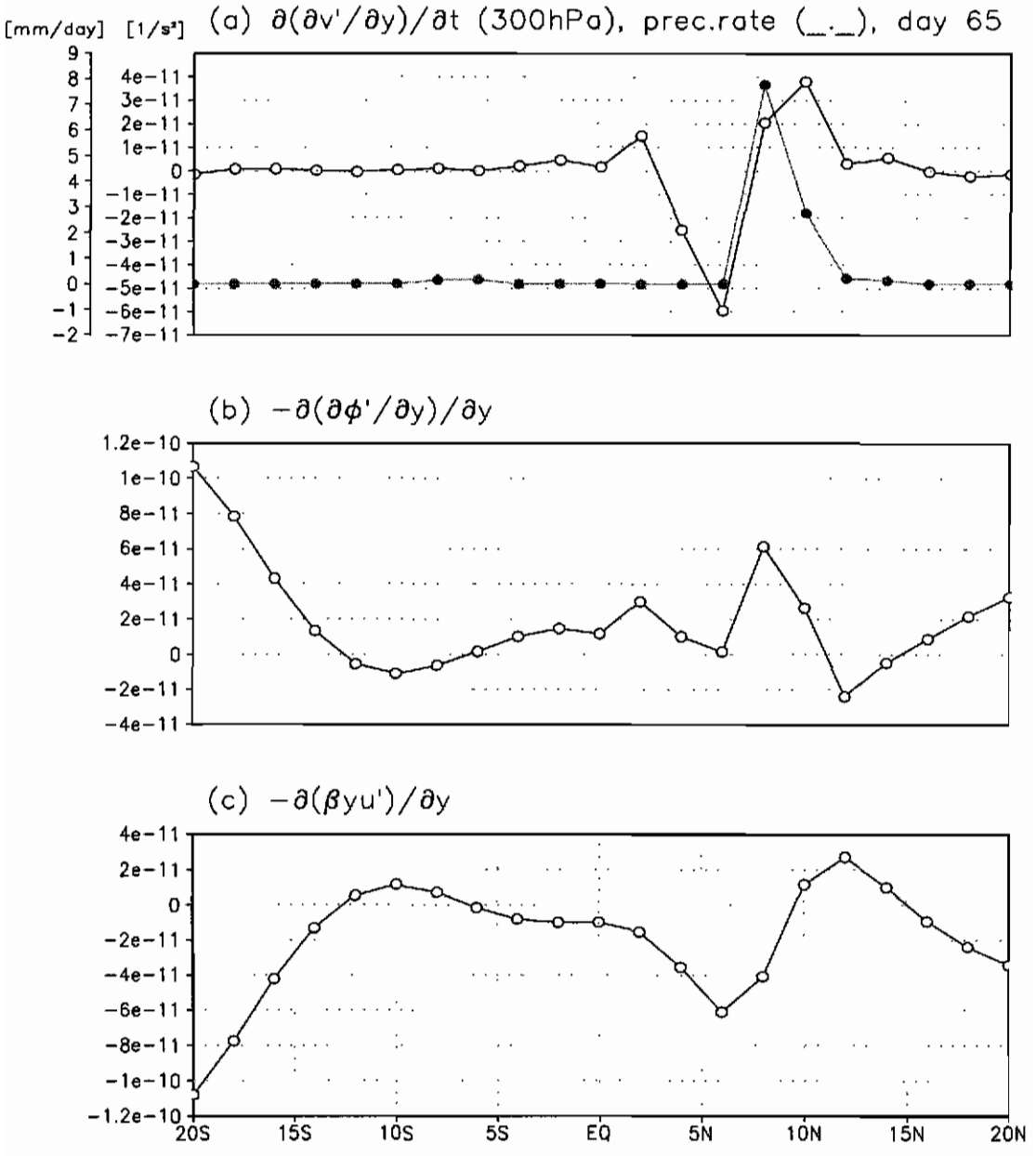

Figure 3.19: (a) Latitudinal variation of precipitation rate(-•-) and $\frac{\partial}{\partial t}\frac{\partial v'}{\partial y}$ (-∘-), (b) $-\frac{\partial}{\partial y}\frac{\partial \phi'}{\partial y}$ (-∘-), and (c) $-\frac{\partial}{\partial y}\beta y u'$ (-∘-) at 300hPa on day 65.

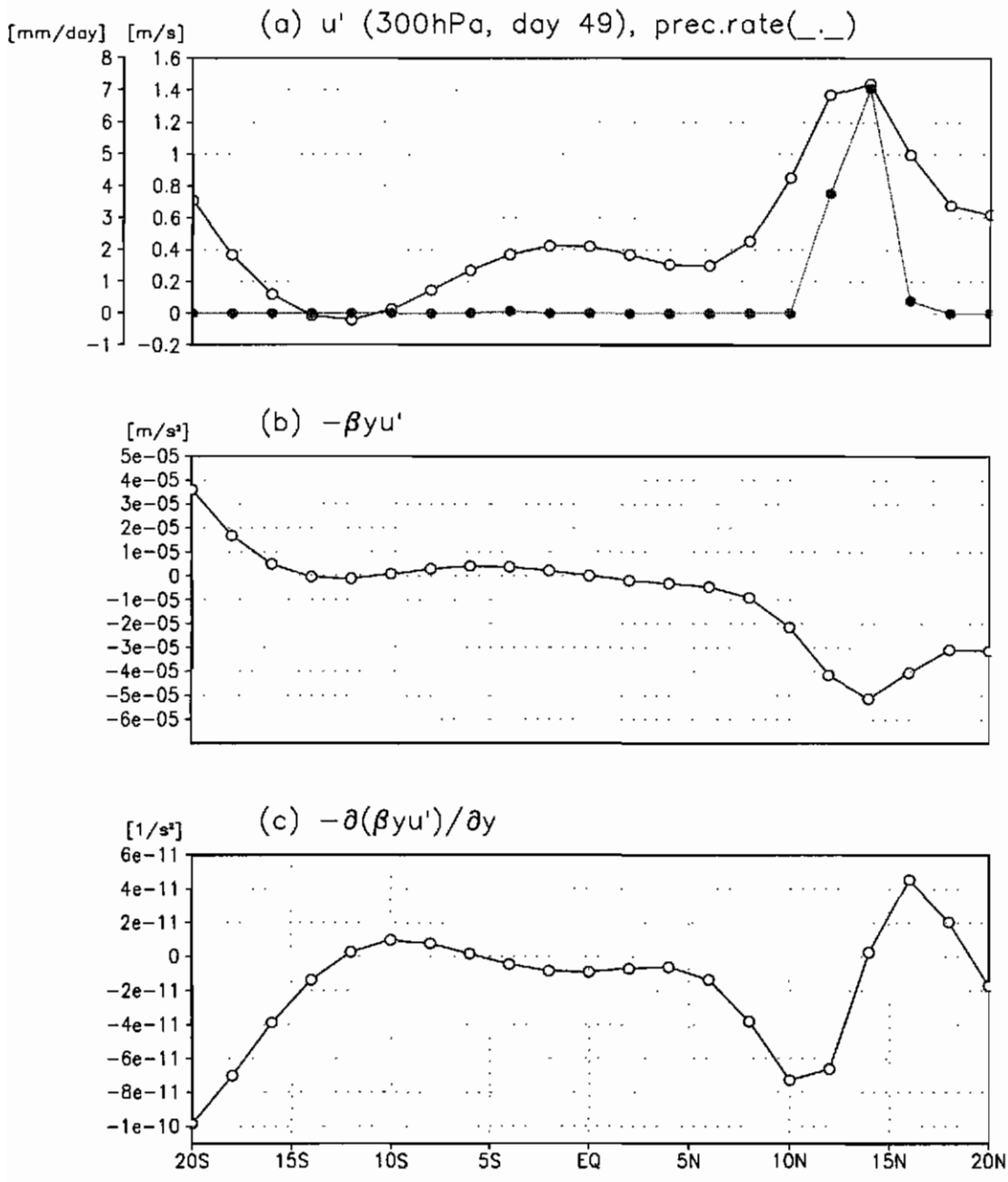

Figure 3.20: (a) Latitudinal variation of precipitation rate(-•-) and u′(-∘-), (b) $-\beta yu'$ (-∘-), and (c) $-\frac{\partial}{\partial y}\beta yu'$ (-∘-) at 300hPa on day 49.

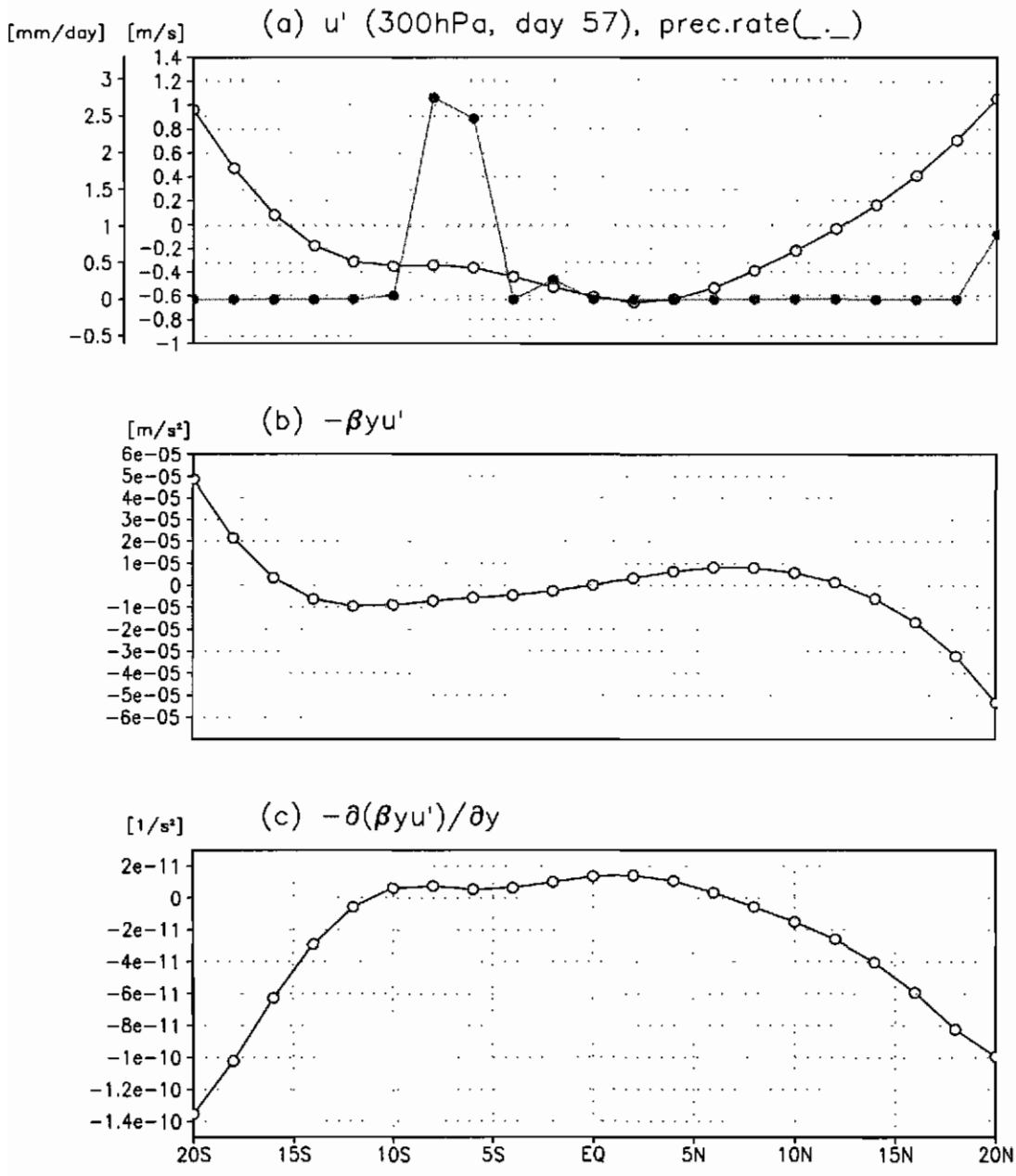

Figure 3.21: (a) Latitudinal variation of precipitation rate(-•-) and u′(-∘-), (b) $-\beta yu'$ (-∘-), and (c) $-\frac{\partial}{\partial y}\beta yu'$ (-∘-) at 300hPa on day 57.

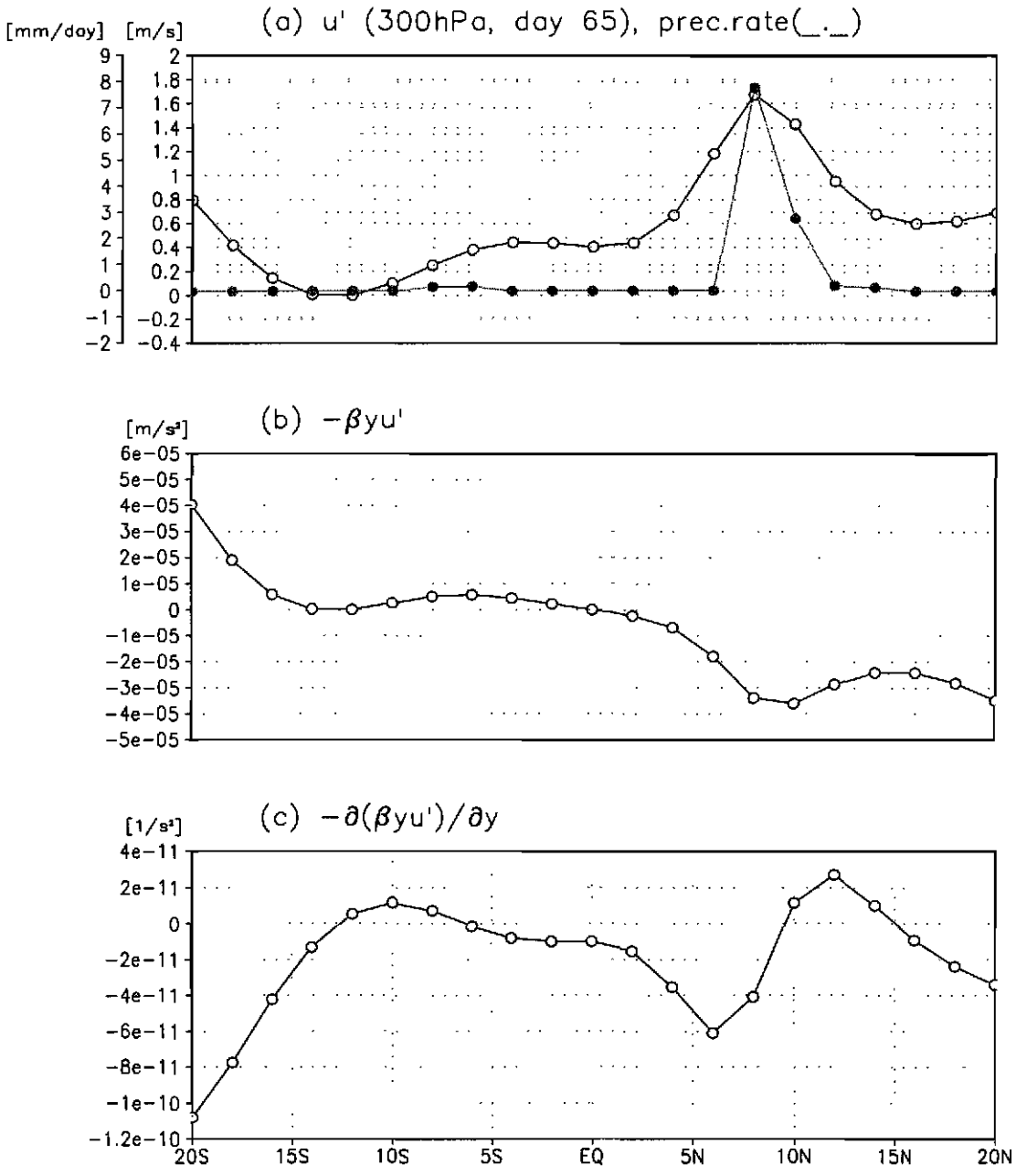

Figure 3.22: (a) Latitudinal variation of precipitation rate(-•-) and u′(-∘-), (b) $-\beta y u'$ (-∘-), and (c) $-\frac{\partial}{\partial y}\beta y u'$ (-∘-) at 300hPa on day 65.

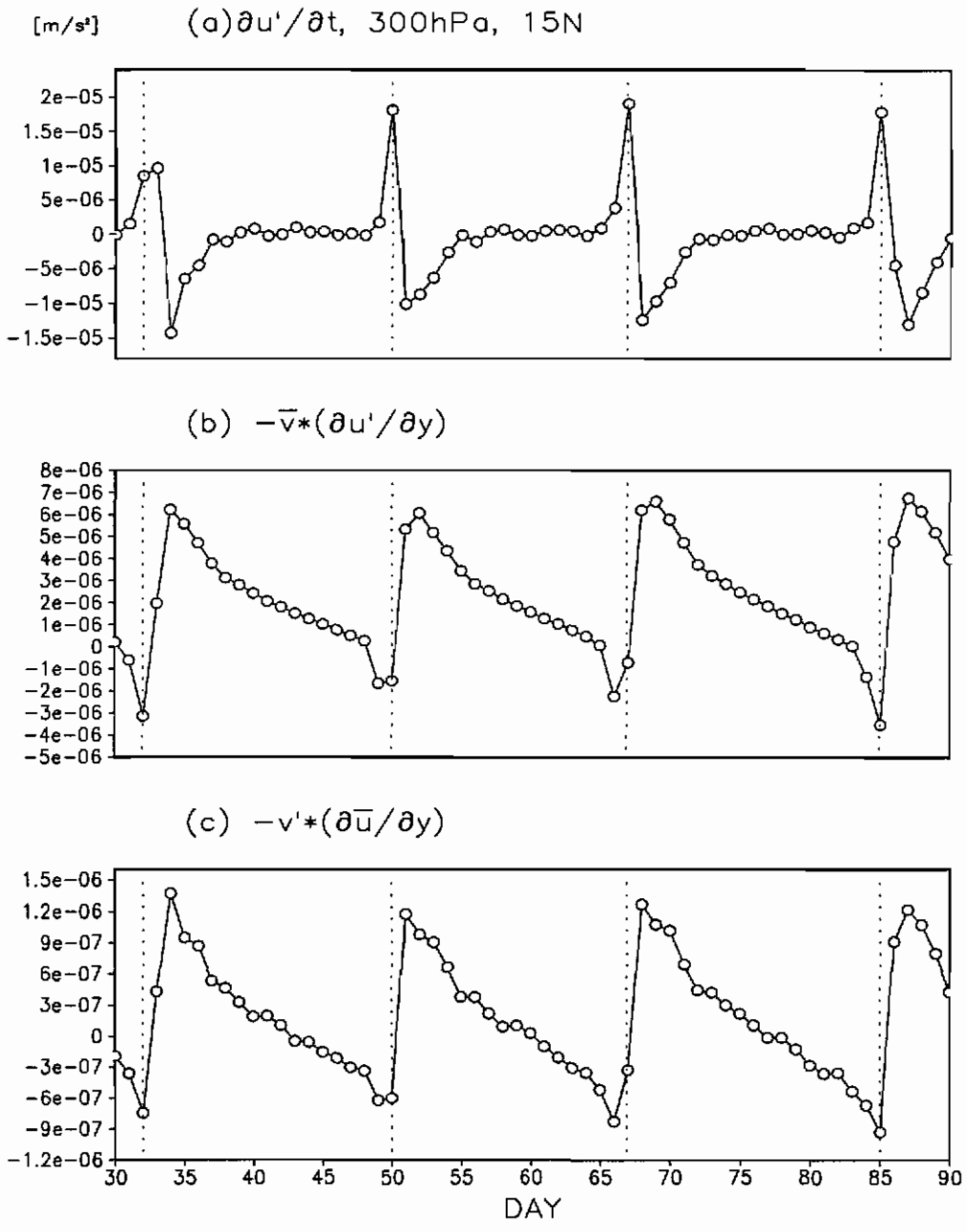

Figure 3.23: Components of momentum equation for 300hPa zonal wind anomaly ($\frac{\partial u'}{\partial t}$) at 15N. (a) $\frac{\partial u'}{\partial t}$, (b) $-\overline{v}\frac{\partial u'}{\partial y}$, (c) $-v'\frac{\partial \overline{u}}{\partial y}$, (d) $-\omega'\frac{\partial \overline{u}}{\partial p}$, (e) $-\overline{\omega}\frac{\partial u'}{\partial p}$, and (f) $\beta y v'$.

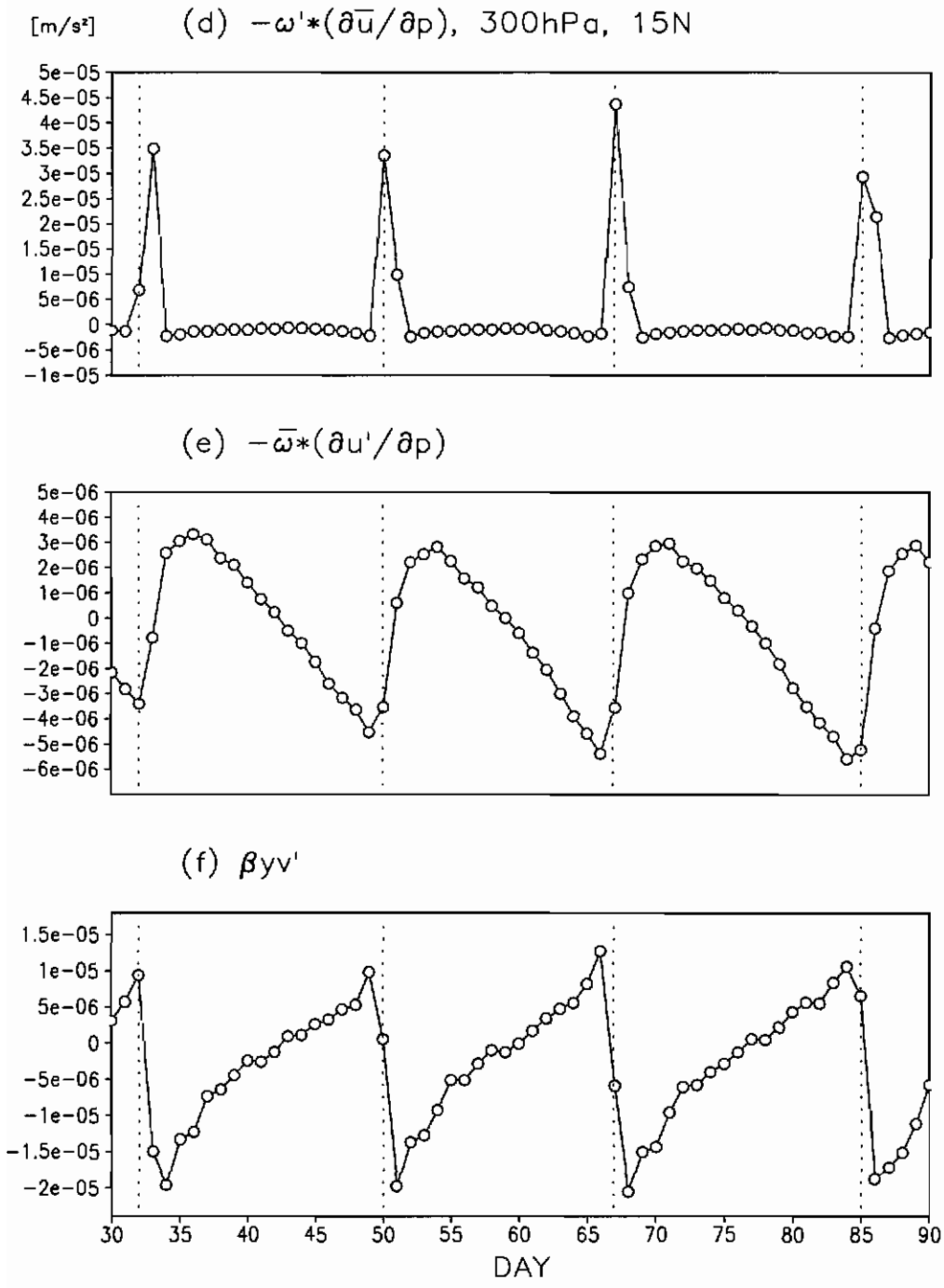

Figure 3.23: (Continued).

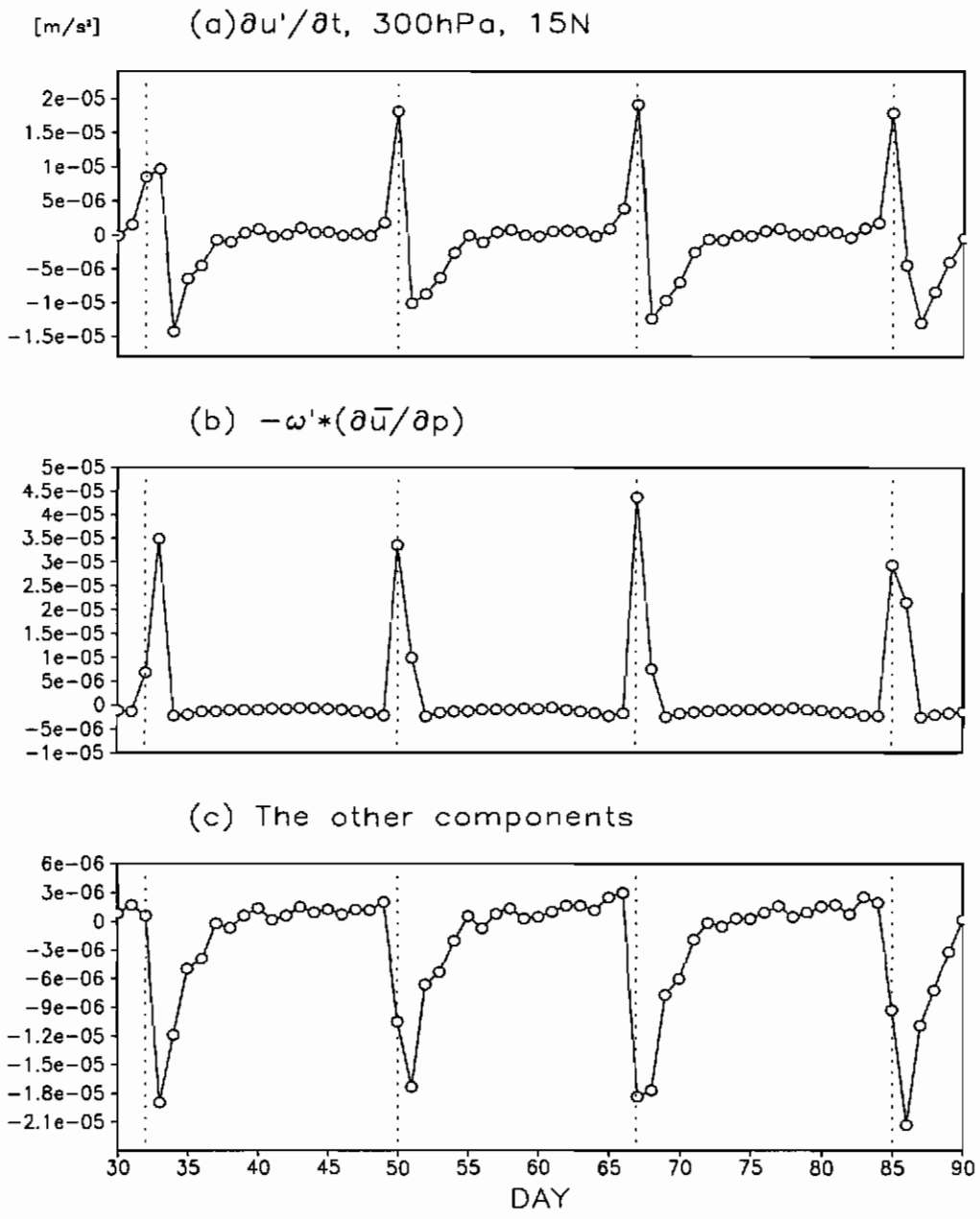

Figure 3.24: Time series (Day) of (a) $\frac{\partial u'}{\partial t}$, (b) $-\omega'\frac{\partial \bar{u}}{\partial p}$, and (c) sum of $-\bar{v}\frac{\partial u'}{\partial y}$, $-v'\frac{\partial \bar{u}}{\partial y}$, $-\bar{\omega}\frac{\partial u'}{\partial p}$, and $\beta y v'$ at 15N, 300hPa.

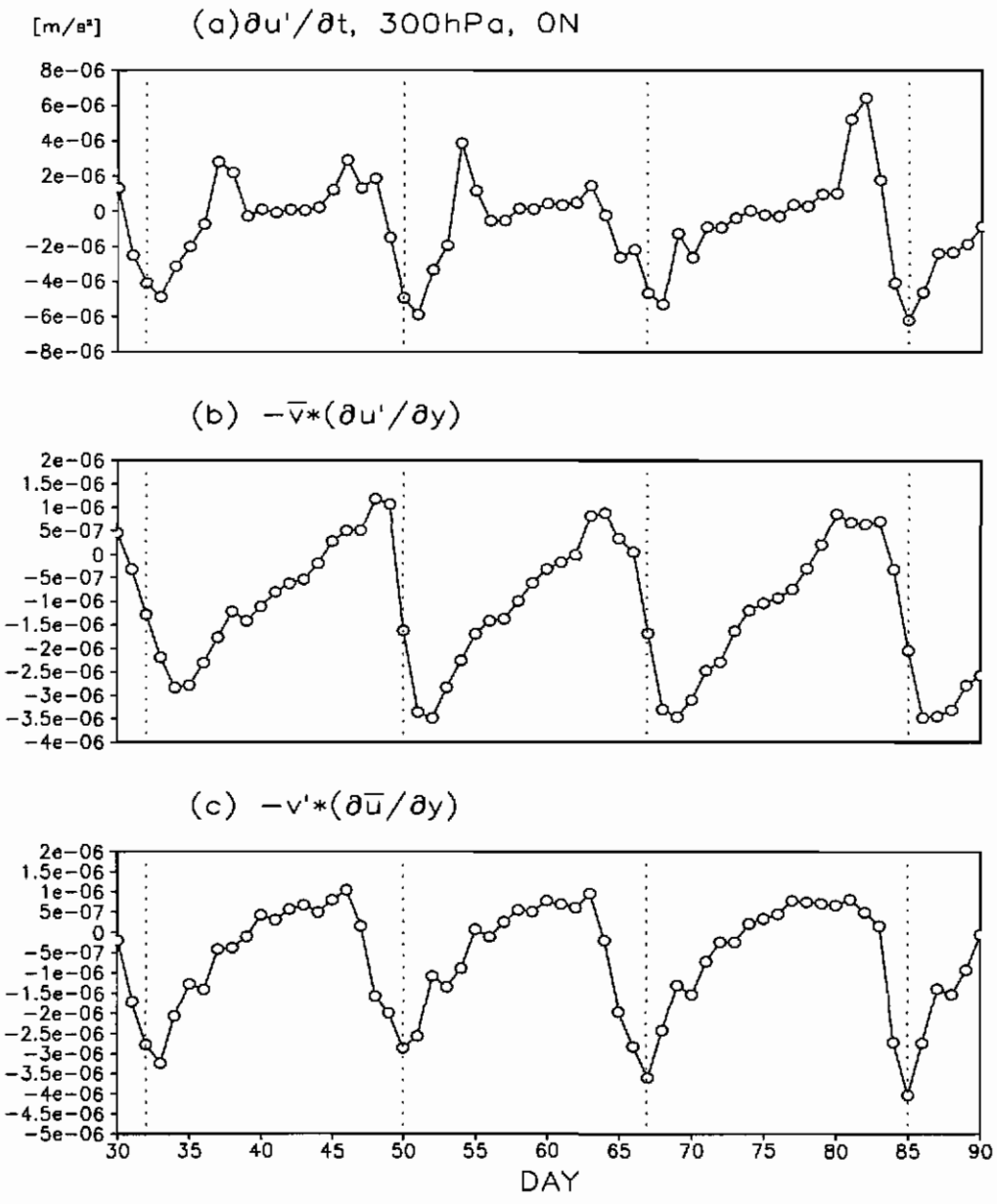

Figure 3.25: Components of momentum equation for 300hPa zonal wind anomaly ($\frac{\partial u'}{\partial t}$) at 0N. (a) $\frac{\partial u'}{\partial t}$, (b) $-\overline{v}\frac{\partial u'}{\partial y}$, (c) $-v'\frac{\partial \overline{u}}{\partial y}$, (d) $-\omega'\frac{\partial \overline{u}}{\partial p}$, (e) $-\overline{\omega}\frac{\partial u'}{\partial p}$, and (f) $\beta y v'$.

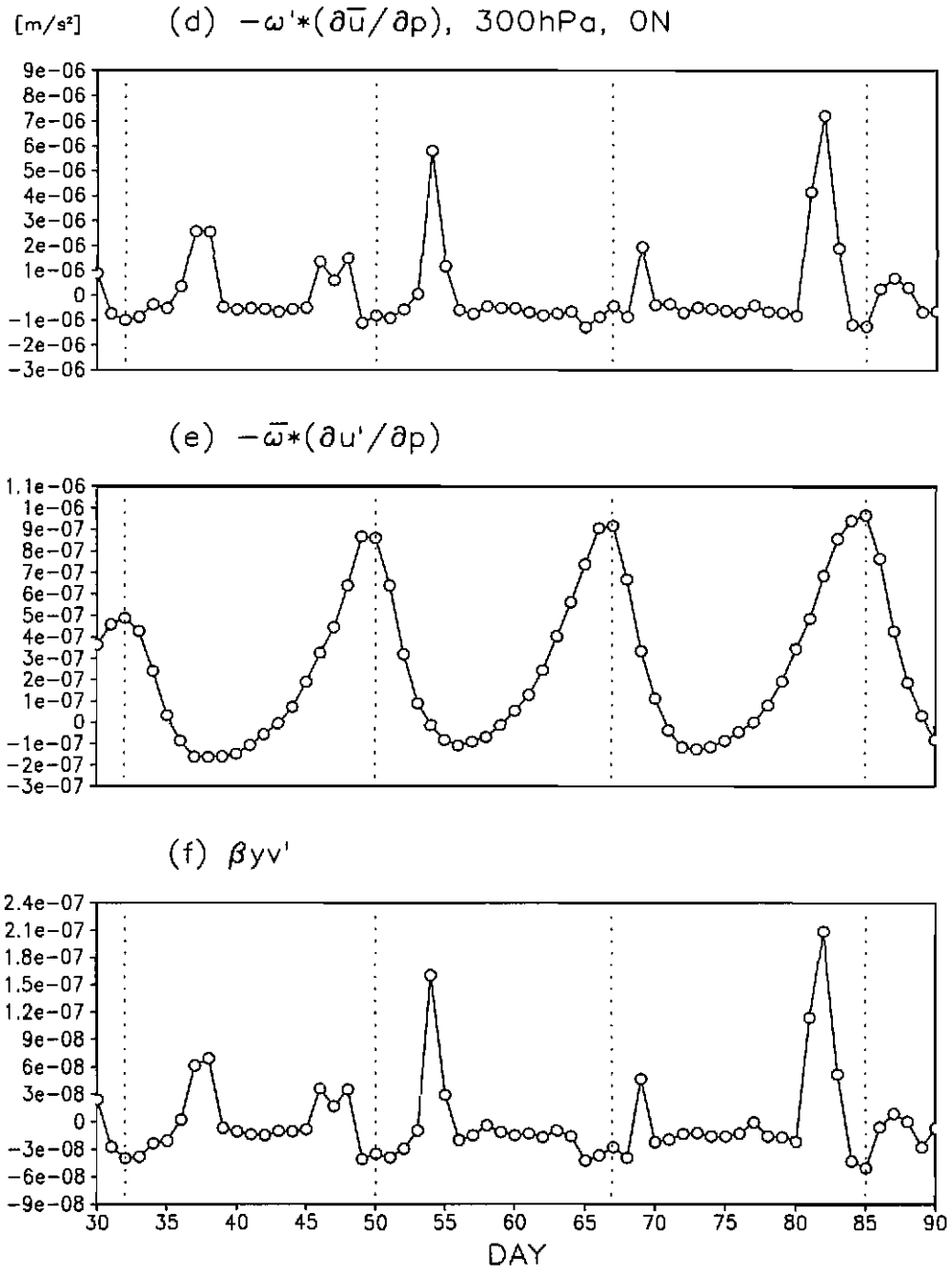

Figure 3.25: (Continued).

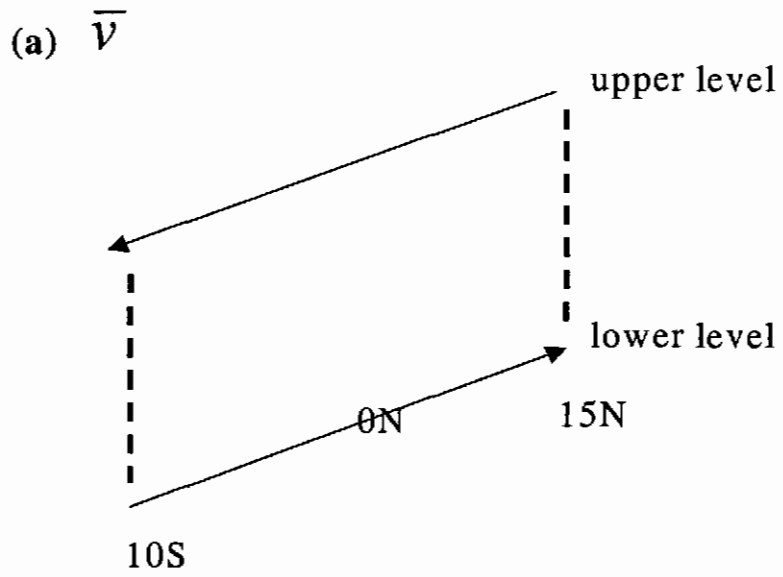

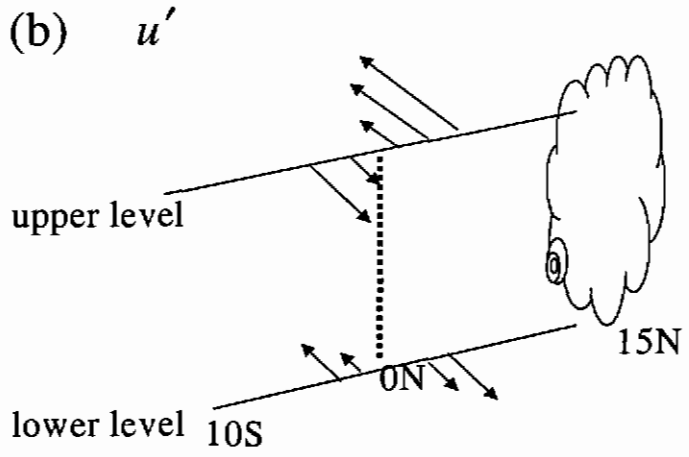

$\therefore$ Upper level., 0N:

$$\overline{v}_{up} < 0,\ \frac{\partial u'_{up}}{\partial y} < 0,\ -\overline{v}_{up}\frac{\partial u'_{up}}{\partial y} < 0$$

Figure 3.26: Schematic diagram of (a) July mean meridional winds ($\overline{v}$) and (b) zonal wind anomalies (u') at upper troposphere and lower troposphere when convection is at 15N.

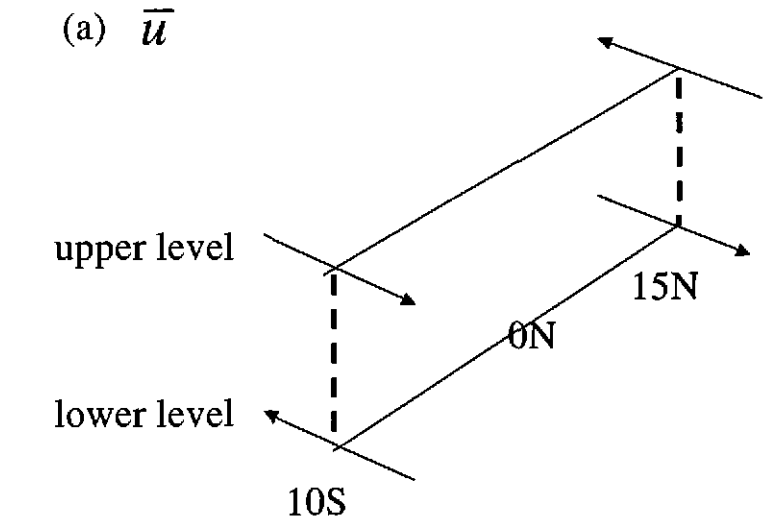

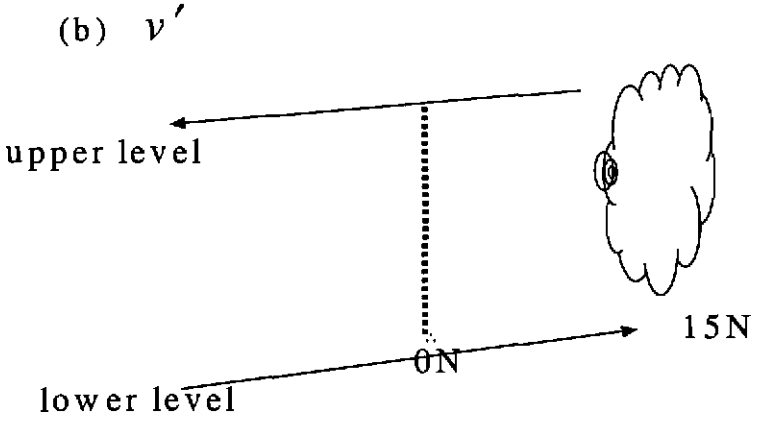

$\therefore$ Upper level, 0N:

$$v'_{up} < 0, \quad \frac{\partial \overline{u}_{up}}{\partial y} < 0, \quad -v'_{up}\frac{\partial \overline{u}_{up}}{\partial y} < 0$$

Figure 3.27: Schematic diagram of (a) July mean zonal winds ($\overline{u}$) and (b) meridional wind anomalies (v') at upper troposphere and lower troposphere when convection is at 15N.

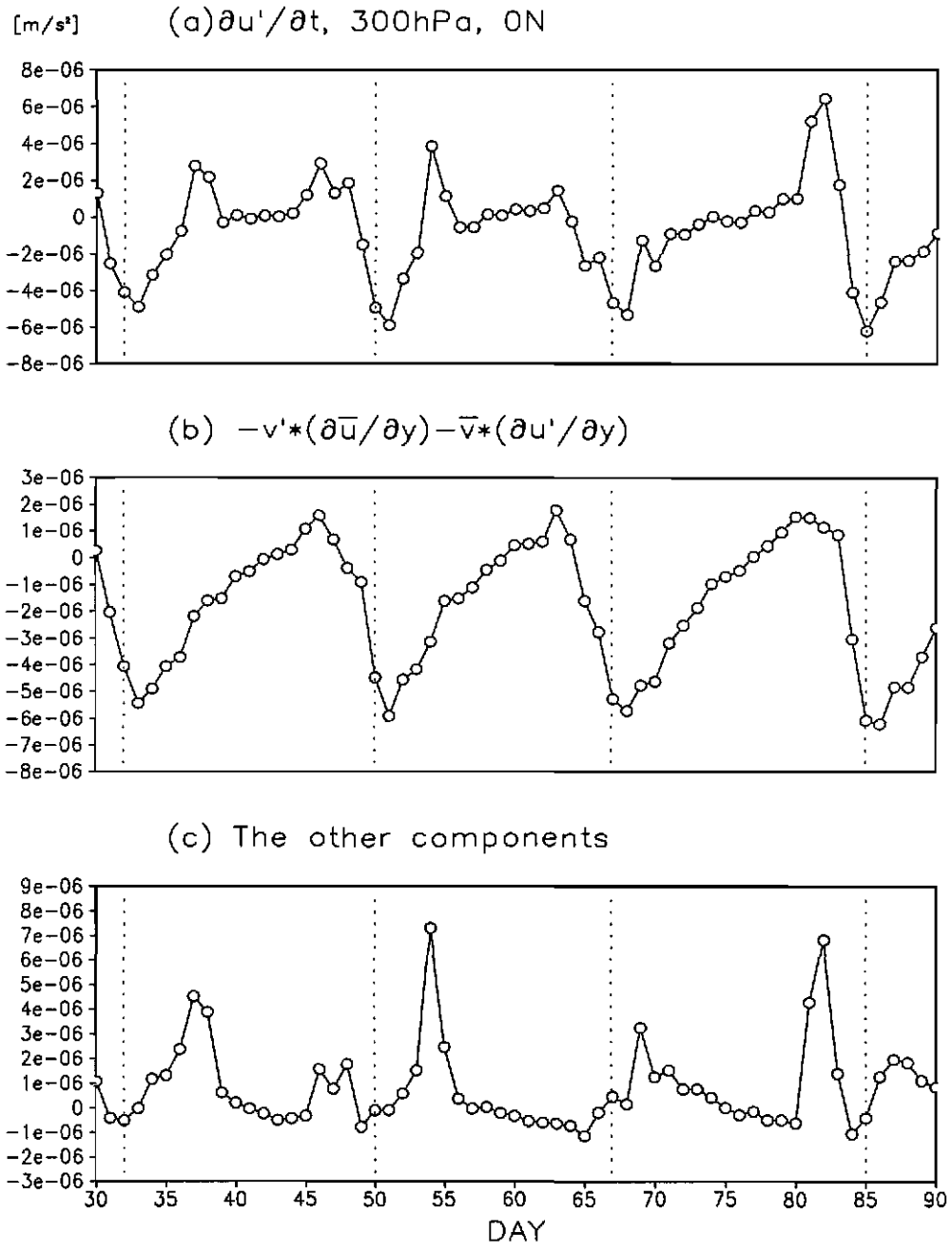

Figure 3.28: Time series (Day) of (a) $\frac{\partial u'}{\partial t}$, (b) sum of $-v'\frac{\partial \bar{u}}{\partial y}$, and $-\bar{v}\frac{\partial u'}{\partial y}$, and (c) sum of $-\omega'\frac{\partial \bar{u}}{\partial p}$, $-\bar{\omega}\frac{\partial u'}{\partial p}$, and $\beta y v'$ at 0N, 300hPa.

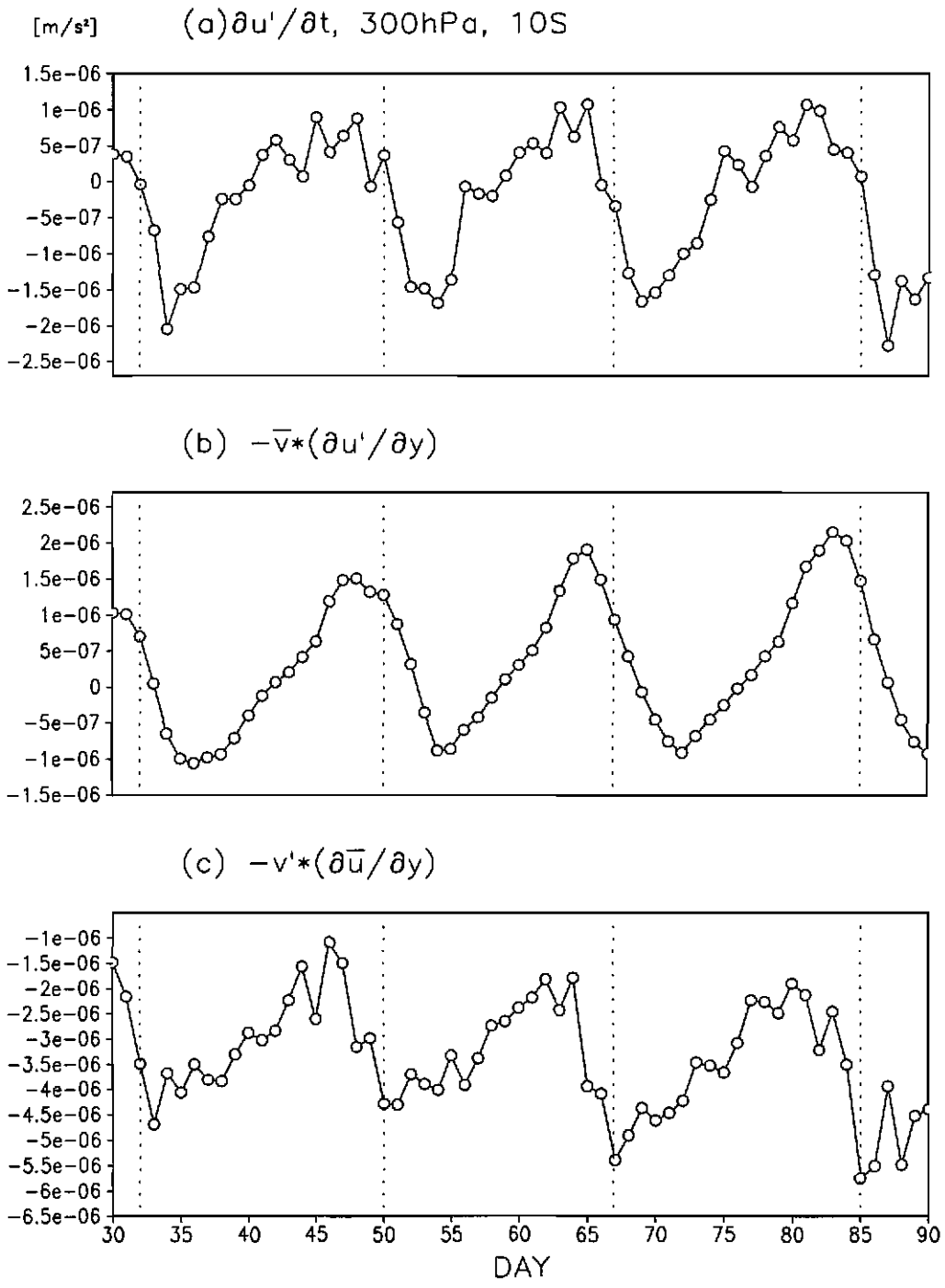

Figure 3.29: Components of momentum equation for 300hPa zonal wind anomaly ($\frac{\partial u'}{\partial t}$) at 10S. (a) $\frac{\partial u'}{\partial t}$, (b) $-\overline{v}\frac{\partial u'}{\partial y}$, (c) $-v'\frac{\partial \overline{u}}{\partial y}$, (d) $-\omega'\frac{\partial \overline{u}}{\partial p}$, (e) $-\overline{\omega}\frac{\partial u'}{\partial p}$, and (f) $\beta y v'$.

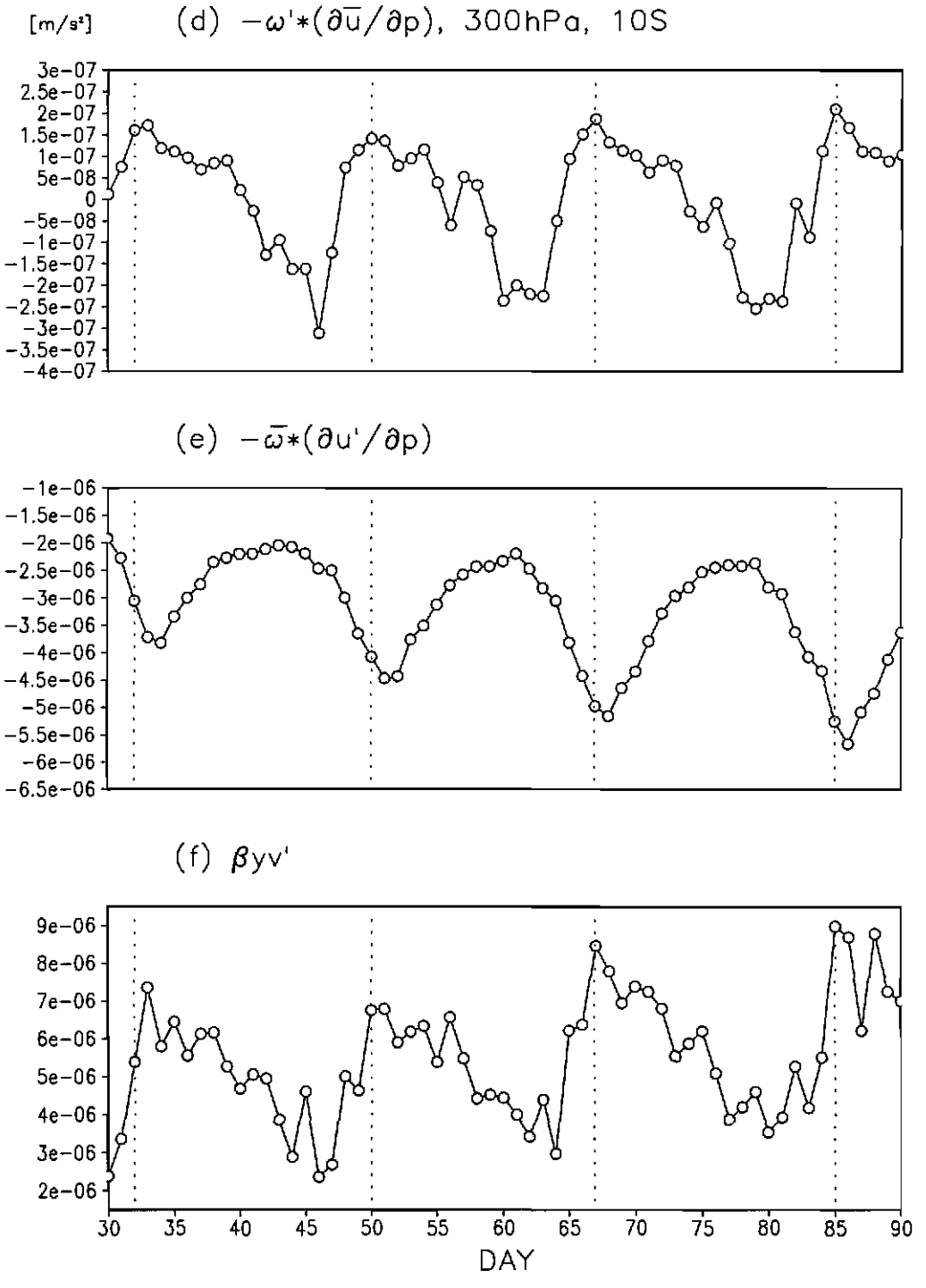

Figure 3.29: (Continued).

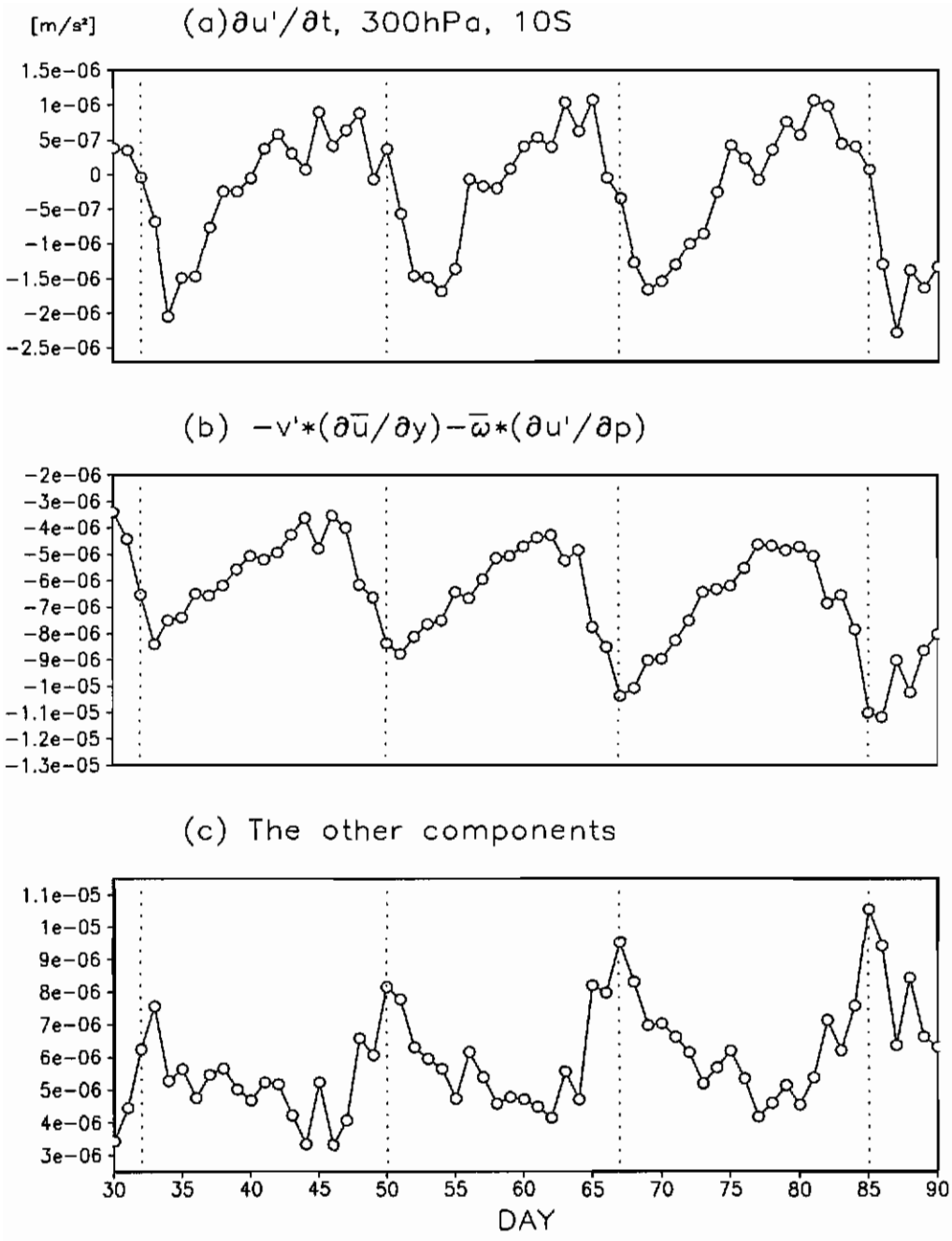

Figure 3.30: Time series (Day) of (a) $\frac{\partial u'}{\partial t}$, (b) sum of $-v'\frac{\partial \overline{u}}{\partial y}$ and $-\overline{\omega}\frac{\partial u'}{\partial p}$, and (c) sum of $-\overline{v}\frac{\partial u'}{\partial y}$, $-\omega'\frac{\partial \overline{u}}{\partial p}$, and $\beta y v'$ at 10S, 300hPa.

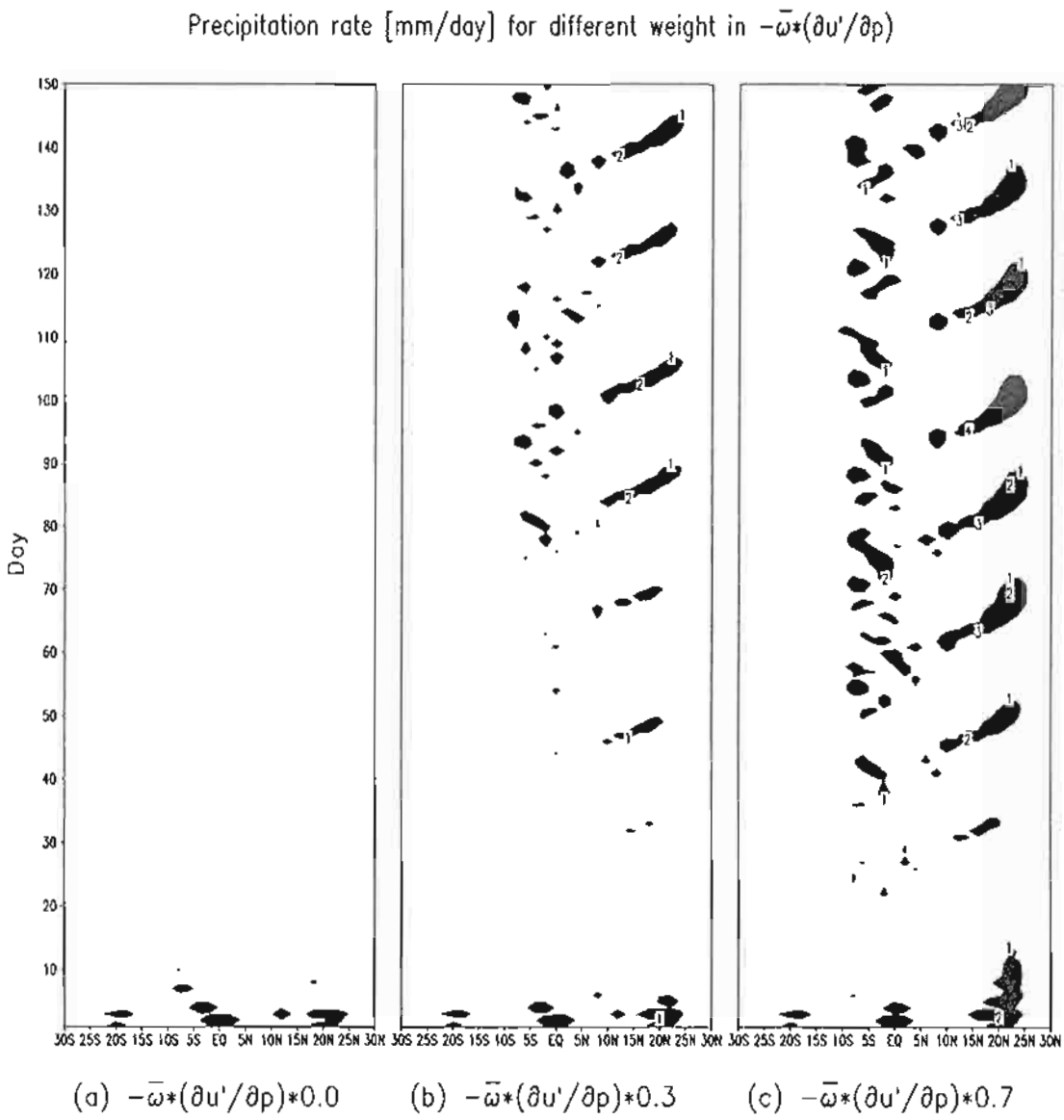

Figure 3.31: Precipitation rate (mm/day) in experiments with
(a) 0% of vertical advection by July-mean vertical motion (i.e. $-\overline{\omega}\frac{\partial u'}{\partial p}*0.$, Expt. 1),
(b) 30% of vertical advection by July-mean vertical motion (i.e. $-\overline{\omega}\frac{\partial u'}{\partial p}*0.3$, Expt. 2),
and (c) 70% of vertical advection by July-mean vertical motion (i.e. $-\overline{\omega}\frac{\partial u'}{\partial p}*0.7$, Expt. 3).

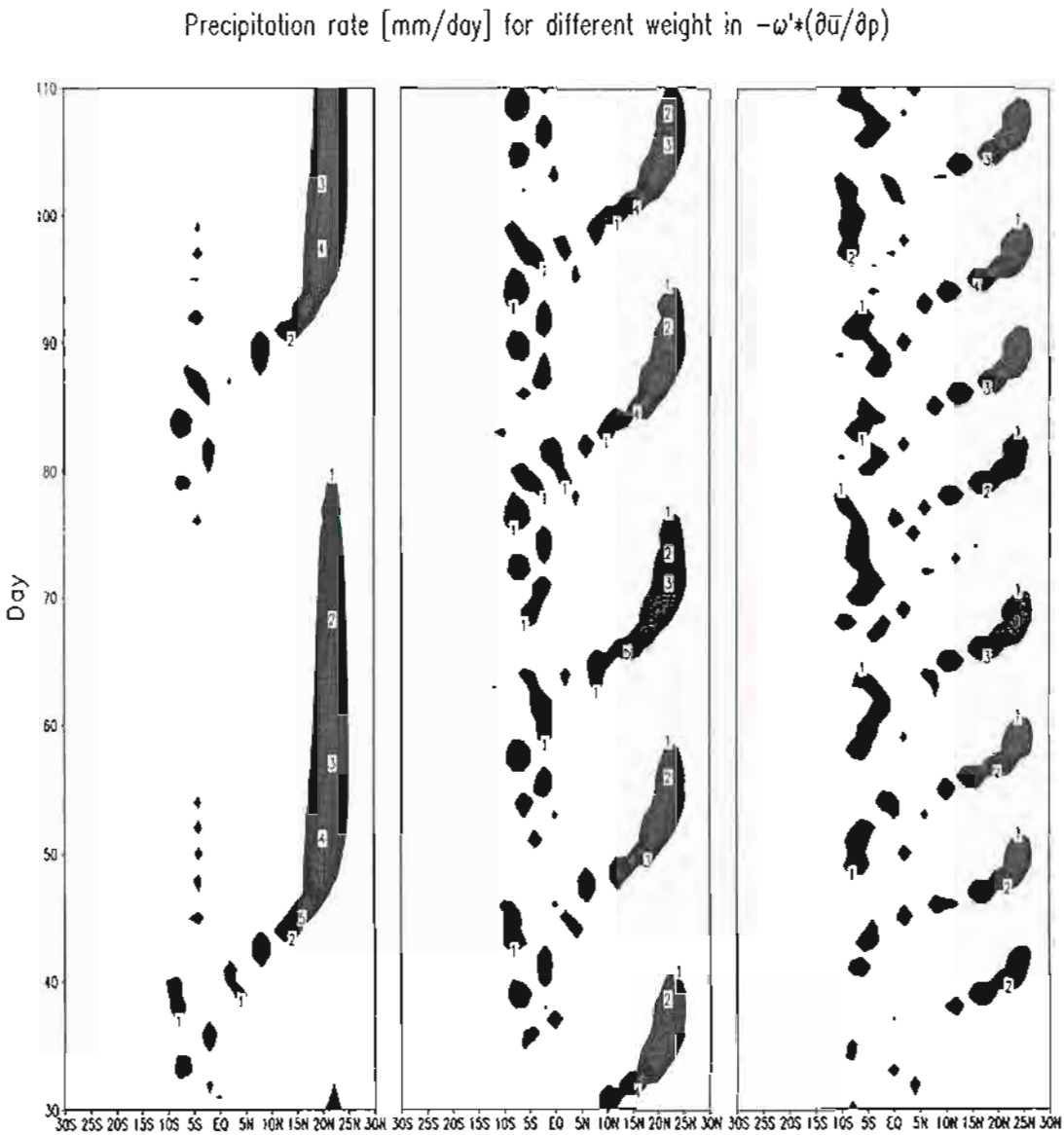

(a) $-\omega'*(\partial\bar{u}/\partial p)*0.7$ (b) $-\omega'*(\partial\bar{u}/\partial p)*1.0$ (c) $-\omega'*(\partial\bar{u}/\partial p)*1.4$

Figure 3.32: Precipitation rate (mm/day) in experiments with (a) 70% of vertical advection of July-mean zonal winds (i.e. $-\omega'\frac{\partial\bar{u}}{\partial p}*0.7$, Expt. 4), (b) 100% of vertical advection of July-mean zonal winds (i.e. $-\omega'\frac{\partial\bar{u}}{\partial p}*1.$, Expt. 5), and (c) 140% of vertical advection of July mean zonal winds (i.e. $-\omega'\frac{\partial\bar{u}}{\partial p}*1.4$, Expt. 6).

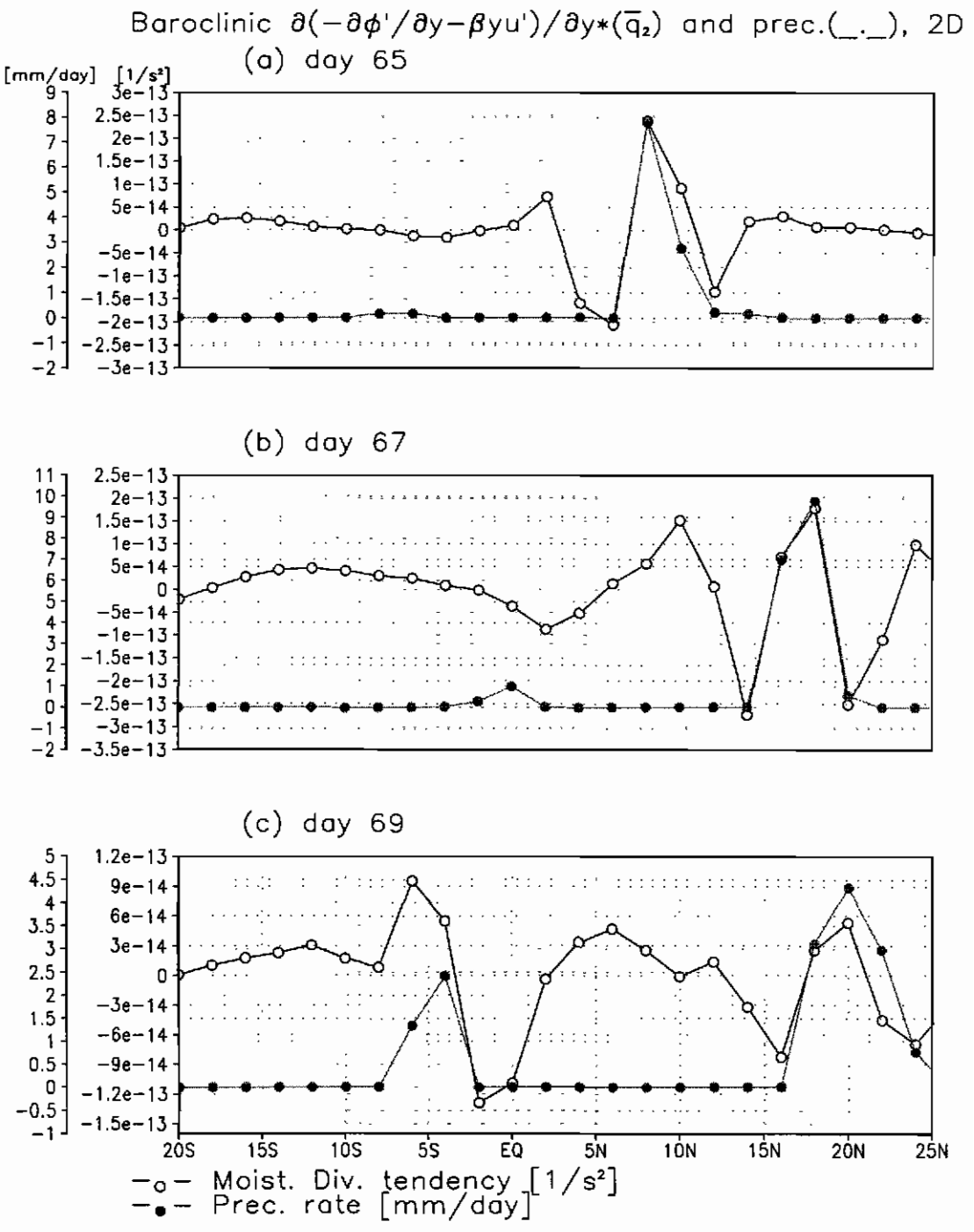

Figure 3.33: Latitudinal variation of precipitation rate (-•-) and $[\frac{\partial}{\partial y}(-\frac{\partial \phi'^{-}}{\partial y} - \beta y u'^{-})\overline{q}_2$, -∘-] on (a) day 65, (b) day 67, and (c) day 69.

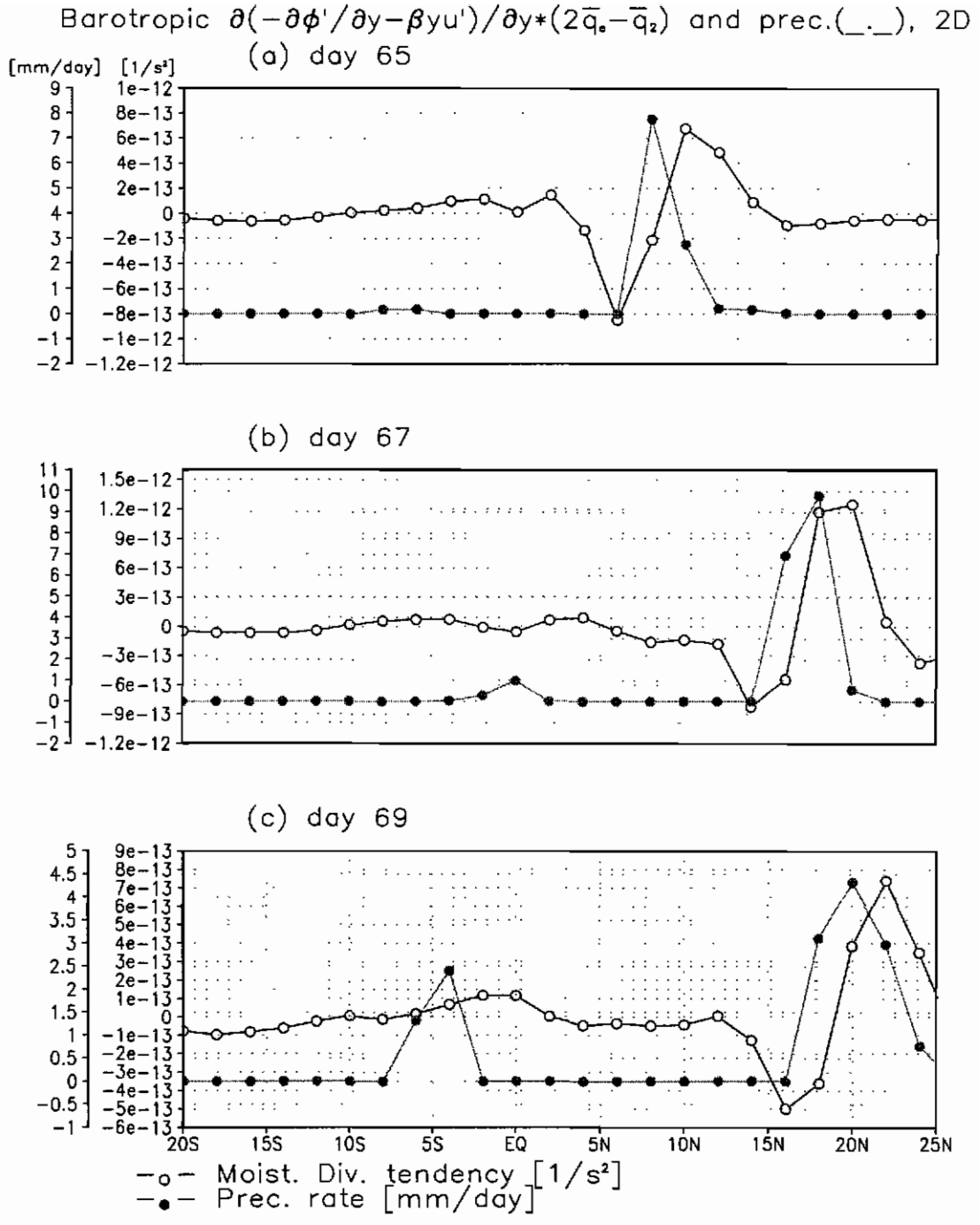

Figure 3.34: Latitudinal variation of precipitation rate (-•-) and $[\frac{\partial}{\partial y}(-\frac{\partial \phi'^{+}}{\partial y} - \beta y u'^{+})(2\overline{q}_e - \overline{q}_2)$, -∘-] on (a) day 65, (b) day 67, and (c) day 69.

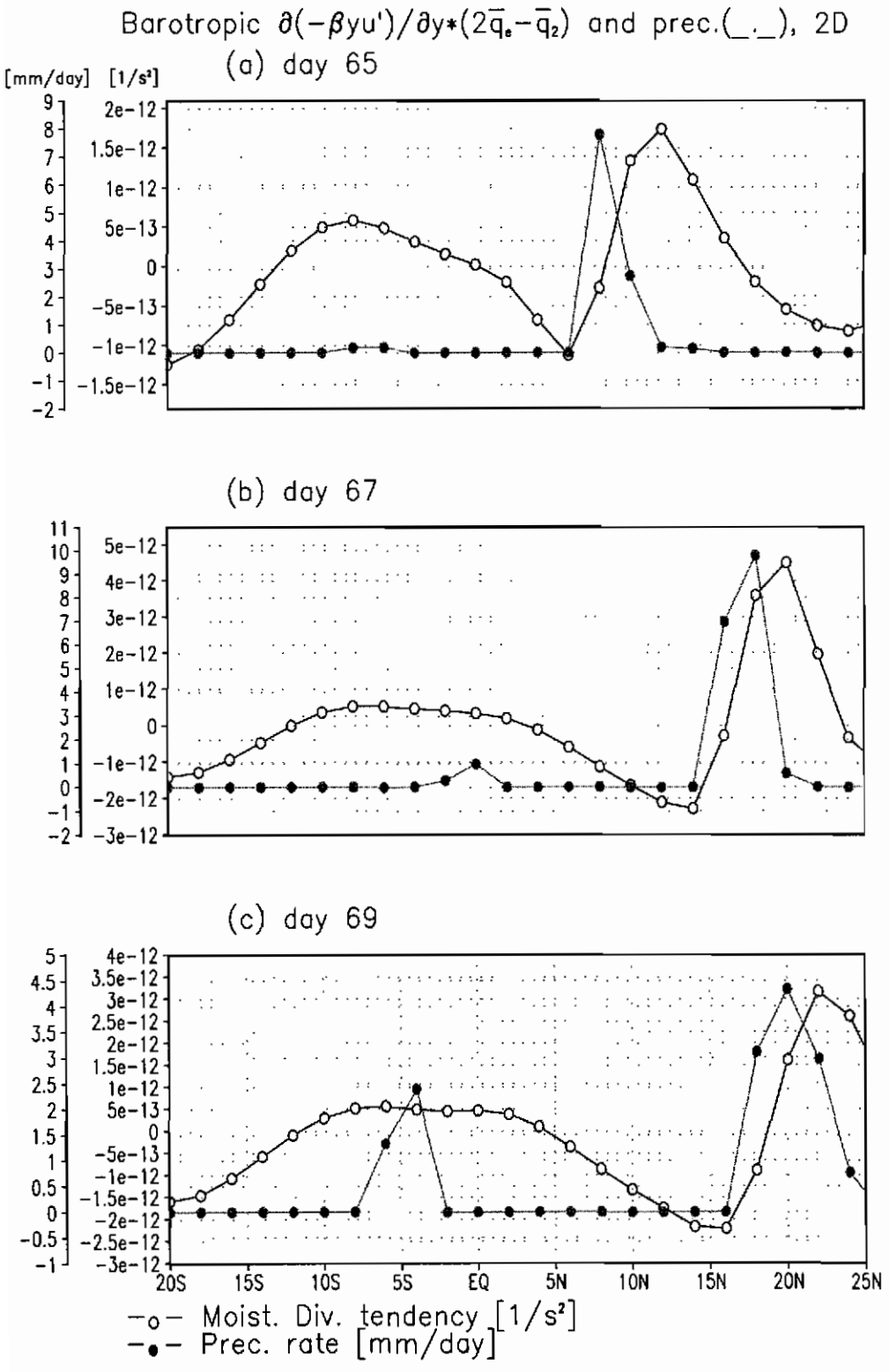

Figure 3.35: Latitudinal variation of precipitation rate (-•-) and [$\frac{\partial}{\partial y}(-\beta y u'^{+})(2\overline{q}_e - \overline{q}_2)$, -o-] on (a) day 65, (b) day 67, and (c) day 69.

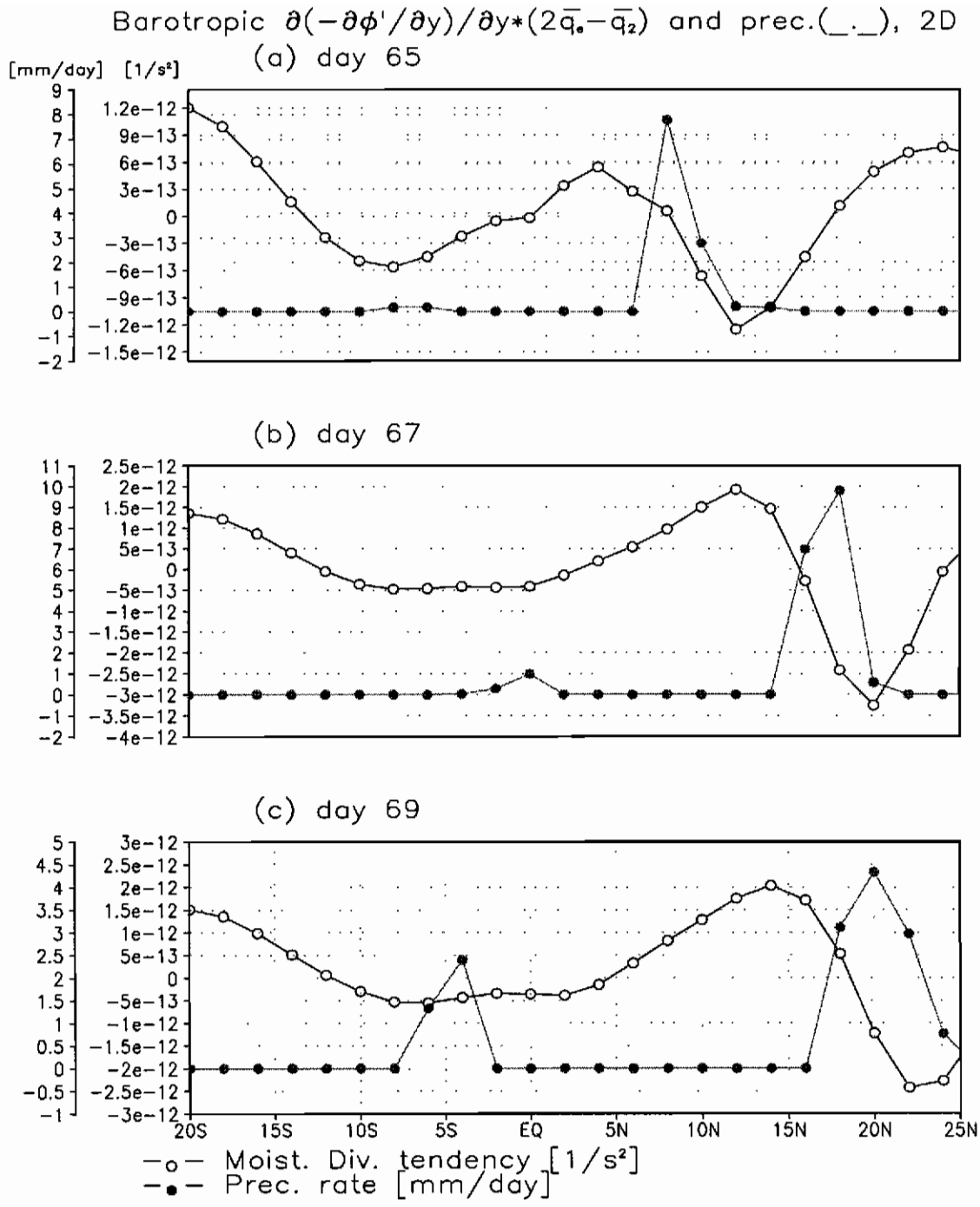

Figure 3.36: Latitudinal variation of precipitation rate (-•-) and

$[\frac{\partial}{\partial y}(-\frac{\partial \phi'^{+}}{\partial y})(2\overline{q}_e - \overline{q}_2)$, -∘-] on (a) day 65, (b) day 67, and (c) day 69.

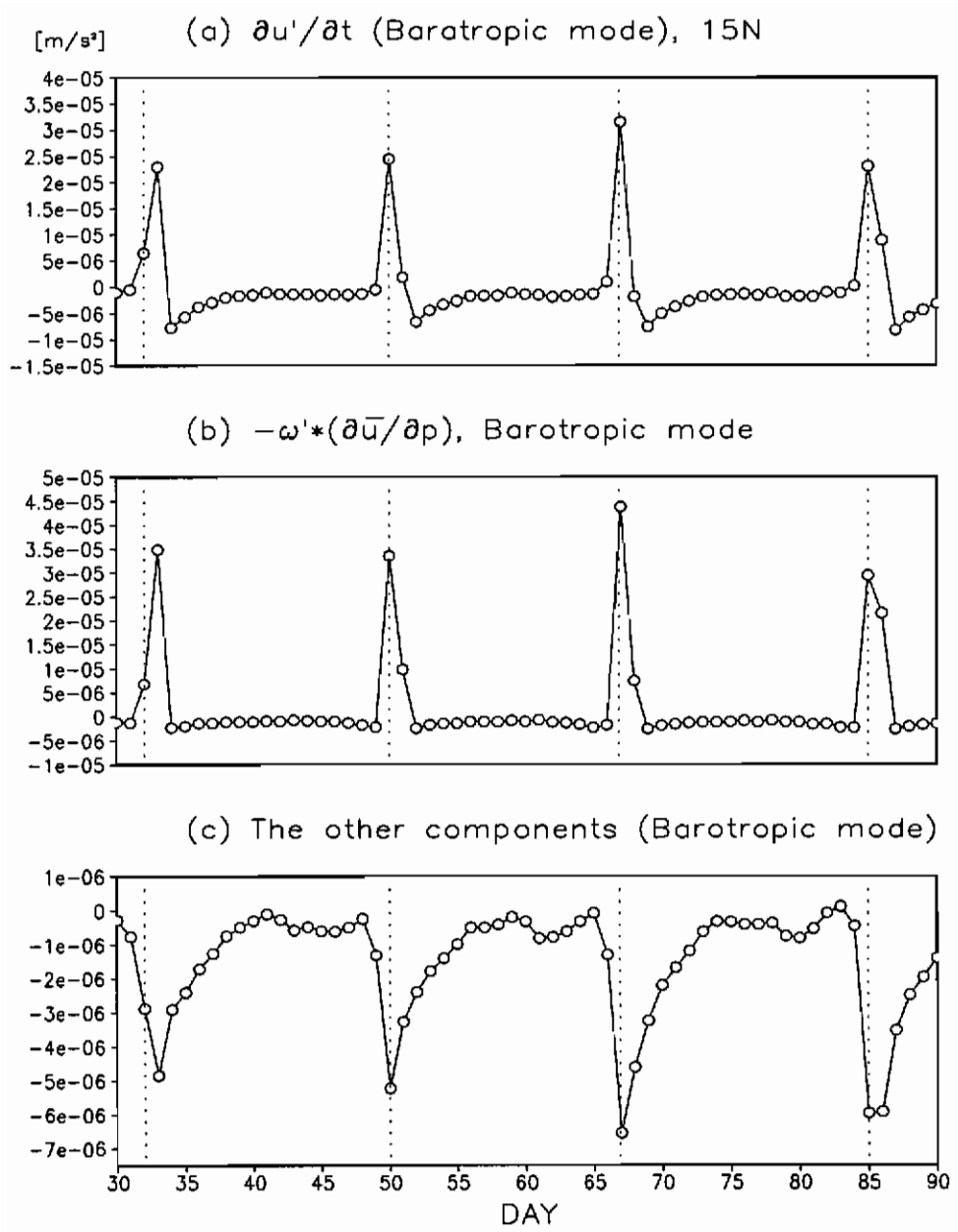

Figure 3.37: Time series of barotropic mode in momentum equation for zonal wind anomaly at 15N (-o-). (a) $\frac{\partial u'^{+}}{\partial t}$, (b) $(-\omega' \frac{\partial \bar{u}}{\partial p})^{+}$, and (c) sum of $(-v' \frac{\partial \bar{u}}{\partial y})^{+}$, $(-\bar{v} \frac{\partial u'}{\partial y})^{+}$, $(-\bar{\omega} \frac{\partial u'}{\partial p})^{+}$, and $\beta y v'^{+}$.

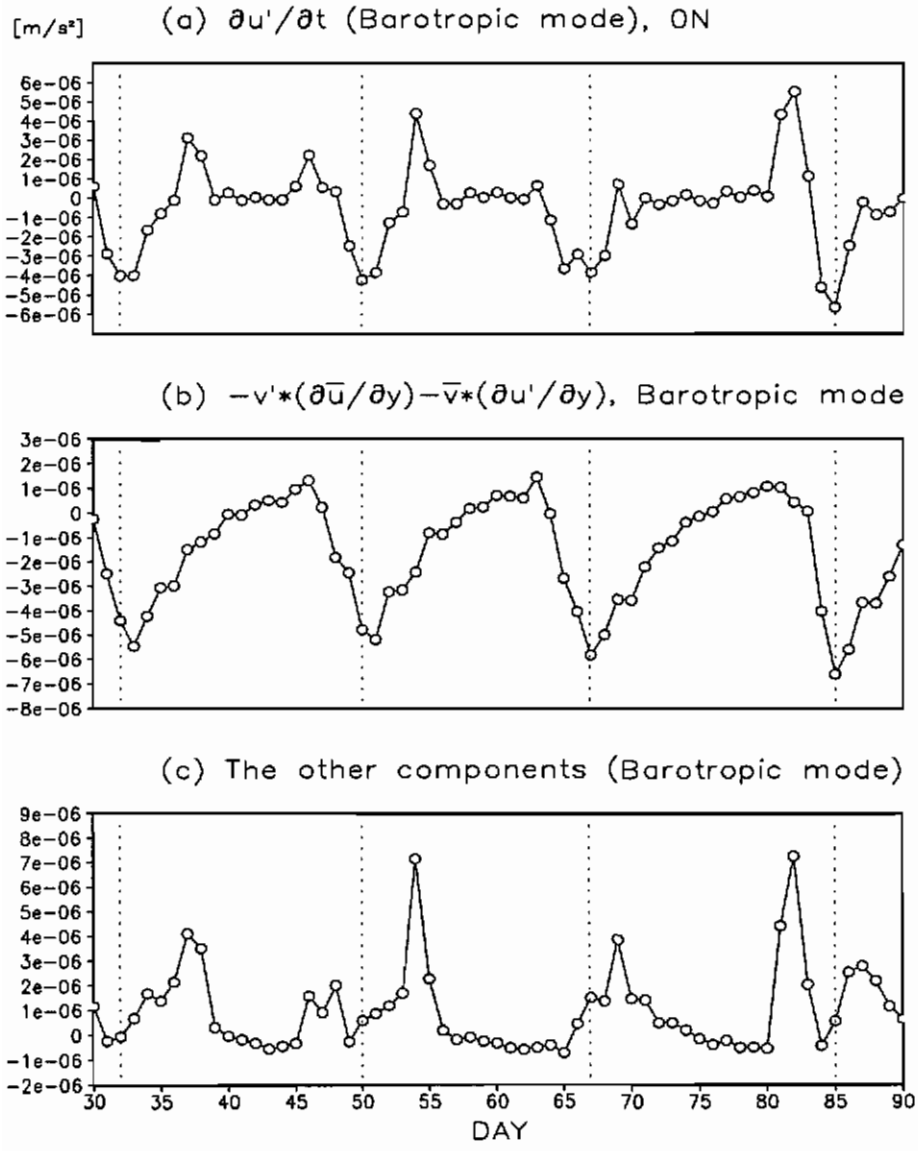

Figure 3.38: Time series of barotropic mode in momentum equation for zonal wind anomaly at 0N (-∘-). (a) $\frac{\partial u'^{+}}{\partial t}$, (b) sum of $(-v'\frac{\partial \bar{u}}{\partial y})^{+}$ and $(-\bar{v}\frac{\partial u'}{\partial y})^{+}$, and (c) sum of $(-\omega'\frac{\partial \bar{u}}{\partial p})^{+}$, $(-\bar{\omega}\frac{\partial u'}{\partial p})^{+}$, and $\beta y v'^{+}$.

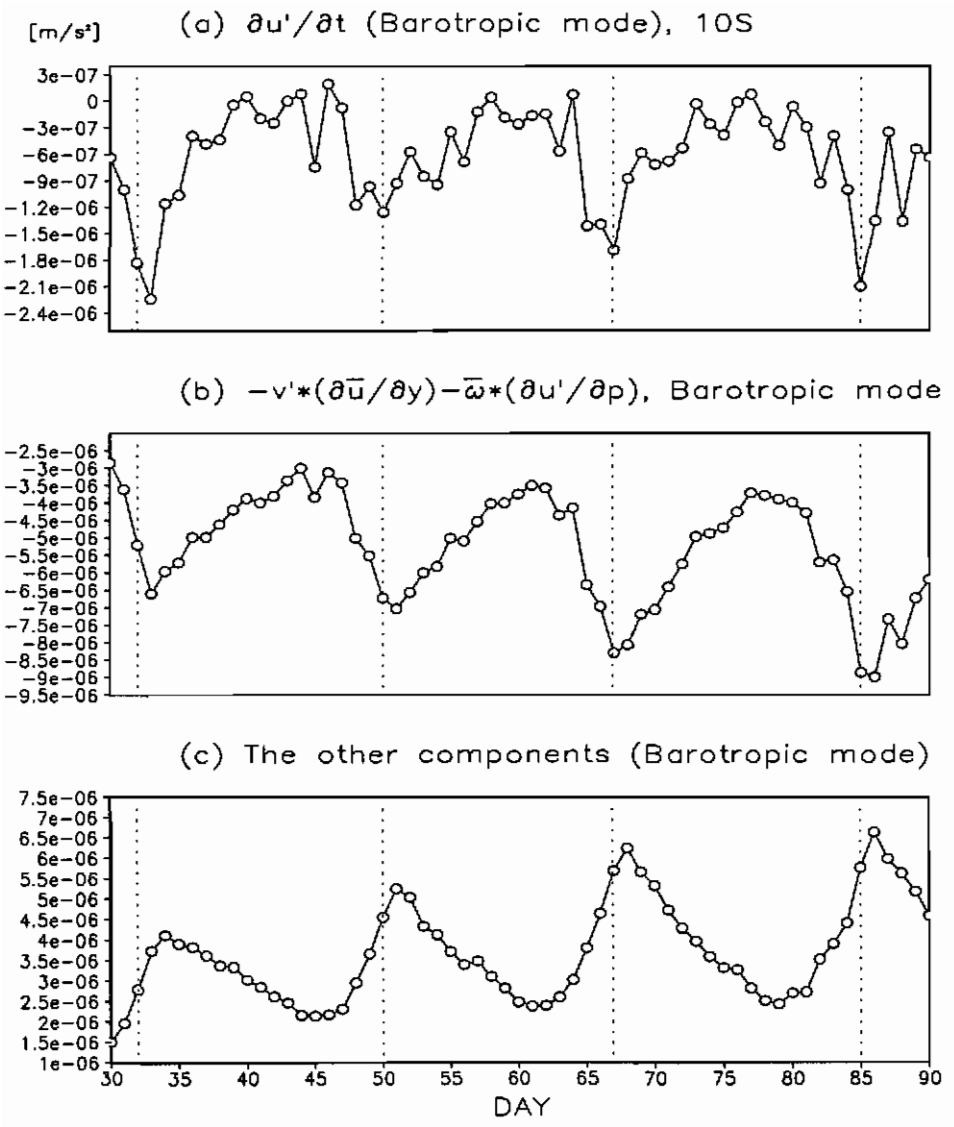

Figure 3.39: Time series of barotropic mode in momentum equation for zonal wind anomaly at 10S (-o-). (a) $\frac{\partial u'^{+}}{\partial t}$, (b) sum of $(-v'\frac{\partial \bar{u}}{\partial y})^{+}$ and $(-\bar{\omega}\frac{\partial u'}{\partial p})^{+}$, and (c) sum of $(-\bar{v}\frac{\partial u'}{\partial y})^{+}$, $(-\omega'\frac{\partial \bar{u}}{\partial p})^{+}$, and $\beta y v'^{+}$.

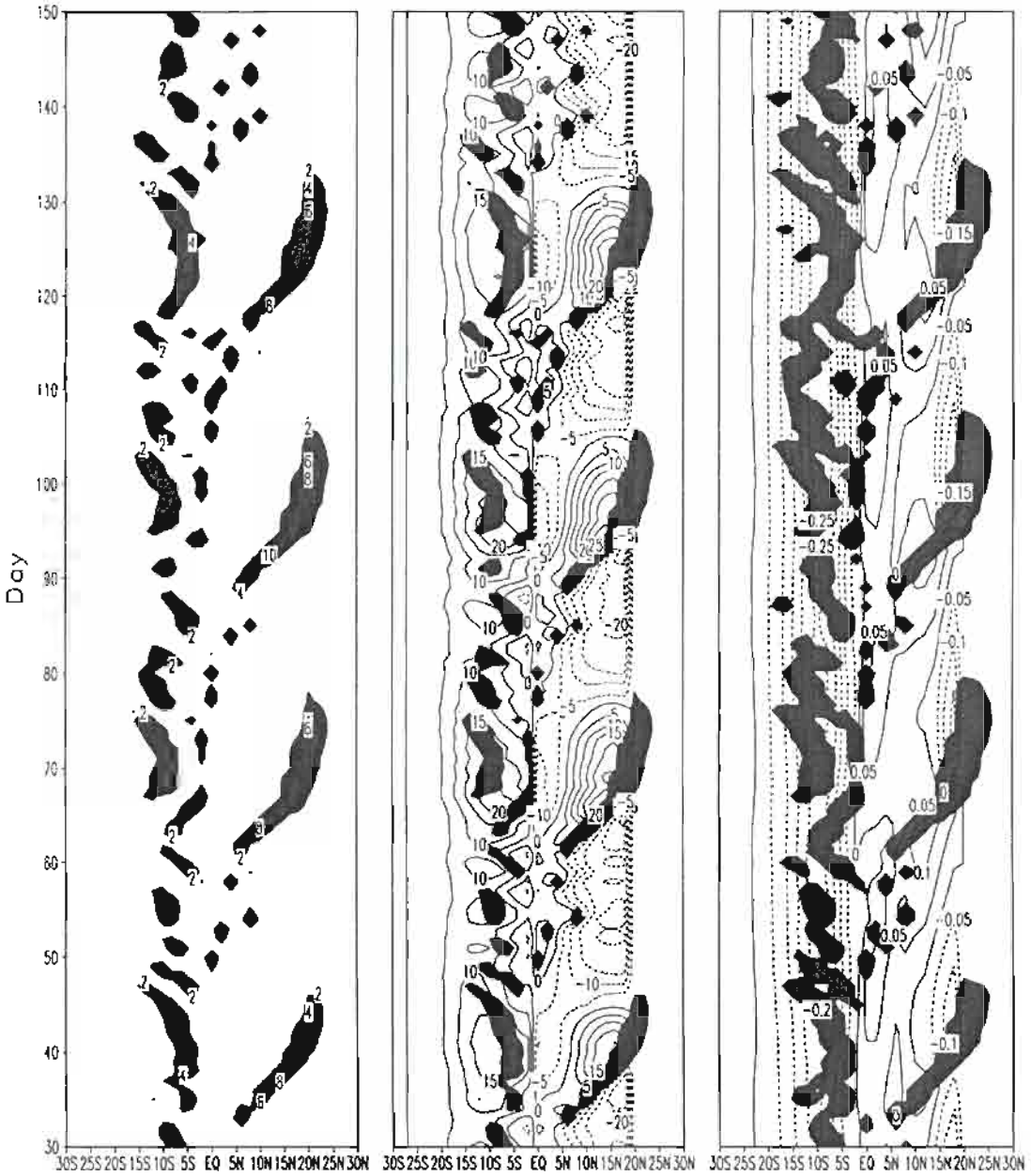

Figure 3.40: Latitude-time section of anomalies from 2D model with ocean mixed layer. (a) precipitation rate (mm/day), (b) latent heat fluxes (W/m^2), and (c) surface temperature (° C).

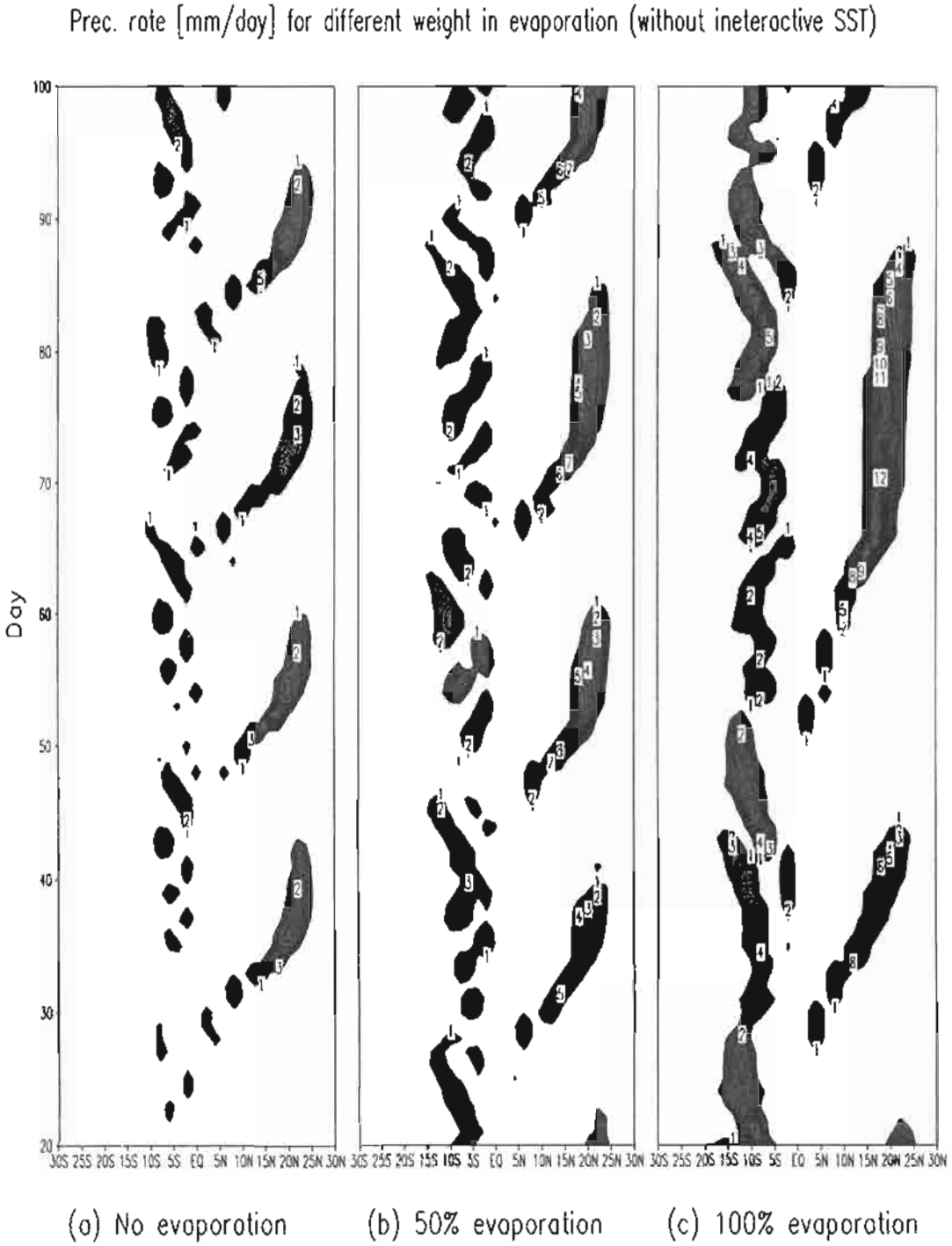

Figure 3.41: Precipitation rate (mm/day) in experiments when (a) no evaporation is added into precipitation, (b) 50% of evaporation is added into precipitation, and (c) 100% of evaporation is added into precipitation.

Prec. rate for different weight in ∂sst'/∂y, and ∂²sst'/∂y², (with LHFL') in 2D

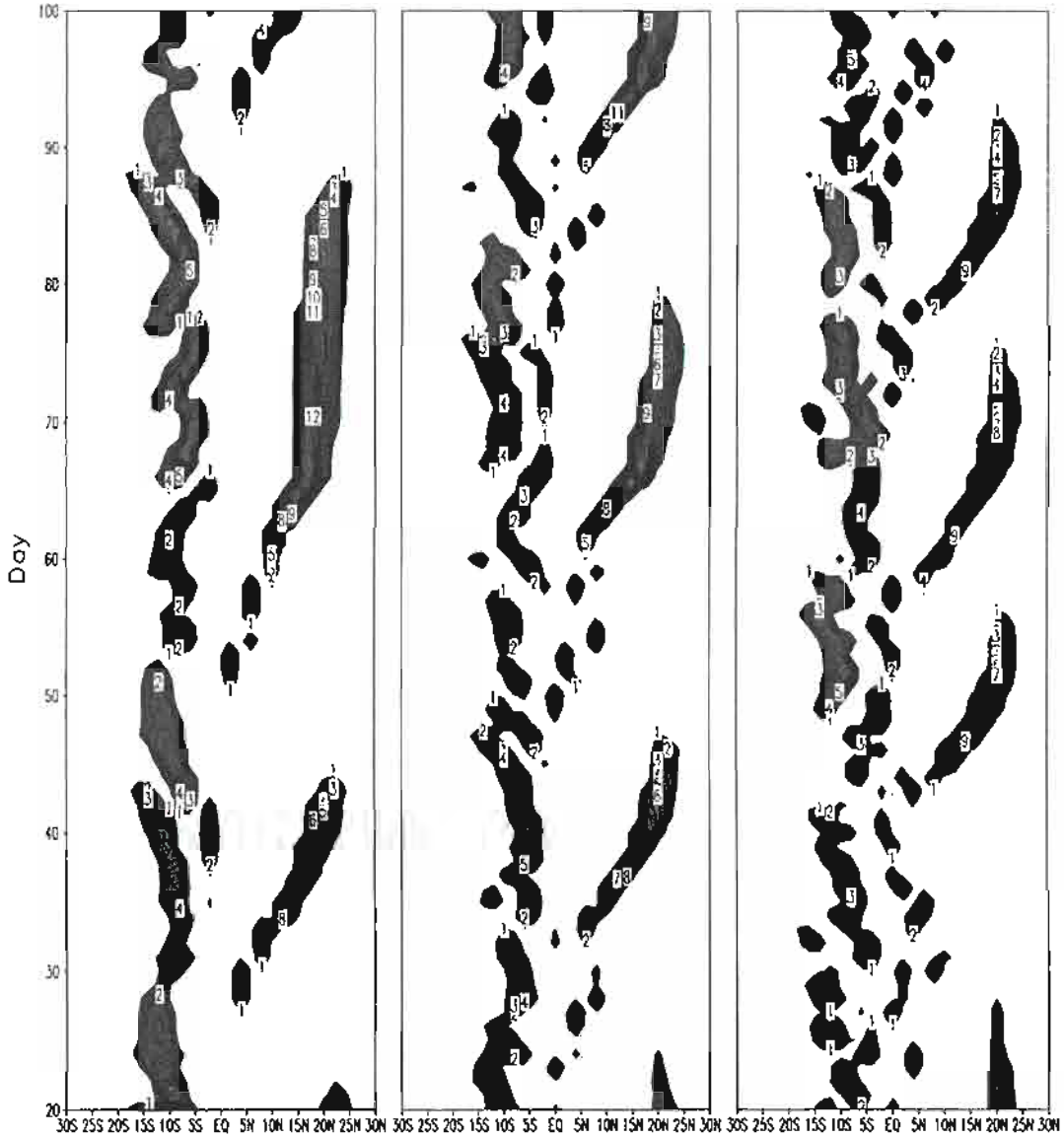

(a) ∂sst'/∂y*0, ∂²sst'/∂y²*0 (b) ∂sst'/∂y*1, ∂²sst'/∂y²*1 (c) ∂sst'/∂y*2, ∂²sst'/∂y²*2

Figure 3.42: Precipitation rate (mm/day) in experiments when

(a) SST has no influence on Ekman pumping ($\frac{\partial sst'}{\partial y} * 0$ *and* $\frac{\partial^2 sst'}{\partial y^2} * 0$),

(b) 100% of influence of SST on Ekman pumping($\frac{\partial sst'}{\partial y} * 1$ *and* $\frac{\partial^2 sst'}{\partial y^2} * 1$), and

(c) 200% of influence of SST on Ekman pumping ($\frac{\partial sst'}{\partial y} * 2$ *and* $\frac{\partial^2 sst'}{\partial y^2} * 2$).

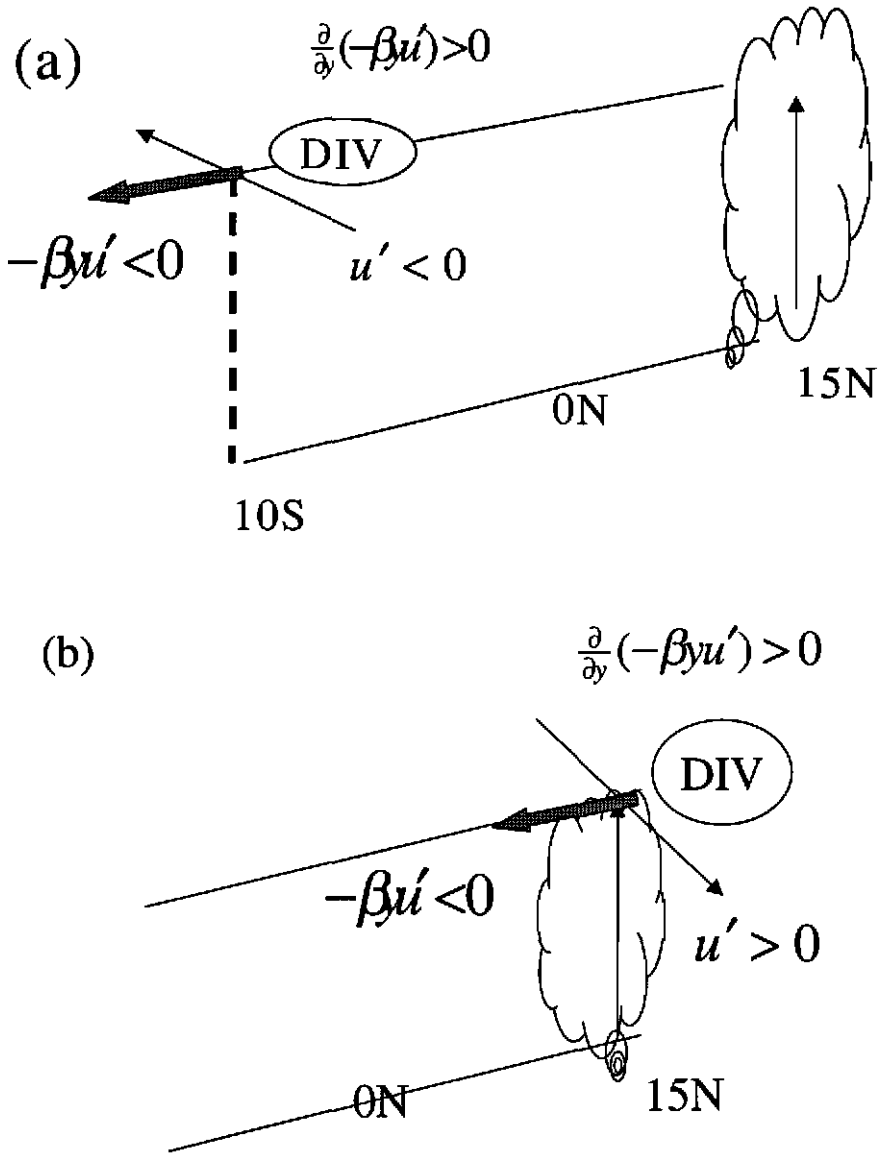

Figure 3.43: Schematic diagram of mechanism for (a) initiation of convection at 10S, and (b) northward propagation of convection at 15N.

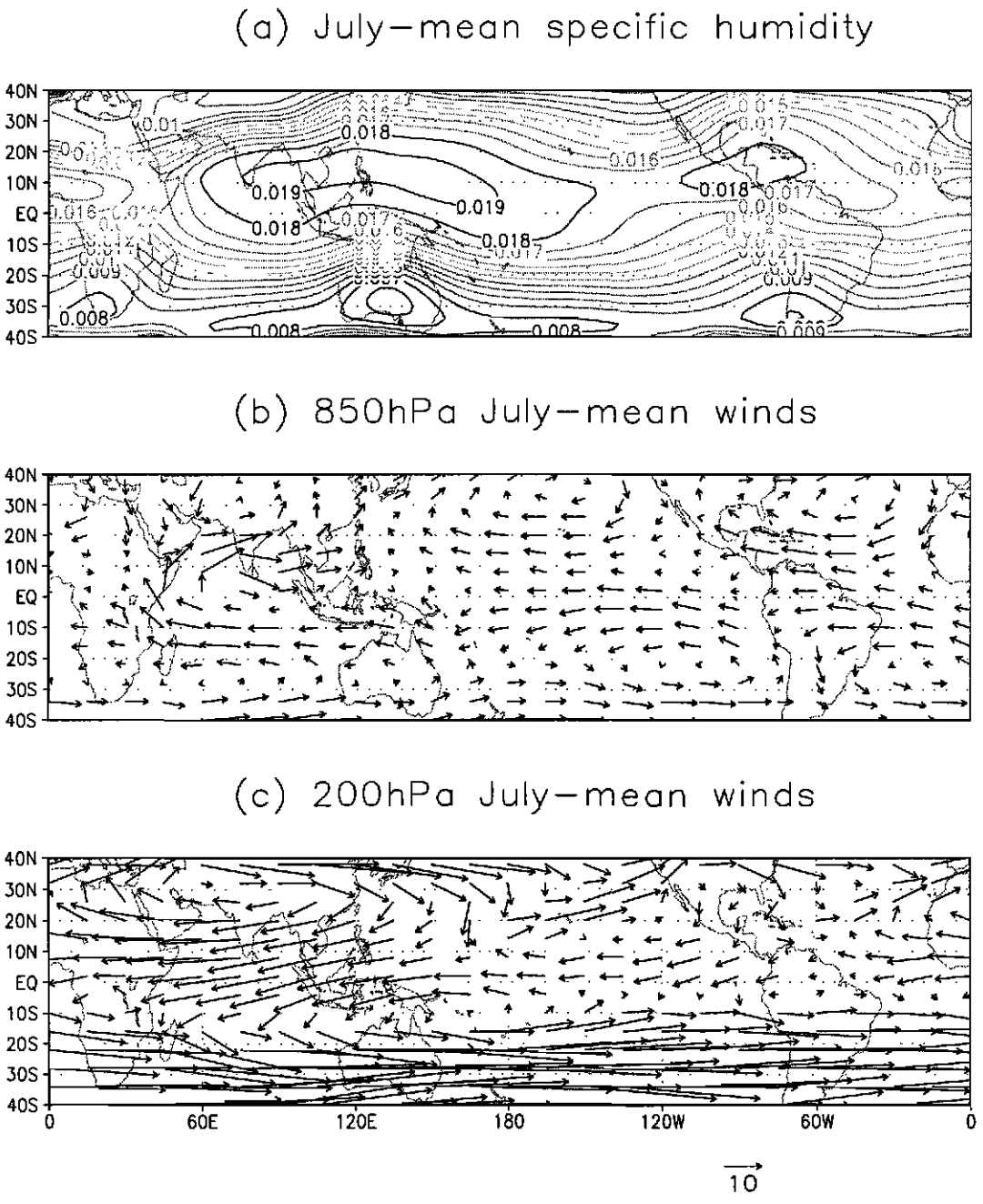

Figure 4.1: The climatological (a) July-mean specific humidity at 1000hPa estimate from using an surface temperature and dew point temperature derived from ECMWF global analyses for the period 1979-92, (b) July-mean winds at 850hPa, (c) July-mean winds at 200hPa.

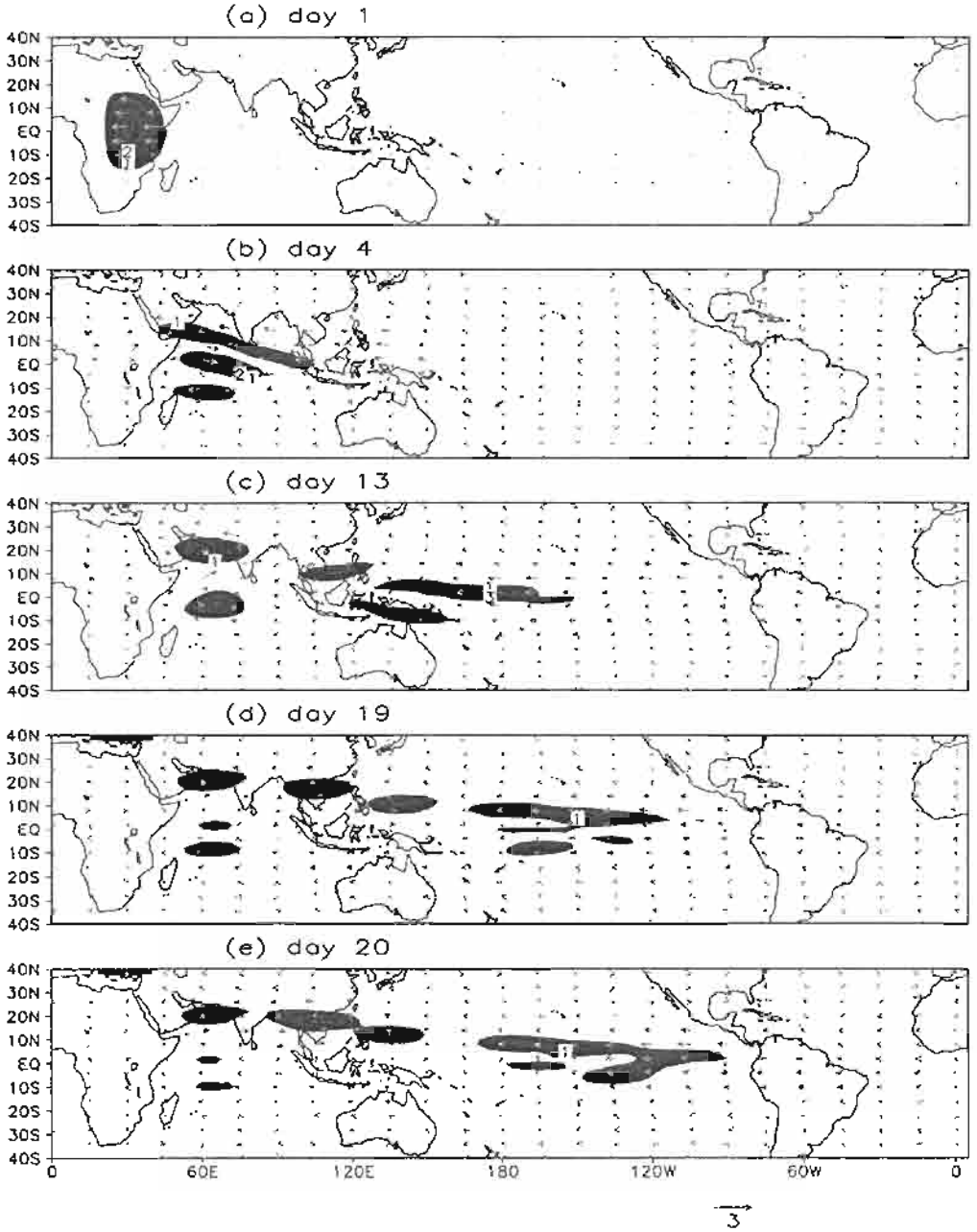

Figure 4.2: Sequential maps for the lower-tropospheric winds and precipitation rate(shaded > 0.1mm/day) for the 3D model without interactive SST on (a) day 1, (b) day 4, (c) day 13, (d) day 19, (e) day 20, (f) day 22, (g) day 25, (h) day 28, (i) day 31, and (j) day 40.

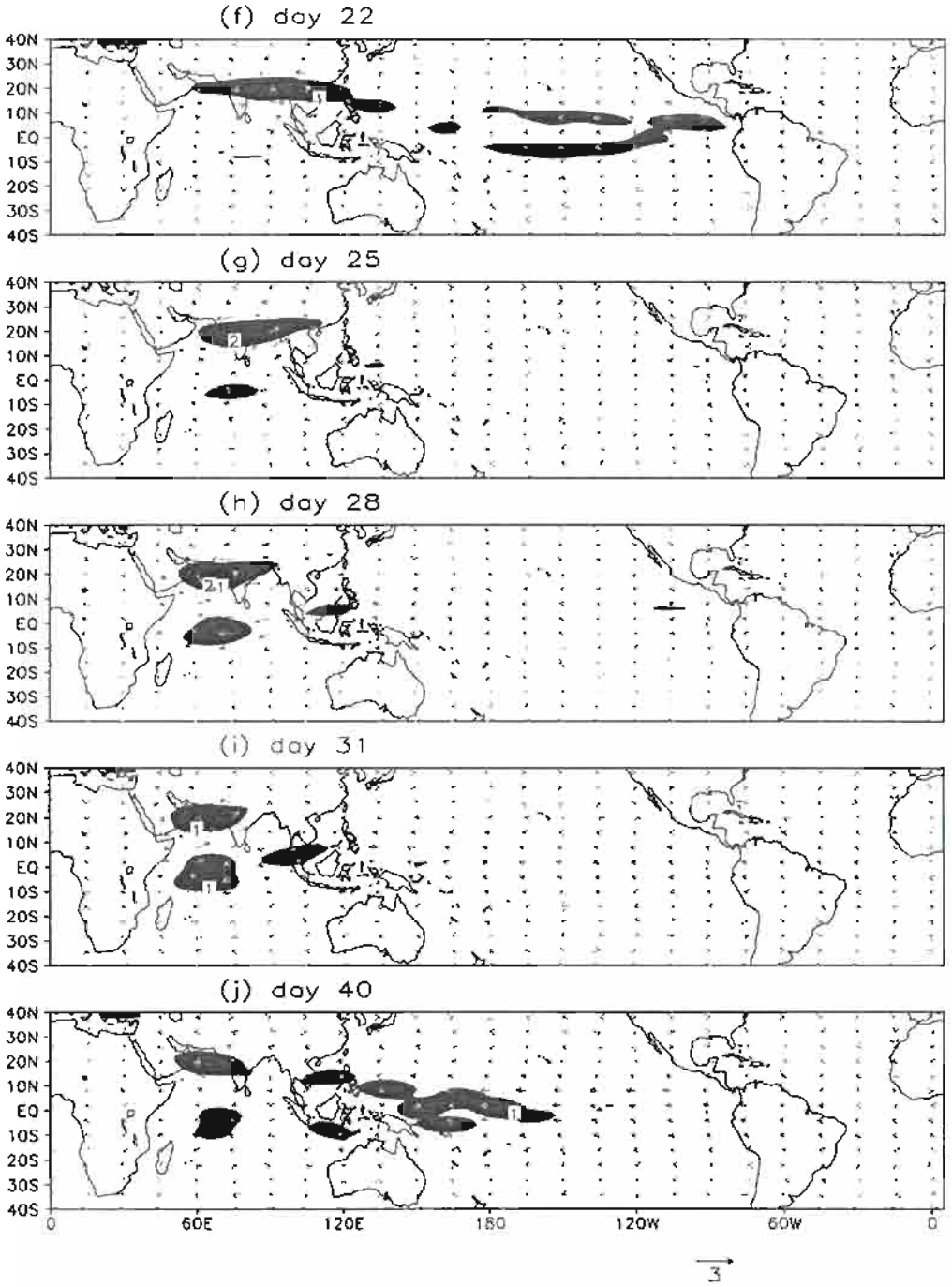

Figure 4.2: (Continued).

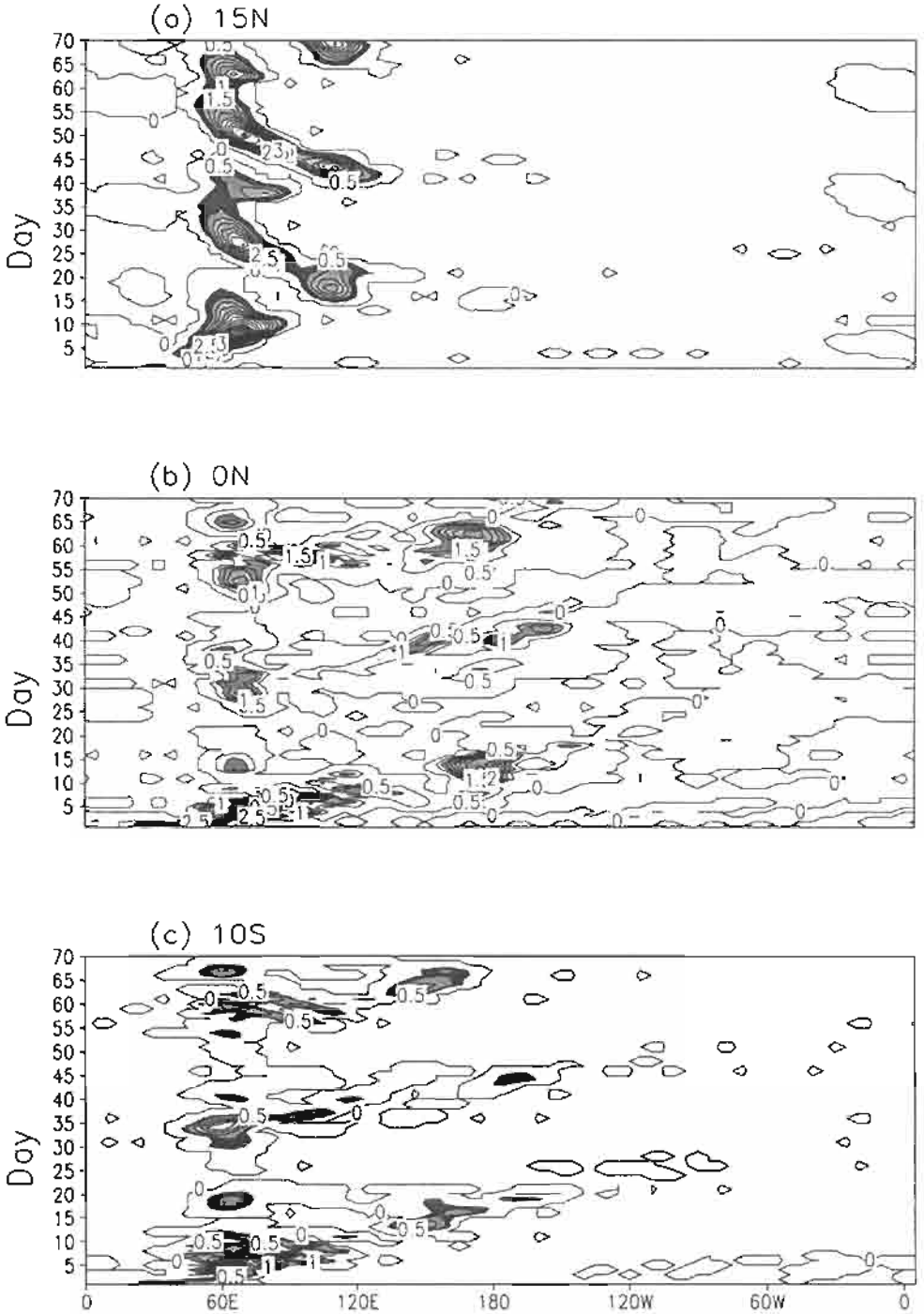

Figure 4.3: Time-longitude cross section of precipitation rate along (a) 15N, (b) equator, and (c) 10S.

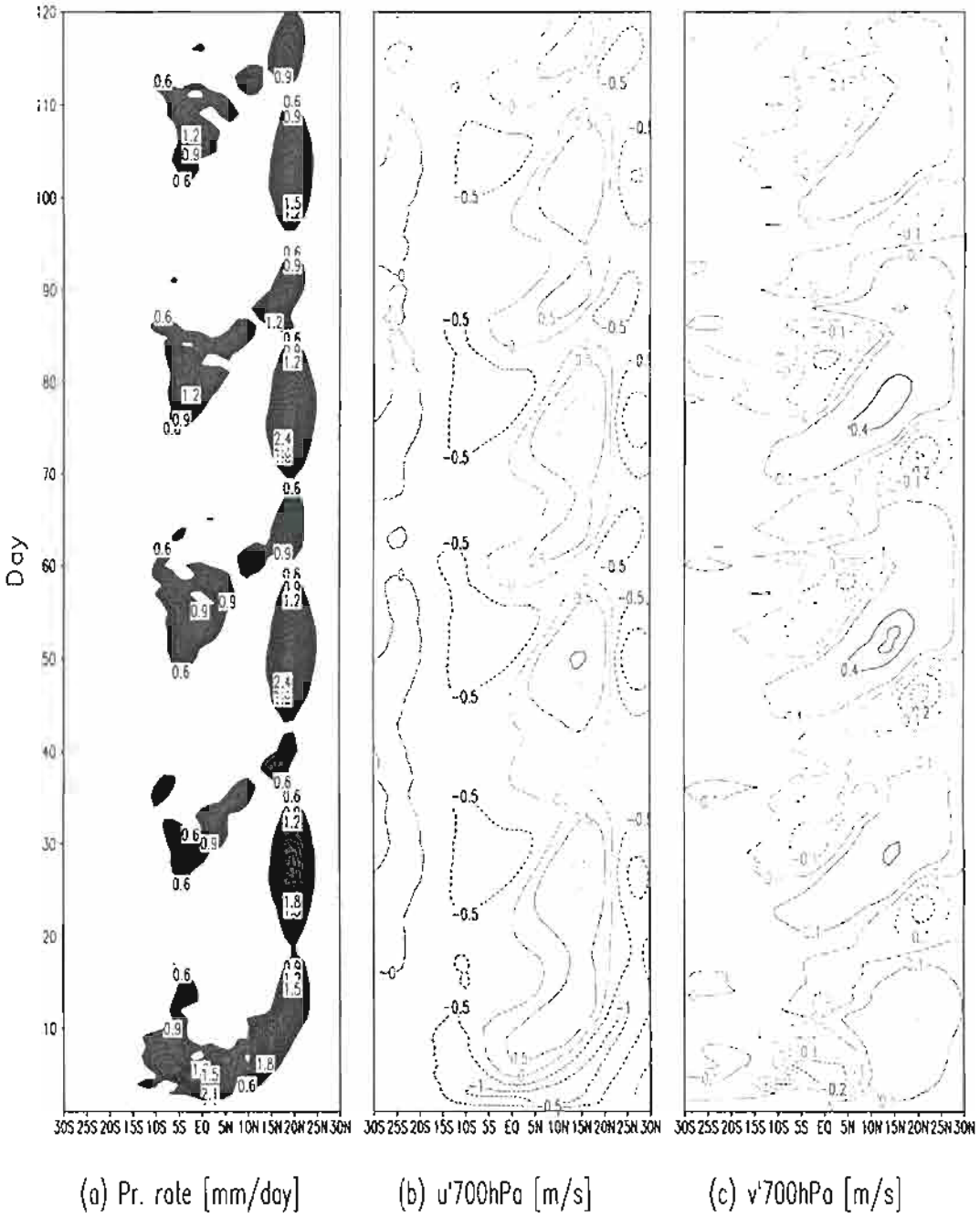

Figure 4.4: Latitude-time section of zonally averaged (60-100E) anomalies from 3D model without interactive SST. (a) precipitation rate (mm/day), (b) low level zonal wind (m/s), and (c) low level meridional wind (m/s).

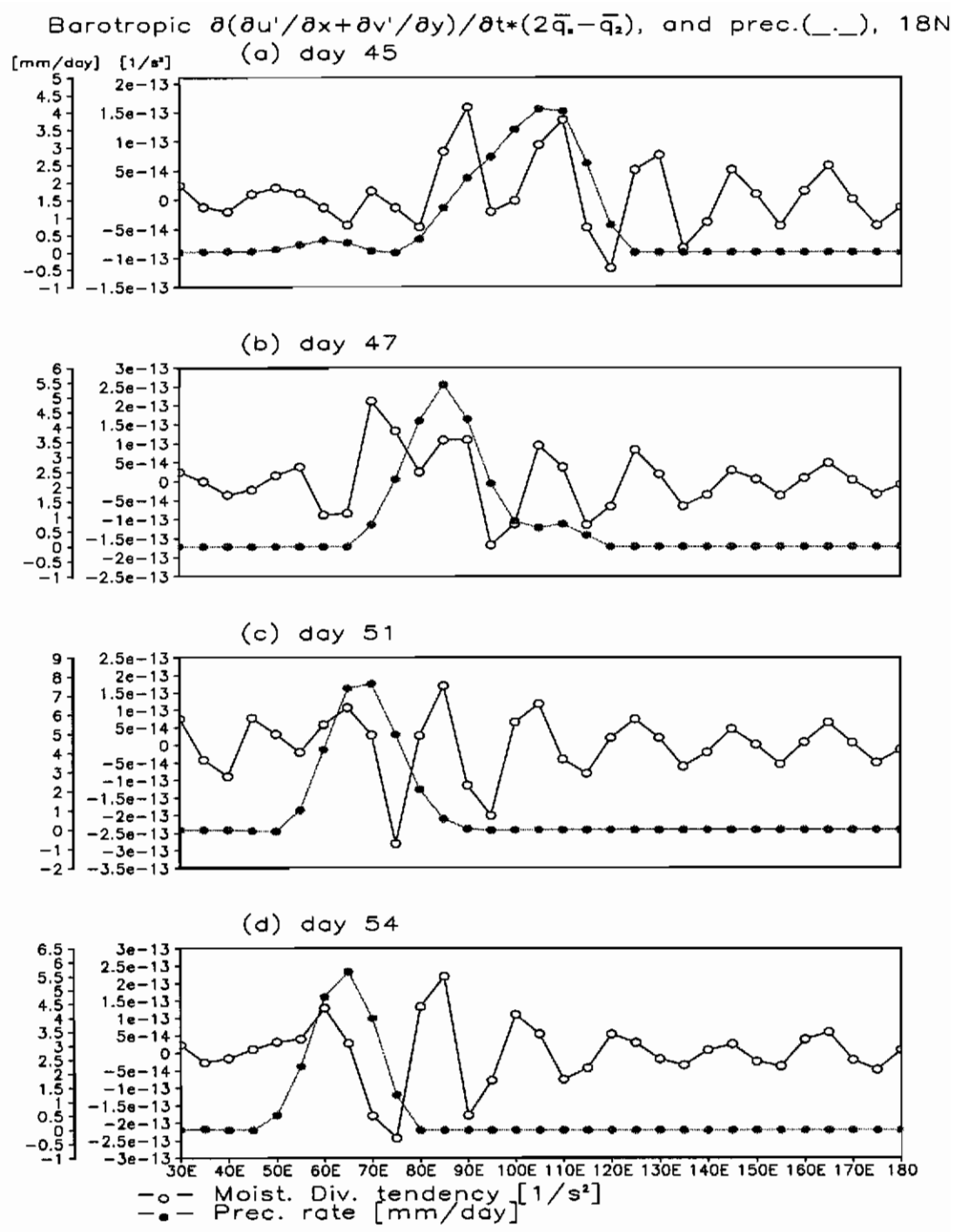

Figure 4.5: Longitudinal variation of precipitation rate (-•-), and $\frac{\partial}{\partial t}(\frac{\partial u'^{+}}{\partial x}+\frac{\partial v'^{+}}{\partial y})(2\overline{q}_e-\overline{q}_2)$ (-o-) at 18N on (a) day 45, (b) day 47, (c) day 51, and (d) day 54.

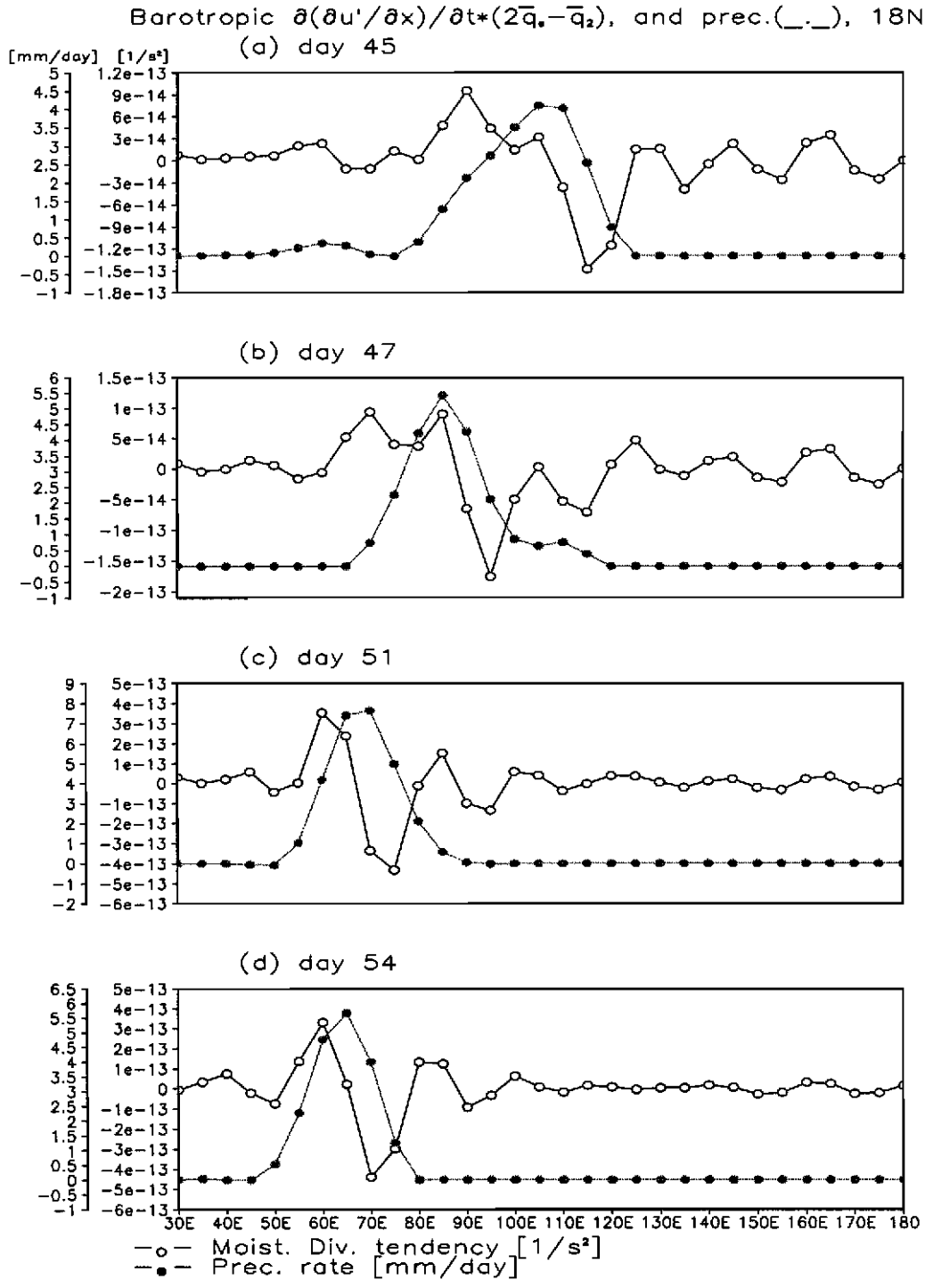

Figure 4.6: Longitudinal variation of precipitation rate (-•-), and $\frac{\partial}{\partial t}(\frac{\partial u'^{+}}{\partial x})(2\overline{q}_e - \overline{q}_2)$ (-∘-) at 18N on (a) day 45, (b) day 47, (c) day 51, and (d) day 54.

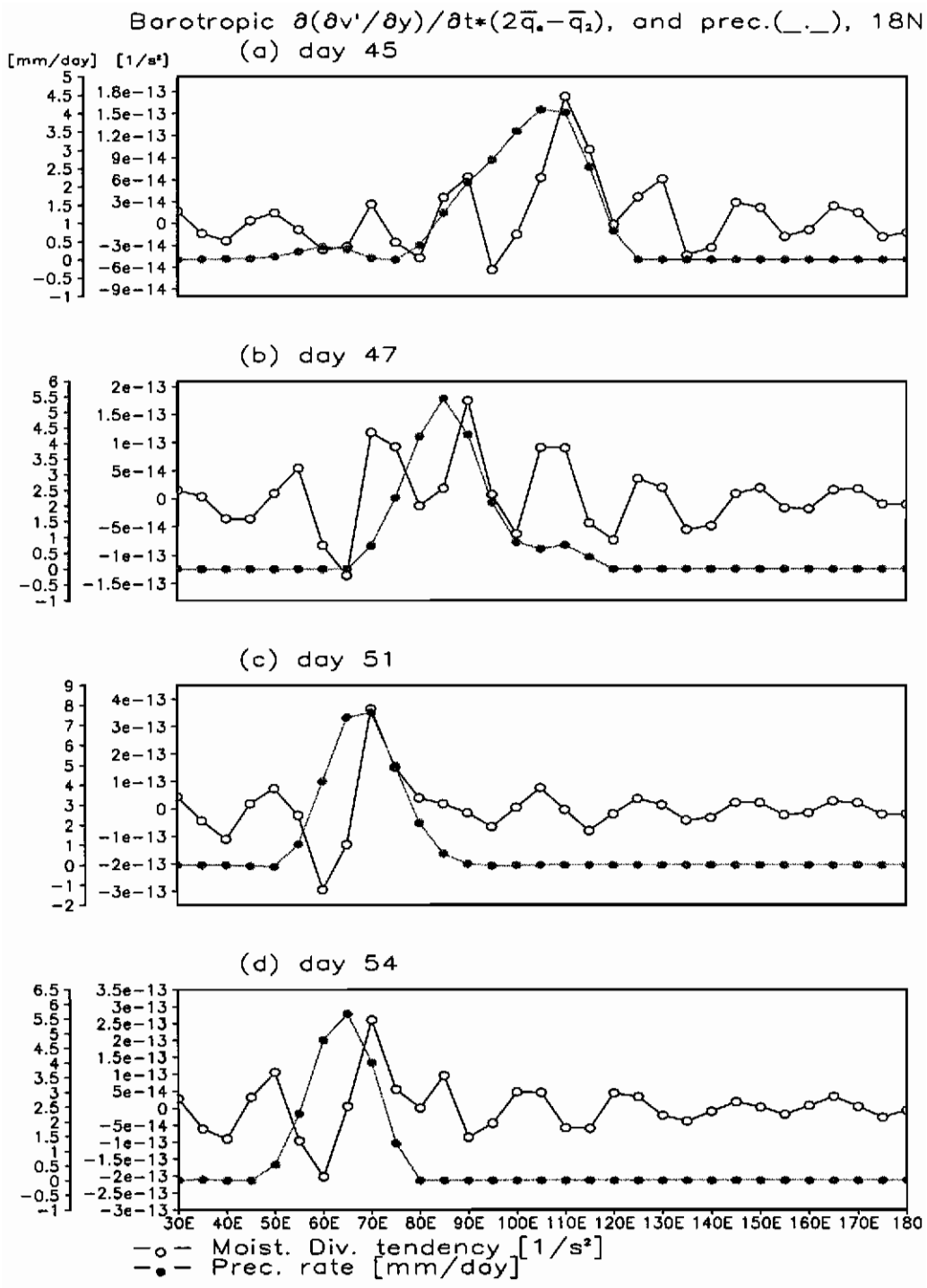

Figure 4.7: Longitudinal variation of precipitation rate (-•-), and $\frac{\partial}{\partial t}(\frac{\partial v'^{+}}{\partial y})(2\overline{q}_e - \overline{q}_2)$ (-∘-) at 18N on (a) day 45, (b) day 47, (c) day 51, and (d) day 54.

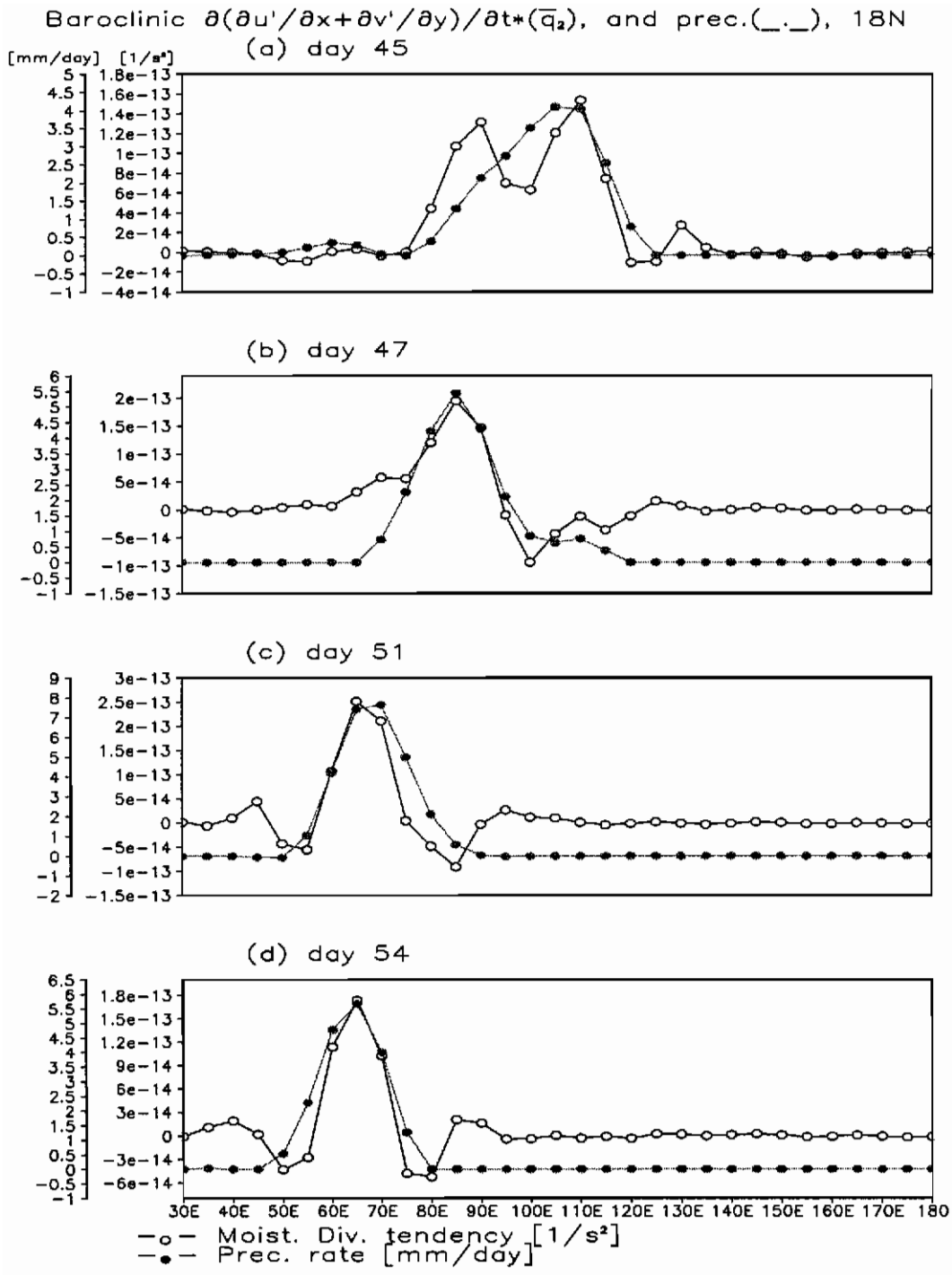

Figure 4.8: Longitudinal variation of precipitation rate (-•-), and $\frac{\partial}{\partial t}(\frac{\partial u'^{-}}{\partial x} + \frac{\partial v'^{-}}{\partial y})\overline{q}_2$ (-∘-) at 18N on (a) day 45, (b) day 47, (c) day 51, and (d) day 54.

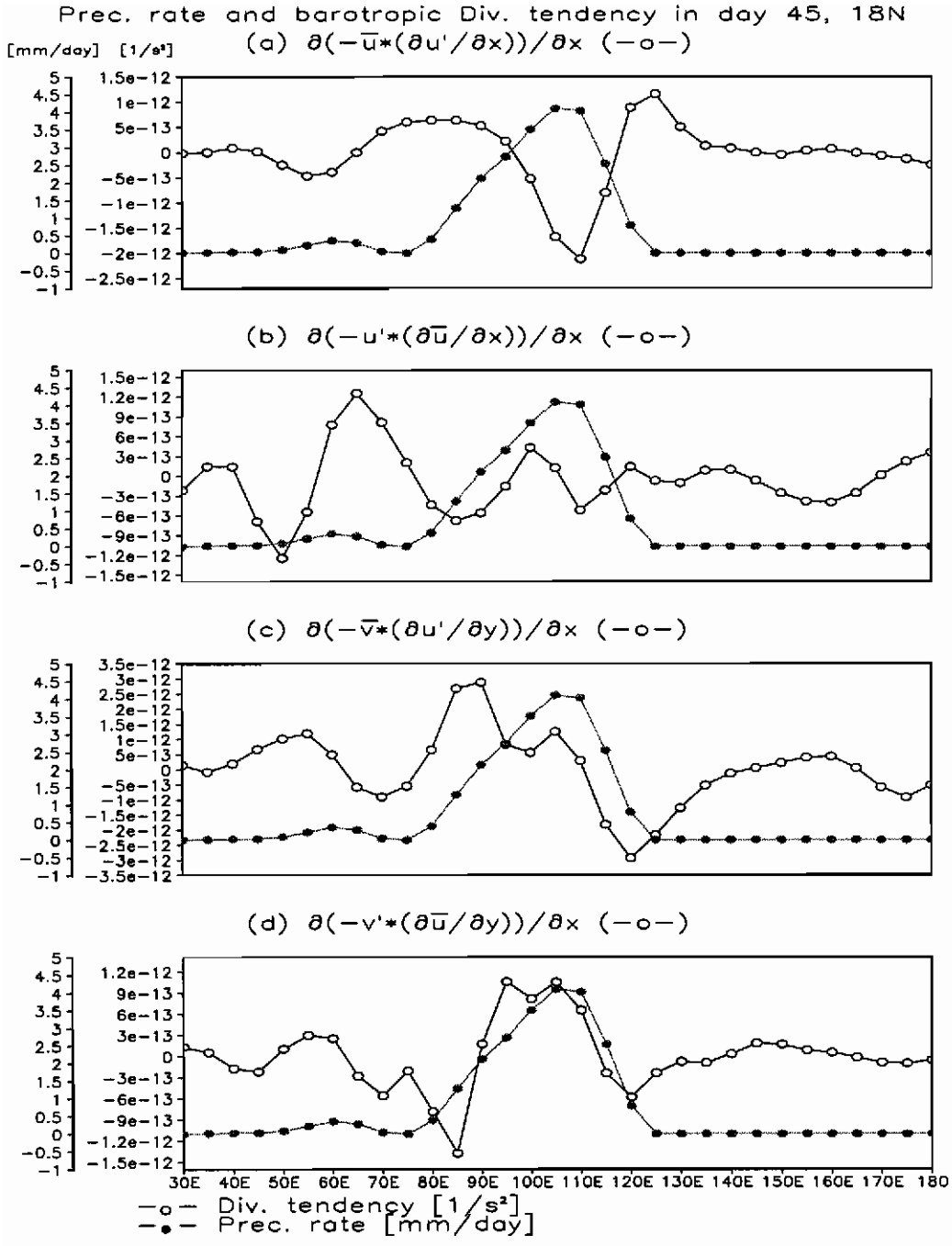

Figure 4.9: Longitudinal variation of precipitation rate (-•-), along with (a) $\frac{\partial}{\partial x}\left(-\overline{u}\,\frac{\partial u'}{\partial x}\right)^{+}$ (-o-), (b) $\frac{\partial}{\partial x}\left(-u'\,\frac{\partial \overline{u}}{\partial x}\right)^{+}$ (-o-), (c) $\frac{\partial}{\partial x}\left(-\overline{v}\,\frac{\partial u'}{\partial y}\right)^{+}$ (-o-), (d) $\frac{\partial}{\partial x}\left(-v'\,\frac{\partial \overline{u}}{\partial y}\right)^{+}$ (-o-), (e) $\frac{\partial}{\partial x}\left(-\omega'\,\frac{\partial \overline{u}}{\partial p}\right)^{+}$ (-o-), (f) $\frac{\partial}{\partial x}\left(-\overline{\omega}\,\frac{\partial u'}{\partial p}\right)^{+}$ (-o-), (g) $\frac{\partial}{\partial x}\left(\beta y v'^{+}\right)$ (-o-), and (h) $\frac{\partial}{\partial x}\left(-\frac{\partial \phi'^{+}}{\partial x}\right)$ (-o-) along 18N on day 45.

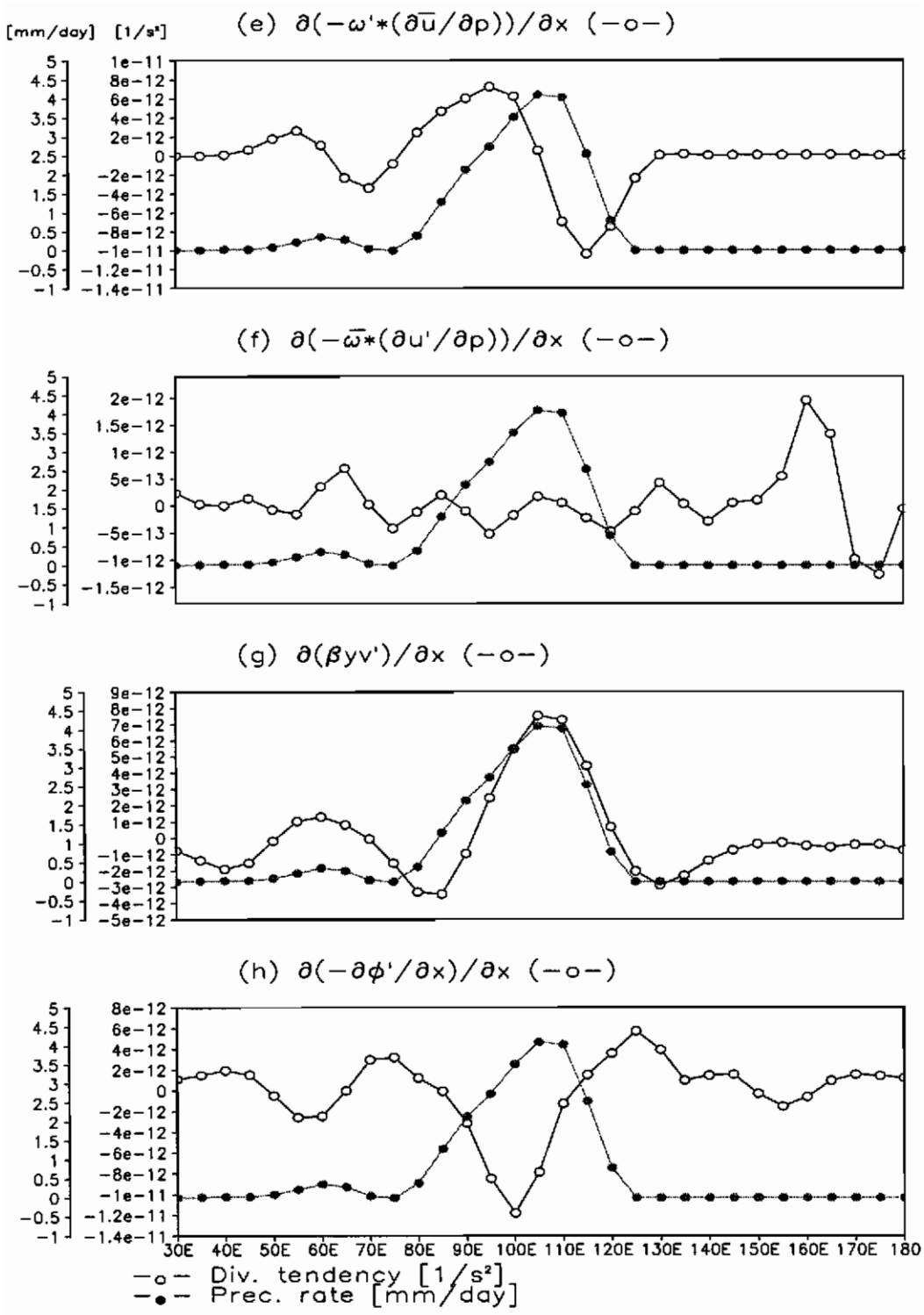

Figure 4.9: (Continued).

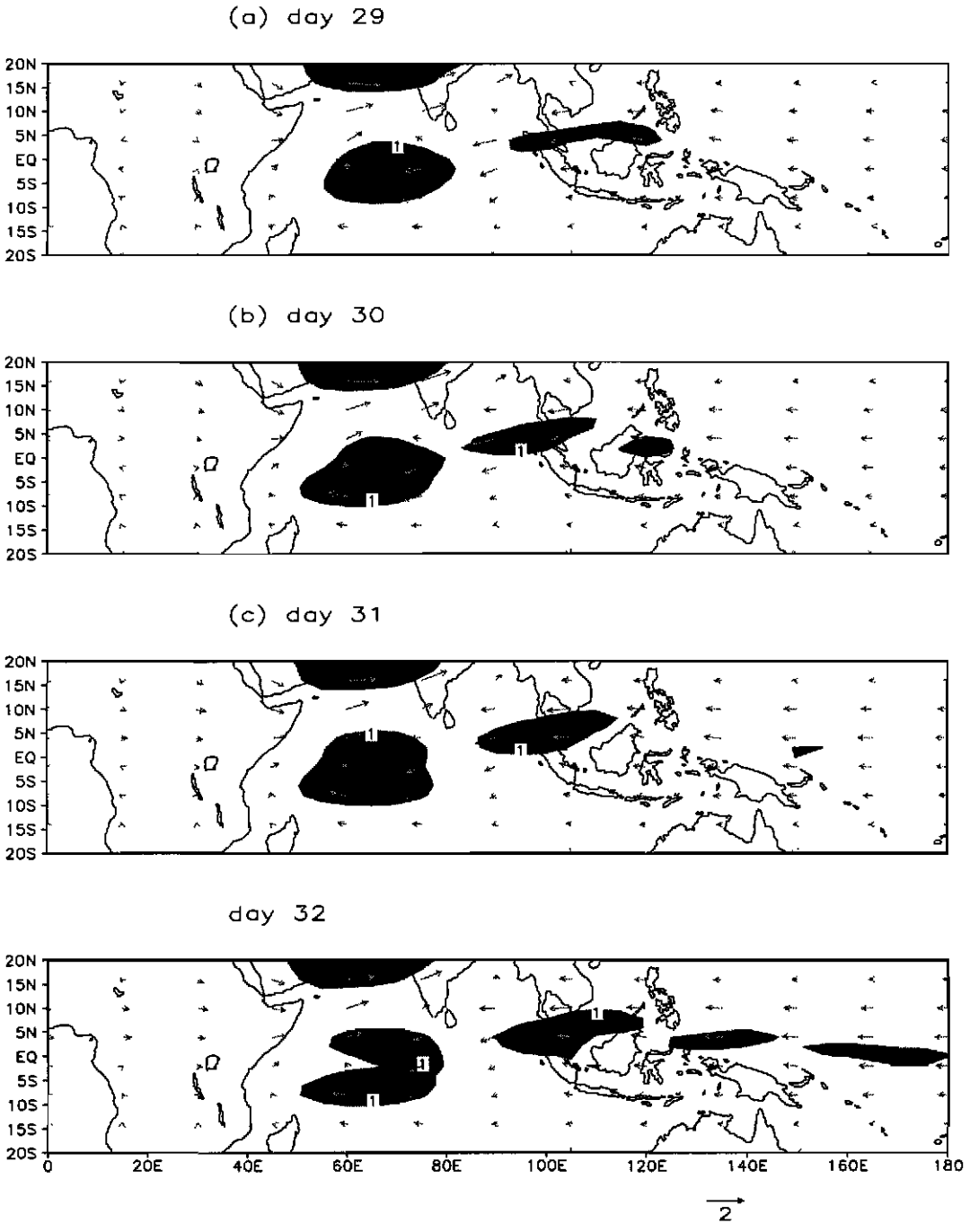

Figure 4.10: Sequential maps for the lower-tropospheric winds and precipitation rate (shaded > 0.1mm/day) in 3D model without interactive SST on (a) day 29, (b) day30, (c) day 31, (d) day 32, (e) day 33, (f) day 34, (g) day 35, and (h) day 38.

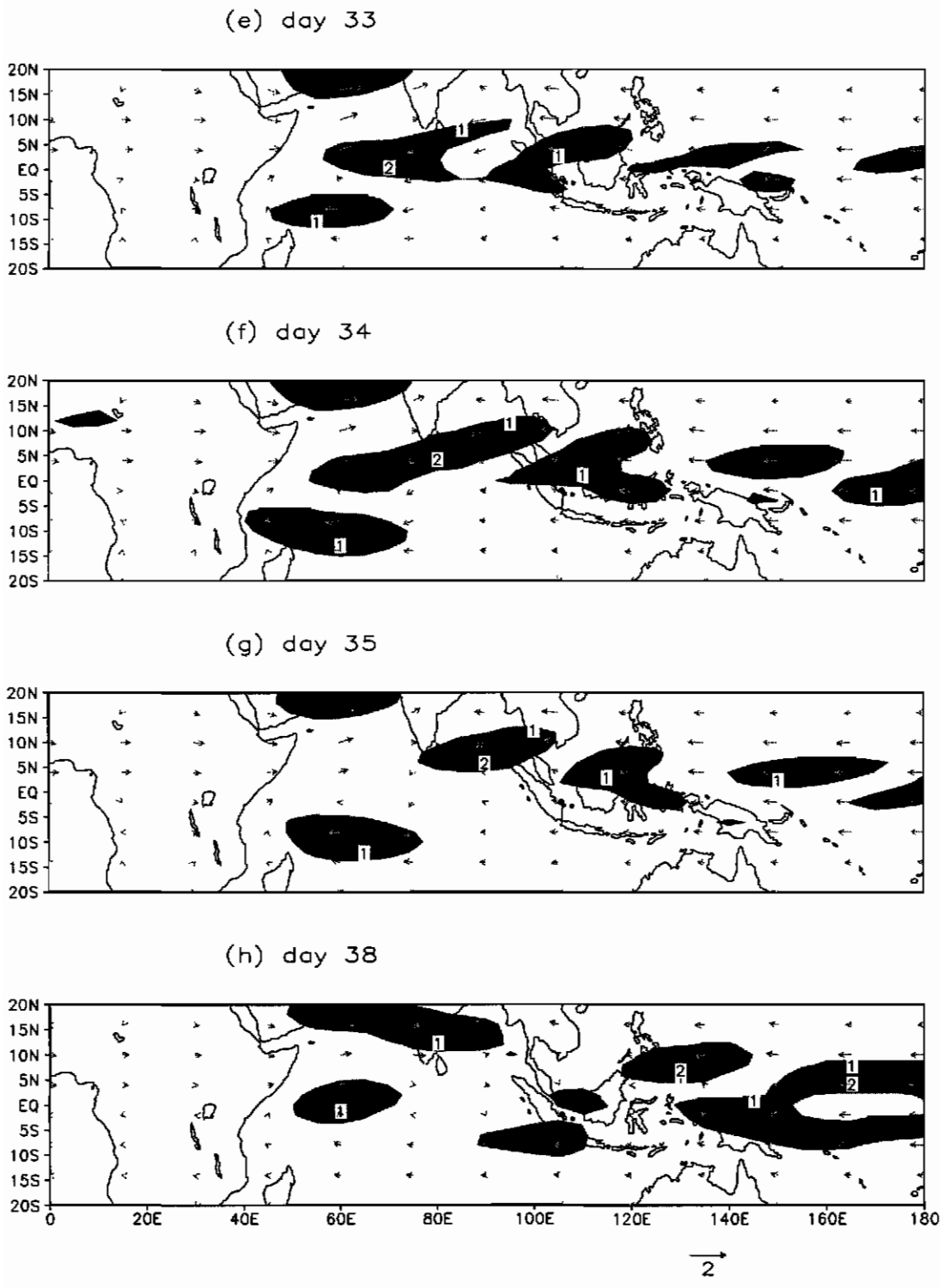

Figure 4.10: (Continued).

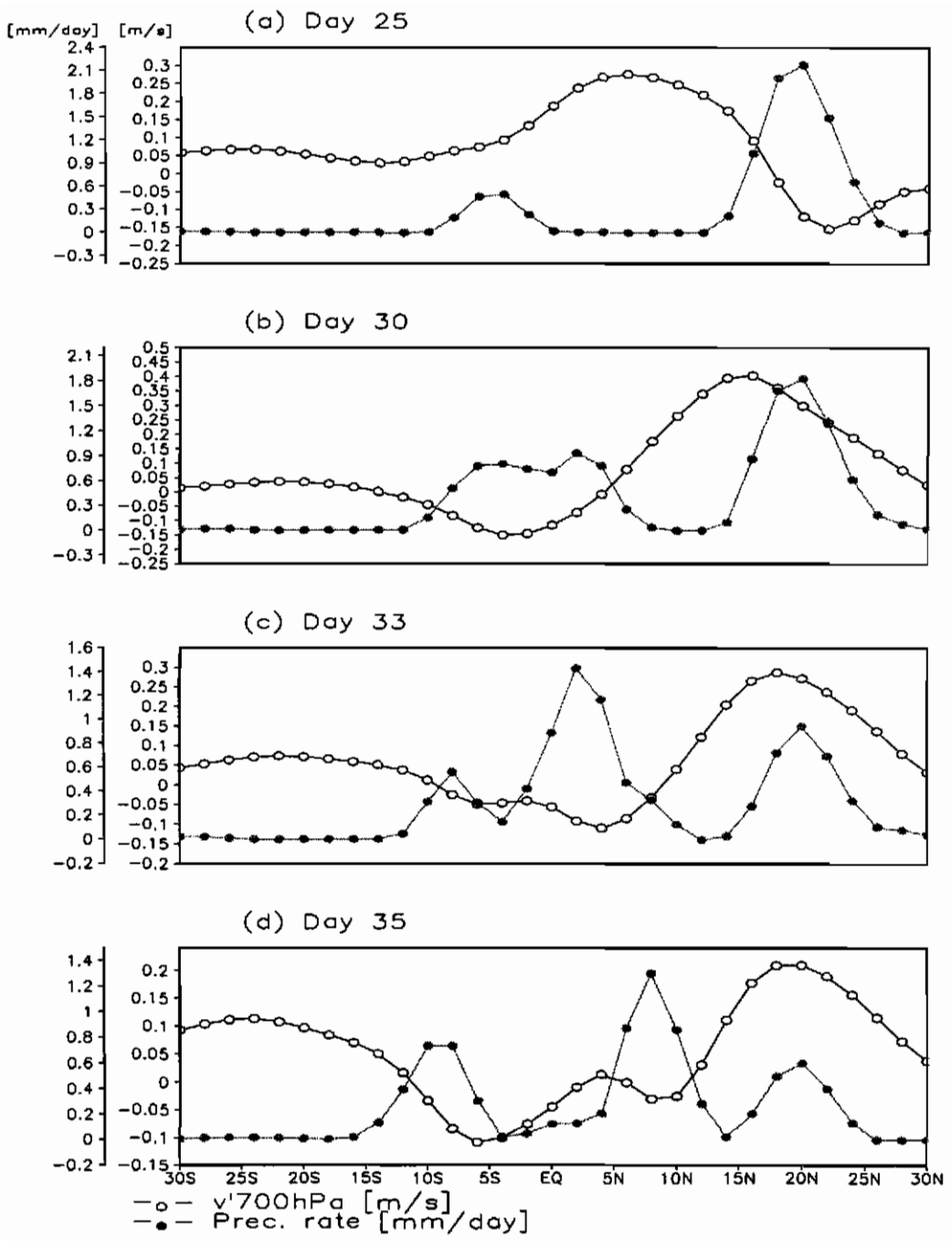

Figure 4.11: Zonally averaged (60-100E) precipitation rate (-•-), and low-level meridional winds (-o-) from 3D model on (a) day 25, (b) day 30, (c) day 33, (d) day 35,(e) day 44, (f) day 50, (g) day 59, (h) day 60, (i) day 61, (j) day 62, and (k) day 66.

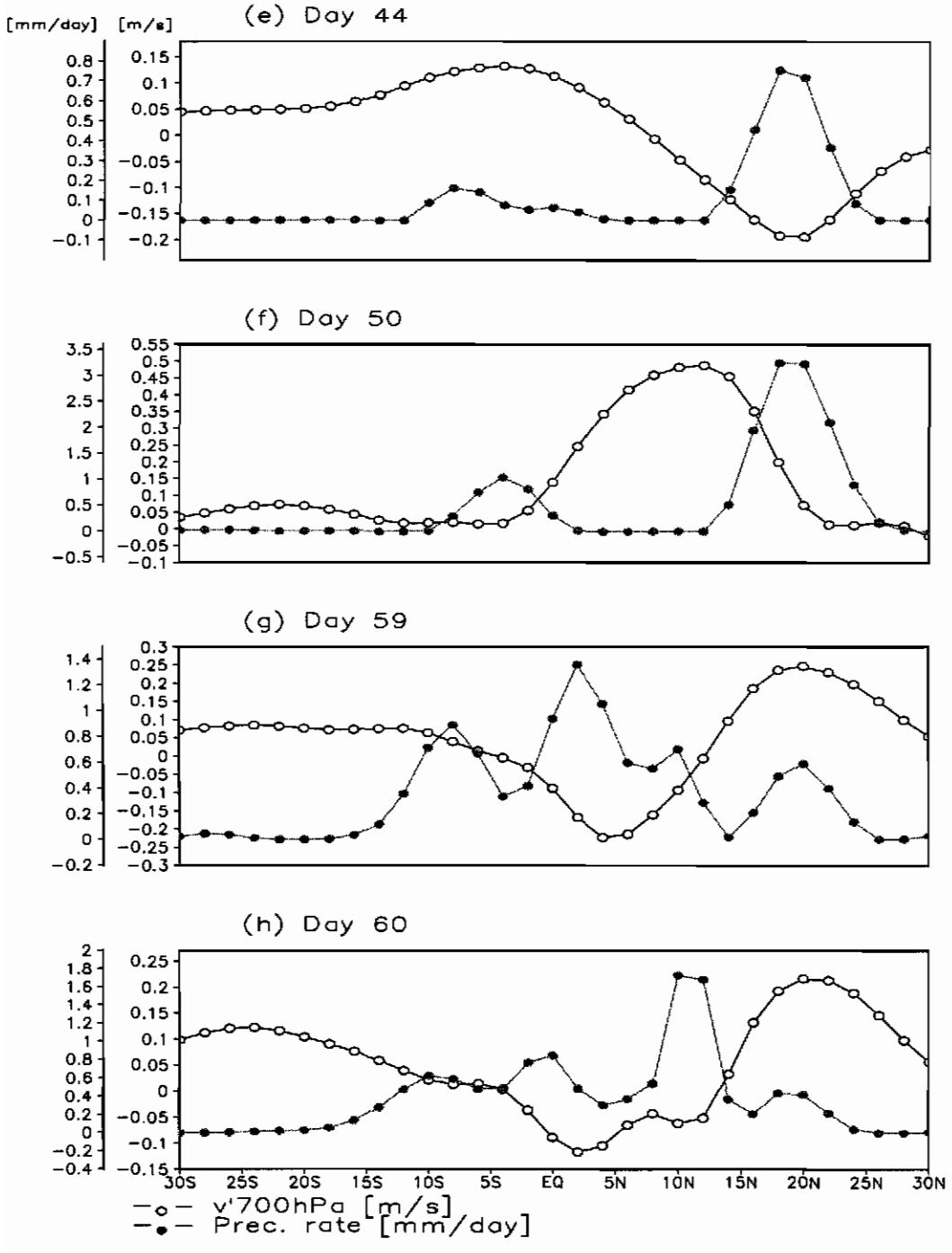

Figure 4.11: (Continued).

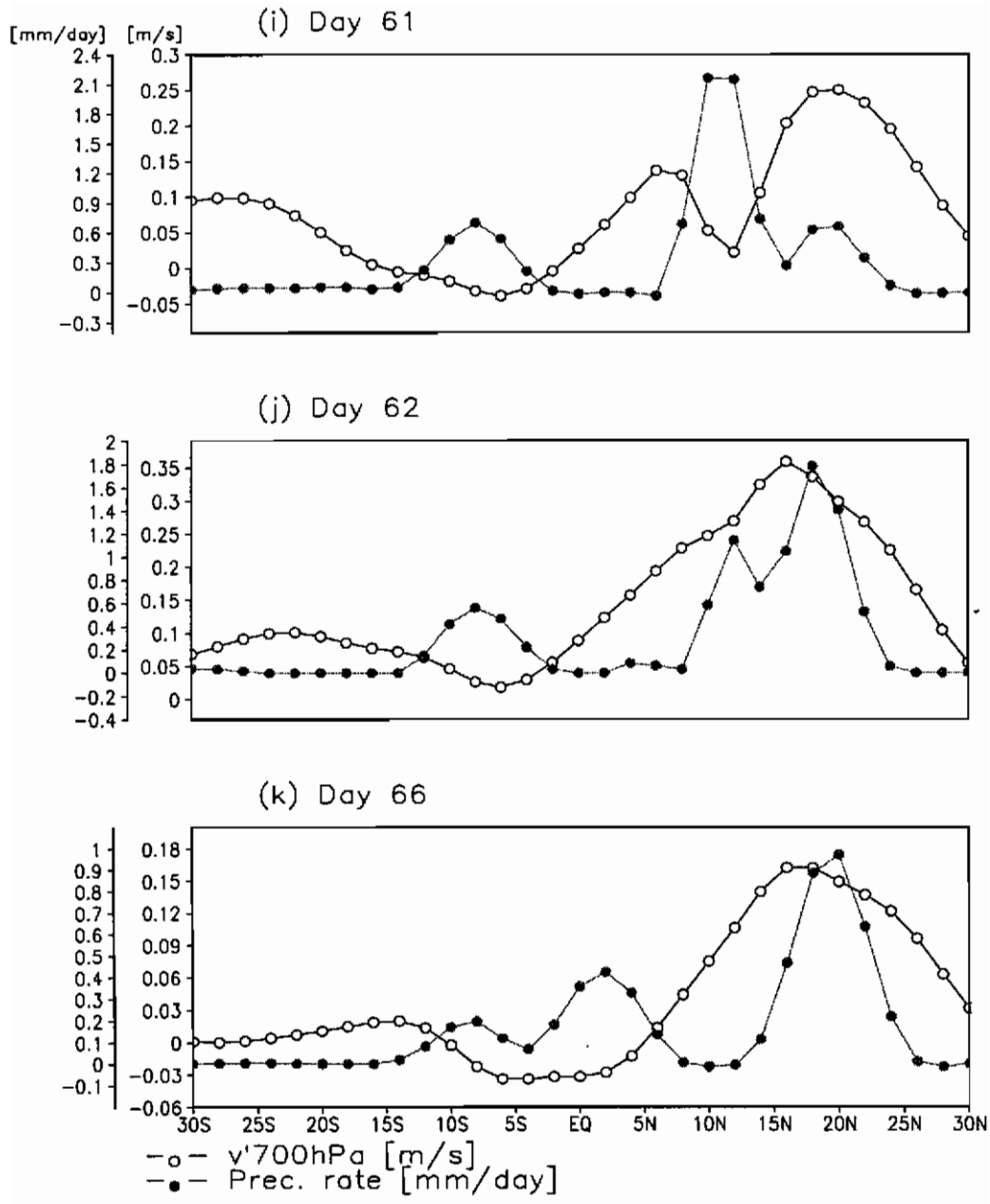

Figure 4.11: (Continued).

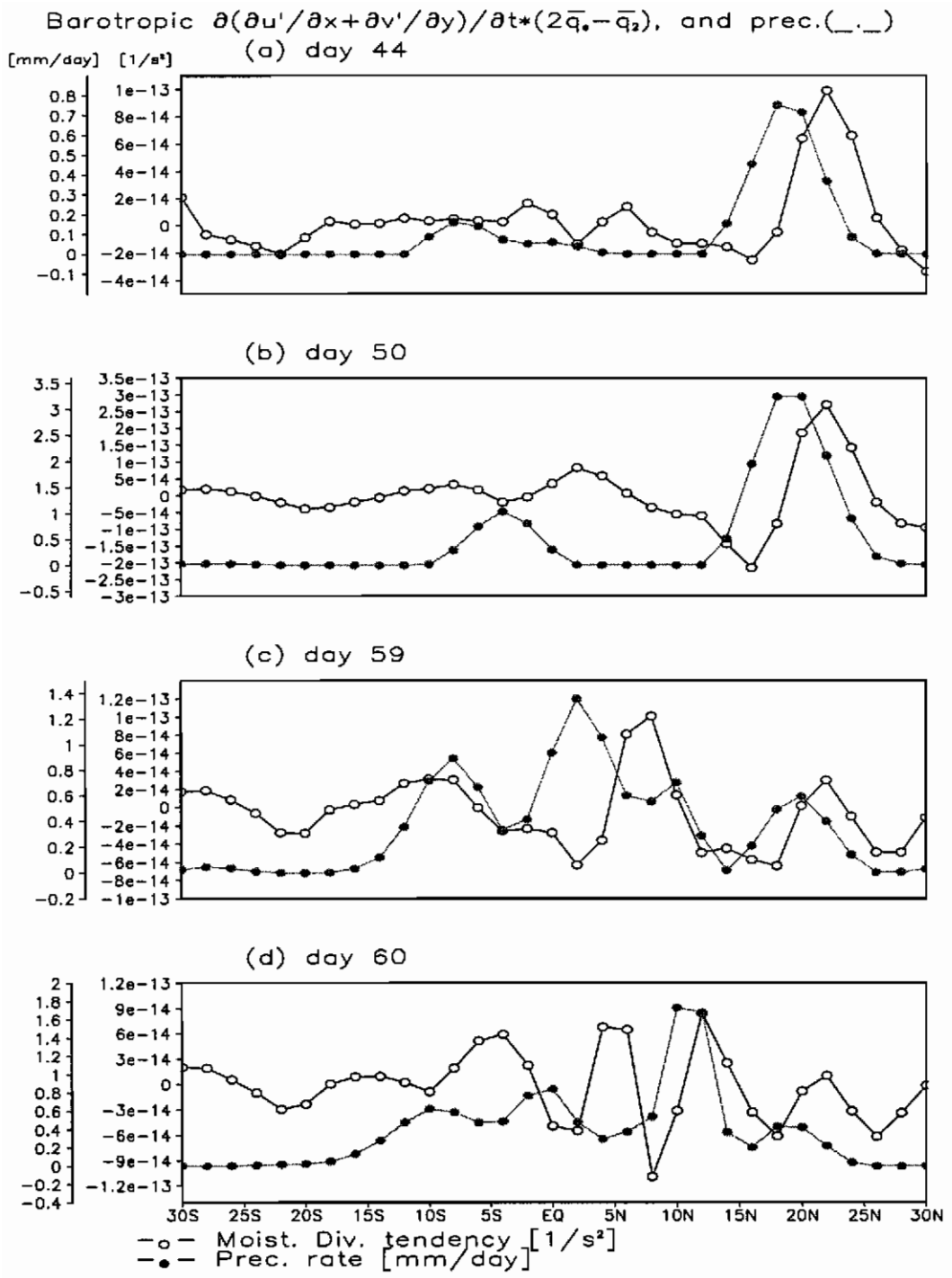

Figure 4.12: Zonally averaged (60-100E) precipitation rate (-•-) and $\frac{\partial}{\partial t}(\frac{\partial u'^{+}}{\partial x}+\frac{\partial v'^{+}}{\partial y})(2\overline{q}_e-\overline{q}_2)$ (-∘-) on (a) day 44, (b) day 50, (c) day 59, (d) day 60, (e) day 61, (f) day 62, and (g) day 66.

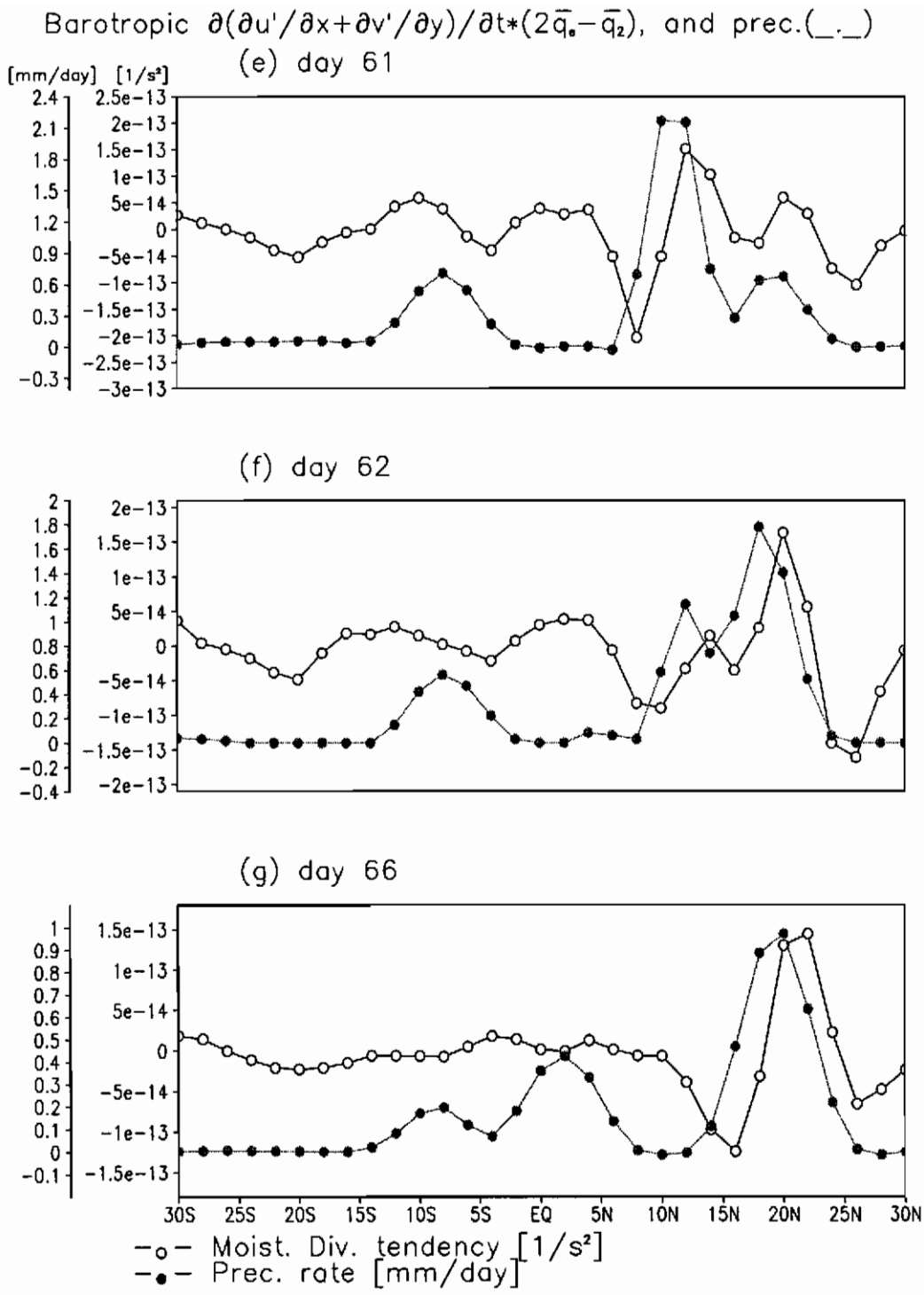

Figure 4.12: (Continued).

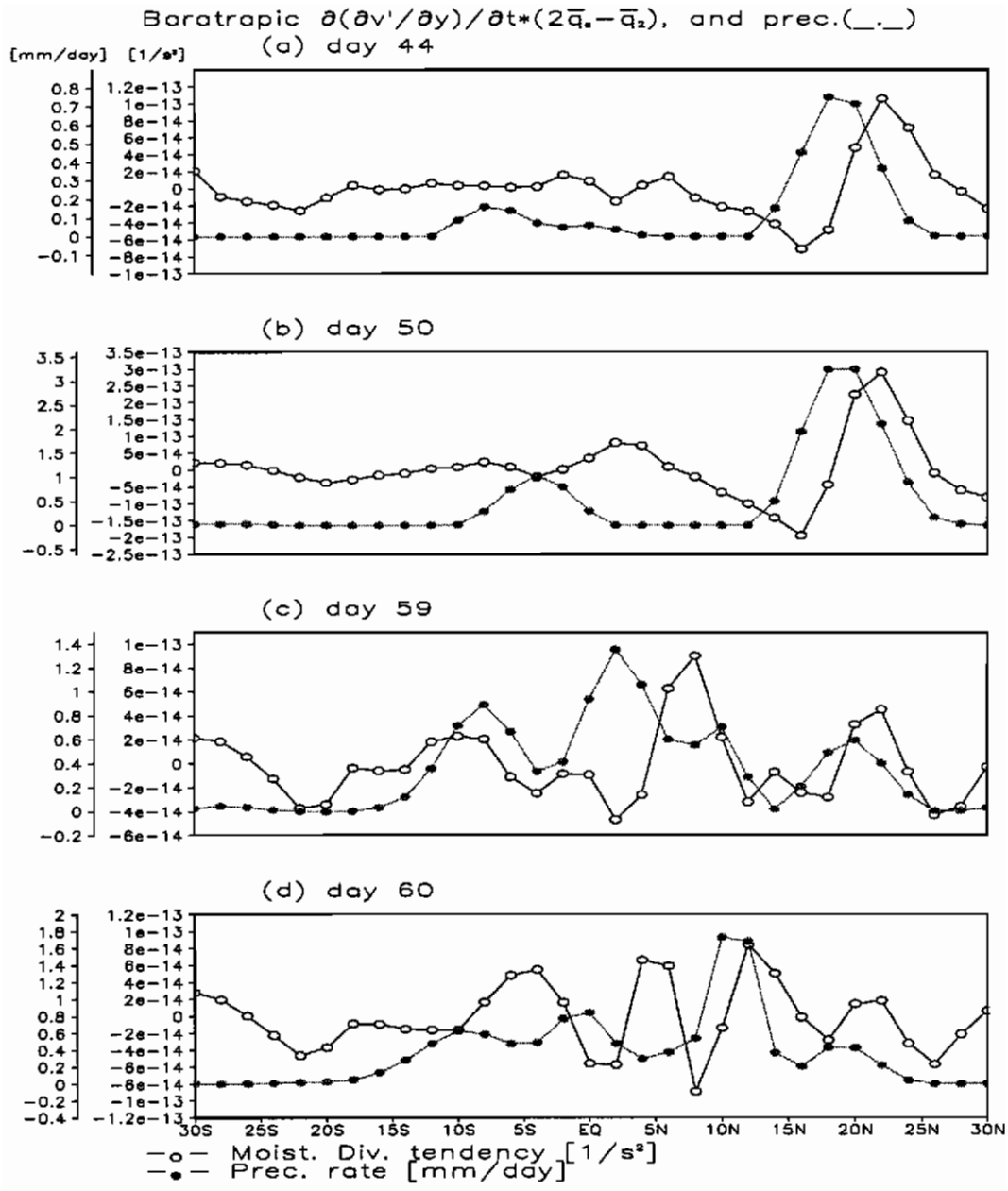

Figure 4.13: Zonally averaged (60-100E) precipitation rate (-•-) and $\frac{\partial}{\partial t}(\frac{\partial v'^{+}}{\partial y})(2\overline{q}_e - \overline{q}_2)$ (-o-) on (a) day 44, (b) day 50, (c) day 59, (d) day 60, (e) day 61, (f) day 62, and (g) day 66.

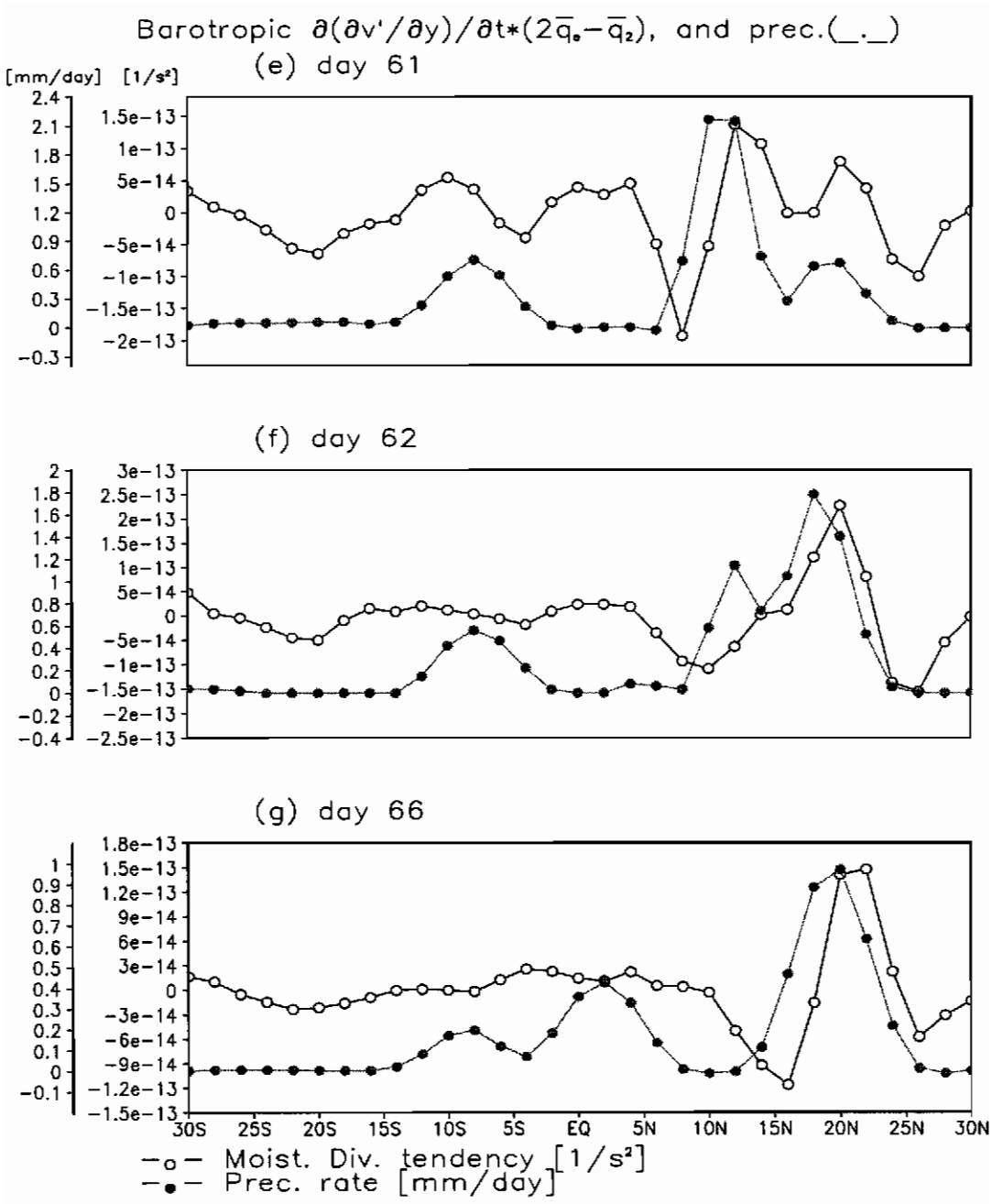

Figure 4.13: (Continued).

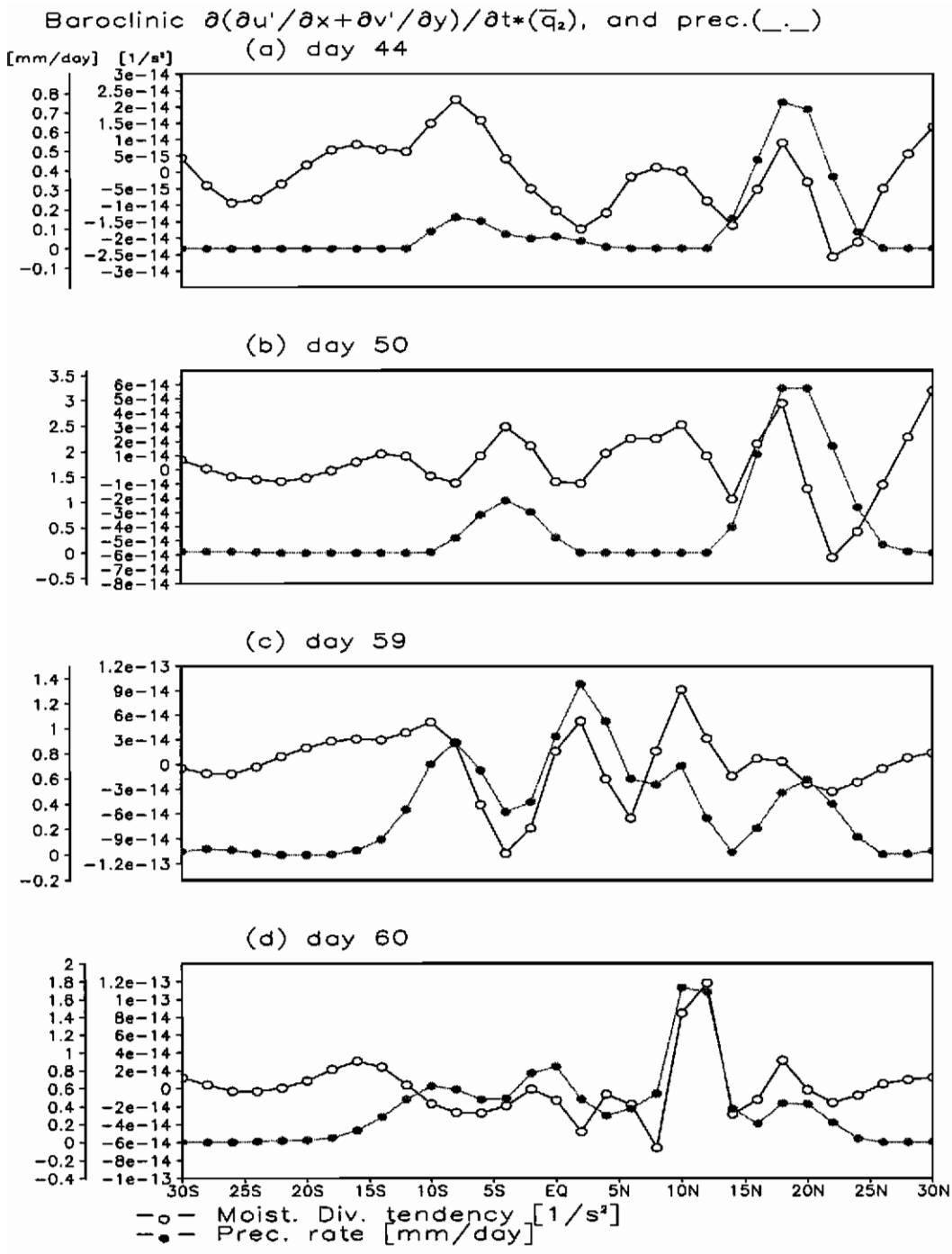

Figure 4.14: Zonally averaged (60-100E) precipitation rate (-•-) and $\frac{\partial}{\partial t}(\frac{\partial u'^{-}}{\partial x}+\frac{\partial v'^{-}}{\partial y})\overline{q}_2$ (-∘-) on (a) day 44, (b) day 50, (c) day 59, (d) day 60, (e) day 61,and (f) day 62, (g) day 66, from 3D model.

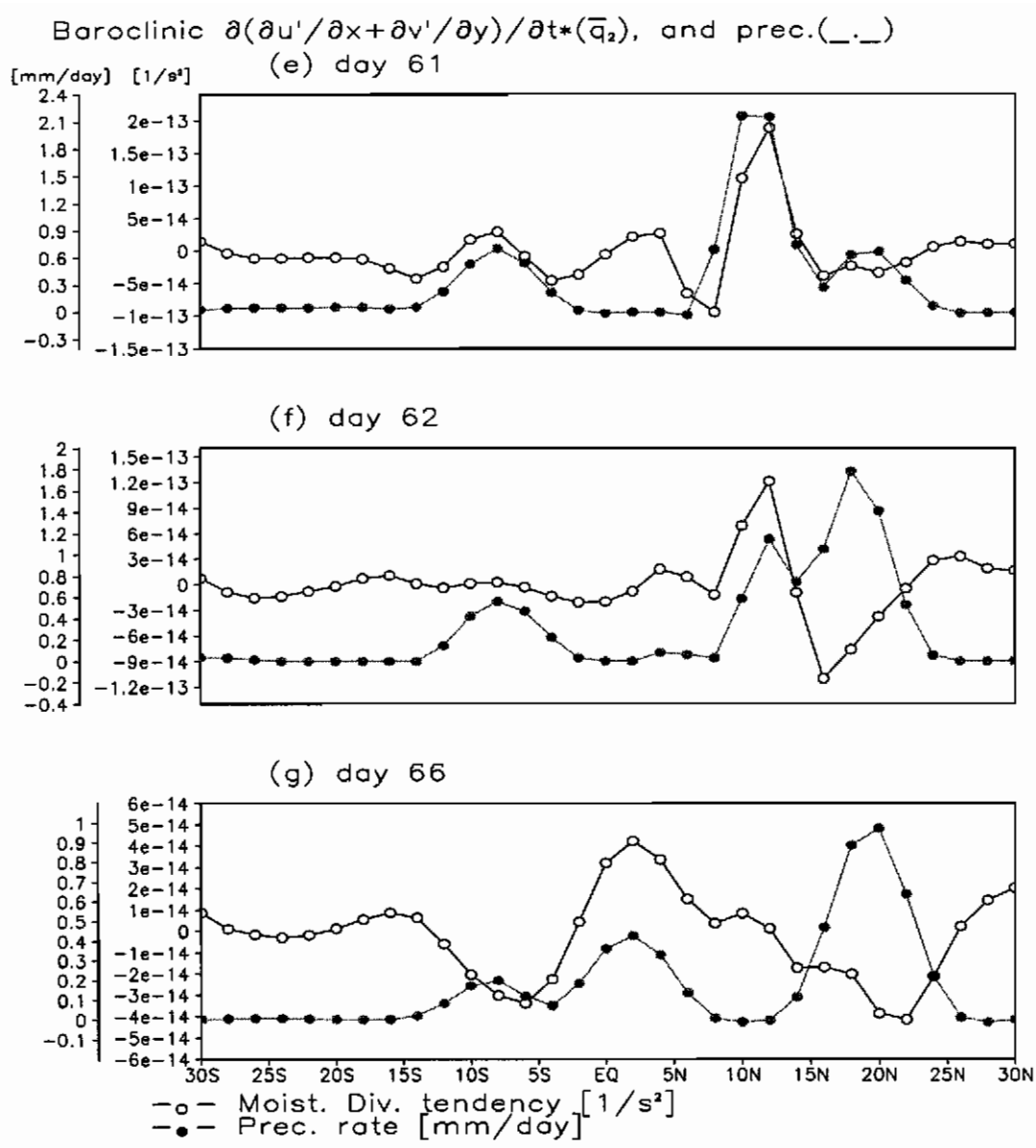

Figure 4.14: (Continued).

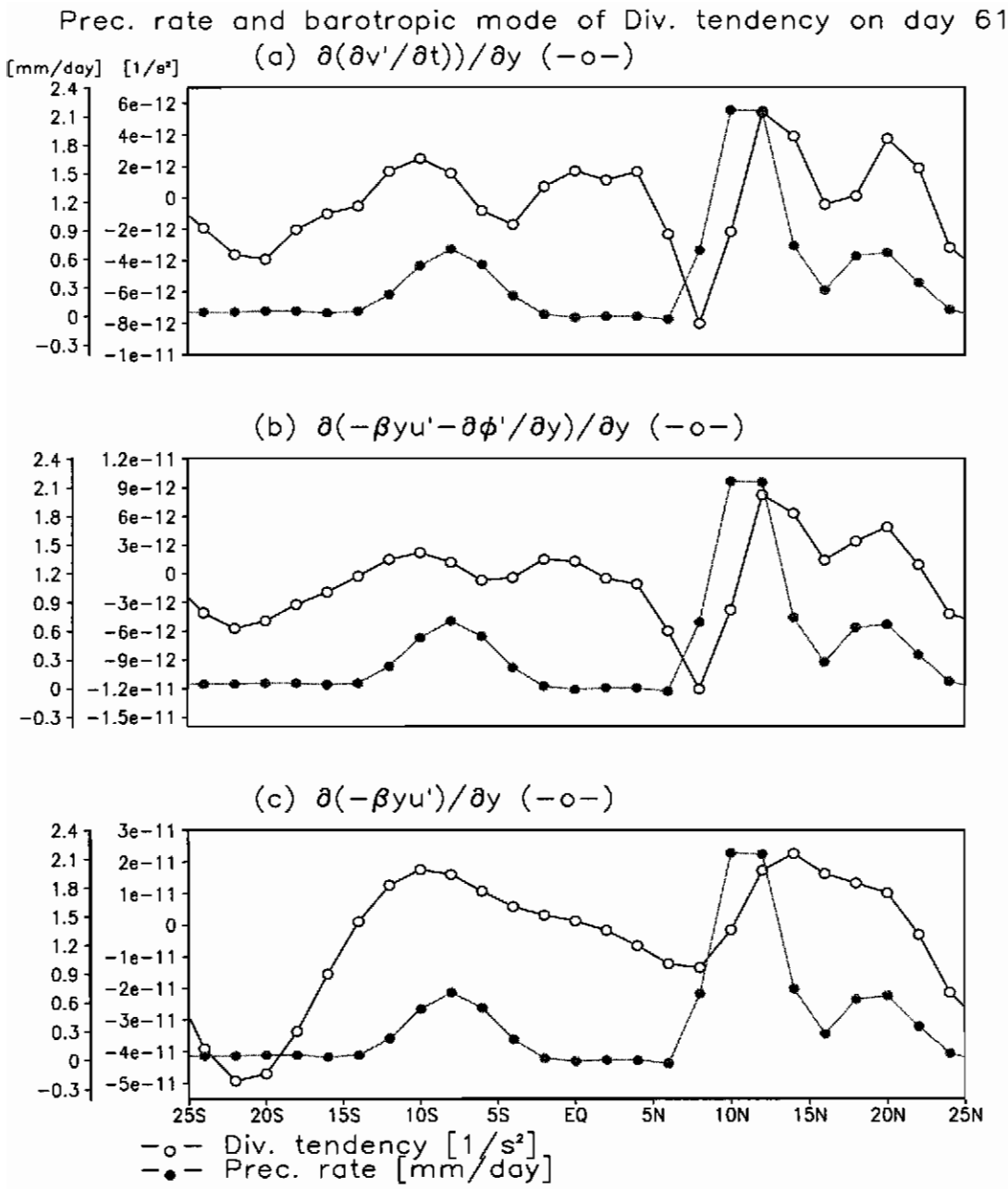

Figure 4.15: Zonally averaged (60-100E) precipitation rate (-•-) and (a) $\frac{\partial}{\partial y}\frac{\partial v'^{+}}{\partial t}$ (-o-), (b) $\frac{\partial}{\partial y}(-\beta y u'^{+} - \frac{\partial \phi'^{+}}{\partial y})$ (-o-), and (c) $\frac{\partial}{\partial y}(-\beta y u'^{+})$ (-o-) on day 61.

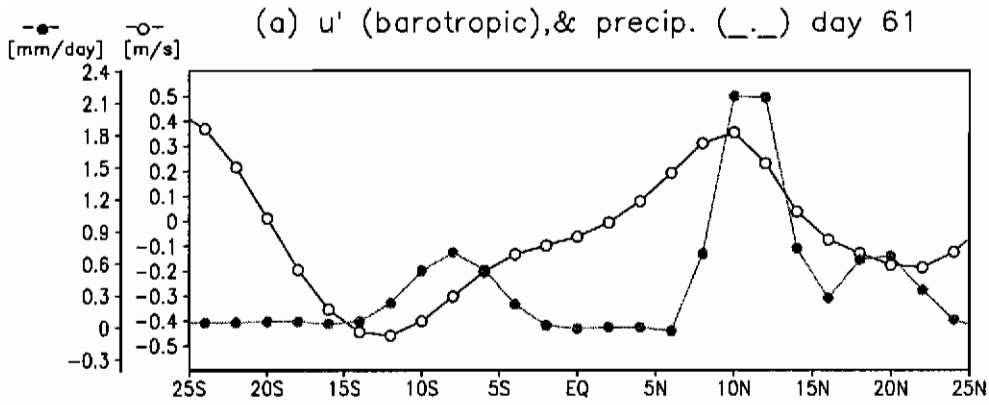

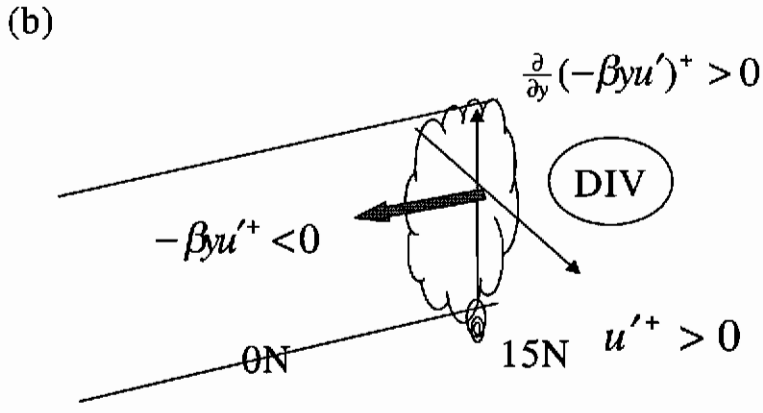

Figure 4.16: (a) Zonally averaged (60-100E) barotropic u′ (u'^{+}, -o-) and precipitation rate (-•-) on day 61, (b) conceptual model for the barotropic divergence [i.e. $\frac{\partial}{\partial y}(-\beta y u'^{+}) > 0$] to the north of the convection forcing by the barotropic Coriolis force (i.e. $-\beta y u'^{+} < 0$) at the center of the convection at 10N.

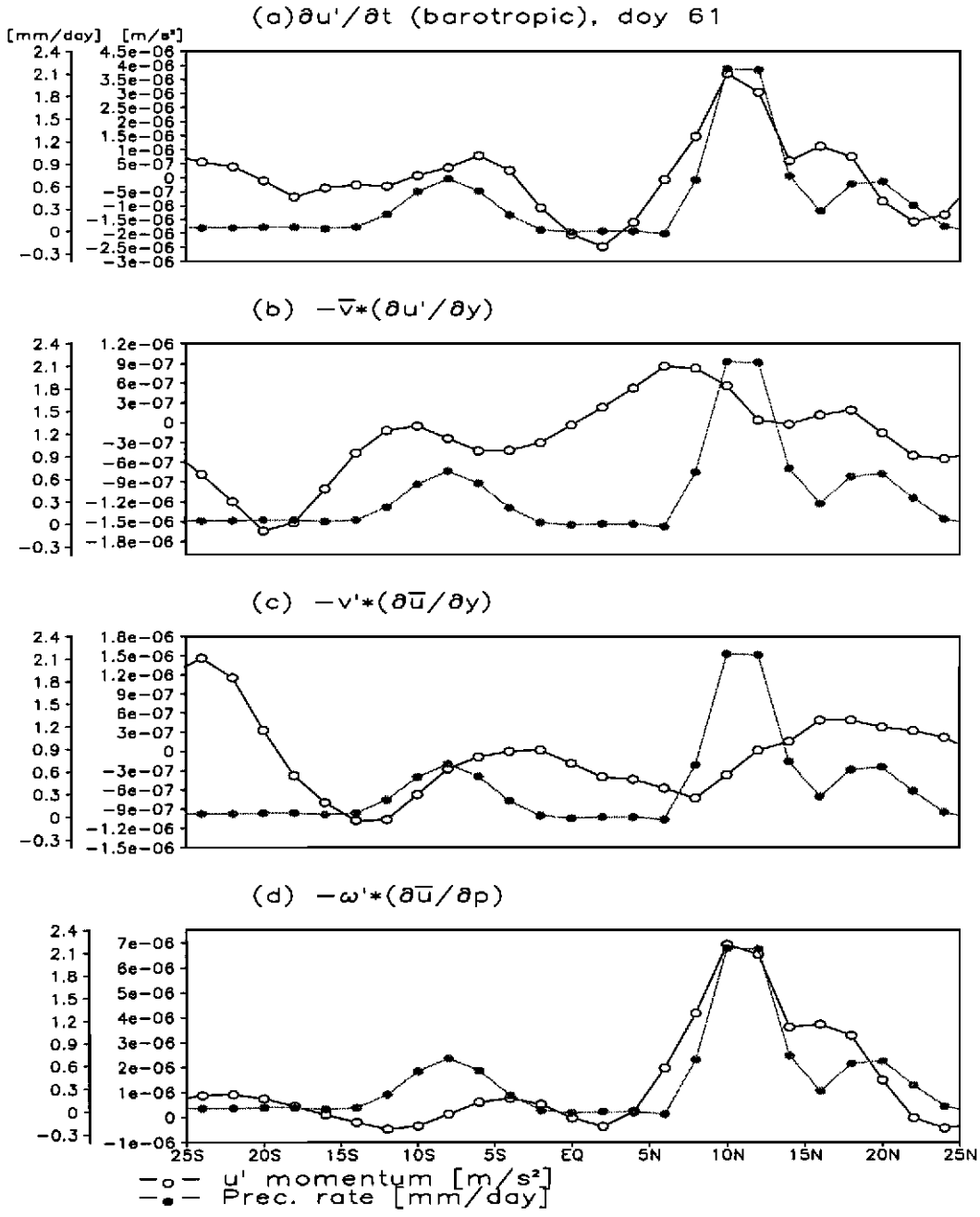

Figure 4.17: Zonally averaged (60-100E) precipitation rate (-•-) and barotropic mode of momentum equation for zonal wind anomaly on day 61 (-°-).

(a) $\frac{\partial u'^{+}}{\partial t}$, (b) $(-\overline{v}\frac{\partial u'}{\partial y})^{+}$, (c) $(-v'\frac{\partial \overline{u}}{\partial y})^{+}$, (d) $(-\omega'\frac{\partial \overline{u}}{\partial p})^{+}$, (e) $(-\overline{\omega}\frac{\partial u'}{\partial p})^{+}$,

(f) $\beta y v'^{+}$, (g) $-\frac{\partial \phi'^{+}}{\partial x}$, (h) $-\frac{\partial \phi'^{+}}{\partial x}+\beta y v'^{+}$, (i) $(-\overline{u}\frac{\partial u'}{\partial x})^{+}$, and (j) $(-u'\frac{\partial \overline{u}}{\partial x})^{+}$.

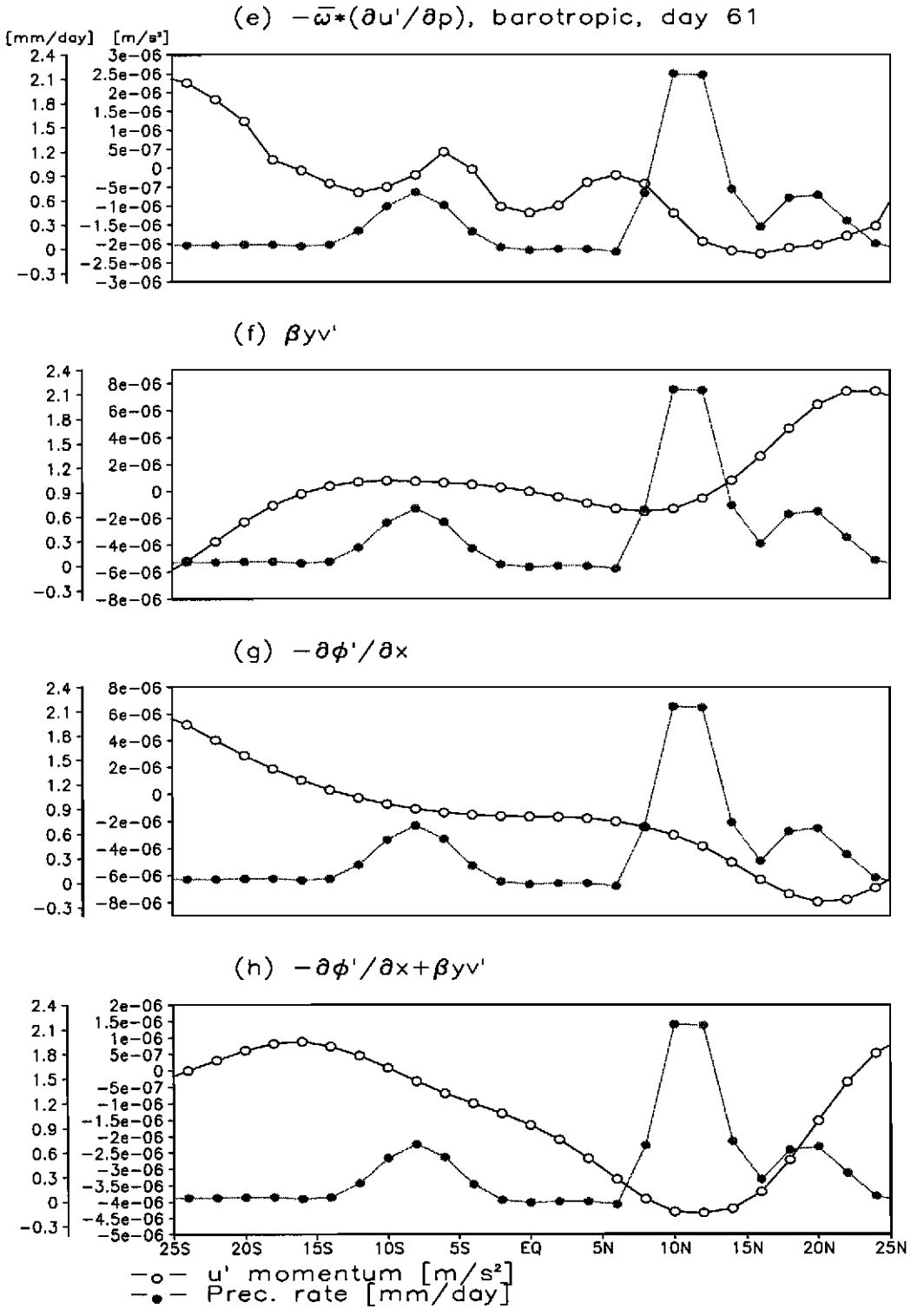

Figure 4.17: (Continued).

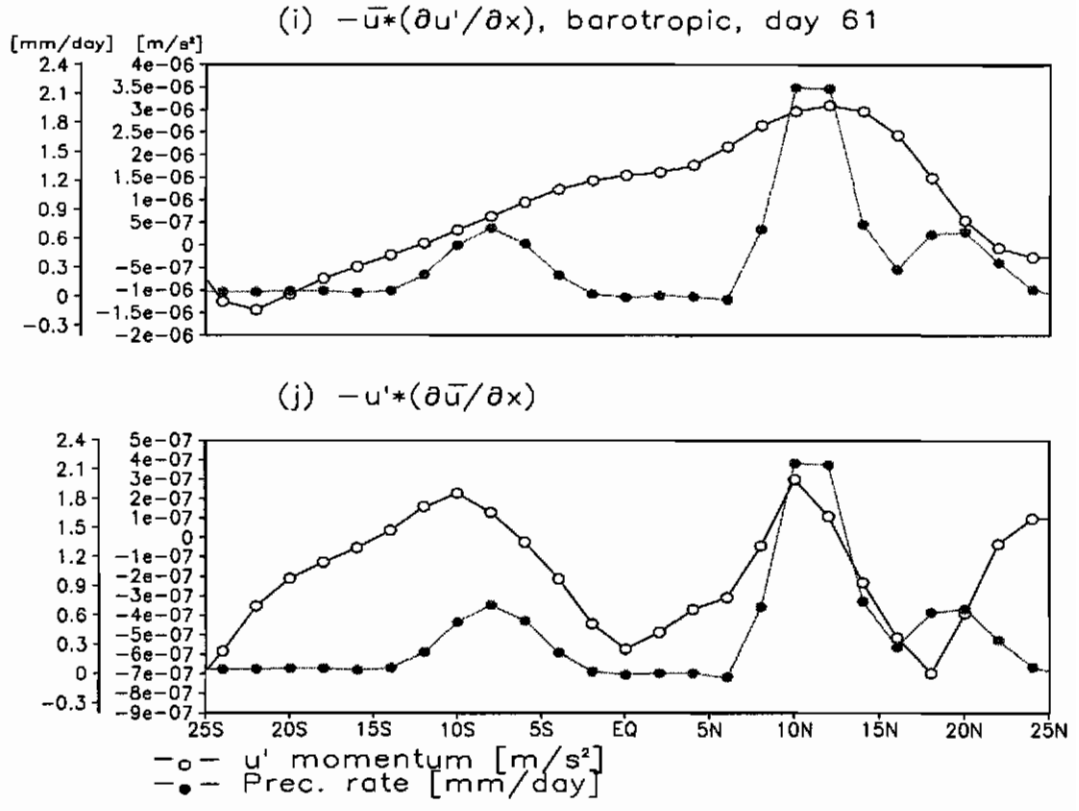

Figure 4.17: (Continued).

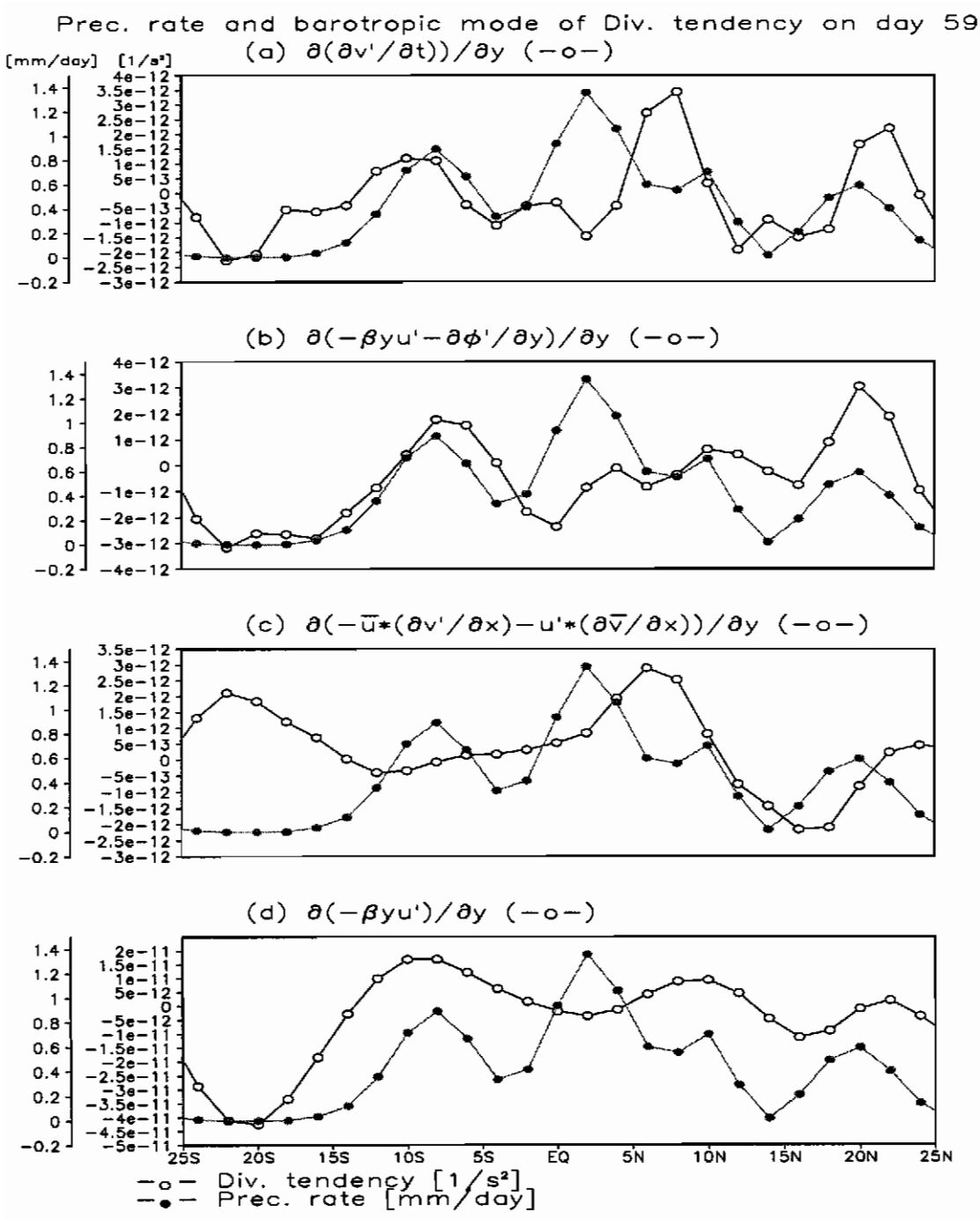

Figure 4.18: Zonally averaged (60-100E) precipitation rate (-•-) and (a) $\frac{\partial}{\partial y}\frac{\partial v'^{+}}{\partial t}$, (b) $\frac{\partial}{\partial y}(-\beta y u'^{+} - \frac{\partial \phi'^{+}}{\partial y})$, (c) $\frac{\partial}{\partial y}\{-(\overline{u}\,\frac{\partial v'}{\partial x})^{+} - (u'\,\frac{\partial \overline{v}}{\partial x})^{+}\}$, and (d) $\frac{\partial}{\partial y}(-\beta y u'^{+})$ on day 59 (-o-).

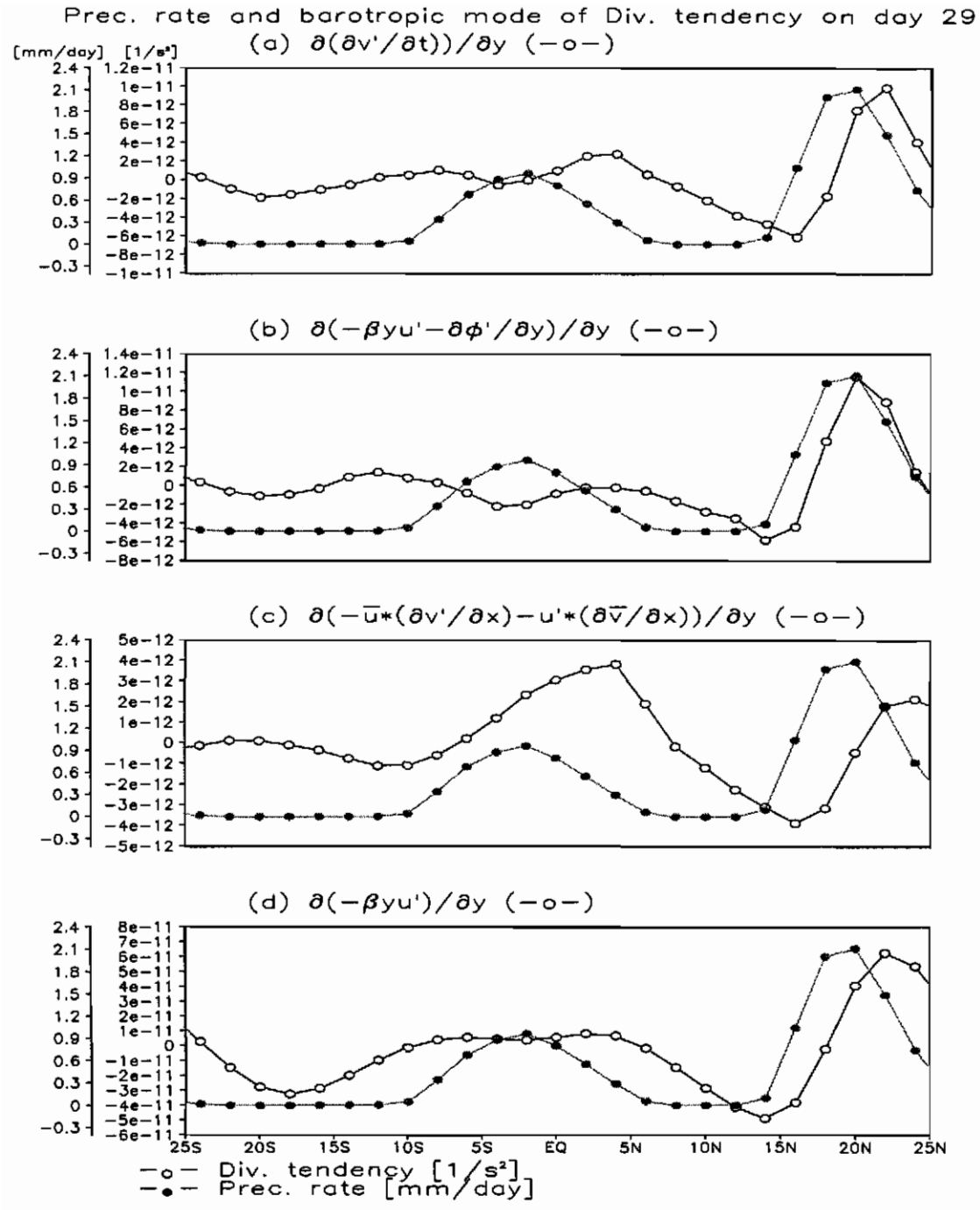

Figure 4.19: Zonally averaged (60-100E) precipitation rate (-•-) and (a) $\frac{\partial}{\partial y}\frac{\partial v'^{+}}{\partial t}$, (b) $\frac{\partial}{\partial y}(-\beta y u'^{+} - \frac{\partial \phi'^{+}}{\partial y})$, (c) $\frac{\partial}{\partial y}\{-(\overline{u}\,\frac{\partial v'}{\partial x})^{+} - (u'\,\frac{\partial \overline{v}}{\partial x})^{+}\}$, and (d) $\frac{\partial}{\partial y}(-\beta y u'^{+})$ on day 29 (-o-).

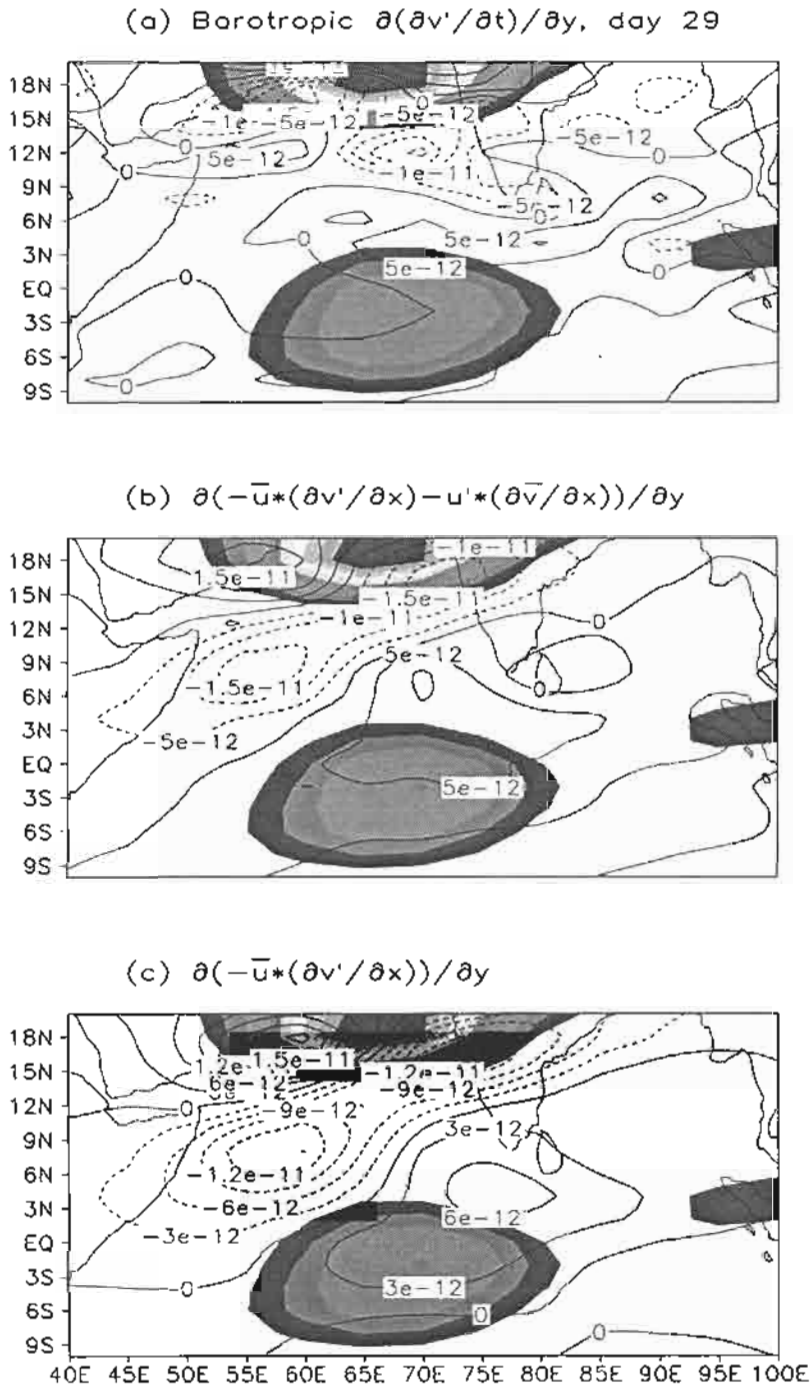

Figure 4.20: Latitude-longitude variation of precipitation rate (shaded >0.1mm/day) and (a) $\frac{\partial}{\partial y}\frac{\partial v'^{+}}{\partial t}$, (b) $\frac{\partial}{\partial y}\{-(\overline{u}\,\frac{\partial v'}{\partial x})^{+} - (u'\,\frac{\partial \overline{v}}{\partial x})^{+}\}$, and (c) $\frac{\partial}{\partial y}(-\overline{u}\,\frac{\partial v'}{\partial x})^{+}$ on day 29.

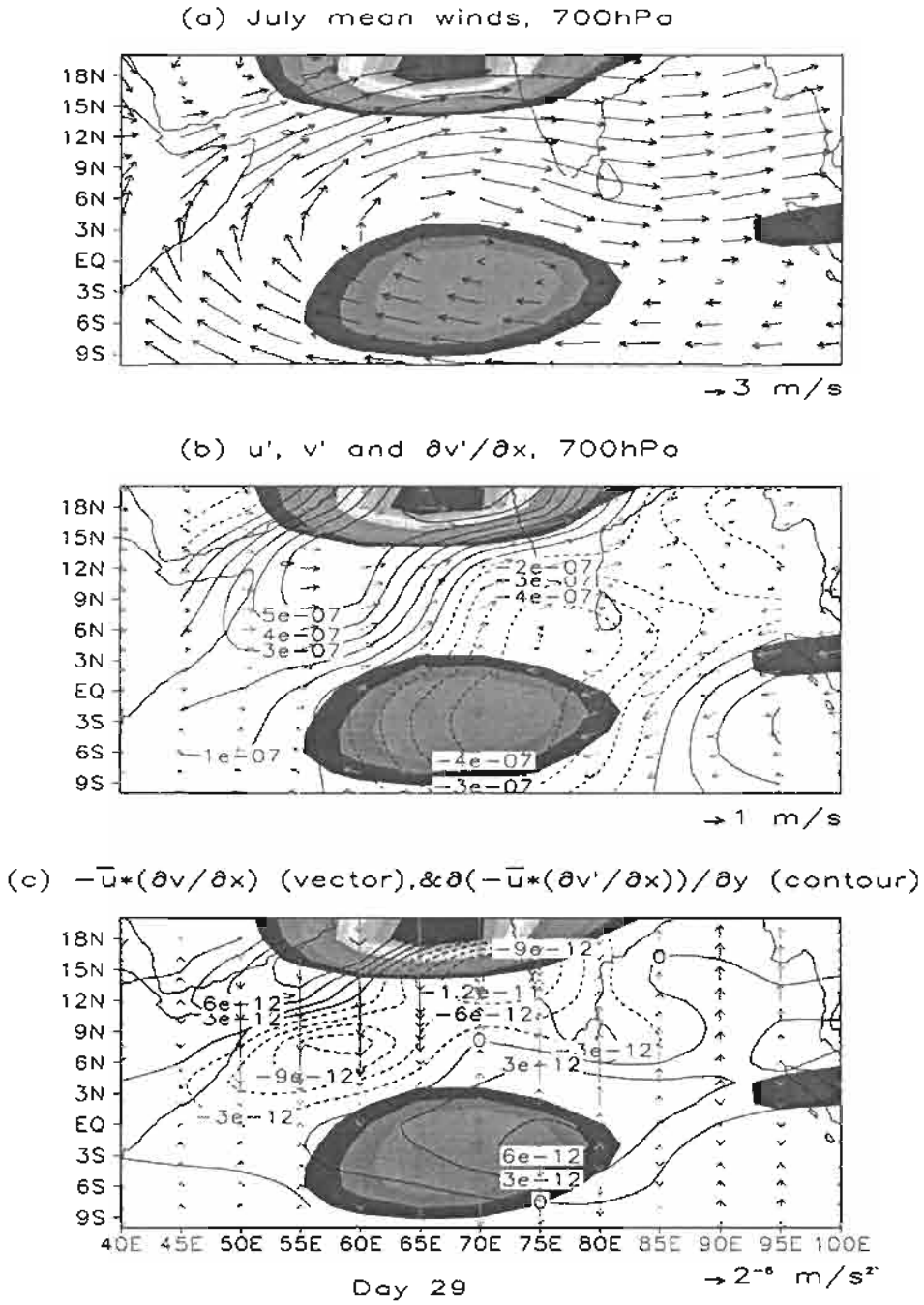

Figure 4.21: Latitude-longitude variation of precipitation rate (shaded >0.1mm/day) and (a) July-mean winds at 850hPa, (b) wind anomalies (vector) and $\frac{\partial v'}{\partial x}$ (contour) at 700hPa, and (c) $-\overline{u}\frac{\partial v'}{\partial x}$ (vector) and $\frac{\partial}{\partial y}(-\overline{u}\frac{\partial v'}{\partial x})$ (contour) at 700hPa.

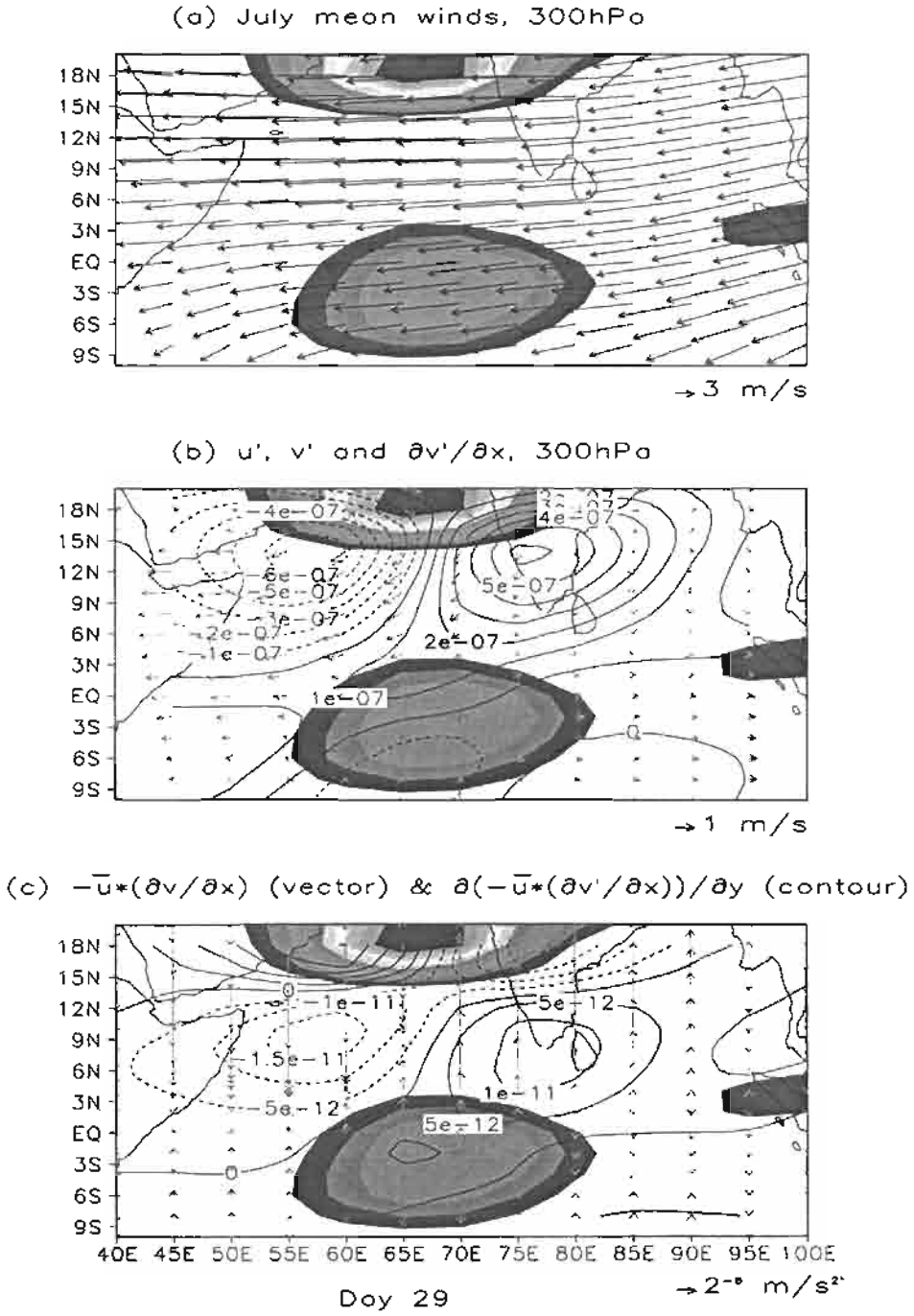

Figure 4.22: Latitude-longitude variation of precipitation rate (shaded >0.1mm/day) and (a) July-mean winds at 200hPa, (b) wind anomalies (vector) and $\frac{\partial v'}{\partial x}$ (contour) at 300hPa, and (c) $-\overline{u}\,\frac{\partial v'}{\partial x}$ (vector) and $\frac{\partial}{\partial y}(-\overline{u}\,\frac{\partial v'}{\partial x})$ (contour) at 300hPa.

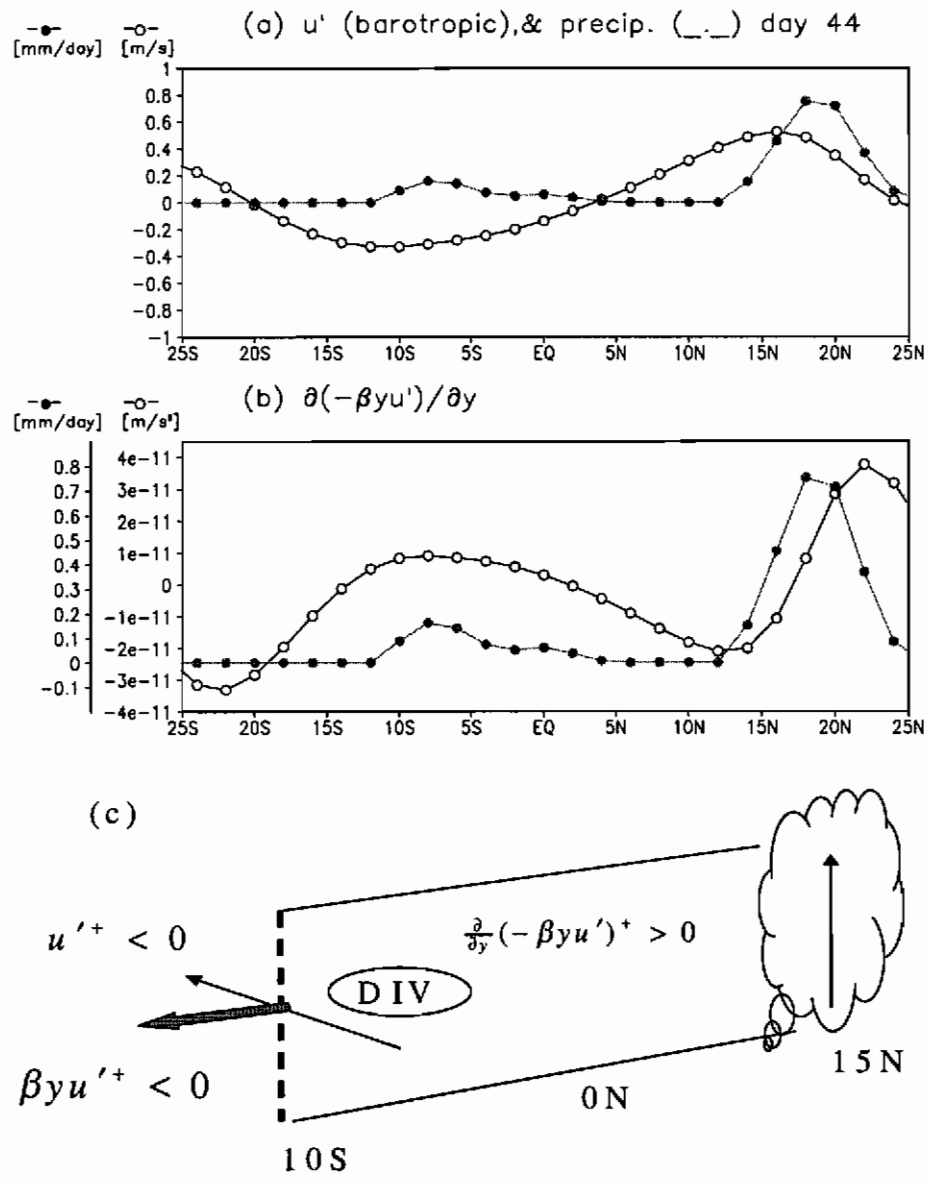

Figure 4.23: (a) Zonally averaged (60-100E) barotropic u′ (u'^{+}, -∘-) and precipitation rate (-•-) on day 44, (b) zonally averaged (60-100E) barotropic divergence [$\frac{\partial}{\partial y}(-\beta y u'^{+})$, -∘-] induced by Coriolis force ($-\beta y u'^{+}$), (c) conceptual model for the barotropic divergence (i.e. $\frac{\partial}{\partial y}(-\beta y u'^{+}) > 0$) to the north of 10S forcing by the barotropic Coriolis force (i.e. $-\beta y u'^{+} < 0$) at 10S.

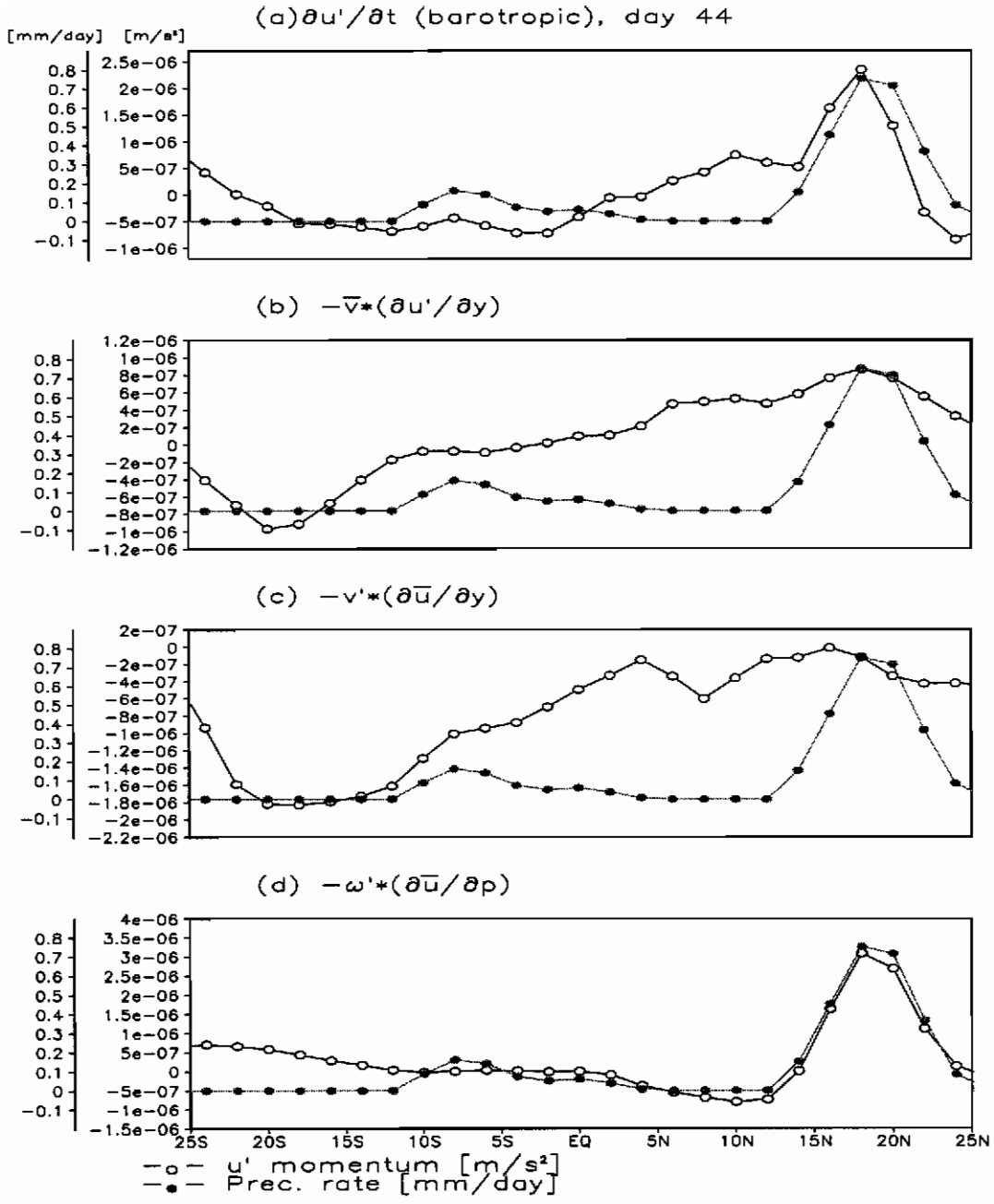

Figure 4.24: Zonally averaged (60-100E) precipitation rate (-•-) and barotropic mode of momentum equation for zonal wind anomaly on day 44 (-∘-).

(a) $\frac{\partial u'^{+}}{\partial t}$, (b) $(-\overline{v}\frac{\partial u'}{\partial y})^{+}$, (c) $(-v'\frac{\partial \overline{u}}{\partial y})^{+}$, (d) $(-\omega'\frac{\partial \overline{u}}{\partial p})^{+}$, (e) $(-\overline{\omega}\frac{\partial u'}{\partial p})^{+}$, (f) $\beta y v'^{+}$, (g) $-\frac{\partial \phi'^{+}}{\partial x}$, and (h) $-\frac{\partial \phi'^{+}}{\partial x} + \beta y v'^{+}$.

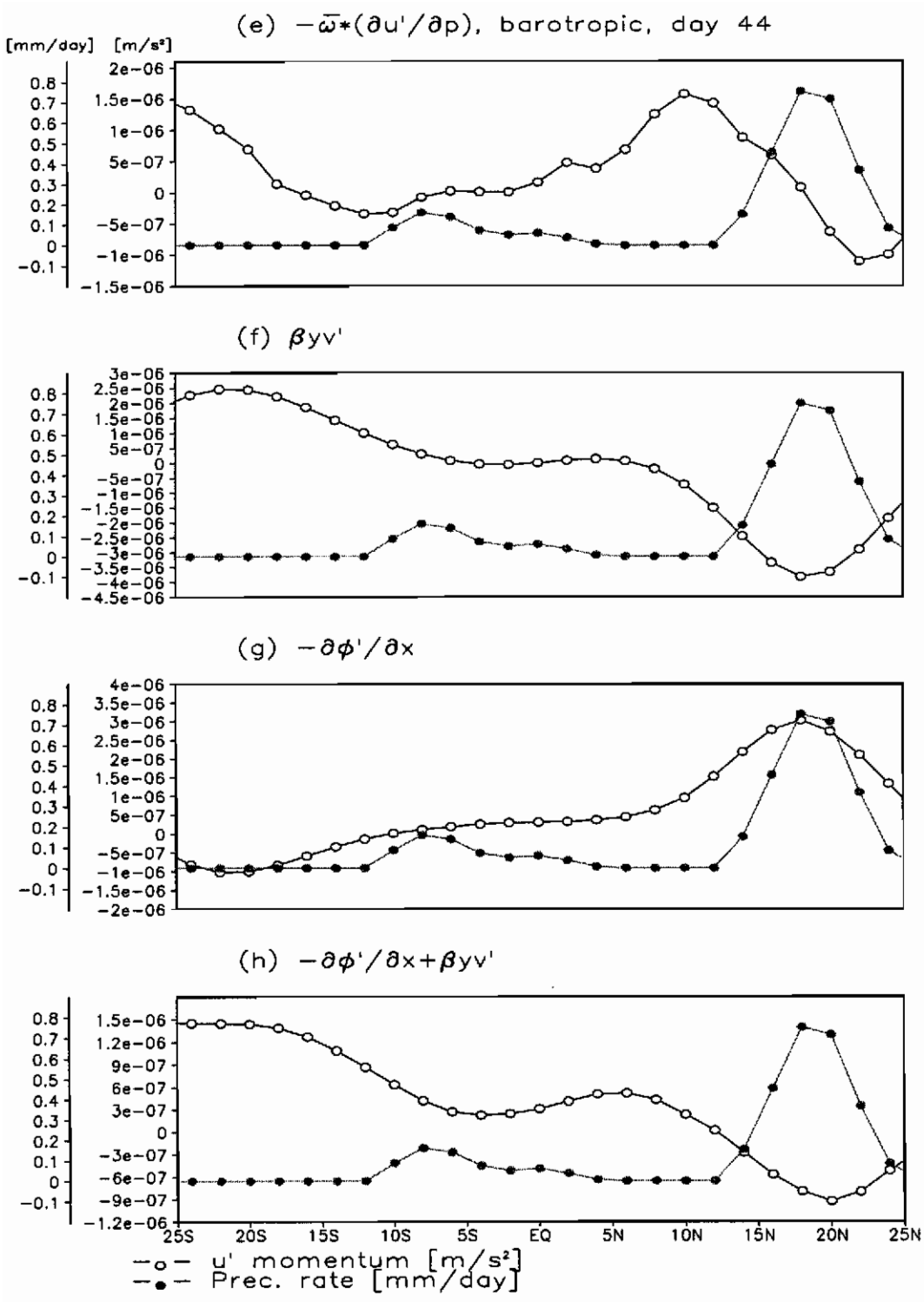

Figure 4.24: (Continued).

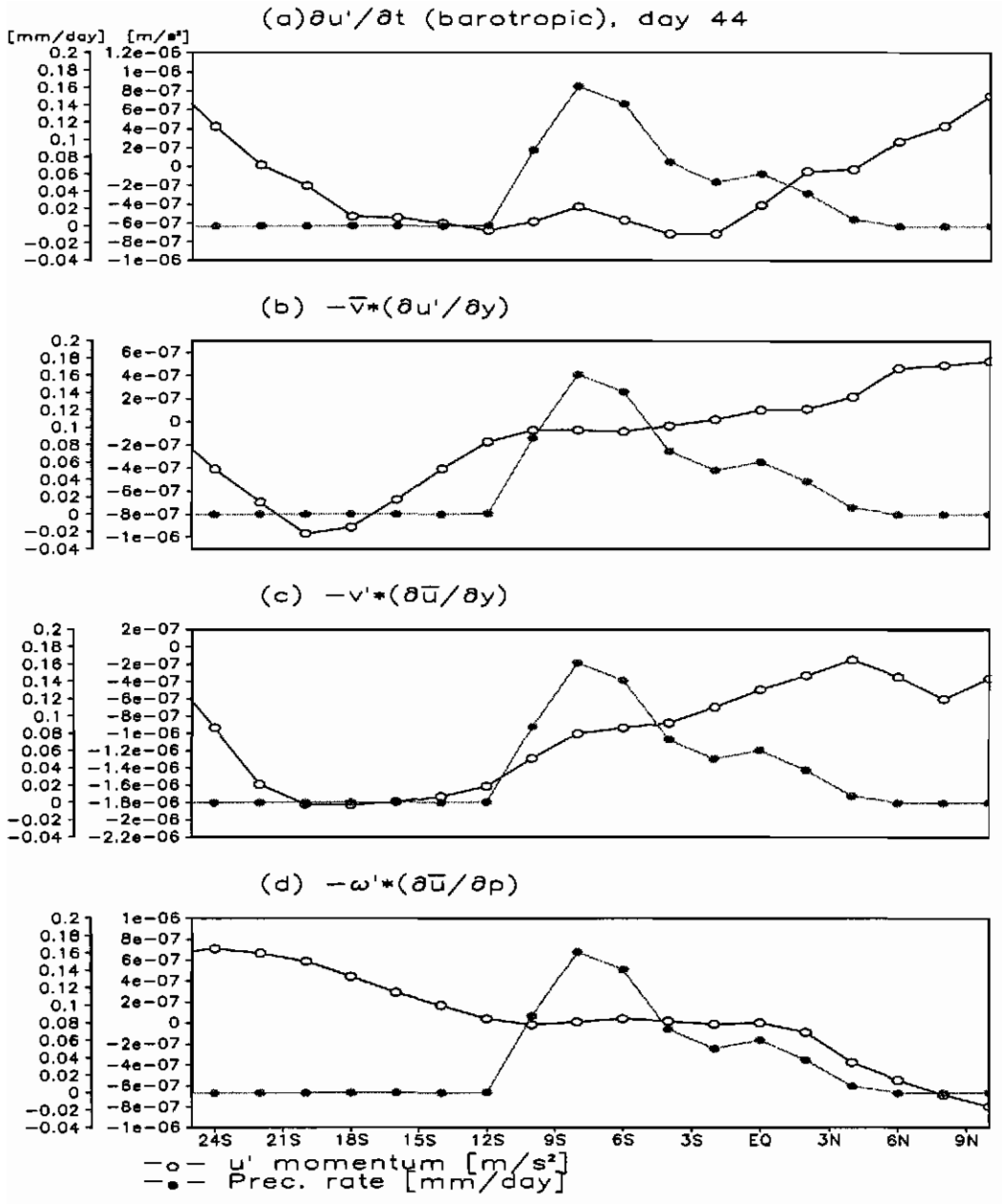

Figure 4.25: Zonally averaged (60-100E) precipitation rate (-•-) and barotropic mode of momentum equation for zonal wind anomaly on day 44 (-∘-). Same as Fig. 4.24 except that the latitudinal variation is ranged from 25S to 10N, only.

(a) $\frac{\partial u'^{+}}{\partial t}$, (b) $(-\overline{v}\,\frac{\partial u'}{\partial y})^{+}$, (c) $(-v'\frac{\partial \overline{u}}{\partial y})^{+}$, (d) $(-\omega'\frac{\partial \overline{u}}{\partial p})^{+}$, (e) $(-\overline{\omega}\,\frac{\partial u'}{\partial p})^{+}$,

(f) $\beta y v'^{+}$, (g) $-\frac{\partial \phi'^{+}}{\partial x}$, (h) $-\frac{\partial \phi'^{+}}{\partial x}+\beta y v'^{+}$, (i) $(-\overline{u}\,\frac{\partial u'}{\partial x})^{+}$, and (j) $(-u'\frac{\partial \overline{u}}{\partial x})^{+}$.

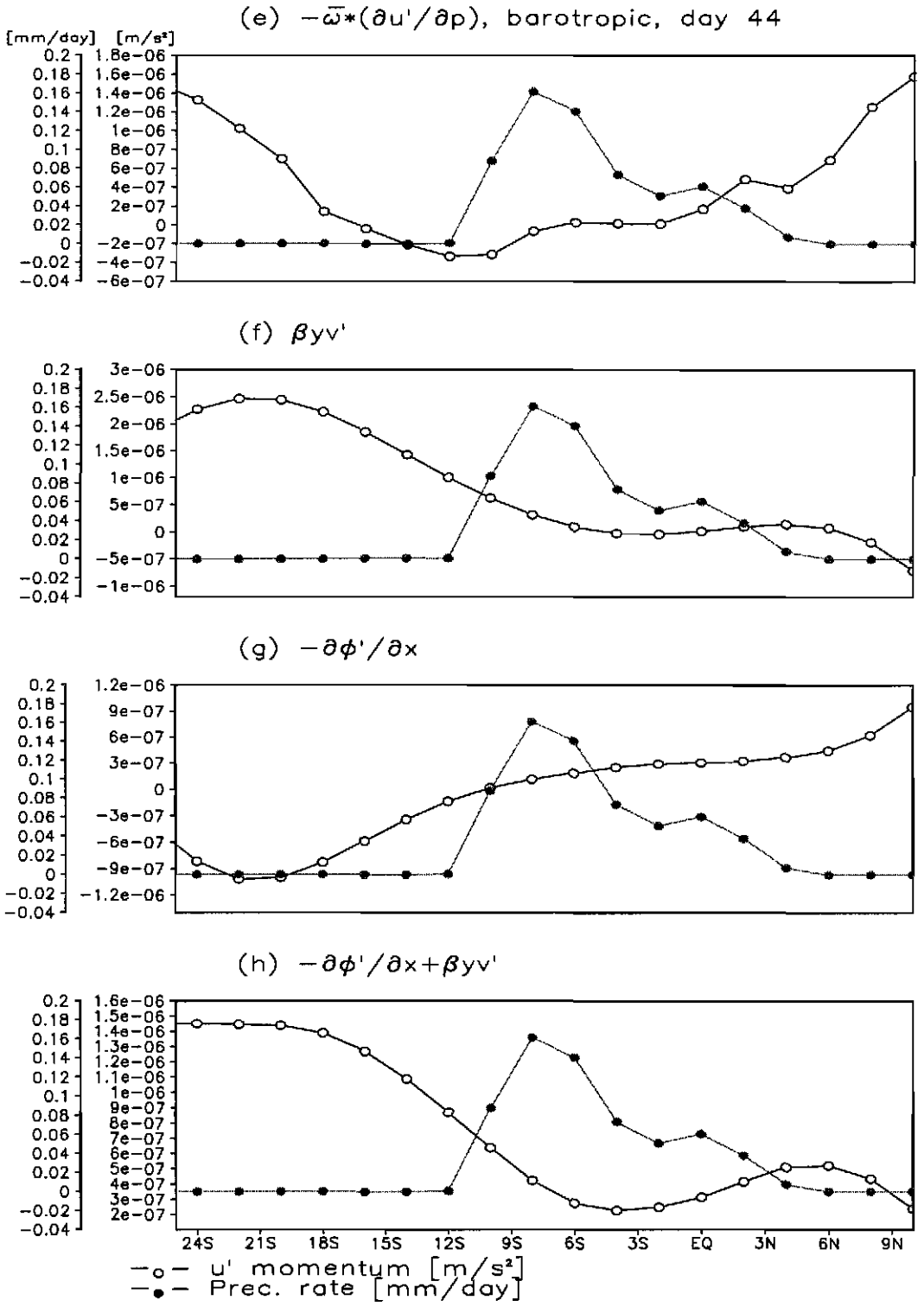

Figure 4.25: (Continued).

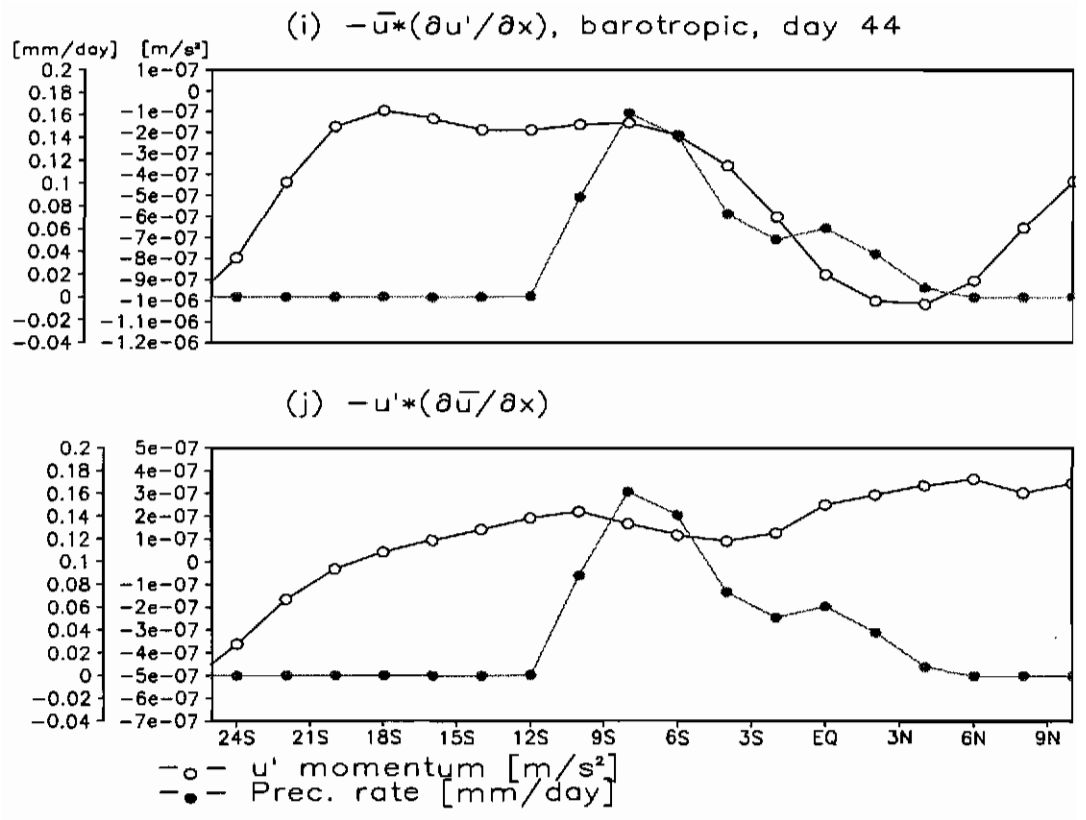

Figure 4.25: (Continued).

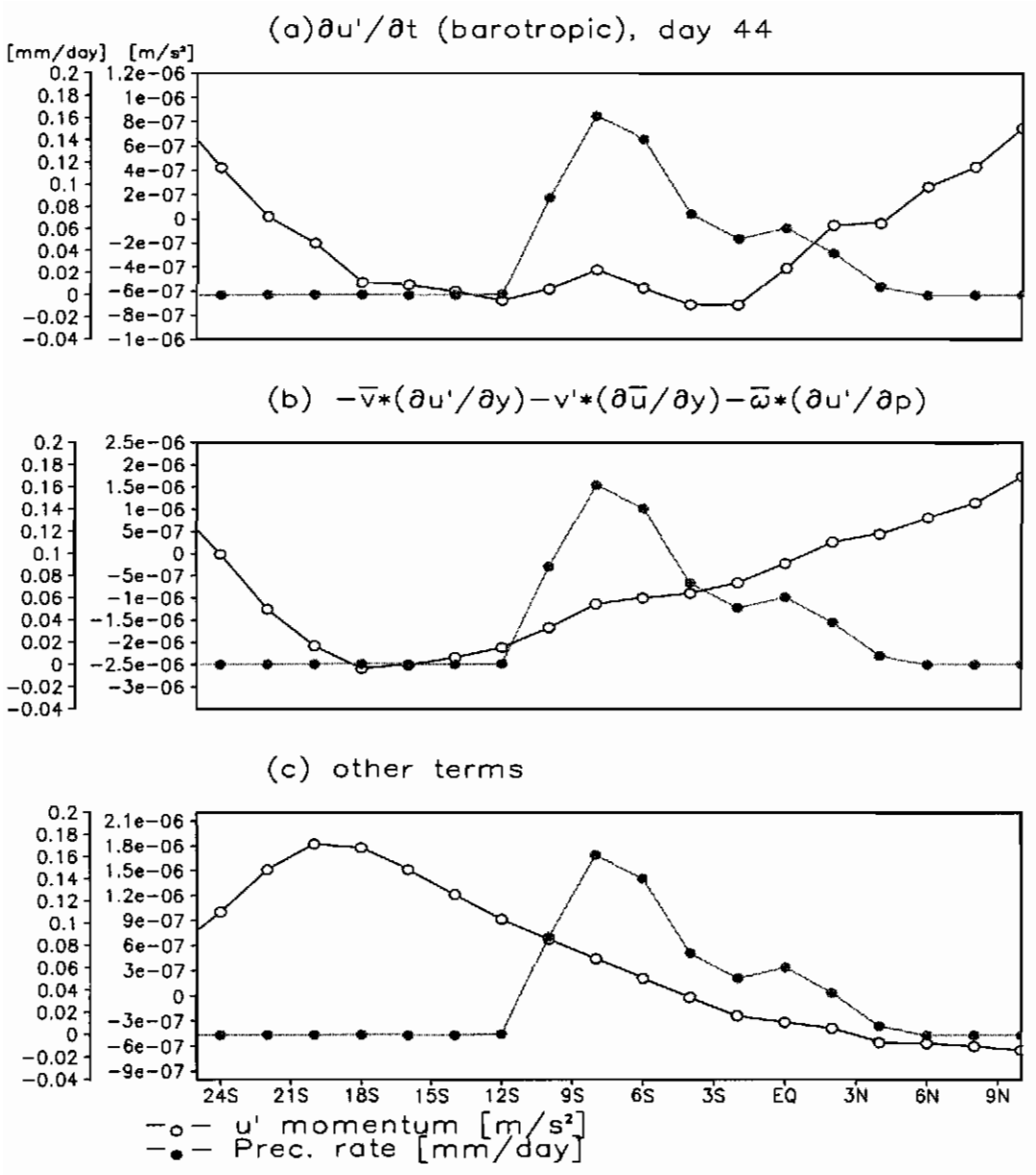

Figure 4.26: Zonally averaged (60-100E) precipitation rate (-•-) and (a) $\frac{\partial u'^{+}}{\partial t}$, (b) sum of $(-\overline{v}\,\frac{\partial u'}{\partial y})^{+}$, $(-v'\frac{\partial \overline{u}}{\partial y})^{+}$, and $(-\overline{\omega}\,\frac{\partial u'}{\partial p})^{+}$, (c) sum of $(-\omega'\frac{\partial \overline{u}}{\partial p})^{+}$, $\beta y v'^{+}$, $-\frac{\partial \phi'^{+}}{\partial x}$, $(-\overline{u}\,\frac{\partial u'}{\partial x})^{+}$, and $(-u'\frac{\partial \overline{u}}{\partial x})^{+}$ on day 44 (-∘-).

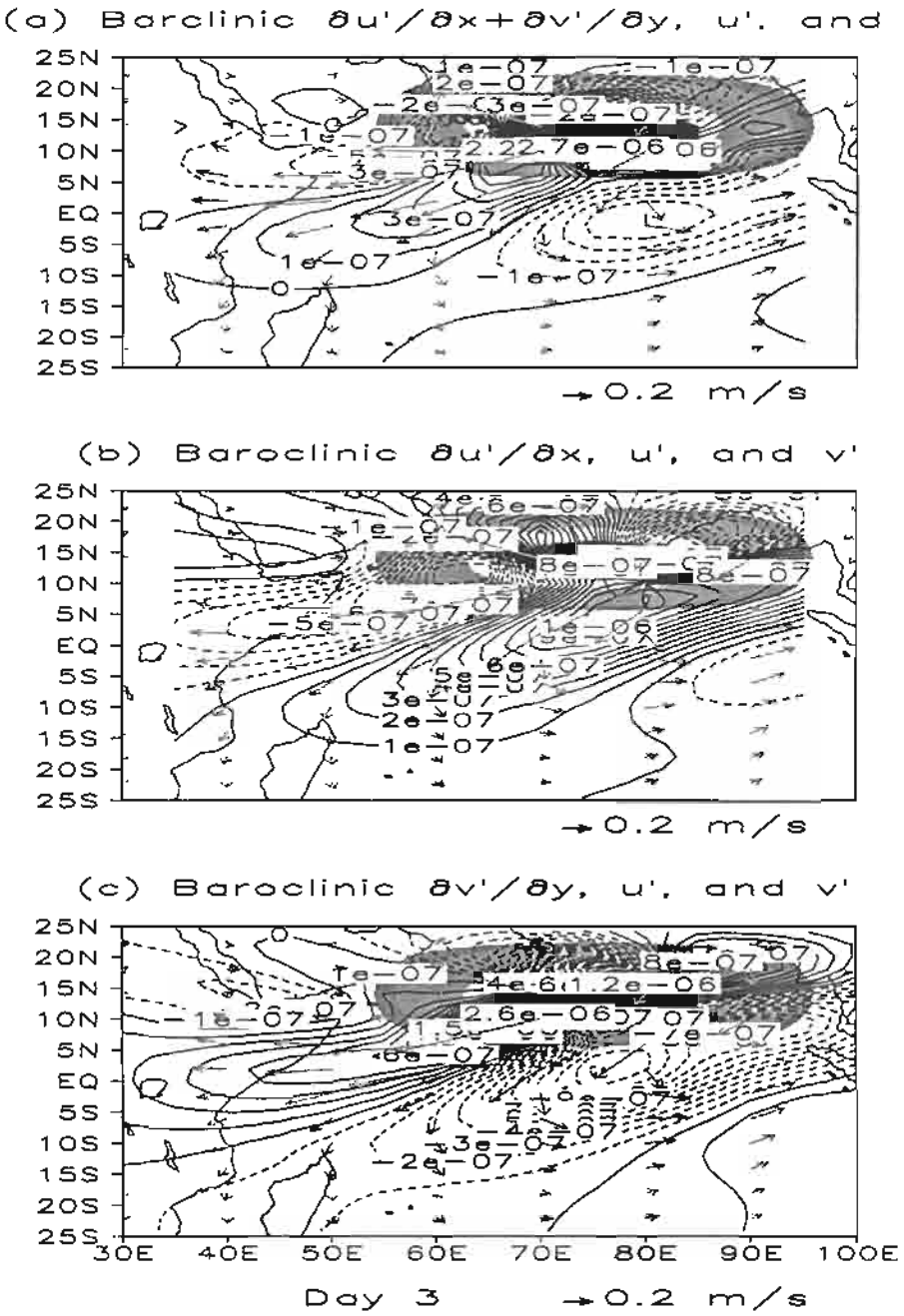

Figure 4.27: Baroclinic response of atmosphere to an isolated heat source in the northern hemisphere (area of precipitation is shaded). (a) Baroclinic wind and $\frac{\partial u'}{\partial x} + \frac{\partial v'}{\partial y}$ (contour), (b) baroclinic winds and $\frac{\partial u'}{\partial x}$ (contour), and (c) baroclinic wind and $\frac{\partial v'}{\partial y}$ (contour).

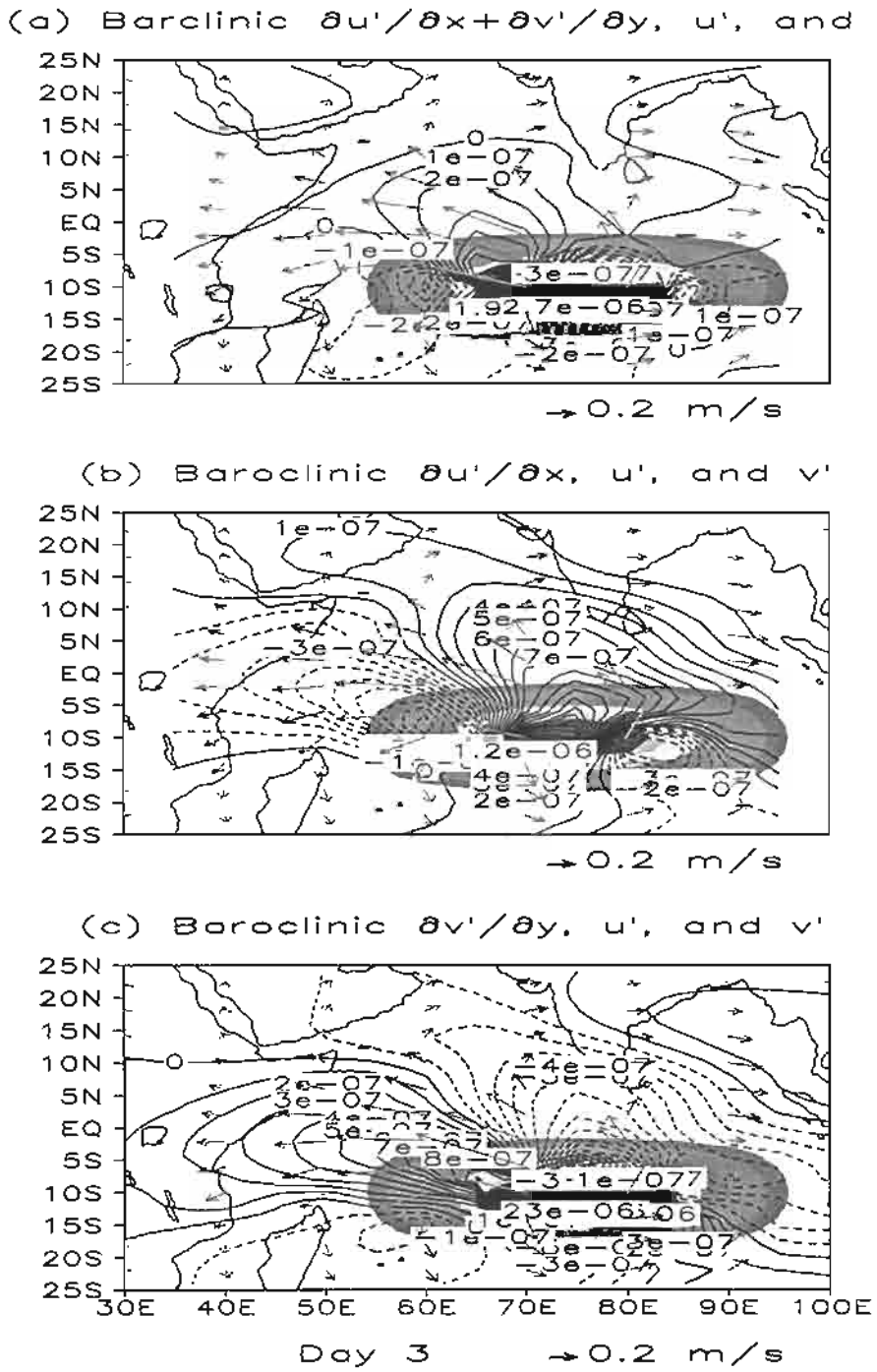

Figure 4.28: Baroclinic response of atmosphere to an isolated heat source in the southern hemispheres (area of precipitation is shaded).

(a) Baroclinic winds and $\frac{\partial u'}{\partial x} + \frac{\partial v'}{\partial y}$ (contour), (b) baroclinic winds and $\frac{\partial u'}{\partial x}$ (contour), and (c) baroclinic winds and $\frac{\partial v'}{\partial y}$ (contour).

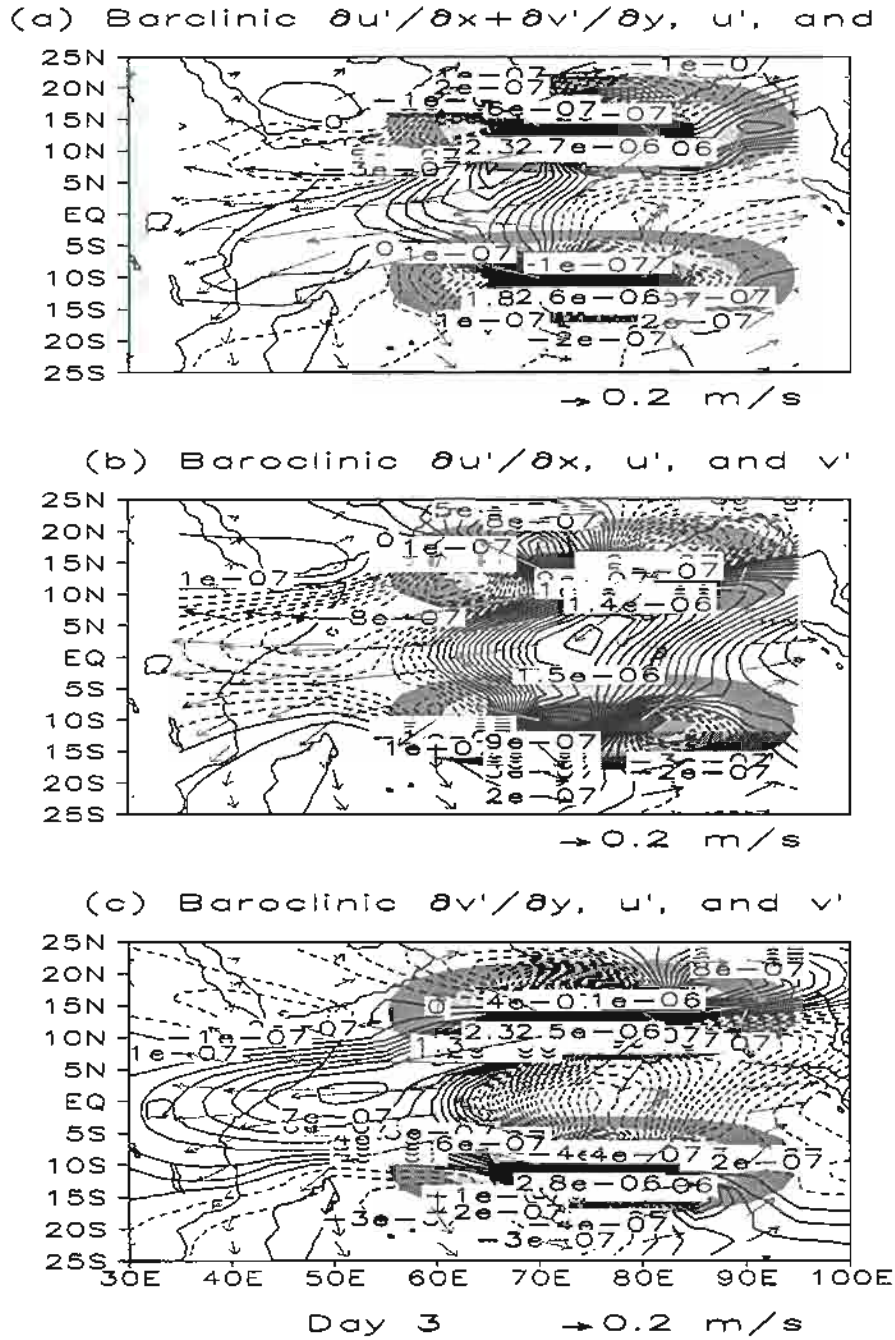

Figure 4.29: Baroclinic response of atmosphere to an isolated heat source in both hemispheres (area of precipitation is shaded). (a) Baroclinic winds and $\frac{\partial u'}{\partial x} + \frac{\partial v'}{\partial y}$ (contour), (b) baroclinic winds and $\frac{\partial u'}{\partial x}$ (contour), and (c) baroclinic winds and $\frac{\partial v'}{\partial y}$ (contour).

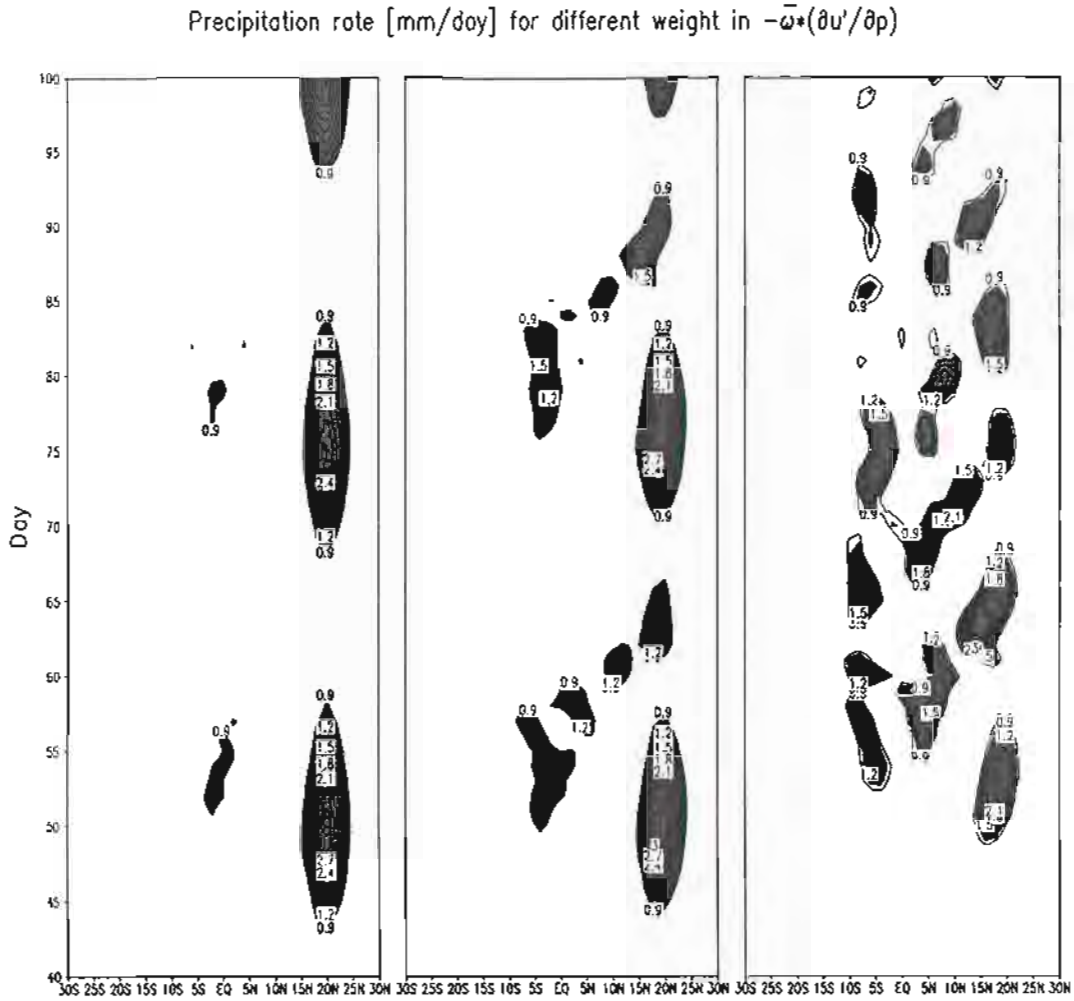

Figure 4.30: Zonally averaged (60-100E) precipitation rate (mm/day) from 3D model when (a) no vertical advection by July mean vertical motion (i.e. $-\overline{\omega}\frac{\partial u'}{\partial p}*0$, Exp. 1), (b) 100% of vertical advection by July-mean vertical motion (i.e. $-\overline{\omega}\frac{\partial u'}{\partial p}*1$, control run), and (c) three times the vertical advection by July mean vertical motion (i.e. $-\overline{\omega}\frac{\partial u'}{\partial p}*3$, Exp.2).

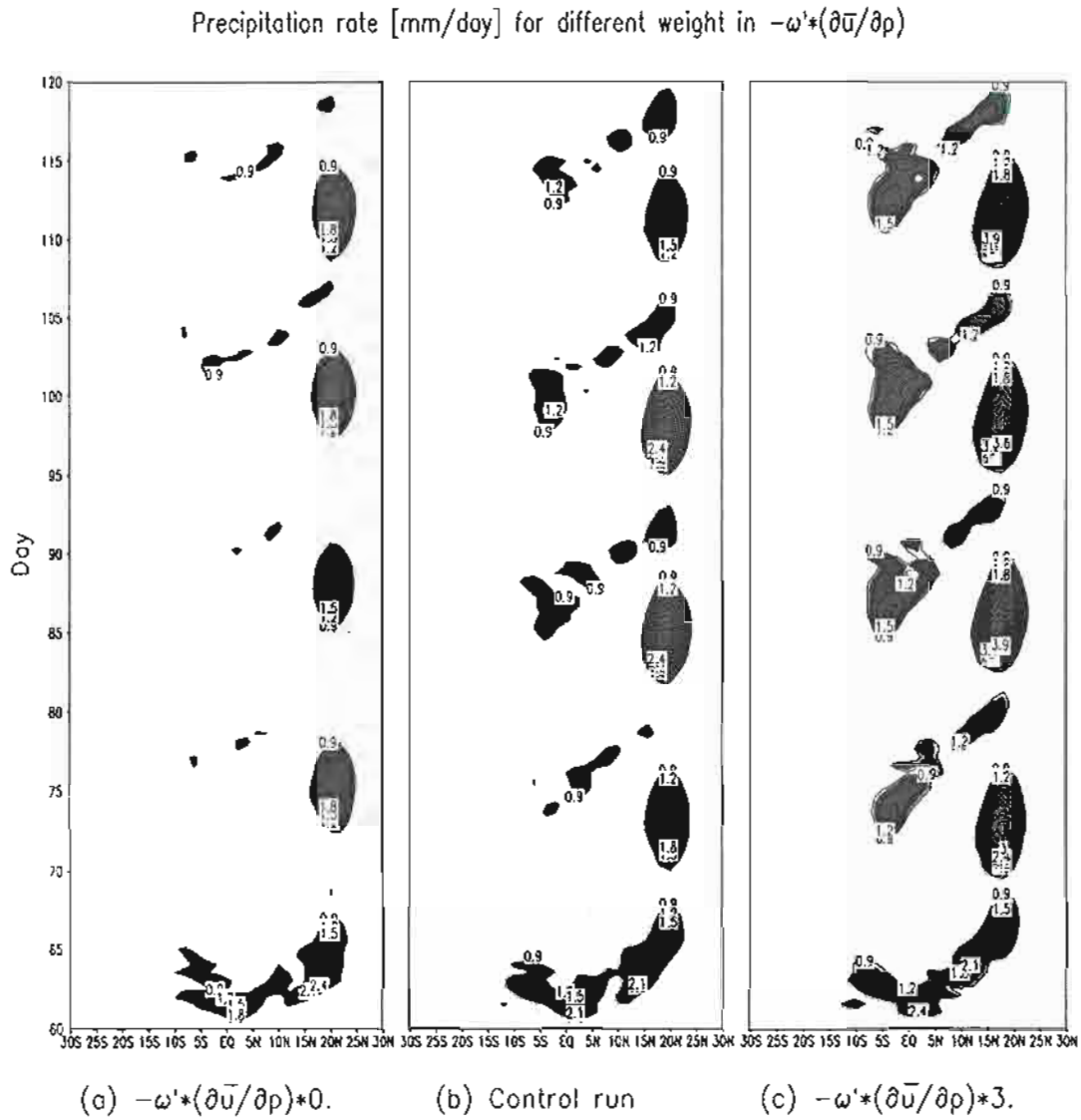

Figure 4.31: Zonally averaged (60-100E) precipitation rate (mm/day) in 3D model when (a) no vertical advection of July-mean zonal winds (i.e. $-\omega'\frac{\partial\bar{u}}{\partial p}*0$, Exp. 3), (b) 100% of vertical advection of July-mean zonal winds (i.e. $-\omega'\frac{\partial\bar{u}}{\partial p}*1$, control run), and (c) three times the vertical advection of July-mean zonal winds (i.e. $-\omega'\frac{\partial\bar{u}}{\partial p}*3$, Exp. 4).

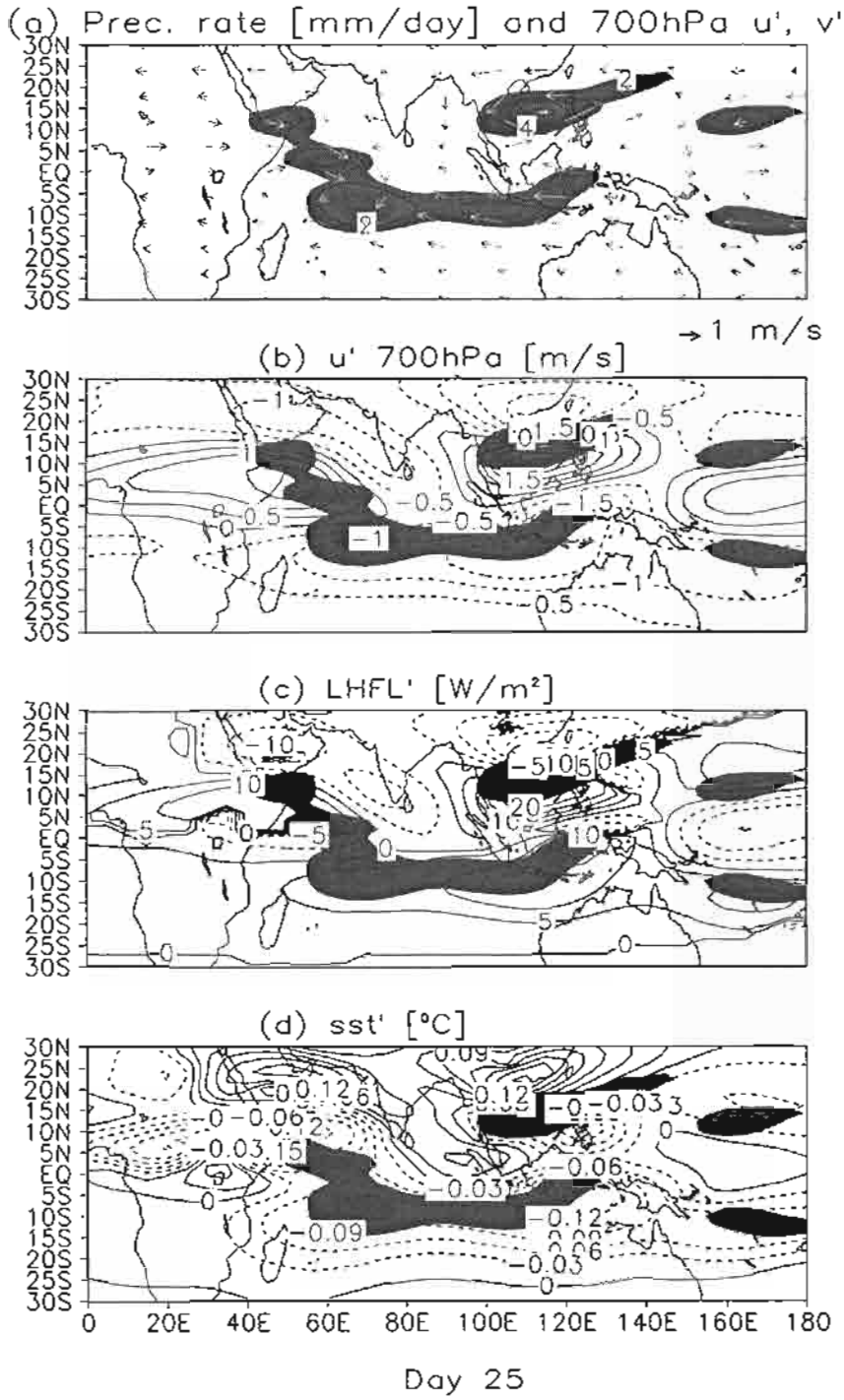

Figure 4.32: Anomalies from 3D model with interactive SST on day 25, (a) precipitation rate (shaded > 0.1 mm/day) and low-tropospheric winds, (b) low-tropospheric zonal winds (m/s), (c) latent heat flux (W/m^2), and (d) sea surface temperature (sst′).

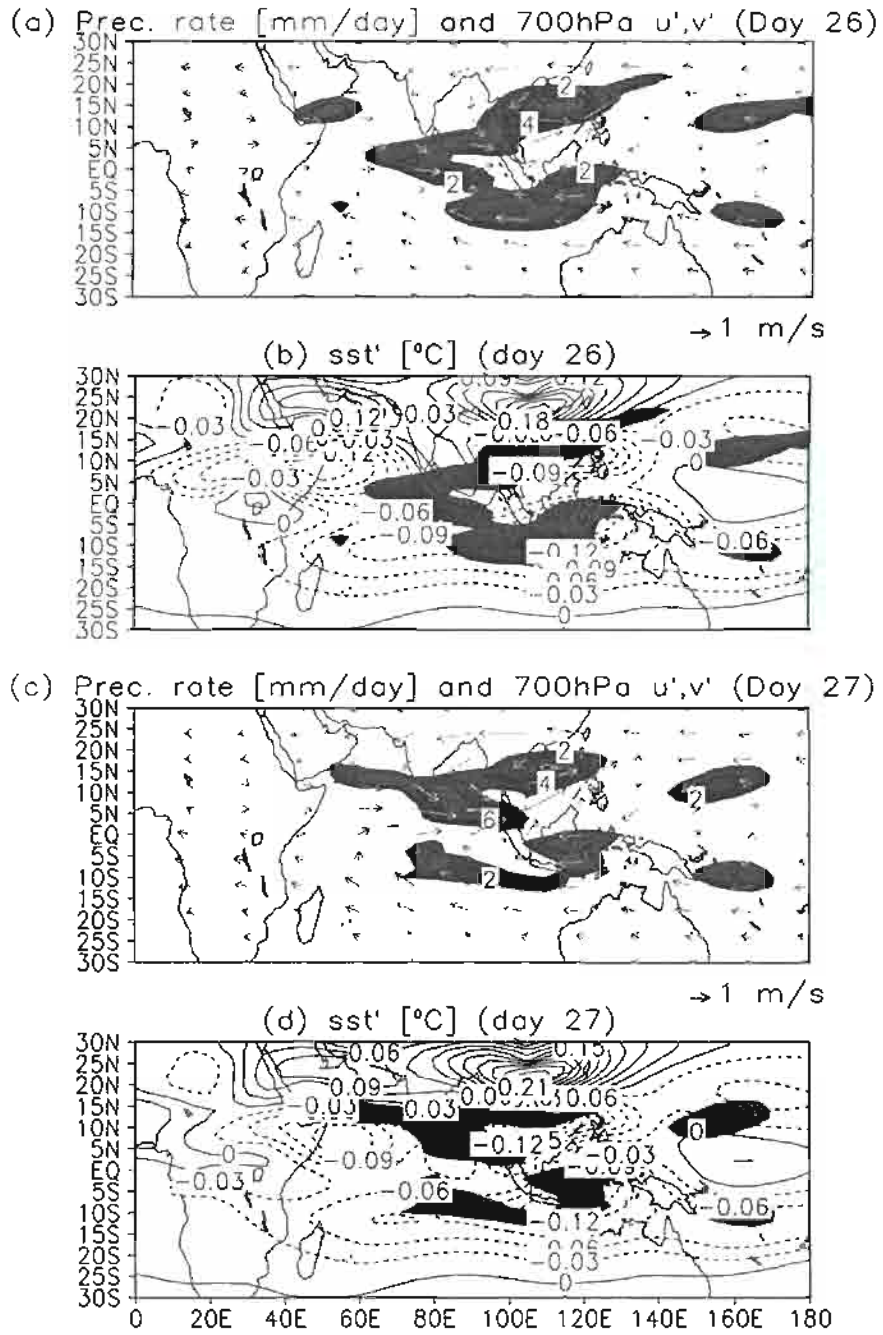

Figure 4.33: Anomalies from 3D model with interactive SST. (a) precipitation rate (shaded > 0.1 mm/day) and low-tropospheric winds on day 26, (b) sea surface temperature (sst′) on day 26, (c) precipitation rate and low-tropospheric winds on day 27, and (d) sea surface temperature (sst′) on day 27.

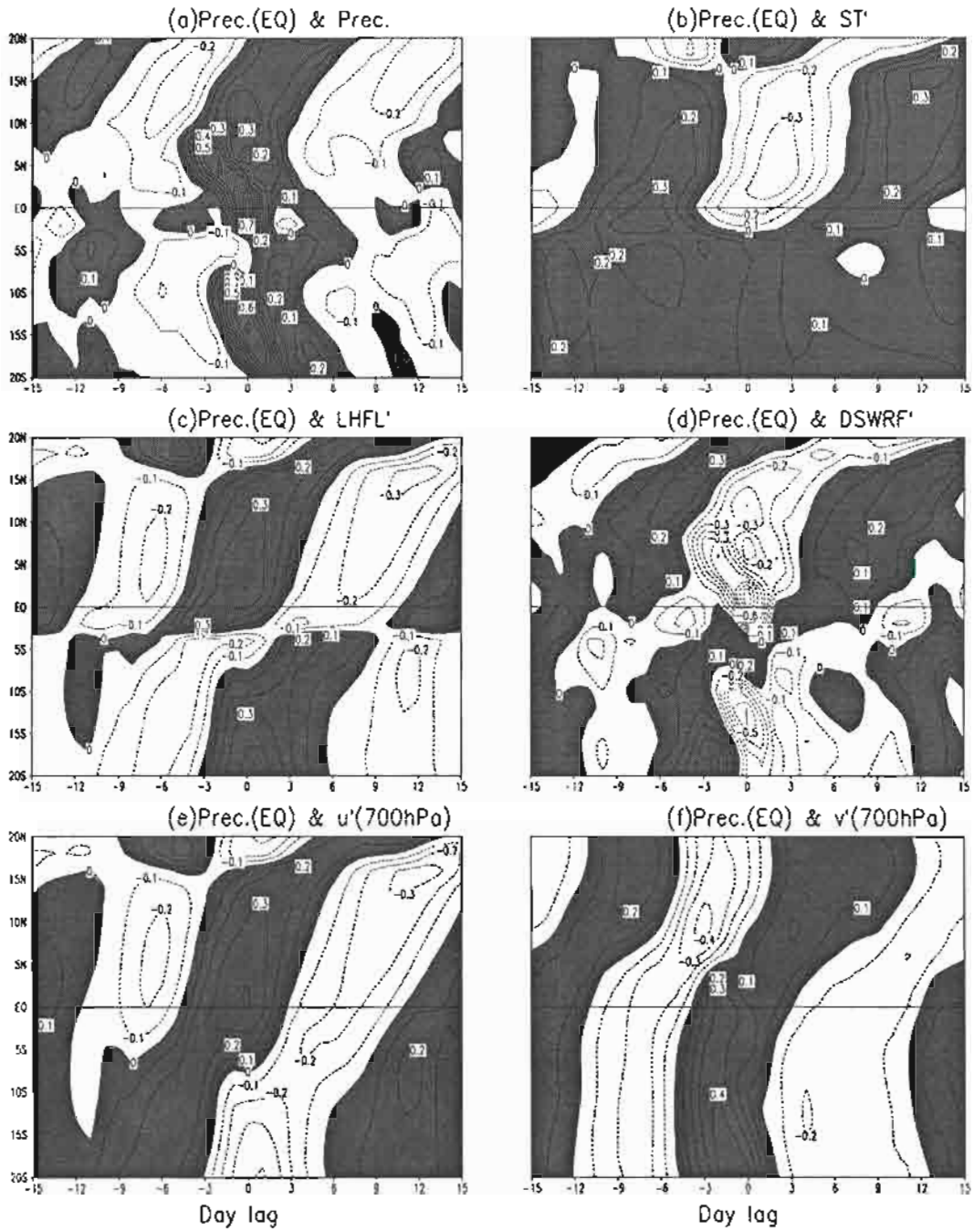

Figure 4.34: Pentad lagged cross correlation of 3D model anomalies between zonally averaged (60-100E) precipitation rate at equator and zonally averaged anomalies of (a) precipitation rate, (b) surface temperature (ST′), (c) latent heat flux (LHFL′), (d) downward shortwave radiation flux (DSWRF′), (e) 700hPa-zonal wind (u′ 700hPa), and (f) 700hPa-meridional wind (v′ 700hPa).

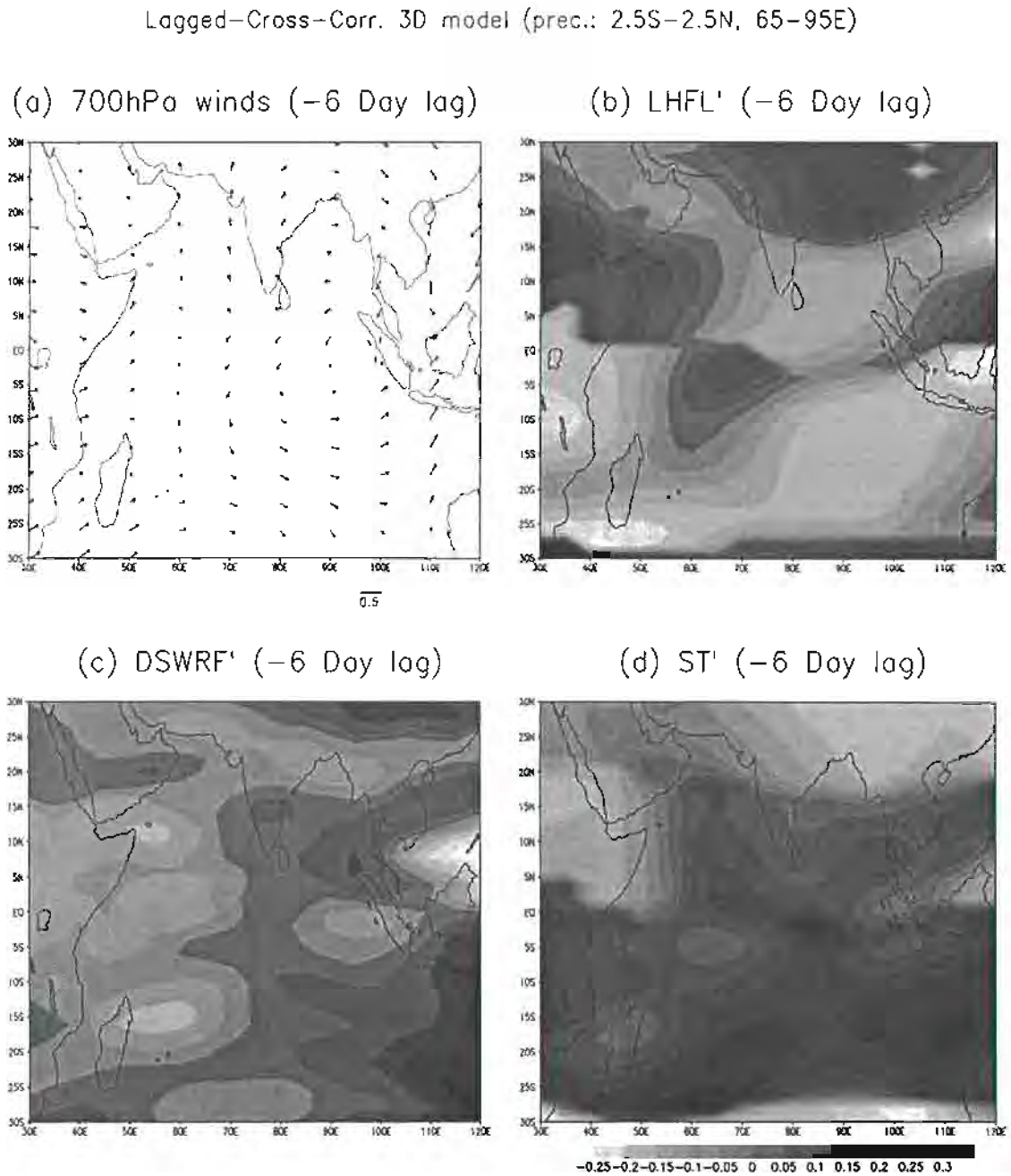

Figure 4.35: Lagged cross correlation of 3D model anomalies between area-averaged (from 65E to 95E, and from -2.5S to 2.5 N) precipitation rate and (a) 700hPa winds at -6 day lag, (b) surface heat fluxes at -6 day lag, (c) downward shortwave radiation flux at -6 day lag, (d) surface temperature at -6 day lag, (e) 700hPa winds at 0 day lag, (f) surface heat flux at 0 day lag, (g) downward shortwave radiation flux at 0 day lag, and (h) surface temperature at 0 day lag.

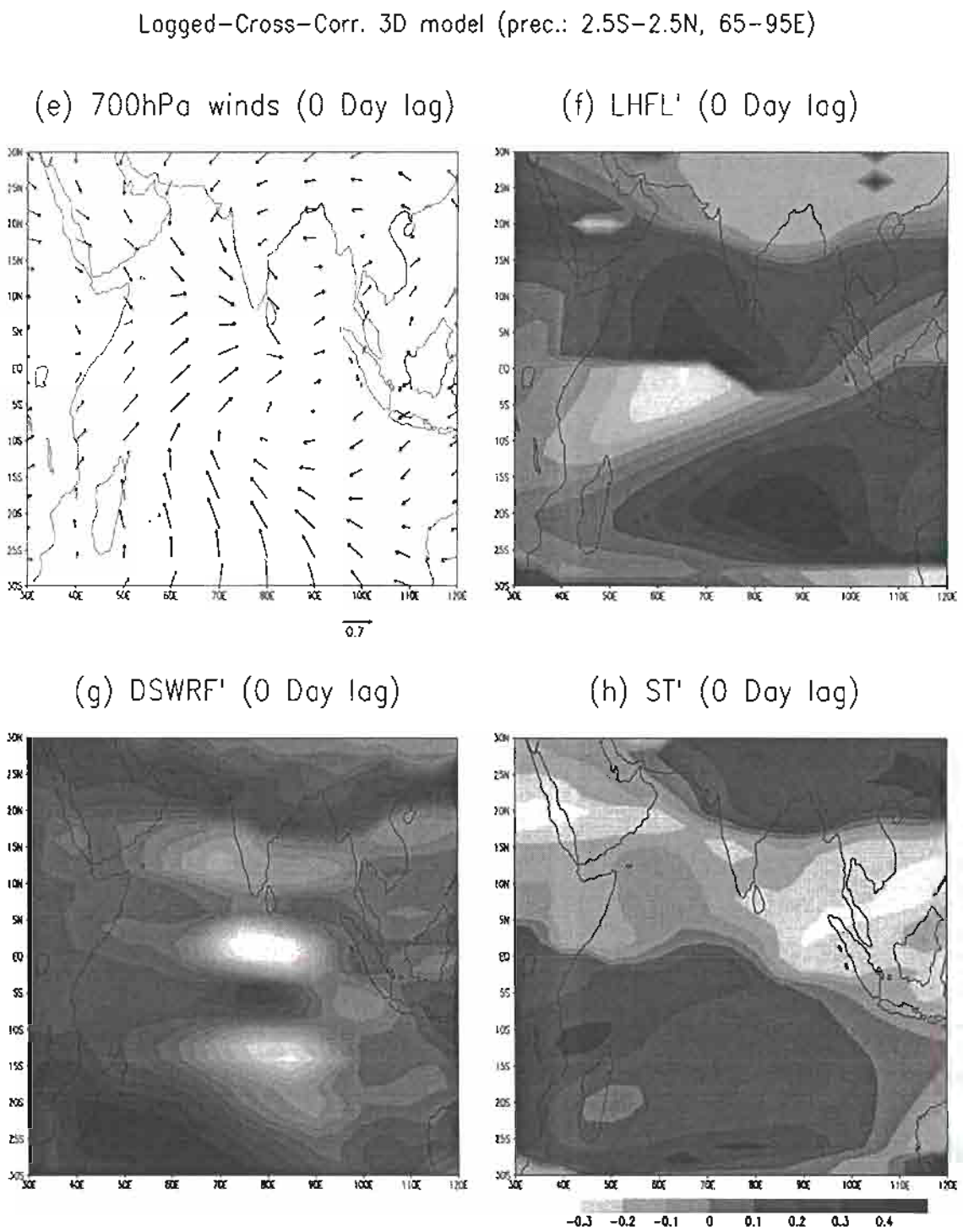

Figure 4.35: (Continued).

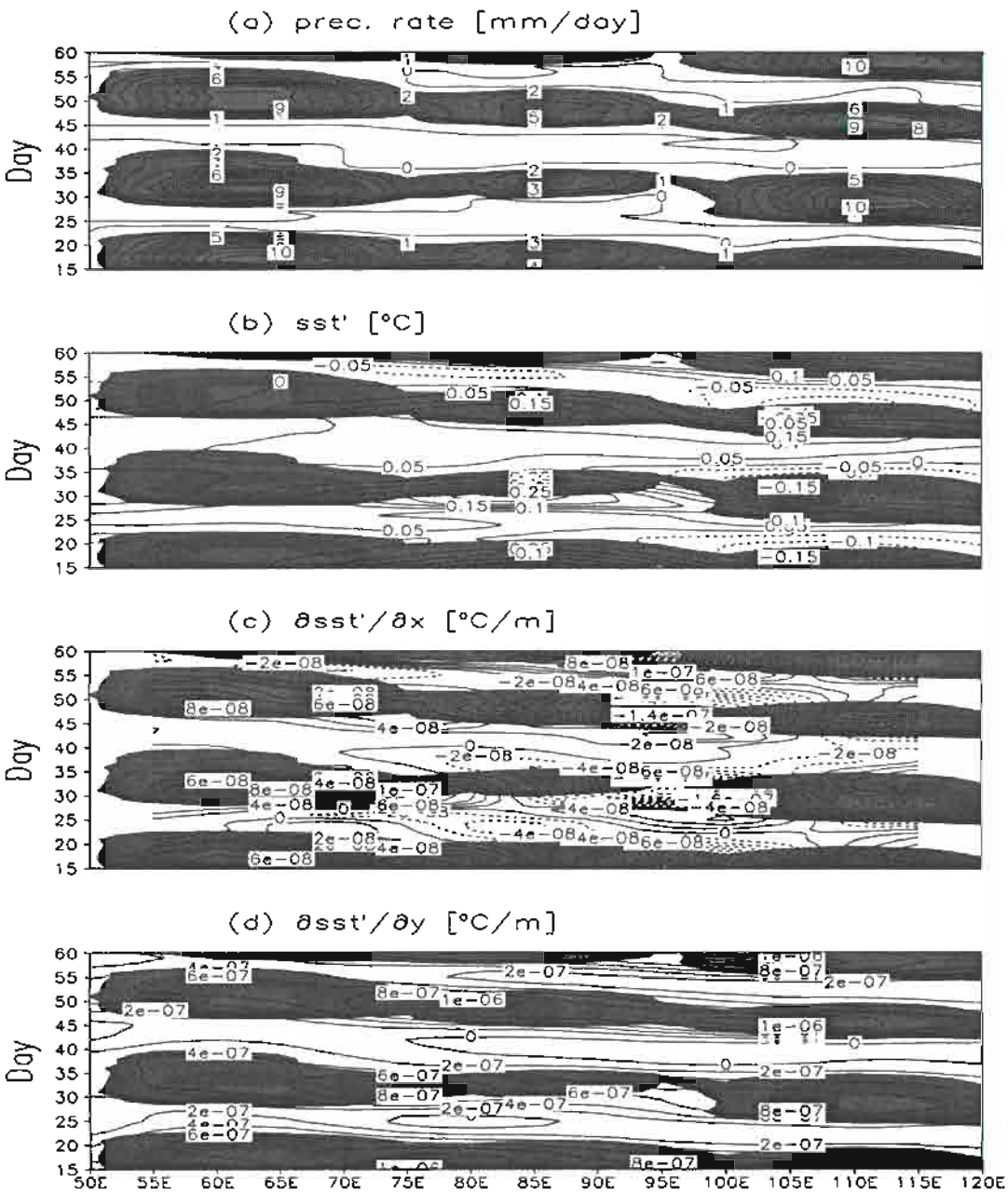

Figure 4.36: Time-longitude cross section of anomalies from 3D model along the latitude of 18N. (a) precipitation rate (shaded > 1mm/day), (b) sst', (c) $\frac{\partial sst'}{\partial x}$, and (d) $\frac{\partial sst'}{\partial y}$.

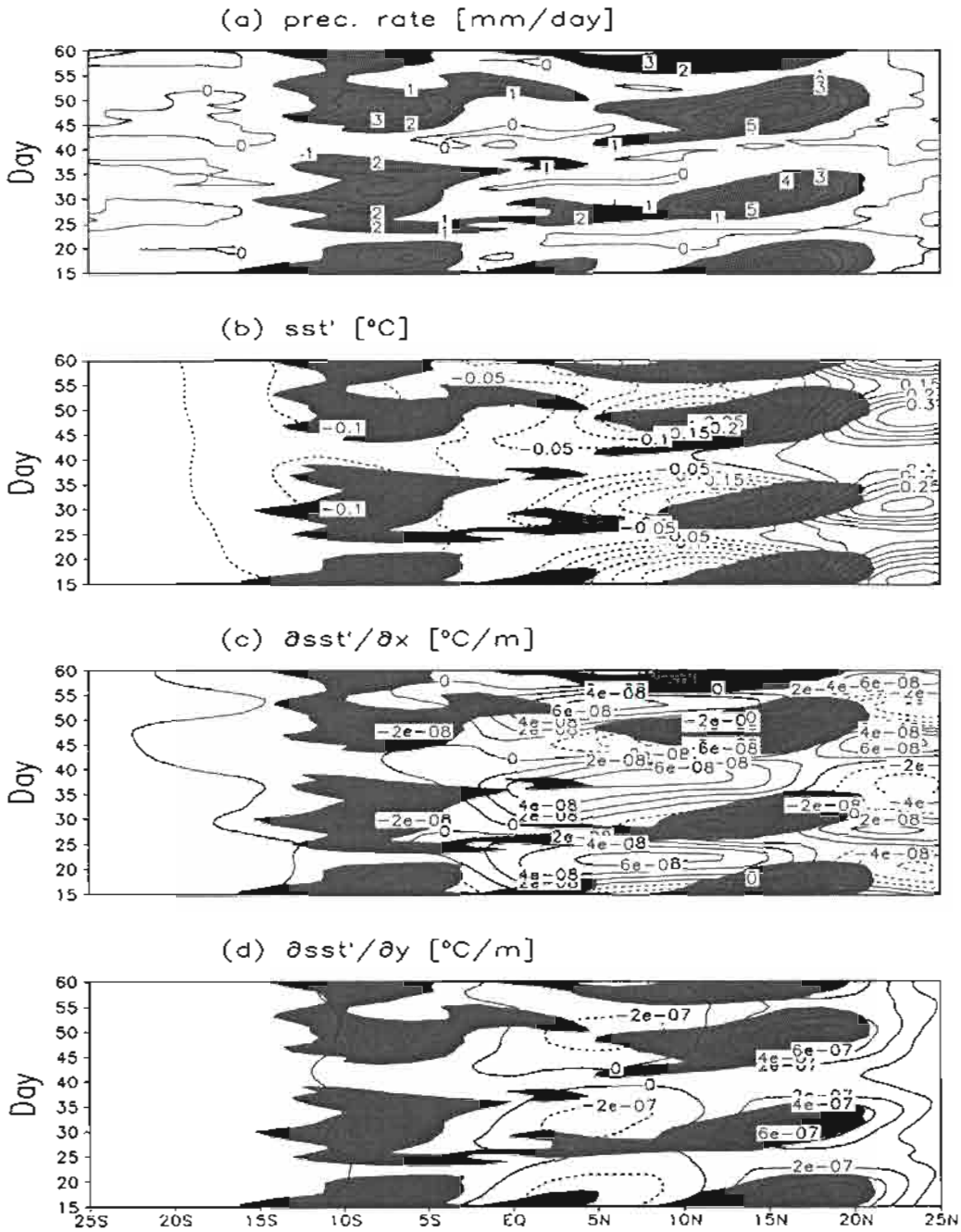

Figure 4.37: Latitude-time section of zonally averaged (60-100E) anomalies from 3D model. (a) precipitation rate (shaded > 1mm/day), (b) sst', (c) $\frac{\partial sst'}{\partial x}$, and (d) $\frac{\partial sst'}{\partial y}$.

(a)

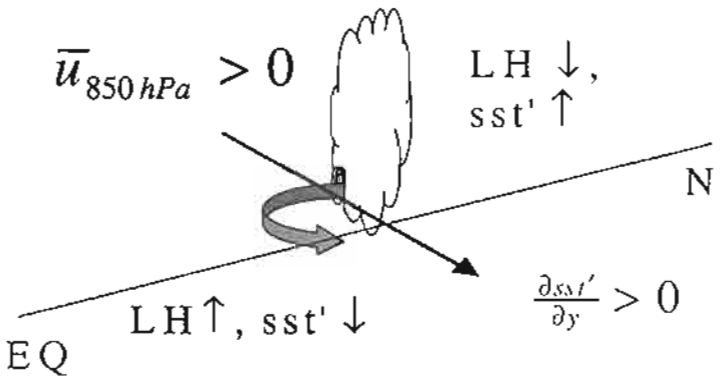

(b)

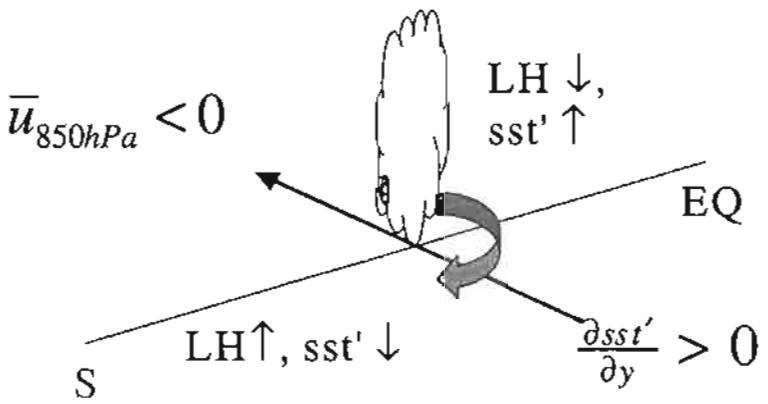

Figure 4.38: Schematic diagram illustrating the formation of sst′ gradient associated with (a) convection in the northern hemisphere, and (b) convection in the southern hemisphere.

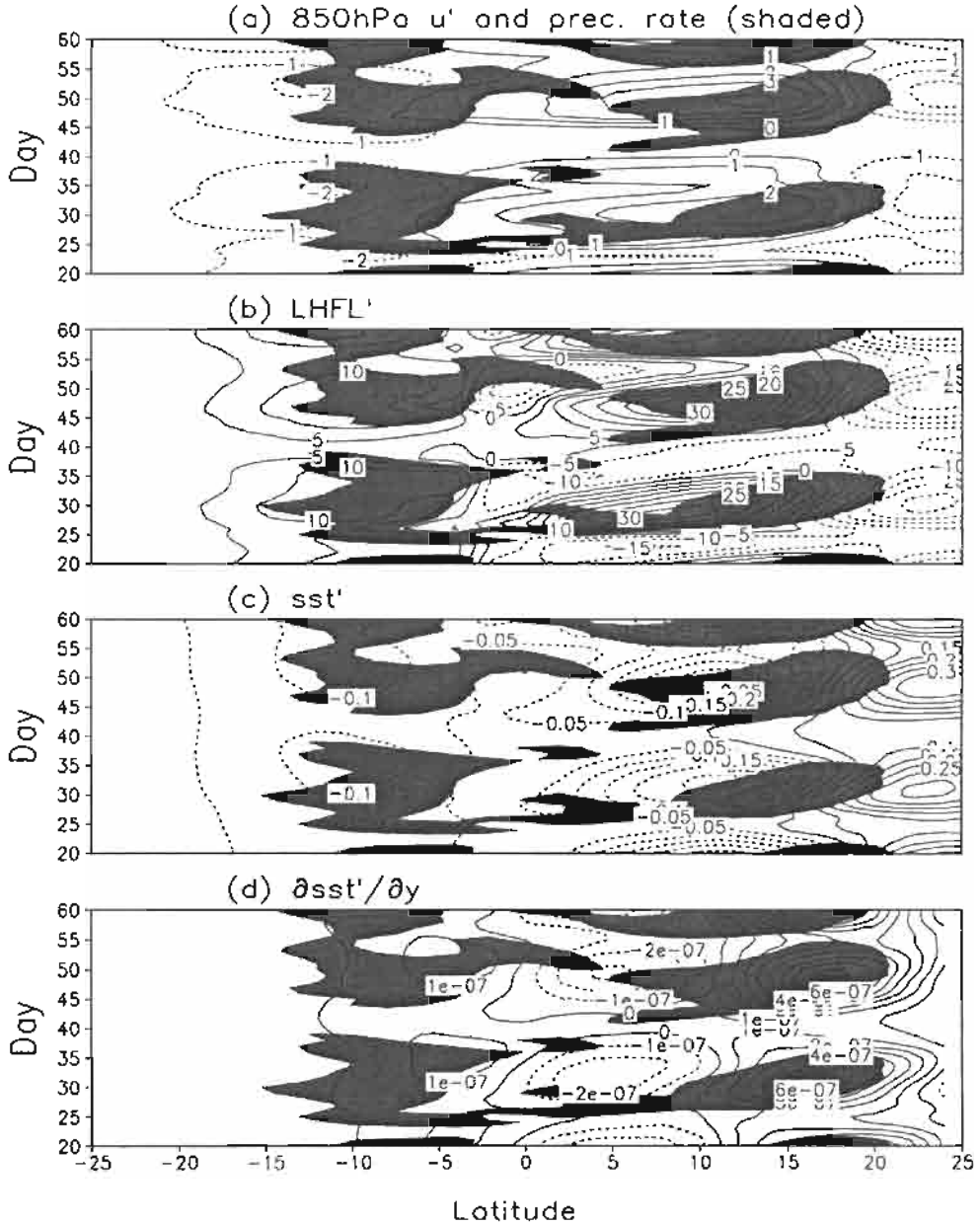

Figure 4.39: Latitude-time section of zonally averaged (60-100E) anomalies from 3D model using interactive SST, and climatology July-mean data as the basic state (control run). (a) low-tropospheric zonal winds (m/s), and precipitation rate (shaded > 0.1mm/day), (b) latent heat fluxes (W/m^2), (c) sea surface temperature (sst′),(d) $\frac{\partial sst'}{\partial y}$, and (e) $\frac{\partial}{\partial y}\left(\frac{\partial sst'}{\partial y}\right)$.

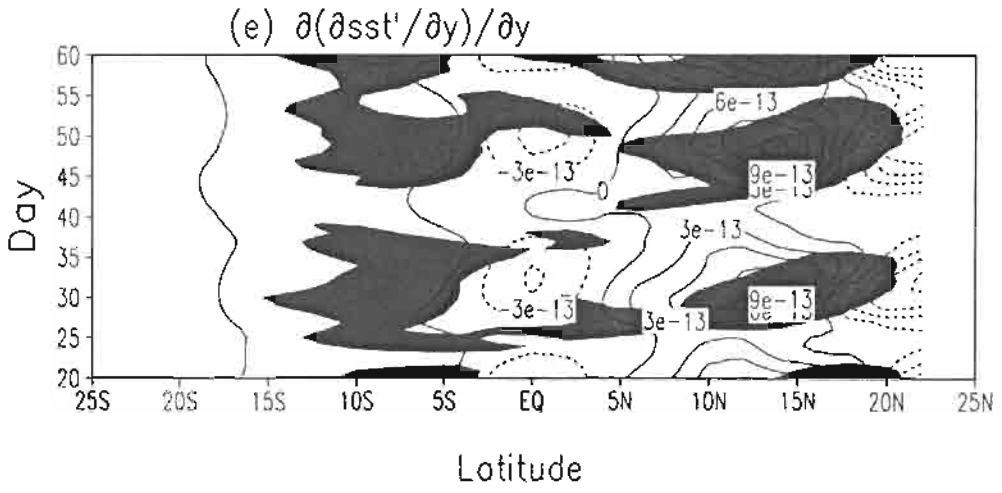

Figure 4.39: (Continued).

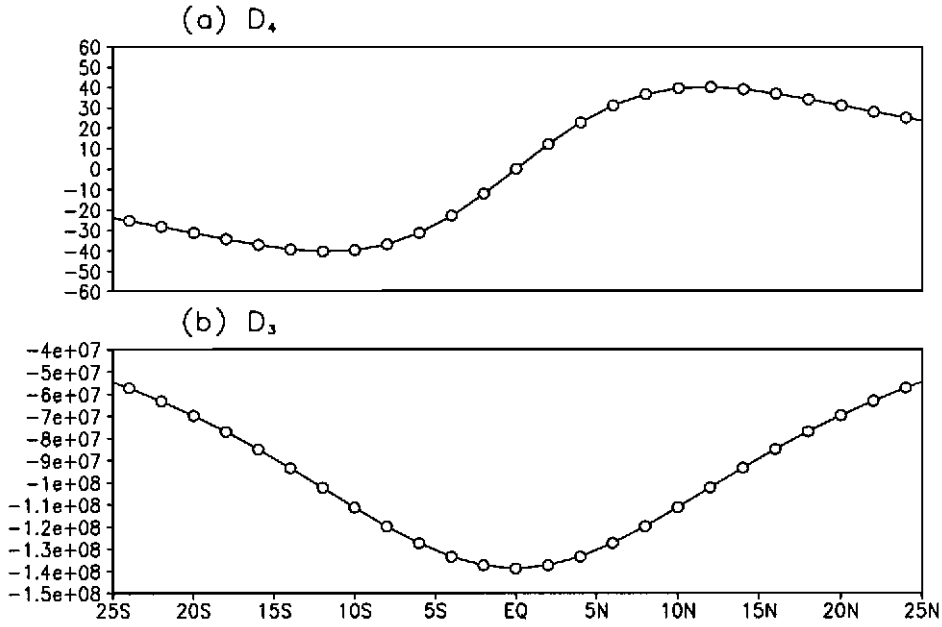

Figure 4.40: Latitudinal variation of the coefficient in the Ekman pumping velocity. (a) D_4, (b) D_3.

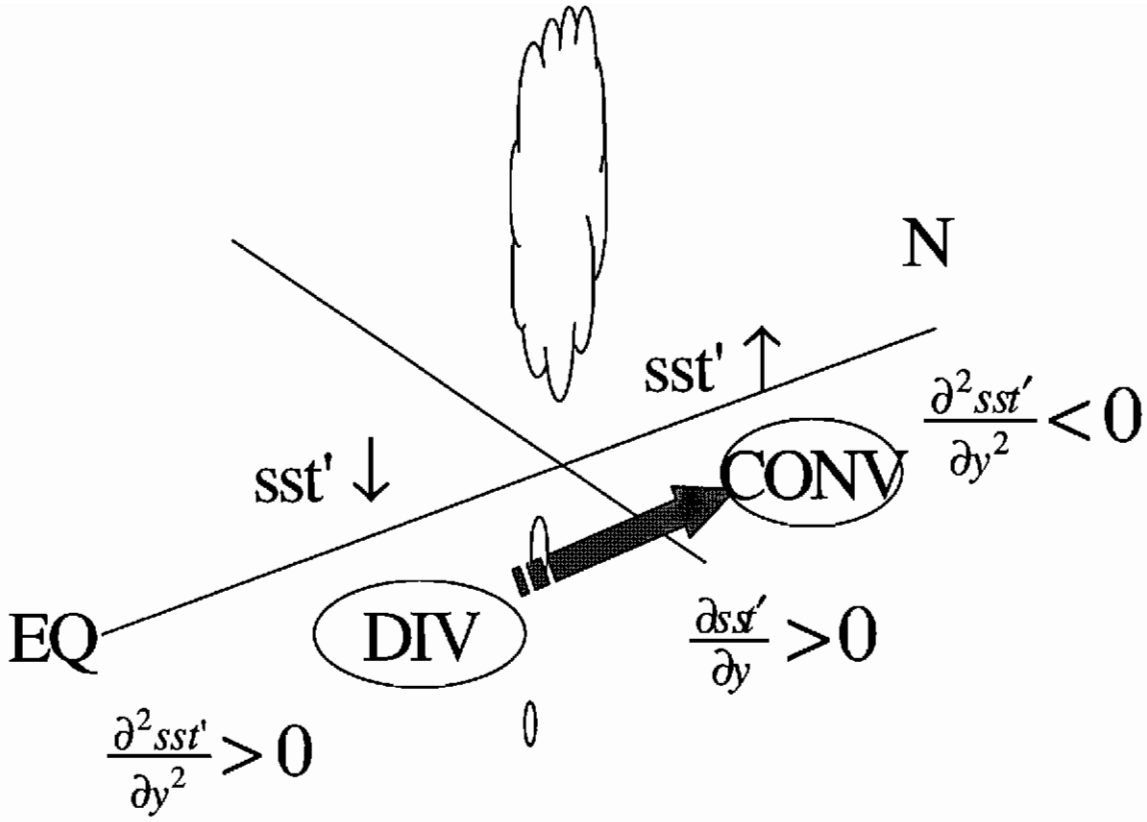

$$\because \frac{R(P_s - P_e)}{2P_e} > 0, \quad D_3 < 0,$$

$$\omega_e' \approx -\frac{R(P_s - P_e)}{2P_e} D_3 \frac{\partial^2 sst'}{\partial y^2} < 0, \ (Conv.)$$

$$\omega_e' \approx -\frac{R(P_s - P_e)}{2P_e} D_3 \frac{\partial^2 sst'}{\partial y^2} > 0, \ (Div.)$$

Figure 4.41: Schematic diagram illustrating the effect of sst′ on the Ekman pumping velocity (ω_e').

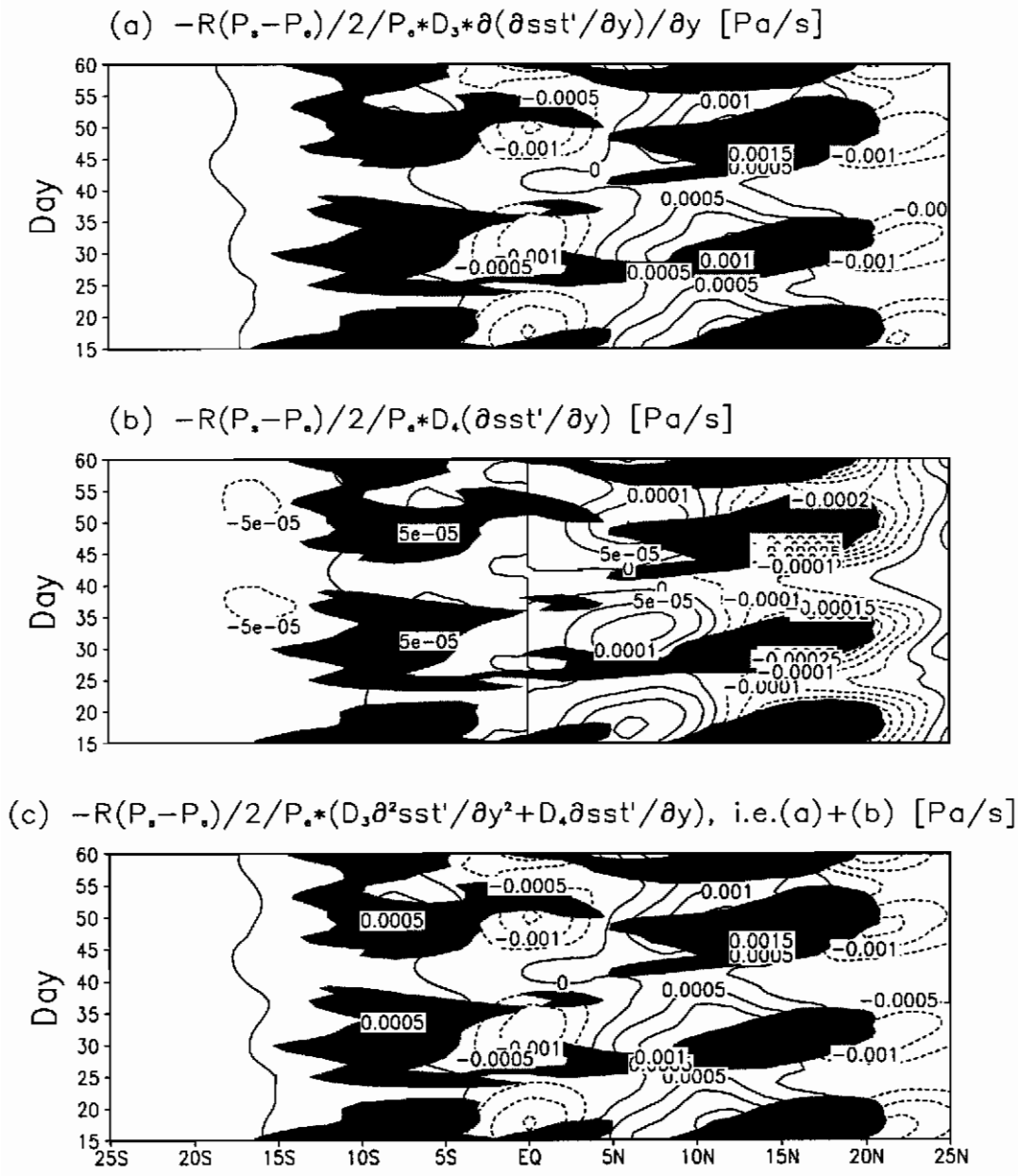

Figure 4.42: Latitude-time section of zonally averaged (60-100E) anomalies from 3D model using interactive SST, and climatology July-mean data as the basic state (control run). (a) $-\frac{R(P_s-P_e)}{2P_e} * D_3 * \frac{\partial}{\partial y}\left(\frac{\partial sst'}{\partial y}\right)$, (b) $-\frac{R(P_s-P_e)}{2P_e} * D_4 * \frac{\partial sst'}{\partial y}$, and (c) $-\frac{R(P_s-P_e)}{2P_e} * \left\{D_3 * \frac{\partial}{\partial y}\left(\frac{\partial sst'}{\partial y}\right) + D_4 * \frac{\partial sst'}{\partial y}\right\}$.

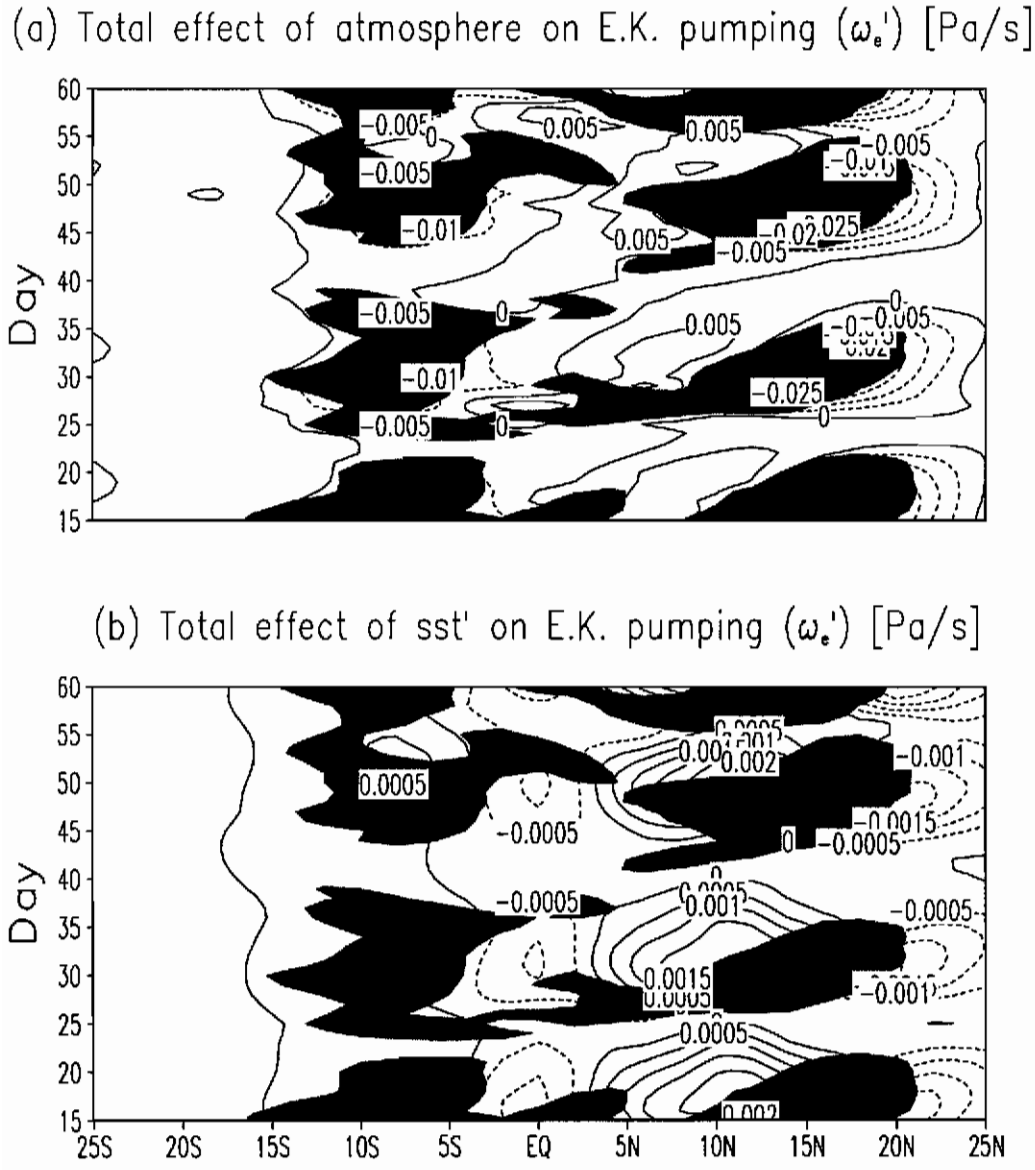

Figure 4.43: Latitude-time section of zonally averaged (60-100E) anomalies from 3D model using interactive SST, and climatology July-mean data as the basic state (control run). (a) $D_1 \frac{\partial^2 \phi_e'}{\partial x^2} + D_2 \frac{\partial \phi_e'}{\partial x} + D_3 \frac{\partial^2 \phi_e'}{\partial y^2} + D_4 \frac{\partial \phi_e'}{\partial y}$, and (b) $-\frac{R(P_s - P_e)}{2P_e} * \{ D_1 \frac{\partial^2 sst'}{\partial x^2} + D_2 \frac{\partial sst'}{\partial x} + D_3 \frac{\partial^2 sst'}{\partial y^2} + D_4 \frac{\partial sst'}{\partial y} \}$.

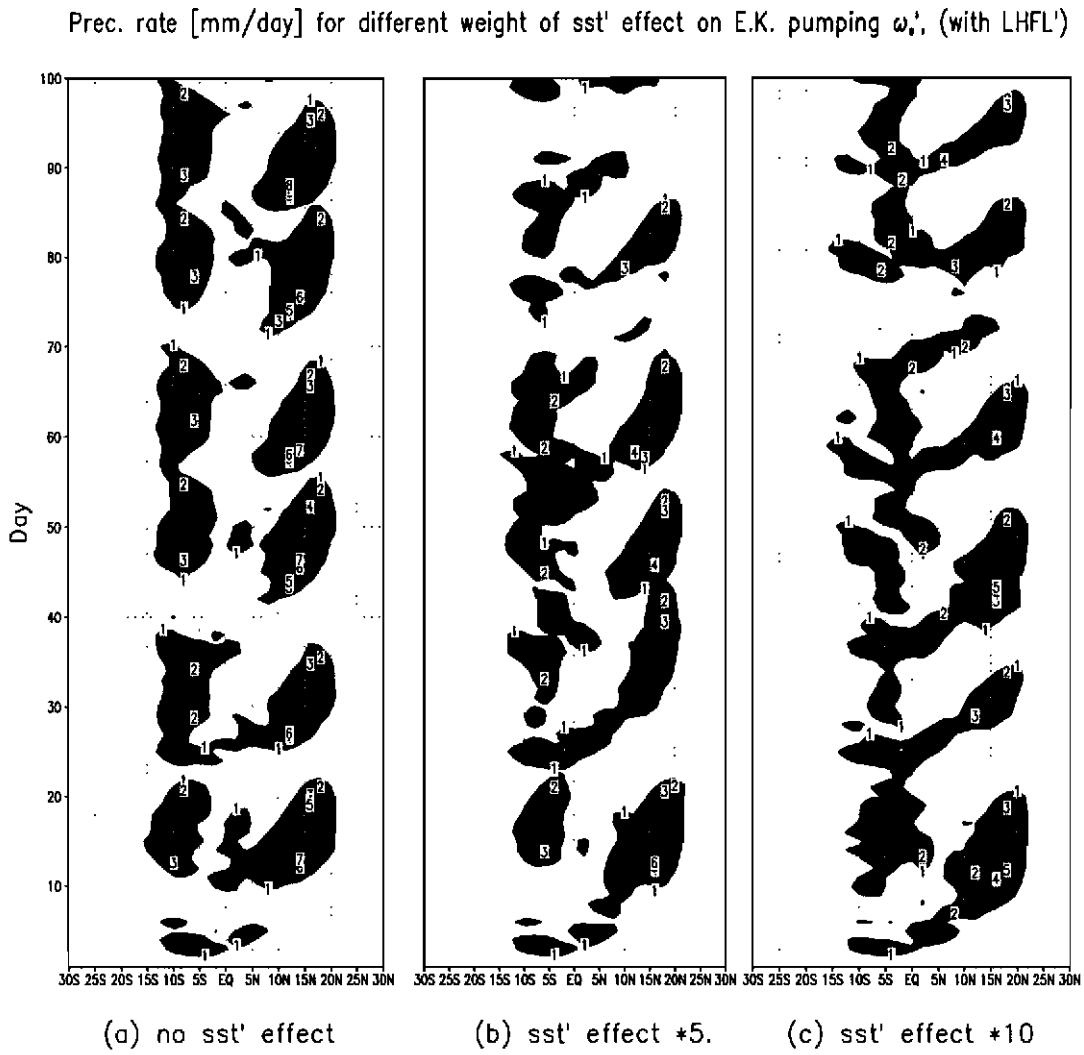

Figure 4.44: Latitude-time section of zonally averaged (60-100E) precipitation rate from 3D model using

(a) $0^* \left[-\frac{R(P_s-P_e)}{2P_e} * \left\{ D_1 \frac{\partial^2 sst'}{\partial x^2} + D_2 \frac{\partial sst'}{\partial x} + D_3 \frac{\partial^2 sst'}{\partial y^2} + D_4 \frac{\partial sst'}{\partial y} \right\} \right]$,

(b) $5^* \left[-\frac{R(P_s-P_e)}{2P_e} * \left\{ D_1 \frac{\partial^2 sst'}{\partial x^2} + D_2 \frac{\partial sst'}{\partial x} + D_3 \frac{\partial^2 sst'}{\partial y^2} + D_4 \frac{\partial sst'}{\partial y} \right\} \right]$,

(c) $10^* \left[-\frac{R(P_s-P_e)}{2P_e} * \left\{ D_1 \frac{\partial^2 sst'}{\partial x^2} + D_2 \frac{\partial sst'}{\partial x} + D_3 \frac{\partial^2 sst'}{\partial y^2} + D_4 \frac{\partial sst'}{\partial y} \right\} \right]$,

instead of $\left[-\frac{R(P_s-P_e)}{2P_e} * \left\{ D_1 \frac{\partial^2 sst'}{\partial x^2} + D_2 \frac{\partial sst'}{\partial x} + D_3 \frac{\partial^2 sst'}{\partial y^2} + D_4 \frac{\partial sst'}{\partial y} \right\} \right]$

for the vertical velocity at the top of the boundary layer (Ekman velocity).

(a) 200hPa basic state zonal wind in Exp.6

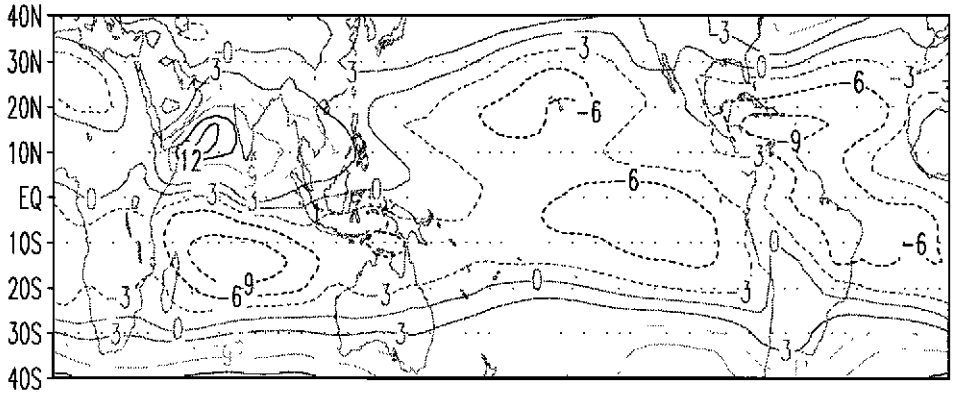

(b) 850hPa basic state zonal wind in Exp.6

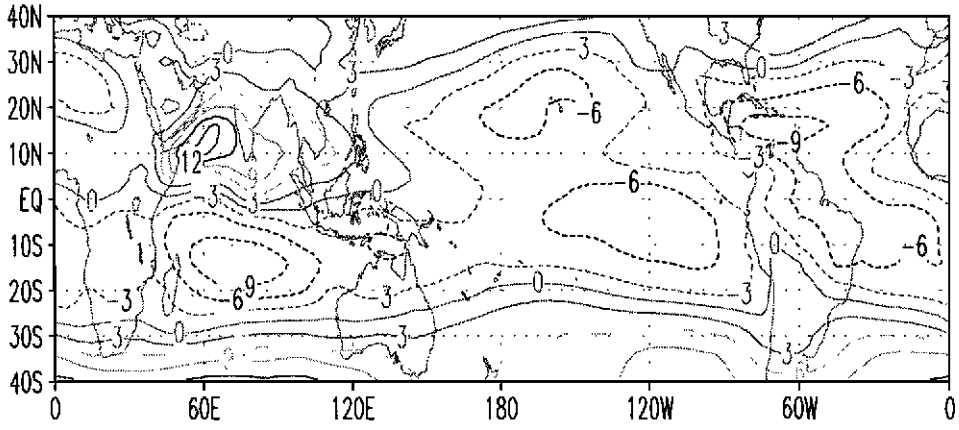

Figure 4.45: Basic state zonal winds at (a) 200hPa and (b) 850hPa used in Experiment 6.

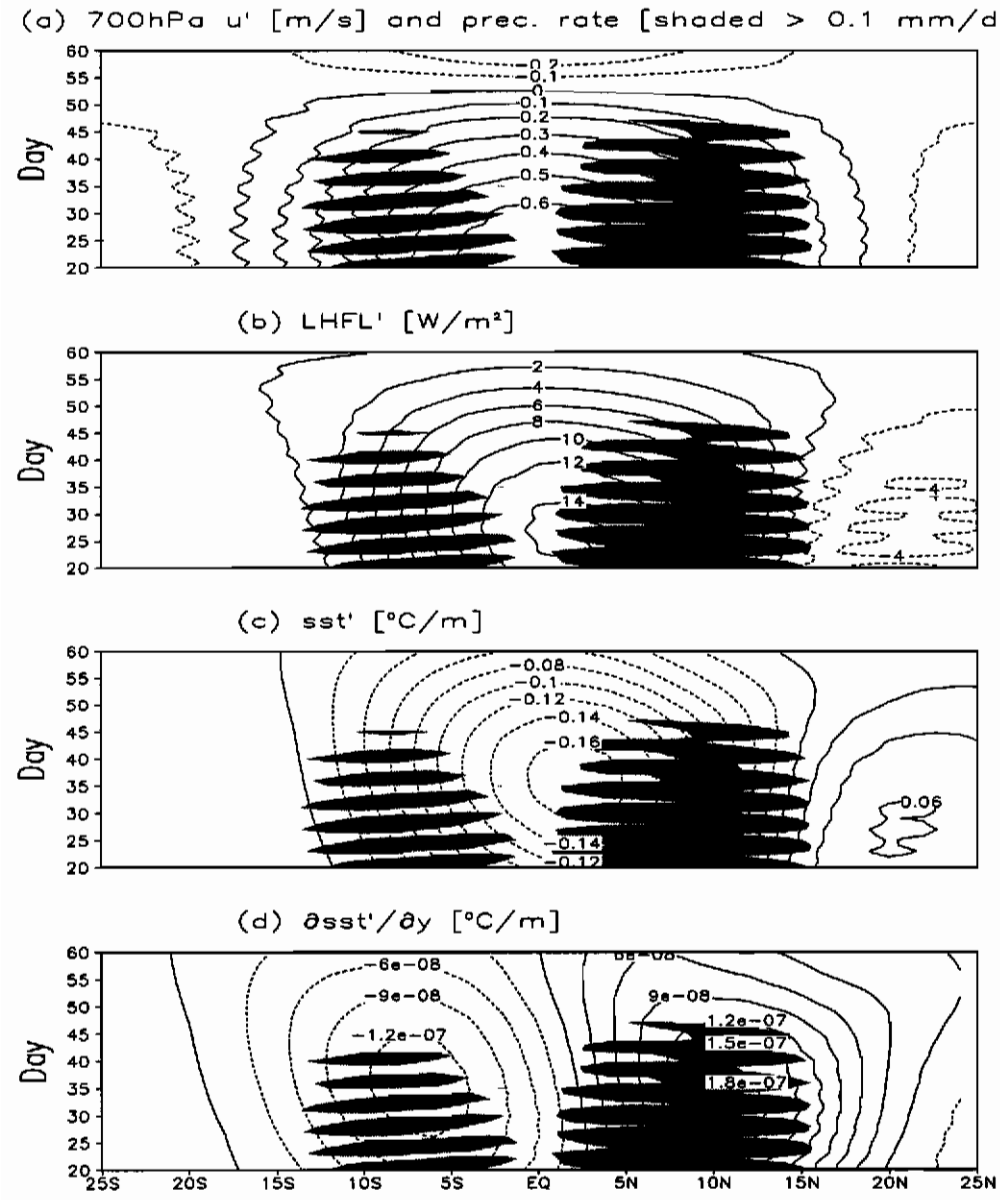

Figure 4.46: Latitude-time section of zonally averaged (60-100E) anomalies from 3D model using interactive SST when basic-state vertical motion ($\overline{\omega}$) = 0 Pa/s, basic state zonal winds at 850hPa ($\overline{u}_{850hPa}$) =11 m/s,

basic state zonal winds at 200hPa ($\overline{u}_{200hPa}$) =11 m/s, and

basic state meridional wind ($\overline{v}$) = 0.

(a) low-tropospheric zonal winds (m/s) and precipitation rate (shaded > 0.1 mm/day), (b) latent heat fluxes (W/m^2), (c) sea surface temperature (sst$'$), and (d) $\frac{\partial sst'}{\partial y}$.

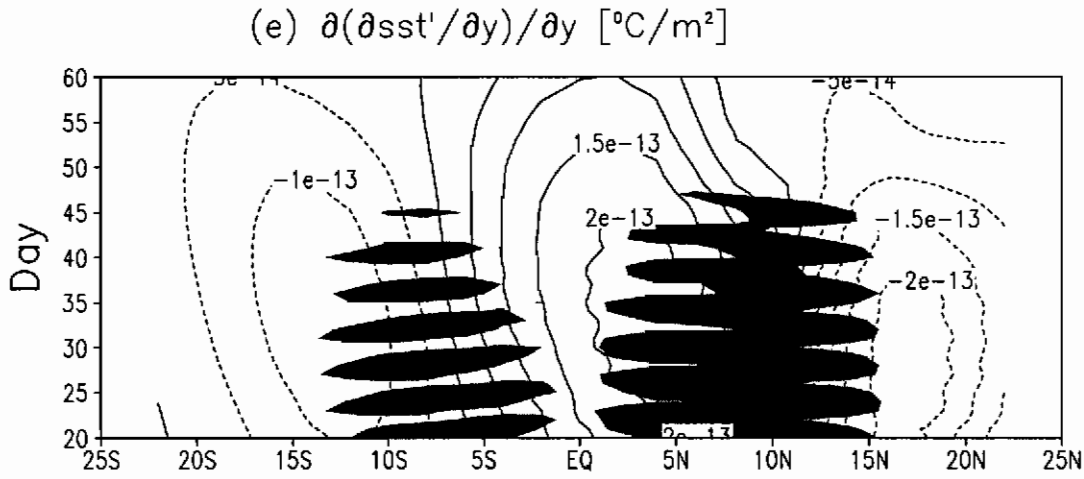

Figure 4.46: (Continued).

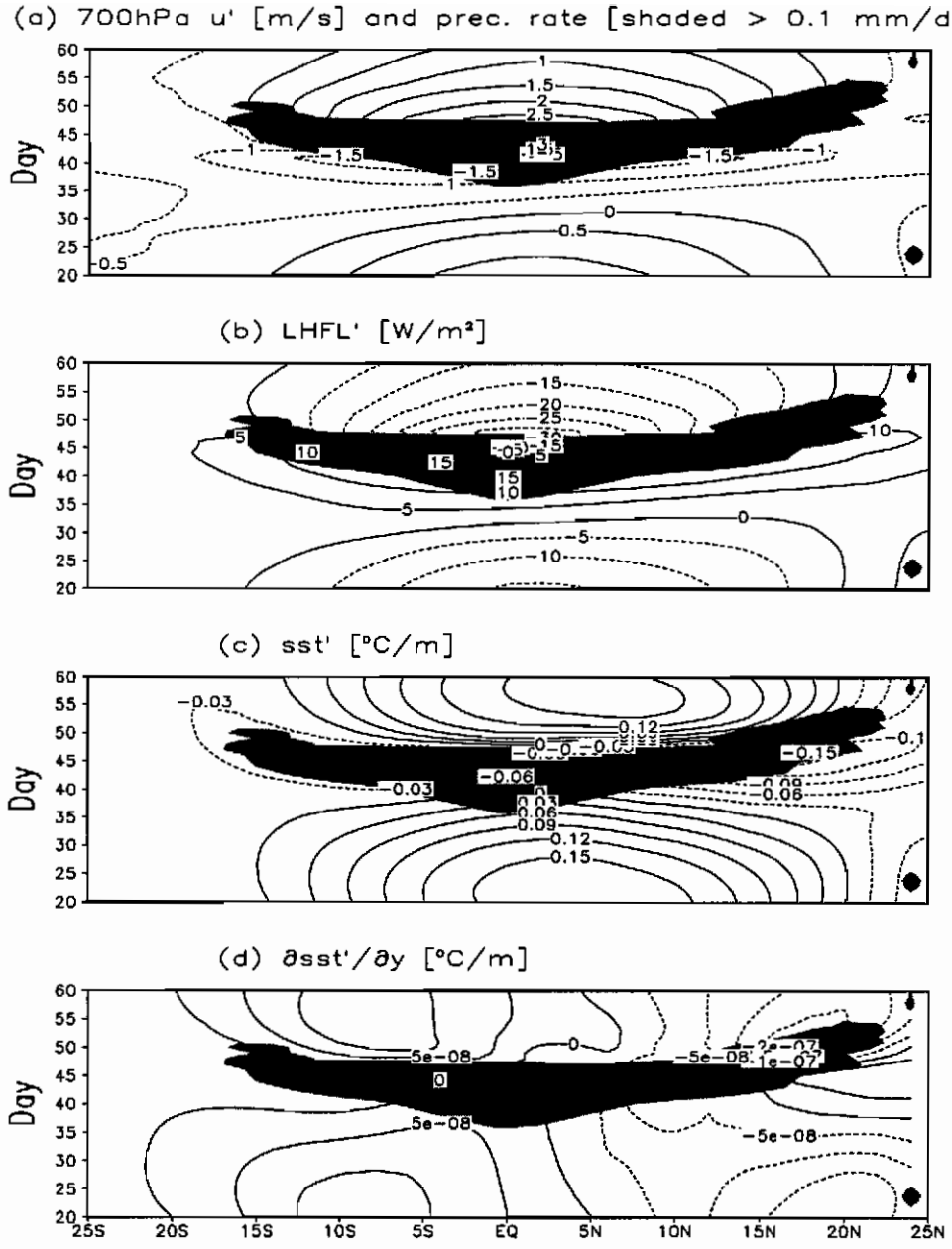

Figure 4.47: Latitude-time section of zonally averaged (60-100E) anomalies from 3D model using interactive SST when basic-state vertical motion ($\overline{\omega}$) = 0 Pa/s, basic state zonal winds at 850hPa ($\overline{u}_{850hPa}$) = -11 m/s,

basic state zonal winds at 200hPa ($\overline{u}_{200hPa}$) = -11 m/s, and

basic state meridional wind ($\overline{v}$) = 0.

(a) low-tropospheric zonal winds (m/s) and precipitation rate (shaded > 0.1 mm/day), (b) latent heat fluxes (W/m^2), (c) sea surface temperature (sst$'$), and (d) $\frac{\partial sst'}{\partial y}$.

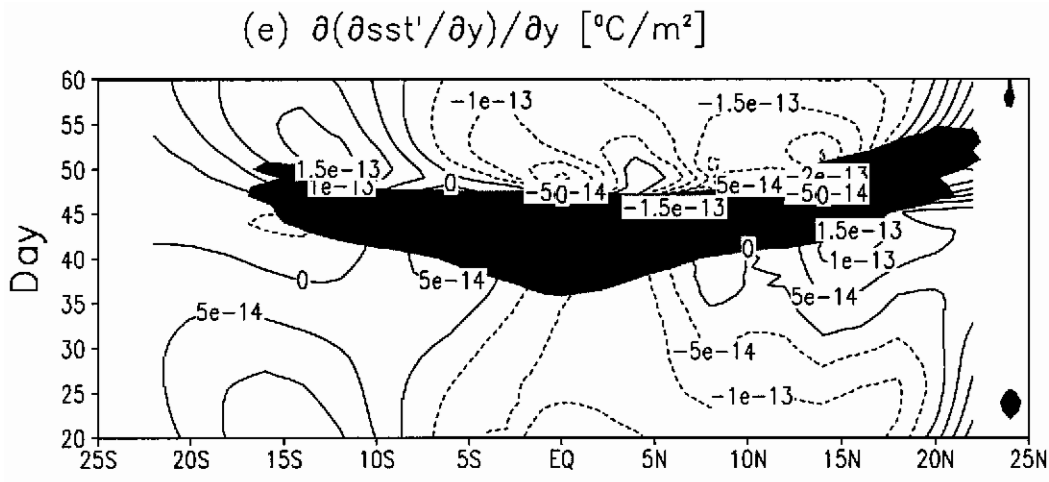

Figure 4.47: (Continued).

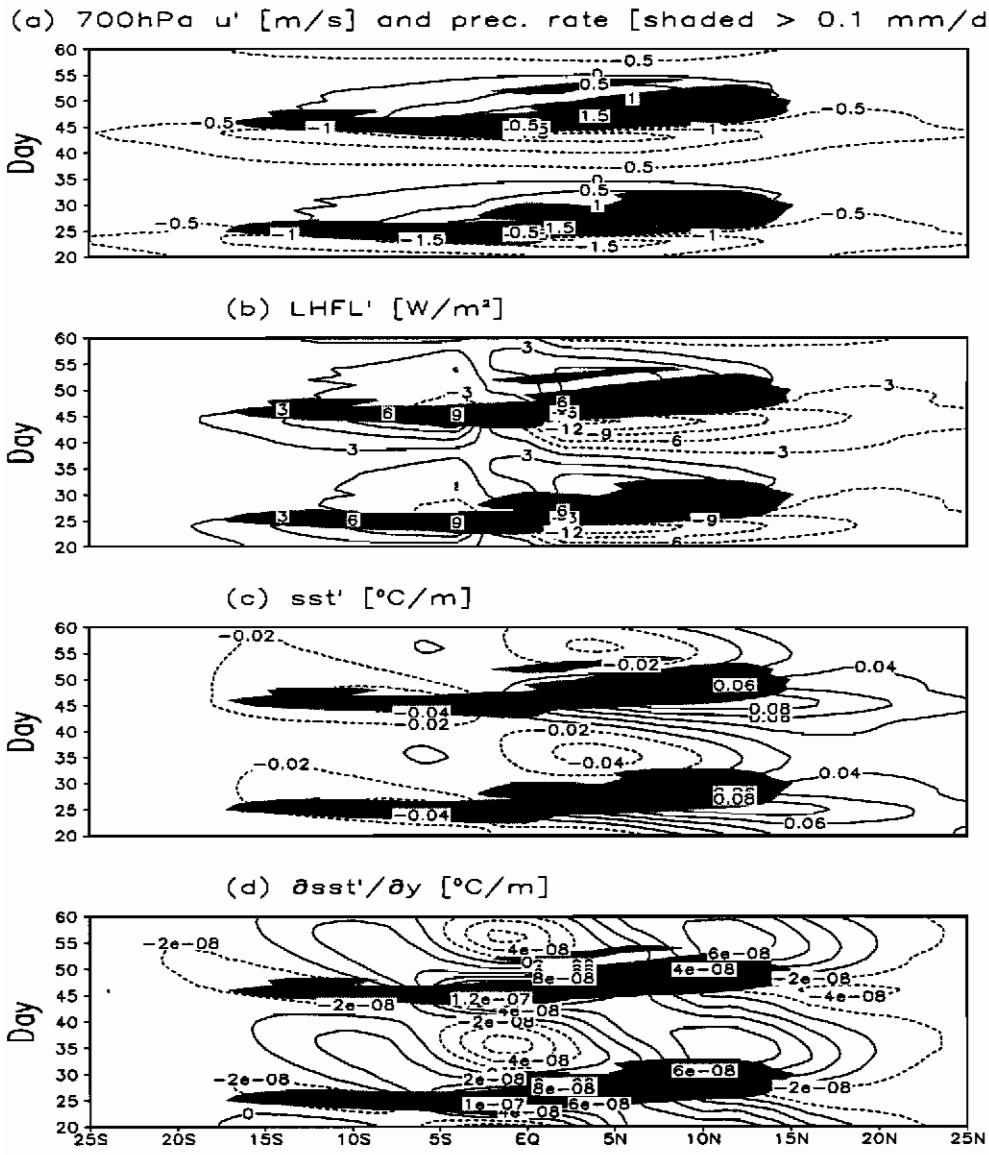

Figure 4.48: Latitude-time section of zonally averaged (60-100E) anomalies from 3D model using interactive SST when basic-state vertical motion ($\overline{\omega}$) = 0 Pa/s, basic-state zonal winds at 850hPa ($\overline{u}_{850hPa}$) =climatology 850hPa July-mean zonal winds, basic-state zonal winds at 200hPa ($\overline{u}_{200hPa}$) =climatology 850hPa July-mean zonal winds, and basic state meridional wind ($\overline{v}$) = 0.
(a) low-tropospheric zonal winds (m/s) and precipitation rate (shaded > 0.1 mm/day), (b) latent heat fluxes (W/m^2), (c) sea surface temperature (sst′), and (d) $\frac{\partial sst'}{\partial y}$.

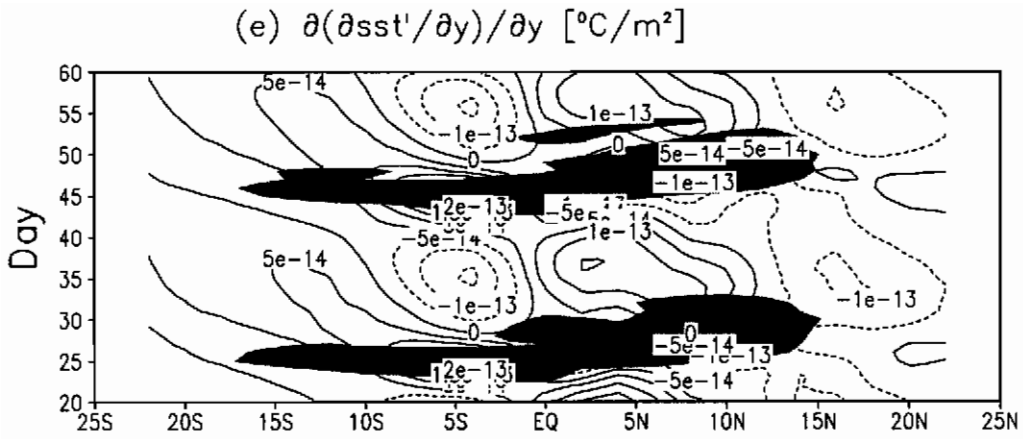

Figure 4.48: (Continued).

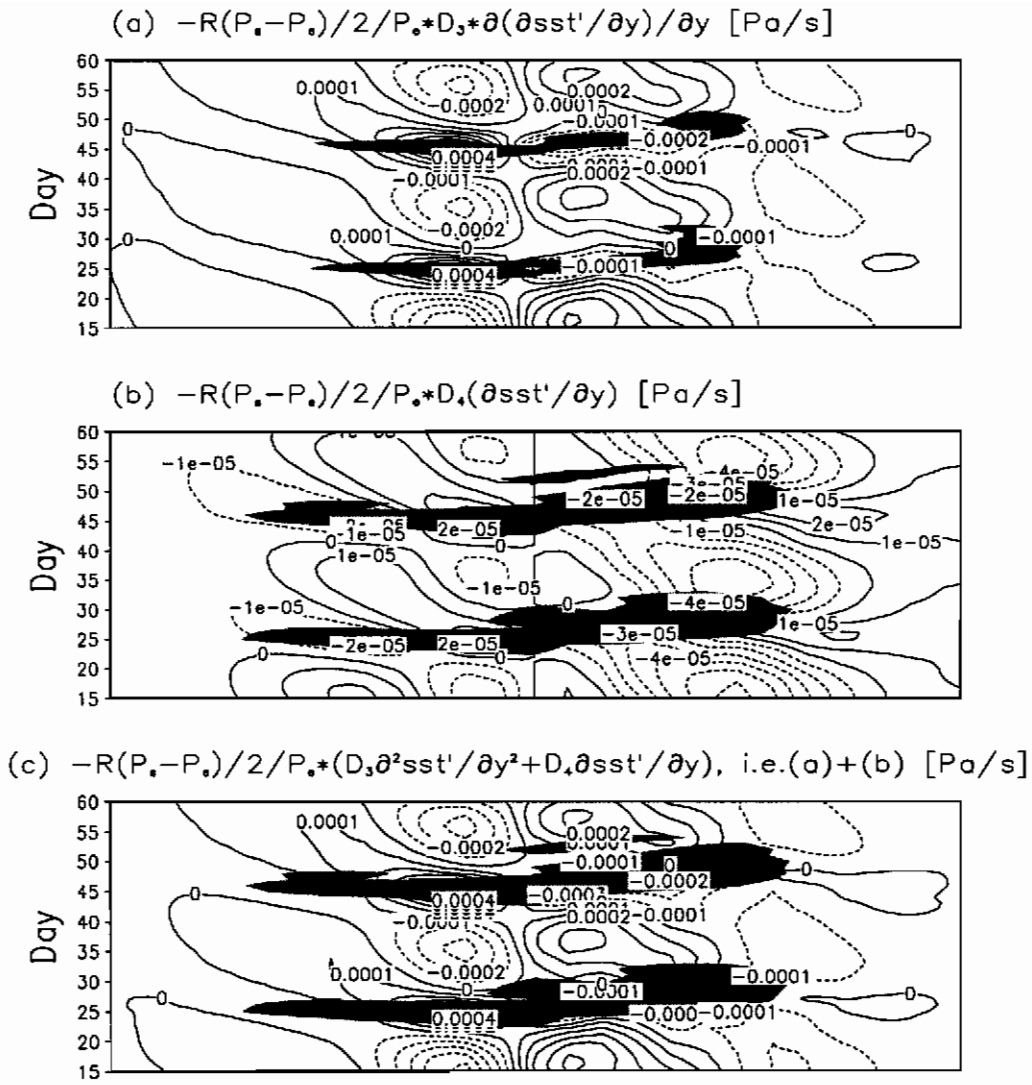

Figure 4.49: Latitude-time section of zonally averaged (60-100E) anomalies from 3D model using interactive SST when basic-state vertical motion ($\overline{\omega}$) = 0 Pa/s, basic-state zonal winds at 850hPa ($\overline{u}_{850hPa}$) =climatology 850hPa July-mean zonal winds, basic-state zonal winds at 200hPa ($\overline{u}_{200hPa}$) =climatology 850hPa July-mean zonal winds, and basic state meridional wind ($\overline{v}$) = 0.

(a) $-\frac{R(P_s-P_e)}{2P_e} * D_3 * \frac{\partial}{\partial y}(\frac{\partial sst'}{\partial y})$, (b) $-\frac{R(P_s-P_e)}{2P_e} * D_4 * \frac{\partial sst'}{\partial y}$,

(c) $-\frac{R(P_s-P_e)}{2P_e} * \{D_3 * \frac{\partial}{\partial y}(\frac{\partial sst'}{\partial y}) + D_4 * \frac{\partial sst'}{\partial y}\}$.